Performance Scaling of Gas-Fed Pulsed Plasma Thrusters

John Kenneth Ziemer

A DISSERTATION

PRESENTED TO THE FACULTY

OF PRINCETON UNIVERSITY

IN CANDIDACY FOR THE DEGREE

OF DOCTOR OF PHILOSOPHY

RECOMMENDED FOR ACCEPTANCE

BY THE DEPARTMENT OF

MECHANICAL AND AEROSPACE ENGINEERING

June, 2001

Performance Scaling of Gas-Fed Pulsed Plasma Thrusters

Prepared by:

John K. Ziemer

Approved by:

Professor Edgar Y. Choueiri
Dissertation Advisor

Professor Robert G. Jahn
Dissertation Advisor

Professor Szymon Suckewer
Dissertation Reader

Abstract

The performance scaling of gas-fed pulsed plasma thrusters (GFPPTs) is investigated theoretically and experimentally. Analytical models of the discharge current suggest that close to critically damped current waveforms provide the best energy transfer efficiency. A characteristic velocity for GFPPTs that depends on the inductance-per-unit-length and the square root of the capacitance-to-initial-inductance ratio is also derived in these models. The total efficiency is predicted to be proportional to the ratio of the exhaust velocity to the GFPPT characteristic velocity. A numerical non-dimensional model is used to span a large parameter space of possible operating conditions and suggest optimal configurations. From the non-dimensional model, the exhaust velocity is predicted to scale with a non-dimensional parameter called the dynamic impedance parameter to a power that depends on the mass loading prior to the discharge.

To test the validity of the predicted scaling relations, the performance of two rapid-pulse-rate GFPPT designs, PT5 (coaxial electrodes) and PT9 (parallel-plate electrodes), has been measured over 70 different operating conditions with argon propellant. The performance measurements are made in a recently renovated facility that uses liquid nitrogen cooled baffles and a micro-thrust stand capable of measuring impulses $< 20\ \mu$Ns within $<10\%$. The measurements demonstrate that the impulse bit scales linearly with the integral of the discharge current squared, as expected for an electromagnetic accelerator. The measured performance scaling in both electrode geometries is shown to be in good agreement with theoretical predictions using the GFPPT characteristic velocity. Normalizing the exhaust velocity and the impulse-to-energy ratio by the GFPPT characteristic velocity collapses almost all the measured data onto single curves that represent the scaling relations for these GFPPTs.

Acknowledgments

When I look back at my time at Princeton, I can think of the many things I've learned and the many friends I've gained. I am very fortunate to have been advised by two experts in the field, Prof. Edgar Choueiri and Prof. Robert Jahn. They have taught me more about electric propulsion and basic research than I ever thought possible. Eddie, I will always be amazed by your ability to dive into a new subject and master it. I look forward to more late-night discussions on baseball, squash, philosophy, art, macs, and just about anything else. Prof. Jahn, your insights into difficult problems are profound and legendary. I was happy to be on the receiving end of your wit and wisdom on more than one occasion. To both, I can't thank you enough for your advice, mentorship, and faith in my abilities. I would also like to thank Prof. Szymon Suckewer for his comments on my dissertation, as well as Prof. Harvey Lam, Prof. Sam Cohen, and Prof. Nat Fisch for their involvement in my research and graduate instruction. For Dr. Daniel Birx, I truly wish he could be here to see this. This dissertation is dedicated in his memory.

My friends at Princeton made all the difference in the time I spent there. I'll always remember the cooking and the midnight plasma sessions with Ted Cubbin and Paolo Gessini. Patrick Mahoney taught me all I really know about computers and barbecuing. Sheff, Harris, Cowles, and Bob Anderson were my roommates at one time or another in 3Q. I'll always remember the times at the D-Bar, reunions, our friend FH, spokey, the recycled furniture, mattress surfing, long nights at the Queen's Tavern, in New York and Philadelphia, Jimmy's Fat Cocoa, late night runs to the Wa, Sunday afternoon Taco Bell runs, Neon Lady, four-wheeling in the rental car, the golf, the olds, the horizon and the jetta, the top hat incident and the night that led up to it, movies with Maria, the noises of the Hibben, cybertubes, softball, all those lunches at George's and Tex-Mex, the playground, the squishy-side, the tour, and all the laughs–we sure laughed a lot. To the band: Bob, Mike, Geoff, Brad, and Scott, I never knew I had it in me–some will argue that I still don't–but when we were in the grove, there was nothing like it. Craig Woolsey is one of the most sincere people I know who tried his best to make the department a fun place to be while we were there. We all owe him a lot for that. Craig, I wish you and Sarah all the best. Best wishes also go out to my friends Armelle, Deborah, Irena, Cristin, Amy, Jill, Heather, Mike, Dave, and Tony who always were the life of the party.

To everybody in the EP lab, you are my good friends and more. Kevin Diamant, George Miller, and Bob Sorenson taught me how to build an experiment that works the first time, or at least how to fix it when it didn't. Vincent Chiravalle is a model of perseverance with a personality and heart that fills the room–literally. Vince, take care always, and I know you'll go far (probably in first class!). Andrei Litvak left a legacy of hard work that gave the lithium thruster its first legs and me a

better understanding of dedication. Kamesh Sankaran is someone I could always share new ideas with easily, no matter how crazy they seemed. Kamesh, I think I still owe you for crawling down into that DP. Tom Markusic, a fellow PPT fanatic, always challenged me to be a better scientist. Tom, I think we both look forward to learning even more from each other in our new jobs at NASA. Say hello to Christa, Elena, and Nate for me. I never saw much of Andrea Kodys and Gregory Emsellem as they always seemed to be just coming in when I was leaving the lab and visa versa. When we did see each other though, we had a great time! Andrea, come out and visit JPL as soon as you can, we need your expertise. To the new guys: Lenny, Kurt, Jack, and Slava, congrats on passing your general exams–now get back to work, slackers!

In all this effort, I had the support of my entire family. Mom, Dad, Grams, Christine and Scott, your support meant the world to me. When I needed someone to lean on and talk to, you were there with understanding. Sometime in the future, I hope I can be there for you in a similar way. To my long time friends that have been with me the whole way: Jeff, Jason, Kris, Jeff, Arjay, and Liz, you're the best, and I'll see you all soon. To my new family members: Al, Mary, Michael, Laura, and Matt, thanks for taking me in during this crazy time. I look forward to the good times to come.

To the true love of my life, Lisa Taneyhill Ziemer, I say what everyone around you knows already, you're amazing. How could I have ever gotten through this without you? Your love and support gave me my reason to stay in Princeton, to keep working the long hours, and finally to give this one last push and finish all together. You could never know how happy it makes me to be with you and to know that for the rest of our lives, we'll be together. (Well, us and the MKT, that is!) I love you very much.

This dissertation carries the designation 3016-T in the records of the Department of Mechanical and Aerospace Engineering.

Contents

List of Symbols

A_e — Nozzle exit area [1.4]

$\vec{B}$ — Magnetic field vector [2.4]

C — Total capacitance of the main discharge capacitor bank [4.4]

d — Outer electrode profile constant [3.32]

E — Stored energy used in one GFPPT pulse [1.8]

$f_c(\psi)$ — Correction factor to the integral of the current squared for a crowbarred discharge [3.8]

$f_J(\psi)$ — Correction factor to the value of the peak current [3.11]

$f_t(\psi)$ — Correction factor to the time when the peak current occurs [3.12]

f_p — Pulse frequency during a burst, $1/\tau_p$ [1.4]

g_0 — Acceleration of gravity at sea level, 9.81 m/s^2 [1.3]

h — Separation (height) between electrodes [4.11]

I_{bit} — Average impulse provided by a single pulse in a burst [1.4]

I_{sp} — Specific impulse [1.3]

I_{total} — Total impulse requirement for a given mission [1.3]

J — Total discharge current [2.1]

J_{peak} — Peak current value during the discharge [3.11]

$\vec{j}$ — Current density vector [2.4]

k — Boltzmann's constant, 1.38e-23 J/K [2.14]

L — Total inductance of the effective discharge circuit [2.1]

L_0 — Initial inductance of the discharge [2.2]

L_f — Final inductance of the discharge [3.14]

ΔL — Change in inductance during the discharge [3.14]

L' — Inductance-per-unit-length [2.2]

ℓ_{elec} — Length of electrodes [2.15]

ℓ_{gas} — Length of propellant gas column before each pulse [2.14]

M_0 — Initial spacecraft mass [1.1]

$M_{payload}$ — Payload mass (total spacecraft mass except for propellant, propulsion system, and power supply masses) [1.1]

M_{power} — Power supply mass used for electric propulsion system [1.6]

$M_{propellant}$ — Propellant mass [1.1]

$M_{thruster}$ — Thruster mass [1.9]

Brackets indicate the equation number where the symbol first appears.

m	Instantaneous amount of propellant mass in the discharge [2.4]
m_0	Initial propellant mass in the current sheet [3.27]
m_{accel}	The amount of propellant mass accelerated by the discharge [2.11]
m_{avail}	The amount of propellant mass available for acceleration [2.11]
m_{bit}	The amount of propellant mass injected before each pulse [1.8]
m_{lost}	The amount of propellant mass lost outside of the electrode volume before the discharge [2.15]
m_{waste}	The amount of propellant mass wasted each burst due to finite amount of time required to open and close the valve [4.7]
m_{eff}	Effective mass of the thrust stand [5.4]
m_w	Molecular weight of the propellant gas [2.14]
$\dot{m}$	Propellant mass accumulation rate in the current sheet [2.6]
$\dot{m}_{avg}$	Average propellant mass flow rate [1.4]
$\dot{m}_{ss}$	Steady-state propellant mass flow rate injected during a burst of pulses [2.15]
m'	Mass-per-unit-length [3.30]
N_{pb}	Number of pulses per burst in an SRL-EPPDyL GFPPT [4.2]
N_{ptot}	Total number of pulses required for a mission or the lifetime of a GFPPT [1.10]
P	Power supplied by spacecraft bus to an EP system [1.5]
P_{avg}	Average power used by a SRL-EPPDyL GFPPT [4.2]
P_{circ}	Instantaneous power in the discharge circuit [2.7]
p_e	Nozzle exit pressure [1.4]
p_∞	Background pressure [1.4]
Q_0	Initial charge on the main discharge capacitor bank [A.5]
R	Total circuit resistance including the internal capacitor resistance and effective plasma resistance [2.1]
r_{in}	Inner electrode radius in a coaxial geometry [4.12]
r_{out}	Outer electrode radius at the breech in a coaxial geometry [4.12]
T	Thrust [1.4]
T_p	Plenum temperature [2.14]
t_{final}	Final time for the discharge current model [3.15]
t_{peak}	Time of peak current in the discharge [3.12]

$\mathcal{U}$	Characteristic GFPPT performance velocity [3.26]
$\tilde{U}$	Langmuir's "characteristic velocity" [1.7]
u	Current sheet velocity in the axial direction [2.4]
u_e	Axial current sheet velocity at the end of the discharge [2.11]
$\bar{u}_e$	Mass average exhaust velocity [1.1]
V_0	Initial voltage on the capacitor bank before each pulse [4.4]
V_{cap}	Instantaneous capacitor voltage [2.3]
ΔV	Change in spacecraft velocity during a maneuver [1.1]
$\tilde{V}$	Pulsed Electric Propulsion (PEP) characteristic velocity [1.11]
v_{th}	Thermal velocity of propellant at plenum conditions [2.14]
$W_{propellant}$	Total weight (at sea level) of the propellant for a mission [1.3]
w	Width of parallel-plate electrodes [4.11]
z	Axial current sheet coordinate (along acceleration axis) [2.2]

Greek Symbols

α	Non-dimensional dynamic impedance parameter [3.43]
α_p	Power supply specific power, kg/W [1.6]
α_e	Thruster specific energy, kg/J [1.9]
γ	Non-dimensional mass distribution parameter [3.43]
δ	Non-dimensional position variable [3.39]
ζ	Non-dimensional current variable [3.39]
ς	Damping coefficient of the thrust stand [5.4]
η	Overall electric propulsion system efficiency [1.5]
η_a	Accelerator efficiency [2.11]
η_{energy}	Energy transfer efficiency [2.11]
$\eta_{dynamic}$	Dynamic efficiency [2.11]
η_{fs}	Feed system efficiency [4.7]
η_{pc}	GFPPT power conditioner efficiency [4.4]
$\eta_{profile}$	Lorentz force profile efficiency [2.11]
η_{pu}	Propellant utilization efficiency [2.11]
η_{sweep}	Current sheet propellant sweeping efficiency [2.11]
η_t	Thruster efficiency [1.8]

κ	Fraction of the mass bit wasted on every burst [4.7]
Λ	Inductance change factor [3.14]
λ	Non-dimensional electrode geometry parameter [3.43]
μ_0	Magnetic permeability of free space, $4\pi \times 10^{-7}$ H/m [4.11]
π	Circumference-to-diameter ratio, 3.14159 [4.11]
ρ	Non-dimensional mass variable [3.43]
ρ_0	Non-dimensional initial mass parameter [3.43]
τ	Length of time the propulsion system is activated during a mission, ultimate thruster lifetime in seconds, and non-dimensional time variable [1.6,3.39]
τ_{opt}	Optimal time of integration for maximum efficiency in the non-dimensional model [3.64]
τ_p	Time between individual pulses in a burst [4.1]
τ_m	Duration of steady propellant mass flow during a burst [4.2]
τ_d	Delay between bursts [4.2]
Φ	Propellant mass fraction, $M_0/M_{propellant}$ [1.2]
ψ	Critical resistance ratio [3.4]
ω	Natural frequency of the effective GFPPT circuit [A.2]
ω_n	Natural frequency of the thrust stand [5.4]

This thesis is dedicated in the memory of Daniel Birx.

Quality is the continuing stimulus which our environment puts upon us to create the world in which we live. All of it. Every last bit of it.

–Robert M. Pirsig

Chapter 1

Introduction

Over the last century, traveling in space has evolved from a science fiction fantasy into a common reality. In just the last few years, a new spacecraft has been launched, on average, every four days worldwide. We now rely on them for communication, observation, exploration, and a variety of other missions that have expanded our available resources and pushed the bounds of human knowledge. Still, with most spacecraft simply orbiting the earth, space travel could be considered to be in its infancy. Even our most distant probe Voyager I, launched in 1977 and currently traveling at a speed of 17 km/s, is only 12 billion kilometers away from earth, less than one one-thousandth of the way to the nearest star. Like the first automobile or airplane built almost a century ago, today's spacecraft use technology that just begins to provide the capability we will need in the next century to travel routinely within and beyond the boundaries of earth's gravity.

In most applications, spacecraft require a means of imparting motion, an engine that accelerates the craft to high velocity. Rocket engines or "thrusters" provide acceleration by expelling propellant mass with a velocity opposite to the direction of intended travel. Assuming a constant thrust and neglecting the influence of gravity and drag during the maneuver, an equation for a spacecraft's velocity change, ΔV, was first expressed in 1903 by Tsiolkovsky [1] and is now commonly referred to as the rocket equation,

$$\Delta V = \bar{u}_e \ln \left(\frac{M_0}{M_0 - M_{propellant}} \right),$$ (1.1)

where $\bar{u}_e$ is the mass average exhaust velocity of the propellant relative to the spacecraft and M_0 is the total mass of the spacecraft including the propellant mass, $M_{propellant}$, before the rocket firing.

The most important goal for any spacecraft is to deliver, and in many cases maintain, the most payload mass possible. Normalized by the total initial mass, the *payload mass fraction*, $M_{payload}/M_0$, can be increased simply by reducing the other mass fractions. For many spacecraft, often the largest mass fraction is related to

the propellant mass, $M_{propellant}/M_0$, which is controlled by the choice of propulsion system and the maximum achievable exhaust velocity. As seen from Eq. (1.1), the propellant mass required to perform a given ΔV decreases as the exhaust velocity increases, leaving a larger mass fraction including payload remaining after the maneuver is complete.

Electric propulsion (EP) is one type of *proven* spacecraft propulsion system that has very large exhaust velocities, between 1-100 km/s or even higher depending on the specific nature of the acceleration mechanism. A number of electric propulsion devices have been studied for over forty years (see Ref. [2] and Refs. [3,4]) and are now routinely used in space. For example, various EP devices are currently the baseline propulsion system for many US satellite manufactures including Hughes, Lockheed Martin, TRW, and Space Systems Loral [4]. NASA has successfully used an NSTAR Program Ion Thruster as the primary propulsion system on one of its latest experimental missions, Space Technology I [5]. Russian satellite designers have routinely used a version of the Hall thruster called the Stationary Plasma Thruster (SPT) for more than ten years on many of their earth orbiting satellites [6].

Electric propulsion systems require a power source for operation, usually in addition to that dedicated to the payload. As the extra power supply and power conditioning equipment add more mass to the spacecraft, the EP device must be designed and operated such that the propellant mass savings offset the power supply penalty. Obviously, the conversion efficiency of the supplied power to the directed kinetic power in the exhaust becomes very important in reducing the propellant, propulsion system, and power supply mass. In addition, as many of these systems are now going from laboratory models to flight hardware, more emphasis is being placed on developing experimentally verified *performance scaling laws* that can be used for selecting and designing an appropriate EP system for a given mission. Improving and predicting the performance of electric propulsion devices is paramount to their utility as spacecraft propulsion systems.

The gas-fed pulsed plasma thruster (GFPPT) is an unsteady, predominantly electromagnetic accelerator that can be used for either primary propulsion or attitude control maneuvers. Due to its pulsed nature, it can operate at variable *average* power and thrust levels that are throttled by altering the pulse frequency, energy per pulse, or the amount of propellant mass accelerated by the discharge. It also has the advantages of using a simple discharge circuit, supplying precise and small impulses ($< 100\mu$Ns) for fine positioning, and the ability to use virtually any type of propellant (a noble gas, hydrazine, water vapor, ammonia, hydrogen, nitrogen, etc.).

Although studied since the late 1950's, purely unsteady GFPPTs have only been tested in the laboratory. In contrast, pulsed, gas-fed *quasi-steady* MPD thrusters were flown, albeit experimentally, on a number of missions including recently on a 1995 Japanese mission, the Space Flier Unit [7]. Another unsteady device, the ab-

lative pulsed plasma thruster (APPT) uses solid Teflon for propellant and has been one of the most flight-tested forms of electric propulsion to date. In 1964, a Russian Zond spaceflight made an APPT the first EP device ever to be launched into space. On a more recent mission ending in 1989, an APPT was used successfully as an attitude control device for ten years on a US Navy Satellite, NOVA/TIP [8]. Two current missions that use APPTs for attitude control include an Air Force Mission, TechSat 21 [9], and a recently launched NASA New Millennium Program mission, EO-1 [10].

Unfortunately for past *gas-fed* PPTs of the 1960's, high pulse energy and relatively poor performance led to massive thruster designs that were not as appealing as some competing EP systems or even as useful as some conventional chemical propulsion systems. In fact, after 1970 and up until 1992, almost no further research on purely unsteady gas-fed PPTs was conducted for those reasons. Furthermore, due to the typically small impulse produced by each discharge, millions or even billions of pulses were required to perform the large total impulse maneuvers GFPPTs were being designed for at the time [11]. For these missions, the lifetime of the thruster electronics and fast-acting gas valves was (and still is) a primary concern. Moreover, even after considerable performance testing in the 1960's, experimentally verified performance scaling relations did not exist, making it difficult to apply or tailor GFPPTs to any specific mission.

Recently, with work at Princeton's Electric Propulsion and Plasma Dynamics Laboratory (EPPDyL) and in cooperation with Science Research Laboratory, Inc. (SRL), GFPPTs have resurfaced as a viable alternative for a variety of missions. These include NASA's Europa Orbiter, Pluto Fly-by and Space Technology Interferometer missions, as well as DARPA's Orbital Express and Motorola's Teledesic Constellation. The current research at EPPDyL and SRL has focused on using all solid-state electronics, operating at low energy, and improving performance to decrease the overall mass. Potentially the most significant improvement has come from grouping pulses together in *bursts* which provides a high propellant mass utilization efficiency while reducing the required number of valve cycles over the lifetime of the device. With this in mind, the goals for this technology were two-fold:

1. Obtaining a 100% mass utilization efficiency while being able to use existing, space-qualified valves that have greater than a one million cycle lifetime.

2. Developing a low-mass, low-energy GFPPT with the same as or better performance than previous GFPPTs tested at higher energy. A target was set for 50% efficiency at a specific impulse of 5000 s using less than 5 J per pulse.

Achieving these goals has included the following research projects which provide the basis for this dissertation:

- Examining the effects of using a solid-state, high-current switching technology at pulse rates above 4 kHz on propellant utilization, reliability, and performance.

- Determining the best way to group pulses together in bursts which allows thrust and power modulation as well as reducing the total number of valve cycles over the lifetime of the device.

- Creating a low-energy discharge initiation system that provides a symmetric current sheet reliably without inducing a large amount of electrode erosion.

- Developing a highly accurate ($< 10\%$ error), low-impulse ($< 20\mu$Ns), thrust stand and high-speed current sheet visualization diagnostics to measure performance.

- Refurbishing a fiberglass high-vacuum facility to reduce the effects of background contaminants and vibrational noise on impulse measurement.

- Designing and testing many thruster prototypes to examine changes in performance from modifications to geometry, propellant injection, and driving circuitry.

- ***Deriving, testing, and verifying performance scaling laws based on physical models for current sheet acceleration.***

This chapter provides motivation for the last item, which consists of measuring and predicting the performance scaling of GFPPTs. We start by laying out detailed propulsion needs for present and future space missions where GFPPTs might prove useful if they can be designed to match the requirements. We also explain the trade-offs between efficiency, lifetime, and mass for a pulsed electric thruster (such as a GFPPT) to explain why performance scaling relations are important. Next, we describe the history of GFPPT research and the need for an accurate, experimentally verified, performance model. Finally, we present a outline for the research presented in this dissertation which aims to fill this need.

1.1 Spacecraft Mass Distribution and Optimization

For most conventional spacecraft, the propellant mass makes up a large fraction of the total mass, even after it has reached orbit. From Eq. (1.1), the propellant mass fraction, Φ, is defined here as the ratio of propellant mass to initial mass and depends on the mission ΔV requirement and the exhaust velocity,

$$\Phi \equiv \frac{M_{propellant}}{M_0} = 1 - e^{-\frac{\Delta V}{u_e}} . \tag{1.2}$$
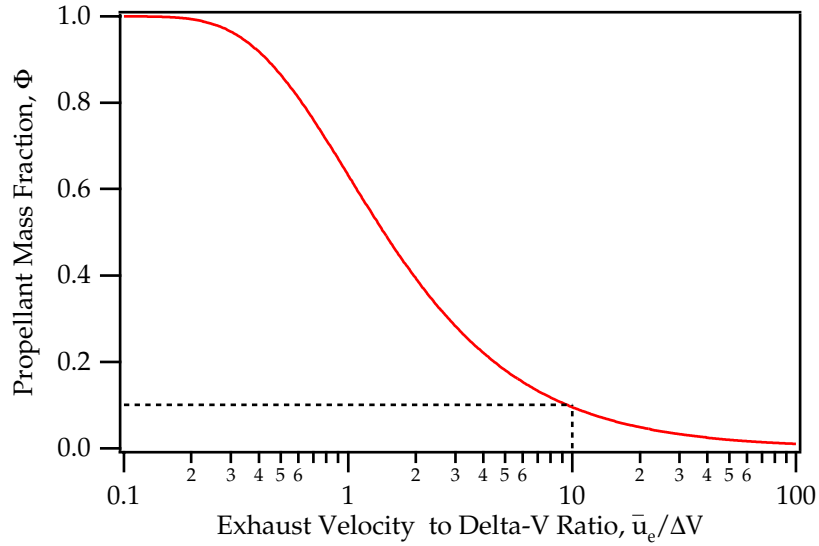
Figure 1.1: Propellant mass fraction as a function of the exhaust velocity-to-ΔV ratio. The dashed line shows a propellant mass fraction value of 10% when the exhaust velocity is approximately ten times the ΔV requirement.

Figure (1.1) plots this relation and shows that for the propellant mass fraction to be less than 10%, the exhaust velocity must be at least 10 times greater than the ΔV requirement. Due to the exponential nature of Eq. (1.2), large gains can be made by increasing the exhaust velocity-to-ΔV ratio from one to ten. For example, using a maneuver where $\Delta V = 3000$ m/s, an EP system with an exhaust velocity of 30,000 m/s will have a significantly lower propellant mass fraction (9.5%) compared to a typical chemical system with a 3,000 m/s exhaust velocity (63%). To find out which missions can benefit from using an EP device, specifically the GFPPT, we must know their ΔV requirements.

1.1.1 Mission Requirements

Each mission can be described by a specific ΔV requirement and a maximum allowable amount of time to complete it. The time limits can be determined, for example, by a maximum radiation dosage, a life support limitation, or a commercial demand to get an immediate return on a satellite investment. Table 1.1 shows examples of typical missions with their ΔV and time requirements. Not immediately obvious is that the ΔV requirements do not depend on the total mass of the spacecraft. For example, the ΔV requirement for a 2,000 kg communications satellite will be nearly the same as for a 10 kg microsatellite performing the same kind of maneuver.

Mission	ΔV (m/s)	Time Requirement
East-West Station Keeping	2	per year
North-South Station Keeping	50	per year
LEO-GEO Transfer	6,000	100 days
LEO to Earth Escape (low thrust)	8,000	200 days
Manned Earth to Mars and Return	14,000	500 days
Interstellar Probe	>100,000	>10 years

Table 1.1: Approximate mission ΔV requirements and acceptable mission durations. The total ΔV requirements for station keeping missions depends on the lifetime of the satellite. Taken from Refs. [2, 12–14].

On the other hand, many missions have time limits which create minimum thrust requirements that change with spacecraft mass and size. Furthermore, thrusting maneuvers that have a long duration must use a modified form of the rocket equation that includes the effects of gravity. Operating in a significant gravitational potential for a long period of time generally increases the ΔV requirement. For an optimized low-thrust trajectory, the increase can be limited to a factor of near $\sqrt{2}$ by using an optimal spiral trajectory with the celestial body at its center [15]. In many cases, the achievable exhaust velocity of an EP system is more than enough to make up for this additional ΔV requirement and still save a significant amount of propellant. The total mass savings can translate into a larger payload mass fraction, longer spacecraft lifetime, and/or a smaller spacecraft that costs less to launch in the first place. All of these possibilities form a strong motivation for using electric propulsion systems in general.

1.1.2 The Optimal Exhaust Velocity

As mentioned previously, there is a balance between the propellant mass that can be saved by having a large exhaust velocity and the extra power supply mass necessary to drive the EP system. The mass of the propulsion device, power supply, and propellant depend on the efficiency of the entire system and the exhaust velocity or *specific impulse*. The specific impulse, I_{sp}, is the ratio of the total impulse provided by the propulsion system to the propellant weight on the surface of the Earth and is essentially the exhaust velocity divided by ten,

$$I_{sp} \equiv \frac{I_{total}}{W_{propellant}} = \frac{\bar{u}_e \, M_{propellant}}{g_0 \, M_{propellant}} = \frac{\bar{u}_e}{g_0} \approx \frac{\bar{u}_e}{10 \, m/s^2}. \tag{1.3}$$

In the absence of any background pressure, p_∞, or significant exhaust pressure, p_e, over the exit area, A_e, the thrust, T, is simply the product of the average propellant

mass flow rate, $\dot{m}_{avg}$, and the mass average exhaust velocity relative to the rocket,

$$T = \dot{m}_{avg}\bar{u}_e + (p_e - p_\infty)A_e = \dot{m}_{avg}\bar{u}_e = f_p I_{bit}, \tag{1.4}$$

where f_p is the pulse frequency and I_{bit} is the impulse supplied by one individual discharge from a pulsed electric propulsion (PEP) system. The overall efficiency, η, is defined as the ratio of the directed kinetic power in the exhaust to the power supplied by the spacecraft bus to the thruster, P,

$$\eta \equiv \frac{\frac{1}{2}\dot{m}_{avg}\bar{u}_e^2}{P} = \frac{\bar{u}_e}{2}\frac{T}{P}. \tag{1.5}$$

In the case where there is a time constraint on the maneuver, a minimum thrust level can be required and the *thrust-to-power ratio*, T/P, becomes another important performance consideration if the amount of power is limited.

The ratio of masses for the power supply dedicated to the EP system and the propellant can be written in the following form,[1]

$$\frac{M_{power}}{M_{propellant}} = \frac{\alpha_p P}{\tau \dot{m}_{avg}} = \frac{\bar{u}_e^2}{\tilde{U}^2}, \tag{1.6}$$

where τ is the mission duration, α_p is the power supply specific mass and $\tilde{U}$, Langmuir's "characteristic velocity," [16] is defined as,

$$\tilde{U} \equiv \sqrt{\frac{2\eta\tau}{\alpha_p}}. \tag{1.7}$$

From Eqns. (1.2) and (1.6), the mass of the power supply and propellant can both be seen to depend on the exhaust velocity. Assuming a constant thrust level, as the exhaust velocity increases the propellant mass decreases exponentially while the power supply mass increases linearly. This leads to an optimum value of exhaust velocity where the remainder of the mass, potentially payload, is maximized. Rather than derive the optimal exhaust velocity for any EP system (which has been shown before in Refs. [2, 16]), Section 1.3.1 describes the specific system optimization for a GFPPT. To do that, however, first we must describe the missions where GFPPTs might prove useful.

1.2   Missions Where GFPPTs Would Be Useful

In general, almost any mission that can make use of low thrust maneuvers can benefit from the high exhaust velocity that comes along with using an EP system

---

[1]See Ref. [16] by D. Langmuir where this form was first derived.

and more specifically a GFPPT. With previously measured efficiency values near 20%, exhaust velocities of over 40,000 m/s (see Refs. [11, 17]), and the capability to easily throttle thrust and power levels, there are three classes of missions where a properly designed GFPPT would be useful:

1. Small or micro-satellite propulsion, including both orbital transfer and attitude control maneuvers.

2. Large or medium-satellite propulsion, including both orbital transfer and attitude control maneuvers where the propellant type is fixed and unique, specified by other constraints, and/or perhaps not usable by another type of EP system.

3. Deep space propulsion where power is limited, including attitude correction along the prime trajectory.

These missions share the requirement of relatively large ΔV maneuvers where the high propellant exhaust velocity of the GFPPT is most useful. They also have special requirements such as power, size, and propellant type limitations that may eliminate other, possibly even more efficient, propulsion systems for consideration. These three types of missions will be explored in more detail in the following subsections.

1.2.1 Orbit Raising and Station Keeping Maneuvers

Orbit raising, from a low-earth orbit (LEO) to a geo-stationary orbit (GEO) for example, is one of the most promising missions for electric propulsion systems due to the relatively large ΔV requirement (3-4 km/s) and the availability of solar power. Studies using a quasi-steady, pulsed MPD thruster, for example, have demonstrated as much as a factor of three reduction in propellant mass (Refs. [18, 19] and others) for such a mission. The time it takes to perform the maneuver, however, is limited due to the unwanted exposure to radiation and energetic particles in the Van Allen belts found between the two orbits. In some cases, the trajectory can be optimized for low-thrust devices [13], or a chemical booster stage can take the satellite beyond the Van Allen belts with a solar-EP system completing the final orbit insertion [20]. In general, however, this requirement keeps thrust demands high unless satellites are modified with sophisticated and more expensive radiation-hardened electronics and solar panels.

For the GFPPT specifically, typical orbit-raising missions are not necessarily the best application due to the GFPPT's relatively low thrust-to-power ratio compared to other EP systems. In missions where the propellant type is unique, however, there may be a limited number of other alternatives. DARPA's Orbital Express is

Spacecraft Class	Mass Range (kg)	On-Board Power (W)	Attitude Control Thrust Req. (mN)
large	>2000	>10000	>50
medium	500-2000	500-10000	20-50
small	100-500	100-500	10-20
micro	10-100	10-100	2-10
nano	1-10	5-20	0.1-2
pico	<1	<1	<0.1

Table 1.2: Conventional definitions of spacecraft class including mass, available on-board solar power, and attitude control thrust requirements. Taken from Refs. [13, 24–27].

one such mission. It requires the propulsion system to use water vapor for propellant that is produced as a by-product from its fuel cells. The Orbital Express is designed to resupply fuel to defense satellites requiring multiple orbital transfers over its lifetime. Studies are underway at NASA JPL and SRL to determine if the GFPPT can be tailored to this mission.

For station keeping, pulsed plasma thrusters (especially APPTs) have long been considered a mass-saving alternative to momentum wheels, cold-gas, or hydrazine thrusters in common use today [8, 10, 21]. With their high specific impulse, the propellant mass required to perform such small ΔV maneuvers is almost insignificant [22, 23]. For these attitude control maneuvers, the masses of the capacitors and power conditioning equipment are typically much more significant. Further study of GFPPT performance scaling is required to optimize the mass distribution between the hardware and propellant.

1.2.2 Small Satellites

Although a majority of satellites in space today have masses greater than 2000 kg, spacecraft designers are looking to save money on launch costs by scaling down satellites to smaller masses, possibly even less than 20 kg. As shown in Table (1.2), the thrust requirements and the available power generally scale with the mass of the spacecraft.

For the micro, nano and pico-satellites, the amount of power available depends on the surface area of the spacecraft as there are typically no extended solar panels. Conversely, for the medium and large spacecraft, a higher specific power is available from much larger solar panels. As the total spacecraft mass decreases, the thrust requirements decrease in general, although typical mission requirements for small to nano-satellites often require many *fast* slew maneuvers to stay in for-

mation with other satellites. For instance, the minimum thrust requirements for a typical micro-satellite in a constellation or fixed-formation are set by the maximum time allowed (normally on the order of a minute) to complete a 180° slew maneuver [25]. This type of requirement generally leads to an increase in the required thrust-to-power ratio for the smaller satellites. Therefore, in addition to the efficiency of a GFPPT system, the thrust-to-power ratio is an important performance indicator for small-satellite mission application.

Due to their capabilities of operating at an arbitrarily low power level, PPTs head the list of possible propulsion technologies that can be used on micro and small-satellites. The EO-1 Spacecraft (a 150 kg small-satellite with 300 W of power) will demonstrate this application testing an APPT for pitch-axis correction [10,23]. NASA's Space Technology 3 Interferometer [28] mission is now in the planning stages and has very small impulse bit requirements due to optical alignment constraints. APPTs are a strong candidate for this mission although there is some concern regarding contamination from the expelled Teflon propellant coating onboard optical devices. For the relatively cleaner GFPPT to fill a similar role, it must be scaled down significantly from the designs of the 1960's. It must operate more efficiently (>20%) at lower energy levels (<10 J) with a smaller mass (<2 kg). Developing experientially verified performance scaling laws is necessary before GFPPTs can be designed to meet small and micro-satellite propulsion requirements.

1.2.3   Power-Limited Deep Space Missions

The type of mission (piloted, unpiloted, interplanetary, etc.) can also change the spacecraft mass, available power, and thrust requirements. For example, interplanetary missions typically have large ΔV maneuvers and small thrust requirements due to long mission durations which are well suited to electric propulsion systems. Available power may be limited, however, if the mission is to an outer planet where solar power is no longer available in useful amounts. The use of low-power, nuclear thermionic power sources precludes the use of many electric propulsion systems for deep space missions, and large-scale nuclear reactors (> 10 kW) have not been tested in space to date. The overall power consumption, efficiency, and the thrust-to-power ratio of the GFPPT then becomes of crucial importance if they are to be used for these missions. Example missions that fall under this category are the Pluto Fast Fly-by [29] and Europa Orbiter [30]. Using APPTs for the Pluto mission has been studied in Ref. [31].

In general, each electric propulsion system must be designed for a specific mission and should also be able to operate predictably over a wide range of desirable thrust, power, and exhaust velocities while using as little mass as possible. As shown in the next section, understanding the performance scaling of GFPPTs dictates their design and use for any future mission.

1.3 The Mass of a GFPPT System

Besides the propellant and power supply masses, the mass of the propulsion system itself (power conditioning equipment, control and discharge electronics, electrodes, etc.) can play a significant role in determining the remaining payload mass. This is, again, related to the efficiency of the acceleration process and the useful lifetime of the device. For a pulsed device, specifically the GFPPT, the *thruster efficiency*, η_t, has a slightly modified definition than that of η in Eq. (1.5),

$$\eta_t \equiv \frac{\frac{1}{2}m_{bit}\bar{u}_e^2}{E} = \frac{\bar{u}_e}{2}\frac{I_{bit}}{E}, \tag{1.8}$$

where m_{bit} is the amount of propellant used per pulse and E is the total energy stored for each pulse. The relation between the thruster and overall efficiency depends on the power conditioner and feed system efficiencies, as will be explained in more detail in Section 2.3. In this dissertation, the generic term *performance* usually refers to *both* the thruster efficiency and the impulse-bit-to-energy ratio of a GFPPT unless otherwise noted.

Generally the mass of a GFPPT can be broken down between its energy storage device, the thruster modulator that conditions the power from the spacecraft bus and controls the charging, and some fixed mass dedicated to the electrodes and thruster casing that does not depend on the discharge energy. Lumping all the energy-dependent masses together and assuming the fixed masses are small,

$$M_{thruster} \approx \alpha_e E, \tag{1.9}$$

where α_e is the thruster specific mass. The ratio of the thruster mass to propellant mass is then,

$$\frac{M_{thruster}}{M_{propellant}} = \frac{\alpha_e E}{N_{ptot}m_{bit}} = \frac{\bar{u}_e^2}{\tilde{V}^2}, \tag{1.10}$$

where N_{ptot} is the total number of pulses in the mission (or effectively the required lifetime of the thruster) and $\tilde{V}$ is the "Pulsed Electric Propulsion Velocity" (PEP velocity, see Ref. [31]) defined as,

$$\tilde{V} \equiv \sqrt{\frac{2\eta_t N_{ptot}}{\alpha_e}}, \tag{1.11}$$

in analogy to the Langmuir Characteristic Velocity in Eq. (1.7). The ratio of the thruster mass to power supply mass is then,

$$\frac{M_{thruster}}{M_{power}} = \frac{\tilde{U}^2}{\tilde{V}^2}. \tag{1.12}$$

The Langmuir and PEP characteristic velocities will be used to optimize the GFPPT system mass in the next subsection.
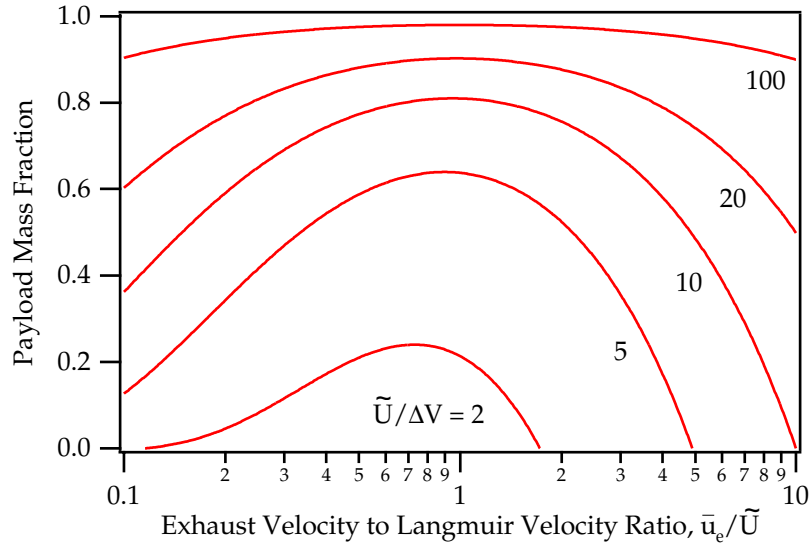
Figure 1.2: Payload mass fraction as a function of exhaust velocity to Langmuir velocity ratio with the Langmuir velocity to ΔV ratio as a parameter.

1.3.1 Achieving the Maximum Payload Mass

As seen in Eqns. (1.6) and (1.10), the efficiency of a GFPPT directly affects the propellant, power supply, and thruster masses. In Ref. [31] we developed the mass scaling relations for the entire spacecraft, including the power supply mass, in detail. Here we will simply state the results divided into two categories depending on the mission type.

GFPPTs for Main ΔV Propulsion

In this case, the thruster mass is assumed to be insignificant compared to the power supply and propellant masses. The largest payload mass occurs when the power supply and propellant masses are nearly equal. The optimum exhaust velocity is then very close in value to the Langmuir Characteristic Velocity, $(\bar{u}_e)_{opt\Delta V} \approx \tilde{U}$. This is shown graphically in Fig. (1.2) where the payload mass fraction is plotted as a function of $\bar{u}_e/\tilde{U}$ with $\tilde{U}/\Delta V$ as a parameter. Note that this result also applies to any EP system that does not require an energy storage device.

The plot in Fig. (1.2) has three important features:

1. For each value of $\tilde{U}/\Delta V$, an optimal value of exhaust velocity exists that is equal to or slightly smaller than the Langmuir velocity.

2. An electric propulsion system should be chosen or designed such that its Langmuir velocity is much greater than the ΔV requirement.

3. At the highest values of $\tilde{U}/\Delta V$, the payload mass fraction is large and a weak function of $\bar{u}_e/\tilde{U}$.

GFPPTs for Attitude Control

In this case, the power supply mass dedicated to the GFPPT is often insignificant compared to the thruster and propellant masses. This is because most spacecraft attitude control maneuvers like station keeping are spread out over a long period of time and do not require high thrust (and therefore high power) levels. The optimum exhaust velocity is then very close to the value of the PEP Characteristic Velocity, $(\bar{u}_e)_{optAC} \approx \tilde{V}$. From Eq. (1.10), the smallest overall GFPPT system mass occurs when the thruster and propellant masses are nearly equal.

For attitude control maneuvers, the trends of payload mass fraction are very similar to those presented in Fig. (1.2) with $\tilde{V}$ replacing $\tilde{U}$. Note, however, that in most of these missions the exhaust velocity and the PEP velocity will be much greater than the ΔV requirement. In this regime, the payload mass is not a strong function of $\bar{u}_e/\tilde{V}$ so the exhaust velocity can actually vary over a wide range and the payload mass fraction will still be large. Furthermore, for GFPPTs operating at low energy, other masses that do not depend on energy directly (the fixed masses) may also play an important role in determining the overall system mass. The mass of these components may depend on current level, inductance, etc., instead of energy which may also impact performance.

For missions where the attitude control maneuvers must occur within a limited amount of time, the thrust requirements may be high enough so that both the power supply and energy storage masses must be minimized. In this case, the value of the optimal exhaust velocity is near the smaller of the two characteristic velocities Ref. [31], and the impulse-to-energy ratio may also impact the mass of the propulsion system. In any case, understanding the performance scaling is necessary to optimize the total propulsion system mass.

1.3.2 Characteristic GFPPT System Velocities

The Langmuir and PEP characteristic velocities depend on mission duration, efficiency, thruster lifetime, and the specific masses of the power supply and energy storage device. Arriving at typical values of these velocities is explained in more detail in Ref. [31]. The results for a typical orbit-raising maneuver, attitude control, and interplanetary mission (trajectory correction only) are shown in Table (1.3).

The values of the characteristic velocities shown in Table (1.3) confirm what has been stated in previous sections. First, the PEP velocity, $\tilde{V}$, is shown to be *independent* of the mission class making it solely a *technology-dependent* parameter. Next, for all the missions, both characteristic velocities, $\tilde{U}$ and $\tilde{V}$, are larger, by almost a factor of two in every case, than the ΔV requirement which leads to large

Parameter	Orbit-Raising	Attitude Control	Inter-planetary
η (%)	18	18	18
η_t (%)	20	20	20
τ (s)	10^7	4×10^8	2×10^8
N_{ptot}	10^8	10^8	10^8
α_p (kg/W)	0.03†	0.03†	0.18‡
α_e (kg/J)	0.03	0.03	0.03
ΔV (m/s)	6000	500	2000
$\tilde{U}$ (m/s)	11000	69300	20000
$\tilde{V}$ (m/s)	36500	36500	36500
Optimal $\bar{u}_e$ (m/s)	10500	32300	17500

Table 1.3: Characteristic mission parameters for orbit raising and attitude control maneuvers. †Indicates solar power, ‡indicates radioactive thermionic generators [31].

payload mass fractions in general. Finally, the ratio of thruster to power supply mass and the optimal exhaust velocity depends on the mission. This indicates that an EP system should be able to function predictably over a wide range of conditions to meet a variety of mission requirements.

All of these calculations, however, depend on the efficiency and lifetime of the GFPPT and the system as a whole. Greater efficiency and lifetime lead to a higher optimal exhaust velocity which then leads to more payload mass. Yet, since the efficiency varies as a function of exhaust velocity, the characteristic velocities will depend on $\bar{u}_e$ as well. The optimization is then no longer as straightforward because the characteristic velocities are not fixed. The performance scaling (the relation of efficiency to exhaust velocity) of any EP device, including GFPPTs, becomes very important for designing and choosing the best propulsion system for any mission.

1.3.3 Balancing Performance, Lifetime, and System Mass

It is interesting to note that as either one of the two characteristic velocities increases, the payload mass fraction increases monotonically, regardless of exhaust velocity or ΔV requirement. In other words, having the largest payload simply follows from having the largest PEP and Langmuir velocities possible. This is reasonable considering their definitions (see Eq. (1.11) and Eq. (1.7)). Increases in efficiency, mission duration, and GFPPT lifetime will increase the payload mass fraction while increases in the specific mass of the power supply (kg/W) or energy storage unit (kg/J) will decrease it. They also show that efficiency and lifetime

trade off *equally* as far as the system mass is concerned. Any change in the thruster design that results in a performance increase must also be judged by its subsequent effect on thruster lifetime.

For example, many researchers of GFPPTs in the past (see the next section and Appendix A on the history of GFPPT research and development) began using very fast solenoid valves that improved propellant utilization and the thruster efficiency by nearly a factor of ten in some cases. The valve seats in these devices, however, typically did not last more than 10^5 pulses before leaking. The valves became the limiting component (as opposed to the capacitors which had expected lifetimes of 10^7 pulses), reducing the lifetime of the device by nearly a factor of 100. Because of the shortened lifetime, impulse bit levels needed to remain high for the same total impulse delivery. This decision led to massive energy storage devices and precluded GFPPTs from being selected for many missions. In this example, the PEP velocity actually *decreased* due to the incorporation of a *more efficient* valve design, and, as a result, the total system mass *increased*. Clearly, an understanding of the performance scaling, including lifetime issues, must be obtained for the proper design of GFPPTs.

1.3.4   The Need for a Performance Scaling Law

As shown in the previous subsections, the optimization of the payload mass fraction changes dramatically if the Langmuir or PEP velocities are dependent on the exhaust velocity. This is actually quite common and can result from either an efficiency, mission duration, or thruster lifetime that is dependent on the exhaust velocity. For example, if the efficiency is linearly dependent on the exhaust velocity, there is no longer a clear optimal exhaust velocity at all. Assuming the EP system is operating at a constant thrust, the power requirement, $T\bar{u}_e/2\eta$, and, therefore, the power supply mass stay *constant* as the exhaust velocity and efficiency increase linearly together. Since the total propellant mass *decreases* with increasing exhaust velocity, the useful mass fraction continues to increase monotonically with exhaust velocity. Obviously the trend of an efficiency linearly increasing with exhaust velocity cannot continue indefinitely, and an optimal operation point may indeed exist where the efficiency begins to break-off from this trend.

With this in mind, since the performance of GFPPTs is variable, it must be known as a function of controllable parameters such as propellant flow rate, power level, energy per pulse, driving circuitry configuration, electrode geometry, etc.,

$$\eta = f(\bar{u}_e, \dot{m}_{avg}, m_{bit}, P, E, geometry, etc.). \tag{1.13}$$

Performance scaling is also important simply from a design point of view. To match a given thruster to mission requirements, or for spacecraft designers to choose and design a particular electric propulsion system, they must know how the thrust, efficiency, and specific impulse scale with various operating conditions.

At this point it is important to examine the history of GFPPT research and discover why developing such a performance scaling relation has proven difficult in the past and merits further work.

1.4   Background of GFPPT Development

Gas-fed PPTs have been developed in many laboratories over the last forty years. In general, they rely on a sheet-like, high current arc discharge to induce a magnetic field which in turn pushes outward on the current sheet with a Lorentz force. As the current sheet moves down the electrodes, gas is swept into the sheet and ionized. The acceleration of the gas is dominated by electromagnetic effects of the self-field acting on the current-carrying plasma. Electrostatic and electrothermal acceleration may also play a significant role depending on the operating conditions. A schematic of two common GFPPT geometries is shown in Fig. (1.3).

Originally developed from magnetic shock tubes [32, 33] and applications to fusion research [34] in the late 1950's, the first "plasma guns" of many laboratories (see Refs. [35–38]) had nearly meter long, coaxial electrodes with outer to inner electrode radius ratios less than two and propellant injection ports near the middle of the electrode length. Typically these first GFPPTs were also operated at high energy (> 1 kJ) and low capacitance ($\approx 10 \mu$F) with the breakdown from pulsed gas injection controlling the discharge initiation. Many of the designs had relatively large amounts of parasitic inductance (≈ 100 nH) and underdamped, oscillatory current waveforms. In these designs energy transferred back and forth between the magnetic fields and capacitor and not necessarily into sheet motion. The acceleration dynamics of these thrusters were dominated by current reversals and subsequent "crowbarring" where a second discharge would form near the original initiation point, uncoupling the first sheet from the driving circuitry.

As the designs progressed with an eye towards propulsion applications in the 1960's, radius ratios were more than doubled, the electrodes were shortened by almost a factor of four, the capacitance was increased by an order of magnitude, and the average energy was reduced to below 100 J (see Refs. [11,39–41] for example). Unfortunately, in many cases multiple design changes were made simultaneously with empirical instead of theoretical studies suggesting the next iteration. Although there were quite a few theoretical performance studies (See Refs. [42,43] for example), the scaling relations they produced were different in almost every case (see Appendix A for more details) and rarely compared to actual performance measurements. At the time, the emphasis was being placed on the ultimate achievable performance, and an experimentally verified set of performance *scaling* relations were not obtained.

In the effort to improve performance, some of the later GFPPT designs did not exhibit crowbarring and had nearly critically damped current waveforms. In other
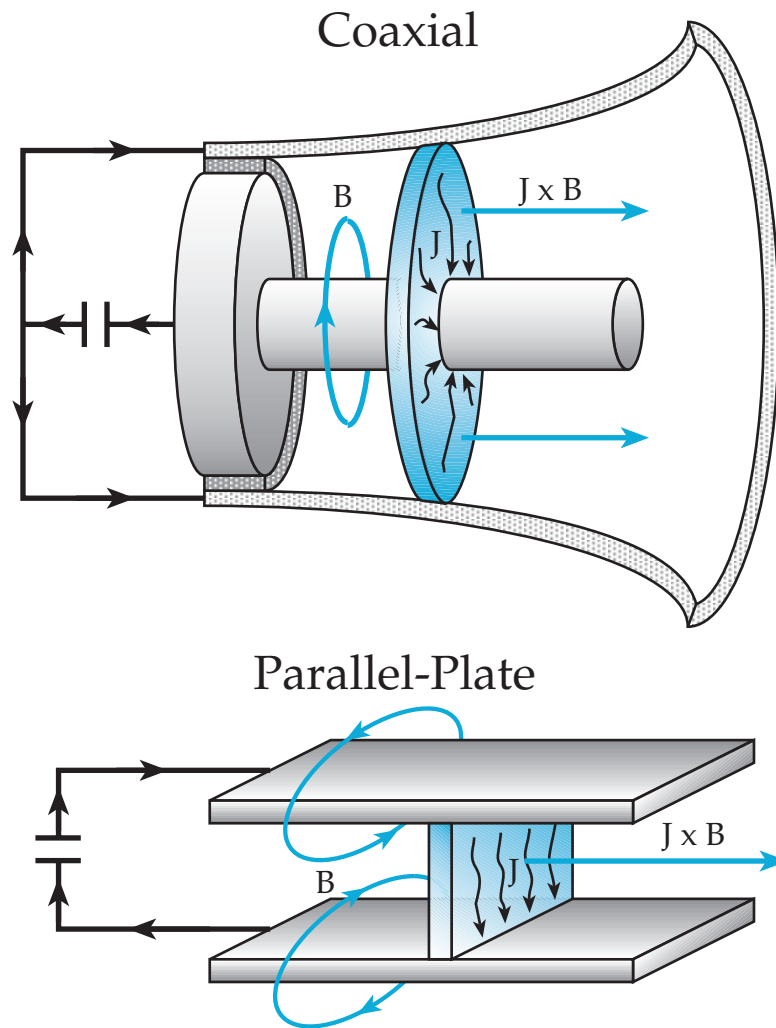
Figure 1.3: Coaxial and parallel-plate electrode geometries for GFPPTs

designs, the current reversal was timed to coincide with the discharge reaching the end of the electrodes so that no energy was wasted [43]. High speed, high voltage valves were introduced to improve propellant utilization which approached close to 100% in many designs [44], but, as mentioned previously, at a significant loss of thruster lifetime. The discharge initiation process was also controlled with either a high-voltage spark trigger or a high current, low inductance gas discharge switch. Efficiencies of these devices finally reached greater than 20% at specific impulse values near 4000 s with thrust-to-power ratios close to 10 μN/W [17].

In parallel with the thruster performance increases, more fundamental research conducted by Lovberg and Jahn focused on the current sheet structure and the underlying acceleration mechanism. Although both research groups found a strong polarization field with the electrons carrying most of the current [45–48], there was some degree of debate on the amount of ion conduction necessary to explain the total current. For Lovberg's experiments using hydrogen, no ion current was required to explain sheet behavior. In Jahn and Burton's work as well as other's [49] using argon, however, a reasonable fraction of the total current needed to be carried by the ions to account for the total current and subsequent ion acceleration. In addition, the permeability of the sheet, i.e. its effectiveness to sweep up the propellant mass in front of it like a "snowplow," seemed to depend on a number of things including,

- Geometry: Lovberg found that a coaxial electrode configuration, in general, produced more permeable current sheets compared to a parallel-plate geometry operating at similar conditions [46, 50, 51].

- Molecular weight: Discharges using lighter molecules were, in general, found to have a higher sweeping efficiency [46, 52, 53].

- Current rise rate: For argon discharges, Jahn empirically determined that 10^{10} A/s-cm (over the breadth of the current sheet) was required in the initiation phase to form an impermeable current sheet [2].

The profile of the current sheet was also investigated as, in many cases, it was found to be non-planar depending on electrode geometry [54, 55], and polarity [56, 57], as well as the molecular weight of the propellant [46, 58–60]. Unfortunately, there are many conflicting results in this area and a complete parametric study with different propellant types and current levels has yet to be completed (detailed studies of this phenomenon are currently underway at Princeton [60]).

Appendix A provides more detail into the theoretical and experimental research related to the GFPPT in the 1950's and 60's. Much of this work was summed up in 1965 when researchers at NASA Lewis (now NASA Glenn) produced a comprehensive review of GFPPT research [11]. It gave the following list of important conclusions reached by that time:

1. Thrust estimates based on calorimetry measurements of the exhaust plume from many labs did not agree with the subsequent performance data measured on thrust stands. Thrust stand data was generally accepted as the most accurate way to measure performance.

2. Crowbar discharges generally occurred at some point between the voltage and current reversal times depending on thruster geometry and driving circuit parameters. The performance reduction due to crowbarring depended on the timing of the reversal.

3. The main acceleration mechanism inside the current sheet was found to be due primarily to the polarization field created by the electrons trapped on an $E \times B$ drift and the subsequent charge separation. It was also noted, however, that many of the labs had very different results and disagreed in this area, especially on the influence and existence of ion current.

4. Including an electric switch in the discharge initiation process (as opposed to using the Paschen breakdown point alone) led to better repeatability, fewer spoking instabilities, and improved propellant utilization. At the same time, however, it introduced some parasitic inductance and resistance as well as adding reliability questions.

5. There was a need for a simple performance model that was confirmed by repetitive experimental performance measurements over a wide range of conditions.

6. A major obstacle keeping GFPPTs from being used in space was their lack of "heat handling capability."

7. Research was shifting to quasi-steady devices which might have better performance.

Unfortunately, GFPPT research began to fade soon after that report and almost completely stopped by 1972 when NASA experienced significant funding reductions. The two main problems of the final designs at the time were: 1) lifetime issues associated with the ultra-fast, high energy solenoid valves, and 2) a large system mass compared to other electric propulsion systems being developed in the same period (ion thrusters for example) for main propulsion.

Research at General Dynamics [17], NASA Lewis [61], and Princeton [62] shifted to *quasi-steady* gas-fed thrusters (Magnetoplasmadynamic Thrusters or MPDTs). In these devices, discharge durations were increased and the current sheet was allowed to stabilize near the end of the electrodes. The MPDT pulse was much longer in duration (>0.3 ms) and did not require the ultra-fast valves of the earlier GFPPT designs. MPDTs also showed promisingly better overall performance as

well as the ability to process many mega-watts of instantaneous power in a relatively small device. Furthermore, as these devices are pulsed, they share the advantage of arbitrarily low steady-state power consumption depending on the pulse rate. Still, system mass was large due to the pulse forming networks that were required to produce the longer, nearly constant-current pulses. As a result, this type of EP system did not experience considerable in-space testing as a propulsion device until recently with the flight of the Japanese Space-Flier Unit mentioned earlier. As the discharge in the MPDT approaches more of a steady-state condition, the performance scaling is very different from purely unsteady GFPPTs.

Research at General Electric [63] and Republic Aviation [64] shifted to ablative pulsed plasma thrusters that used much lower energy and were geared more towards attitude control applications. Many performance scaling studies have been conducted using APPTs; however, the ablation rate of the Teflon dominates almost all the relations [64–70]. Although it has been shown that there is initially a fast moving current sheet in APPT discharges, there is also a significant amount of late-time ablation that does not get accelerated to high velocity. In many cases, this slower Teflon vapor dominates the performance over the electromagnetic acceleration of the current sheet. This significantly limits the application of APPT performance scaling laws to GFPPTs.

Our recent research at Princeton has been divided into two projects: performance scaling of GFPPTs (see Refs. [71–77] (co-written by this author) and current sheet structure and stability [60]. The research relating to performance scaling is the primary topic of this dissertation.

1.5 Dissertation Outline

This rest of this dissertation consists of six chapters that explain and present experimentally verified, performance scaling relations for GFPPTs. In Chapter 2, a GFPPT discharge is described in more detail including the relation between the driving circuit and the discharge dynamics. In Chapter 3, theoretical performance scaling relations are derived with two approximate analytical models and a more detailed, numerically solved, non-dimensional model. In Chapter 4, the SRL-EPPDyL family of GFPPTs is described in more detail including both the thruster designs used for the experimental study, PT5 and PT9. In Chapter 5, the techniques for measuring performance and the test results from two GFPPT designs with modular capacitance and inductance-per-unit-length are presented. In Chapter 6 the theoretical performance models and the experimental measurements are brought together to form a complete picture of GFPPT performance scaling. Finally, Chapter 7 provides a summary of this dissertation work.

The appendices cover the history of GFPPT research, renovations to the high-vacuum test facility, other GFPPT designs, and a 2 million pulse lifetime test.

Chapter 2

The Dynamics of a GFPPT Discharge

This chapter starts with a detailed description of a GFPPT discharge. The characteristics of the driving circuit are related to the dynamics of the discharge showing how energy is distributed during a pulse. Finally, the efficiency of a GFPPT is broken down and defined in terms of propellant utilization, energy transfer, and dynamic efficiency which are examined throughout this dissertation.

2.1 Discharge Description

To predict the physical scaling of the thruster efficiency, the development of the current sheet must be understood as well as how the energy from the capacitor couples to the motion of the discharge. This section discusses the nature and dynamics of the discharge which can be broken up into three segments: initiation, propagation, and expulsion of the current sheet.

2.1.1 Initiation

The discharge can be initiated in many ways, three of which are common in laboratory devices. First, with the main energy storage device charged to a high potential and directly connected to the electrodes, the propellant may be injected into the electrode volume in such a way that a breakdown occurs. As the breakdown voltage can vary depending on propellant loading, electrode geometry, and electrode surface conditions, the timing and symmetry of the breakdown is difficult to control [78] and other techniques have become more common. Another scheme relies on a low-inductance switch, such as a spark gap or ignitron, to apply the potential to the electrodes after the electrode volume has already been filled with the desired amount of propellant (See Refs. [17, 52] and others). After the switch is closed, a breakdown quickly occurs and a current sheet forms at the minimum inductance point of the thruster electrode geometry by a process that is similar to

the skin-effect in solid conductors. The lifetime of these high-current switching devices, however, is often limited by electrode and insulator wear. In addition, although possibly to a minimal extent, they add an extra impedance to the plasma discharge circuit. As a third option useful at lower voltages or when conditions do not permit a normal breakdown, high voltage spark plugs are used to provide an ionization seed at the desired position and time [39,74]. The timing is usually set to coincide with the completion of the propellant filling the electrode volume. Spark plugs are also used in Teflon propellant APPTs where a small amount of solid propellant is ablated during the spark providing the necessary plasma to begin the full discharge and further ablate more propellant. The negative aspects of using a secondary initiation source include limitations on lifetime and the additional erosion products that come from these type of discharges [77]. Furthermore, using a finite number of spark plugs in discrete locations can lead to a localized initiation and a non-uniform discharge [74].

The symmetry and uniform quality of the discharge initiation can be very important to the later stages of the discharge and can significantly affect performance. The degrading effect of asymmetry has been measured (see Ref. [77]) with performance reduced as much as 40% compared to a symmetric discharge. In those same experiments, it was noticed that the greatest amount of electrode erosion occurs at the point of initiation. Electrode erosion leads to the introduction of other atomic species that may influence the discharge or possibly limit the lifetime of the device. Finally, current rise times over the breadth of the current sheet must be very large (10^{12} A/s-m using argon, for example) during this portion of the discharge to ensure a stable, impermeable current sheet [2,79].

2.1.2   Propagation

After the discharge is initiated, the current quickly reaches its peak value due to the low impedance nature of the plasma-completed circuit. A large magnetic field forms within and behind the finite-width current sheet as a Lorentz force pushes to expand the circuit. As the current sheet propagates down the electrodes, the effective load on the circuit increases with the changing magnetic field that is generated over a larger and larger volume. In the case of a GFPPT, the current sheet sweeps up propellant as it travels like a snowplow or piston moving through a cylinder. As the capacitor is drained, the current and the magnetic field begin to decrease. If designed correctly, the current sheet reaches the end of the electrodes just as the current and magnetic fields have decayed to zero. This timing requires a very good understanding of the dynamic interaction of the driving electric circuit, the propagation of the current sheet, and the mass-loading of the discharge volume before the pulse. As can be expected, it is very difficult to achieve this synchronicity and the next paragraph describes more common, alternative possibilities.

2.1.3 Expulsion

Upon reaching the end of the electrodes, if there is voltage remaining on the capacitor or energy stored in the magnetic fields, then the following situations may occur which can affect performance. First, the current sheet may expand beyond the electrodes, potentially reaching some quasi-steady state [62]. In coaxial electrodes this can also lead to a pinching condition where axially directed current forces the propellant inward at the center electrode and outward near the outer electrode. In parallel-plate devices, the current sheet remains attached to the ends of the electrodes and expands in all directions. In both cases, the sheet spreads outward unconstrained by the electrode walls, potentially reducing the fraction of axially directed plasma. Since the expansion also allows the circuit to stay completed by the plasma, some energy is consumed that otherwise would have been completely lost. In this case, the net effect on performance is unclear. In the underdamped case, the energy stored in the magnetic fields may be enough to recharge the capacitor (in the opposite polarity) before the current sheet has reached the end of the electrodes. In this case, when the *current* begins to reverse direction, the current sheet may become detached from the electrodes and a new current sheet may form at the backplate of the thruster (See Refs. [45,52] and others). This "crowbar" discharge then usually consumes the remaining energy stored in the capacitor that would have otherwise gone into further accelerating the first current sheet. Typically the second current sheet does not provide a significant amount of impulse with smaller currents and magnetic fields, as well as very little gas remaining to be swept up in the electrode volume. This phenomenon also presents an additional problem to effectively modeling the dynamics of the discharge.

Again, the focus of this dissertation is to examine overall performance scaling with similar energy and current levels using one type of propellant (constant molecular weight). It is assumed that the current sheet structure and the resulting acceleration mechanism will be similar in all the test cases presented in this research. The *scaling* of the current sheet profile and permeability losses from changes in propellant type will be left to continuing work at EPPDyL. With that in mind, we begin to examine the transfer of stored energy from the capacitor to directed kinetic energy in a GFPPT discharge. Being able to predict the dynamics of the discharge is critical to the development of performance scaling relations.

2.2 Effective Models for the GFPPT Discharge

This section presents a simple and commonly applied model for the unsteady, nonlinear dynamics of a GFPPT discharge. We will also examine the partition of energy in these devices, although more detailed solutions and theory on performance *scaling* will be left to the next chapter.
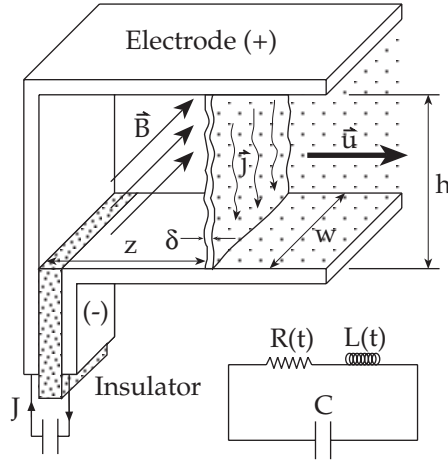
Figure 2.1: Current sheet in a parallel-plate GFPPT with the effective LRC circuit.

2.2.1   The Equivalent Circuit and Snowplow Model

In the relevant literature, many basic models for pulsed plasma thrusters include an effective circuit model for the discharge potential and a "snowplow" model for the gas accumulation during the discharge (see Refs. [2, 37, 41–43, 53, 73, 80–82] which are also reviewed in Chapter 1 and Appendix A). Here we will go over the basic principles of these models and describe the equations which will be solved in the next chapter by analytic approximations and numerical methods. These relations, for now, will allow us to examine the energy partitioning and efficiency breakdown in a GFPPT. A schematic for the idealized discharge and its electric circuit analog is shown in Fig. (2.1).

Conservation of Charge.

Treating the discharge as an effective LRC circuit with changing inductance produces a simple and convenient model for the discharge potential. In this analog, the total inductance, $L(t)$, includes the internal inductance of the capacitor bank and the changing inductance of the discharge as the current sheet propagates down the electrodes. The total resistance, R, includes the effective plasma resistance, the resistance of the electrodes, and the internal resistance in the capacitor bank. The total resistance is considered constant in this analysis for simplicity and because the fixed internal resistance of the capacitor bank makes up nearly half of the total resistance in the GFPPTs studied in this dissertation[1]. Although, potentially, the internal resistance of the capacitor bank could be reduced by using higher quality,

---

[1]Measurements of the total resistance and internal capacitor bank resistance are presented in later Chapters.

specially designed capacitors and/or increasing the cross-section of the conducting plates between them, changing the type, placement, or number of capacitors could adversely affect the initial inductance and the lifetime of the device. Furthermore, determining the effective plasma resistance accurately would require a much more detailed model of the plasma physics and conductivity inside the current sheet which is beyond the scope of this dissertation. For this model to produce a useful set of performance scaling relations, we keep R constant and begin by using Kirchhoff's Law around the plasma completed circuit,

$$V_0 = \frac{1}{C} \int_0^t J dt^* + \frac{d}{dt}(LJ) + RJ, \tag{2.1}$$

where the total current, J, and the inductance are both a function of time. For parallel electrodes and a planar current sheet that remains perpendicular to the electrodes, the total inductance can be separated into an initial inductance plus an "inductance-per-unit-length", L', times the axial position of the current sheet, z,

$$L = L_0 + L' z. \tag{2.2}$$

For now, the inductance-per-unit-length will remain fixed although it can vary as a function of time in real GFPPTs (see Chapter 3). Inserting this relation for the inductance into Eq. (2.1) and carrying out the differentiation leads to,

$$V_0 - \frac{1}{C} \int_0^t J dt^* = V_{cap} = \left(L' \dot{z} + R \right) J + \left(L_0 + L' z \right) \dot{J}, \tag{2.3}$$

where V_{cap} is the instantaneous capacitor voltage. This equation states that, at any instant, the voltage on the capacitor is split between the motion of the current sheet, the resistance, and the changing magnetic field.

Conservation of Momentum.

Assuming the current sheet can only travel in one dimension along the electrodes, the equation for the conservation of momentum with a Lorentz force is,

$$\frac{d}{dt}(mu) = \int \vec{j} \times \vec{B} \, dV_{ol}, \tag{2.4}$$

where m is the instantaneous amount of mass contained in the current sheet, $\vec{j}$ is the current density vector, and $\vec{B}$ is the magnetic field vector. Using a self-induced magnetic field the integral can be evaluated over the volume of the current sheet,

$$\frac{d}{dt}(mu) = \frac{1}{2} L' J^2. \tag{2.5}$$

If we further assume that the discharge sweeps up the mass ahead of it as it travels, the mass of the sheet will be increasing with time and the conservation equation can be expanded,

$$m\dot{u} = \frac{1}{2}L'J^2 - \dot{m}u. \tag{2.6}$$

This equation shows that the acceleration of the mass in the current sheet is proportional to the Lorentz force minus a "drag" term that describes the losses associated with accumulating mass that was initially at rest. To minimize this loss, most of the mass accumulation should occur while the sheet velocity is small. This "dynamic efficiency" will be discussed in more detail in Section 2.3.5.

The combination of the two conservation equations leads to a non-linear but stable set of equations. As the sheet moves, the inductance grows and acts as a greater load on the circuit. The increase in impedance decreases the current which, in turn, decreases the acceleration. As the current sheet trajectory changes, once again, the total inductance changes, and so on. The equations are globally stable as the Lorentz force always works to expand the current loop (regardless of the current direction) and the increasing inductance always serves to dampen the circuit response.

2.2.2   Energy Distribution in GFPPTs

Multiplying the capacitor voltage, V_{cap}, in Eq. (2.3) by the total current, J, yields the instantaneous distribution of power, P_{circ}, in the rest of the circuit,

$$P_{circ} = \left(\frac{1}{2}L'\dot{z} + R\right)J^2 + \frac{d}{dt}\left(\frac{1}{2}LJ^2\right). \tag{2.7}$$

Note that power going into the increasing inductance, $L'\dot{z}/2$, and the total resistance, R, are both proportional to J^2. Multiplying Eq. (2.6) by the sheet velocity, $\dot{z}$ or u,

$$\frac{1}{2}L'\dot{z}J^2 = \frac{d}{dt}\left(\frac{1}{2}mu^2\right) + \frac{1}{2}\dot{m}u^2, \tag{2.8}$$

and substituting for the first term in Eq. (2.7) yields,

$$P_{circ} = \frac{d}{dt}\left(\frac{1}{2}mu^2\right) + \frac{1}{2}\dot{m}u^2 + \frac{d}{dt}\left(\frac{1}{2}LJ^2\right) + RJ^2. \tag{2.9}$$

This equation represents how the power from the capacitor is distributed within the discharge. The first term is related to the power used to change the kinetic energy of the current sheet. This is the most useful term in the equation as far as any propulsion application is concerned. The second term is related to the power that goes into the inelastic process of accumulating propellant mass. This term comes from the conservation of momentum, Eq. (2.6), as has already been discussed. The

$$\int_0^{t_f} \left[\frac{1}{2}\dot{m}u^2 + RJ^2\right] dt,$$

Circuit Heating

Electrode Heating

Radiation

Initial Stored Energy

Plasma Heating

Undirected ETKE

E

Directed Kinetic Energy

$\frac{1}{2}mu^2$

Electromagnetic Energy

Undirected EMKE

Dissociation, Ionization, etc.

$$\text{Thruster Efficiency} = \frac{\text{Directed Kinetic Energy}}{\text{Initial Stored Energy}}$$
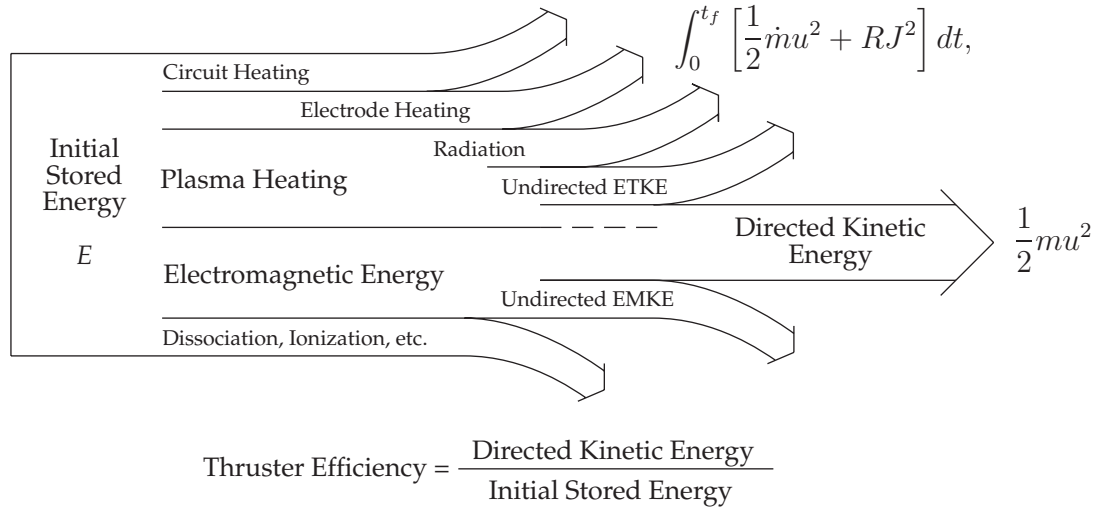
Figure 2.2: Distribution of energy in a GFPPT discharge.

third term is related to the power that goes into changing the magnetic field. This term will be positive when the current and magnetic fields are increasing, and negative (giving power back to the capacitor and/or the rest of the discharge) when the current is decreasing. The fourth term is related to the power that goes into resistive heating distributed between the electronics and plasma. Plasma heating, in turn, contributes to the power going into ionization and radiation.

Integrating the discharge power over the duration of the pulse yields the partition of energy,

$$E = \left(\frac{1}{2}mu^2\right)_f + \int_0^{t_f} \left[\frac{1}{2}\dot{m}u^2 + RJ^2\right] dt, \tag{2.10}$$

where the current is assumed to be zero at the beginning and end of the discharge so that any power going into changing the magnetic field is later recovered (note that this is not necessarily the case in a crowbarred discharge). Equation (2.10) is presented graphically in Fig. (2.2) with measurements of the instantaneous power and energy in a typical GFPPT discharge presented in Fig. (2.3). From these figures, we see that the initial energy stored in the capacitor is divided between the directed kinetic energy and two loss terms including a dynamic loss and a resistive loss. This energy goes into heating the plasma with subsequent inelastic electron-ion collisions and a certain amount of radiation. Most of the plasma heating is practically unrecoverable due to the optically-thin, low-density nature of the plasma (see Ref. [83]) and the quick acceleration time-scales. To date, any attempt to use a physical nozzle to direct the plasma has had little or no effect on improving performance in these low-energy GFPPTs [76, 84].
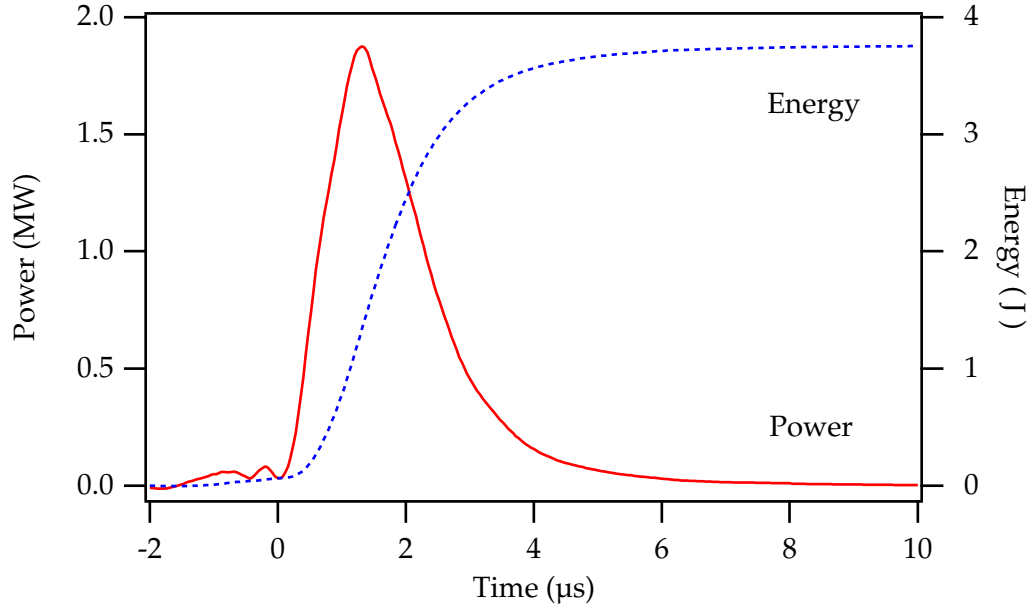
Figure 2.3: Measurements of power and energy in a GFPPT discharge. Taken with PT9, 4 J per pulse, 2.0 μg argon, 130 μF, 1″ × 1″ electrodes.

2.3 The Efficiency of a GFPPT

The overall *system* efficiency is related to the *thruster* efficiency by the power conditioning and feed system efficiencies which will be described in Chapter 4 in the context of a specific GFPPT. Here we focus on the thruster efficiency which is the ratio of the kinetic energy in the exhaust to the energy stored in the main capacitors prior to the discharge. We can gain more understanding of the thruster efficiency by creating an analogy to a common voltage divider using the characteristic impedances found in the GFPPT discharge. In the circuit model presented in the last subsection, for a good accelerator the effective resistance, $(\frac{1}{2}\frac{dL}{dt} + R)$, should be dominated by the time varying inductance caused by the plasma sheet motion. In the later part of the discharge cycle, this impedance should also be greater than the imaginary impedance ($\sqrt{L/C}$) that represents the recharging of the capacitors. If these conditions are met, the corresponding voltage and current waveforms are close to critically damped with the energy coupled efficiently from the electrical power source to the plasma. As we will discuss further, this does not in itself result in an efficient thruster. Besides the energy that goes into forward directed acceleration of the plasma, energy can also be deposited in the plasma internal energy modes through the mass accumulation process, in the electrodes from the current conduction process, or in non-axial motion.

$$\eta \;=\; \frac{T^2}{2\dot{m}_{avg}P} \;=\; \eta_{fs}\;\eta_{pc}\;\eta_t$$

Feed System

Power Conditioner

Thruster Efficiency

$$\frac{\dot{m}_{ss}}{\dot{m}_{avg}} \qquad \times \qquad \frac{f_p C V_0^2}{2P} \qquad \times \qquad \frac{I_{bit}^2}{2m_{bit}E} \;=\; \eta_{pu}\;\eta_a$$

Propellant Utilization

Acceleration Efficiency

$$\frac{m_{avail}}{m_{bit}} \qquad \times \qquad \frac{I_{bit}^2}{2m_{avail}E} \;=\; \eta_{energy}\;\eta_{dynamic}\;\eta_{profile}\;\eta_{sweep}$$

Energy Transfer

Lorentz Force Profile

Dynamic Efficiency

Sweeping Efficiency

$$\frac{\int_0^{t_f} \dot{L}J^2 dt}{2E} \quad \times \quad \frac{m_{accel}u_e^2 + \int_0^{t_f} \dot{m}u^2 dt}{\int_0^{t_f} uL'J^2 dt} \quad \times \quad \frac{m_{accel}u_e^2}{m_{accel}u_e^2 + \int_0^{t_f} \dot{m}u^2 dt} \quad \times \quad \frac{m_{accel}}{m_{avail}}$$

Figure 2.4: Breakdown of overall efficiency.

To further understand and evaluate how the initial stored energy is distributed, we separate the thruster efficiency into a collection of other efficiencies. From Eq. (4.9), the thruster efficiency can be broken up into five other efficiencies that will prove useful in examining the performance of GFPPTs,
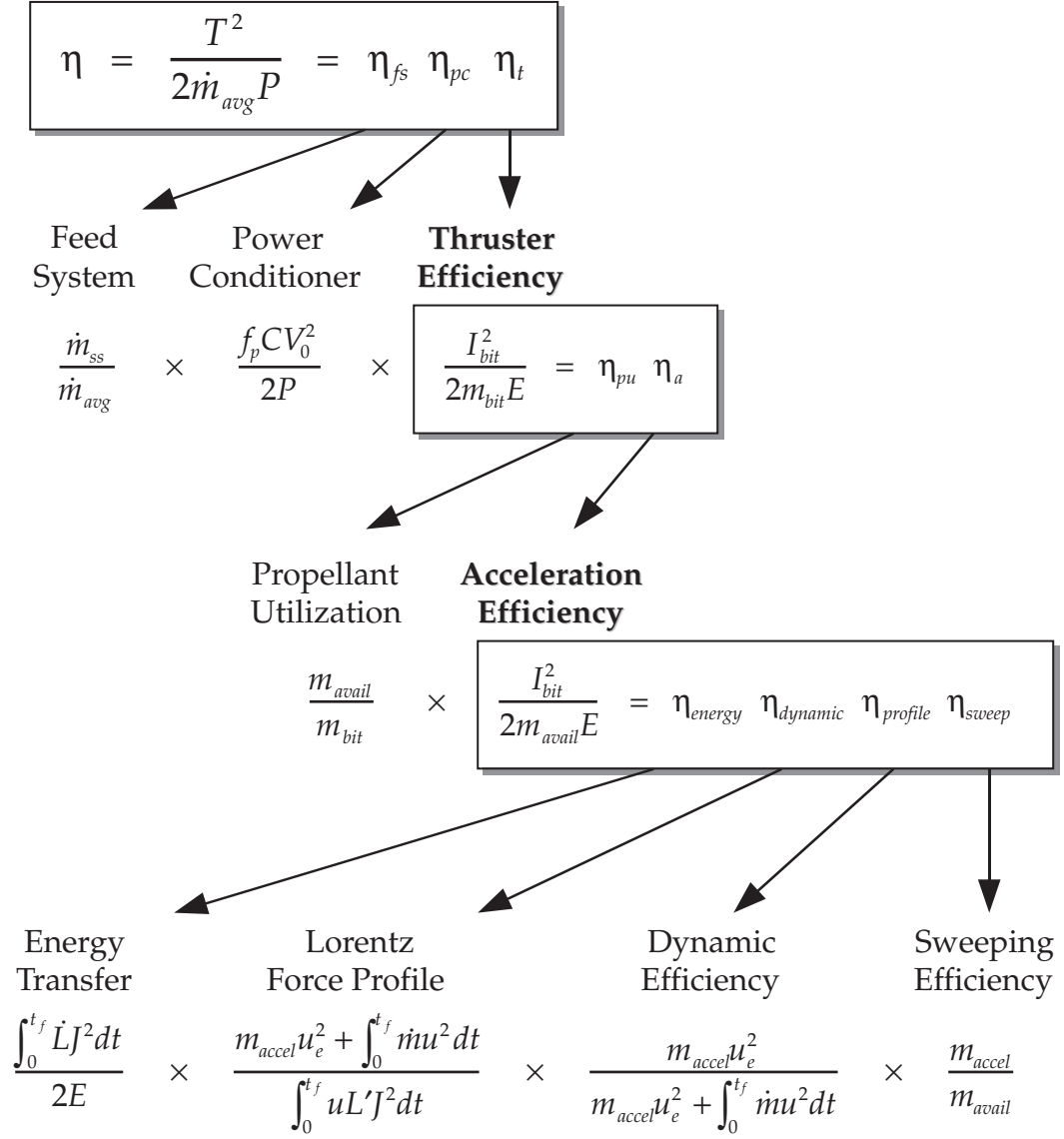
$$
\begin{aligned}
\eta_t &= \quad \eta_{pu} \qquad \eta_a & & & & & (2.11)\\
&= \quad \eta_{pu} \qquad \eta_{energy} \qquad\qquad \eta_{dynamic} \qquad\qquad\qquad \eta_{profile} \qquad\qquad \eta_{sweep},\\
&= \quad \frac{m_{avail}}{m_{bit}} \quad \frac{\int_0^{t_f} \dot{L}J^2 dt}{2E} \quad \frac{m_{accel}u_e^2 + \int_0^{t_f} \dot{m}u^2 dt}{\int_0^{t_f} \dot{L}J^2 dt} \quad \frac{m_{accel}u_e^2}{m_{accel}u_e^2 + \int_0^{t_f} \dot{m}u^2 dt} \quad \frac{m_{accel}}{m_{avail}}.
\end{aligned}
$$

Only the propellant mass accelerated to the final sheet speed (m_{accel} and u_e, respectively) is expected to contribute significantly to the impulse,

$$
I_{bit} = m_{accel}u_e = m_{bit}\bar{u}_e, \tag{2.12}
$$

where it follows from the definition of the propellant utilization and sweeping efficiencies that the final mass averaged velocity, $\bar{u}_e$, is related to the final sheet velocity, u_e,

$$
\bar{u}_e = \eta_{pu} \quad \eta_{sweep} \quad u_e. \tag{2.13}
$$

It is interesting to note that I_{bit}, u_e, and m_{bit} are *measurable* quantities while m_{accel} and $\bar{u}_e$ are inferred or calculated quantities.

We will discuss each efficiency from Eq. (2.11) in a separate subsection.

2.3.1 Propellant Utilization Efficiency, η_{pu}

As shown schematically in Fig. (2.5), depending on the electrode length and the mean thermal velocity of the propellant, v_{th}, some of the mass included in the "mass bit" might not actually be accelerated by the discharge. Using the maximum possible thermal velocity, v_{th}, based on the propellant plenum temperature, T_p, the maximum axial extent of the cold-gas column before each discharge, ℓ_{gas}, can be estimated by,

$$
\ell_{gas} \approx \tau_p v_{th} \approx \tau_p \sqrt{\frac{3kT_p}{m_w}}, \tag{2.14}
$$

with the total mass bit including *all* the injected propellant mass,

$$
\begin{aligned}
m_{bit} = \dot{m}_{ss}\tau_p &= \dot{m}_{ss}\frac{\ell_{elec}}{v_{th}} + \dot{m}_{ss}(\tau_p - \frac{\ell_{elec}}{v_{th}})\\
&= m_{avail} + m_{lost}, \tag{2.15}
\end{aligned}
$$

where $\dot{m}_{ss}$ is the steady-state mass flow rate of propellant into the discharge volume before each pulse. As an example, using argon and a pulse frequency of
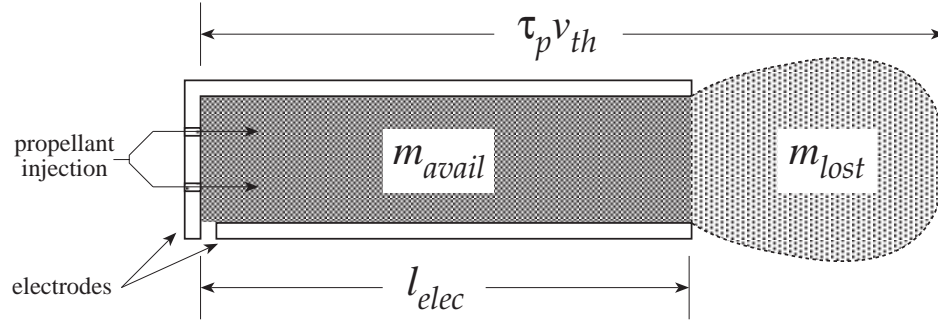
Figure 2.5: Schematic showing the division of the total mass bit between the mass available for acceleration, m_{avail}, and the mass lost, m_{lost}, before each pulse.

4 kHz, $\ell_{gas} \approx 10$ cm and the electrodes must be made at least 10 cm long or some portion of the gas will escape the electrode volume. A more accurate kinetic model for determining the propellant distribution will be presented in Chapter 3.

The propellant mass utilization efficiency, η_{pu}, can now be defined as the ratio of the propellant mass available to the discharge, m_{avail}, to the total injected mass, m_{bit},

$$\eta_{pu} \equiv \frac{m_{avail}}{m_{bit}} = \frac{\ell_{elec}}{\ell_{gas}} \approx \frac{\ell_{elec}}{\tau_p} \sqrt{\frac{m_w}{3kT_p}}. \tag{2.16}$$

Obviously even if the electrodes are longer than the gas column, the propellant utilization efficiency cannot exceed 100%. The pre-discharge propellant distribution may affect the *dynamic efficiency*, however, as described later.

2.3.2   Accelerator Efficiency, η_a

The accelerator efficiency is commonly used as a performance parameter in the previous GFPPT literature (See Refs. [11, 17, 37], for example) and is included here for that reason. In in our context, it is made up of the energy transfer, Lorentz force profile, dynamic, and sweeping efficiency making it completely independent of the power conditioning and propellant losses.

2.3.3   Energy Transfer Efficiency, η_{energy}

By integrating Eq. (2.7) directly, the initial energy can be distributed among the equivalent circuit elements,

$$E = \int_0^{t_f} \frac{1}{2}\dot{L}J^2 dt + \left(\frac{1}{2}LJ^2\right)_{t_f} + \left(\frac{1}{2}CV^2\right)_{t_f} + \int_0^{t_f} RJ^2 dt. \tag{2.17}$$

The first term is related to the energy going into physically expanding the circuit in any direction, the second and third terms are related to the energy stored in the magnetic fields and capacitor, respectively, at the end of the discharge (the current and voltage might not be zero when the discharge reaches the end of the electrodes), and the last term is related to the energy deposited by Joule heating in the electronics and the plasma due to its finite-conductivity. Assuming that the only useful energy in this equation is going into expanding the circuit, the energy transfer efficiency is,

$$\eta_{energy} \equiv \frac{\int_0^{t_f} \dot{L} J^2 dt}{2E}. \tag{2.18}$$

This efficiency also accounts for losses due to ionization and dissociation in creating the plasma originally.

2.3.4 Lorentz Force Profile Efficiency, $\eta_{profile}$

Examining Eq. (2.5), the ratio of the work done by the *axially* directed force on the accelerated propellant mass to the total work done by the Lorentz force is the profile efficiency,

$$\eta_{profile} \equiv \frac{m_{accel} u_e^2 + \int_0^{t_f} \dot{m} u^2 dt}{\int_0^{t_f} \dot{L} J^2 dt} = \frac{m_{accel} u_e^2 + \int_0^{t_f} \dot{m} u^2 dt}{\int_0^{t_f} u L' J^2 dt}. \tag{2.19}$$

This efficiency is less than unity if the current sheet is canted or has a non-planar profile. For example, this may be the case in a coaxial geometry GFPPT due to the radially non-uniform Lorentz force. Again, this efficiency is mainly related (through an as yet to be identified relation) to the molecular weight, current level and electrode geometry. Most of these parameters will be kept constant for this particular study.

2.3.5 Dynamic Efficiency, $\eta_{dynamic}$

As the accelerated propellant is swept up and contained by the current sheet, some portion of the axially directed Lorentz force work will go into heating the plasma,

$$\eta_{dynamic} \equiv \frac{m_{accel} u_e^2}{m_{accel} u_e^2 + \int_0^{t_f} \dot{m} u^2 dt}. \tag{2.20}$$

In general this electrothermal energy is difficult to recover into directed kinetic energy except at much higher pressures, as explained in Section 2.2.2. Even then, in these devices the conversion efficiency for this type of acceleration is generally very poor and the exhaust velocities can be relatively small (< 5000 m/s) even at the highest pressures. This process of sweeping up the gas has been examined

more thoroughly under the name "Dynamical Efficiency" originating in Ref. [85]. There it was shown that the dynamic efficiency can go from a value of 50% in a uniformly filled GFPPT to 100% for a discharge where all the mass is captured in the initiation process. Current sheet trajectories where the propellant is gradually swept up at the beginning of the discharge and then accelerated vigorously when $\dot{m} = 0$ are preferred. In general, the dynamic efficiency is a strong function of the initial propellant loading.

2.3.6 Current Sheet Sweeping Efficiency, η_{sweep}

The ratio of the propellant mass that is in the electrode volume to that accelerated by the discharge is the sweeping efficiency,

$$\eta_{sweep} \equiv \frac{m_{accel}}{m_{avail}} = \frac{\bar{u}_e}{\eta_{pu} \; u_e}. \tag{2.21}$$

The sweeping efficiency depends on two factors: the likelihood of continual propellant ionization as the current sheet travels through the propellant, and the flux of ions to the cathode and insulator walls where recombination and subsequent loss of axial momentum can occur. The likelihood of ionization in these discharges is quite high with almost every investigator observing a fully ionized plasma using spectroscopic techniques [46,52,61,86]. Investigators at Princeton [48,52] and at Avco Everett [32,87] have also noticed a precursor region with approximately a 10% ionization fraction in front of the current sheet, possibly caused by photoionization. Some propellant may not stay ionized, however, either recombining before significant acceleration takes place or, more likely, recombining with an electron on a wall surface. When an ion strikes a wall, either as part of the total current conduction or because of thermal diffusion with electrons, the resulting neutral particle will no longer move with current sheet speed. Although some of the neutrals may be ionized again, they do not, in general, contribute to the thruster performance. Lovberg and others have noticed a dense layer of plasma near the cathode, especially in devices where the sweeping efficiency is less than unity [46,50,60].

Jahn [2] provided an empirical rule for maintaining a high sweeping efficiency which requires initial current rise-times above 10^{12} A/s per meter width of current sheet for argon propellant with $E/m_{bit} < 5 \times 10^9$ J/kg. In the experiments presented in this dissertation, we will use only argon propellant with similar current rise-times to keep the sweeping efficiency relatively constant. Other research at EPPDyL is examining the scaling of the sweeping efficiency and current sheet stability with propellant type and current levels [60].

2.3.7 Choice of Parameters for Performance Scaling Studies

Each of the efficiencies described in Eq. (2.11) changes with modifications to electrode geometry, discharge energy, mass bit, propellant species, capacitance, voltage, pulsing frequency, inductance profile, internal circuit and plasma resistance, insulator and electrode material, electrode surface conditions, initiation source, and even propellant plenum temperature. It is no surprise that, to date, the performance measurements from various laboratories vary drastically with even some conflicting results from the effects of various parameter changes [11]. The goal of *this* research work is to carefully examine the performance scaling (thruster efficiency versus exhaust velocity, for example) as a function of three parameters: mass bit, capacitance, and inductance-per-unit length, with the other variables tightly controlled. These three parameters are expected to have the most dramatic effect on the energy transfer and dynamic efficiency.

Chapter 3

GFPPT Performance Models

In this chapter we develop GFPPT performance models for predicting the effects of capacitance, inductance-per-unit-length, initial inductance, energy, and mass bit on the exhaust velocity, efficiency, and impulse-to-energy ratio. Three different approaches are presented with progressive levels of complexity. The first is a circuit model that uses fixed elements to demonstrate that a slightly underdamped or critically damped current waveform provides the best energy transfer efficiency. The second model is an analytical approximation of a nearly critically damped current waveform which is used to examine the discharge dynamics with variable inductance and mass in more detail. Finally, in the third model we develop a set of non-dimensional equations including the effects of variable propellant loading, finite electrode length, and flared electrode geometries. The full set of equations are non-linear and can only be solved numerically. The solutions to the last model will be discussed in detail as they will be used in Chapter 6 to collaborate the performance scaling found in experimental performance measurements.

3.1   Analytical Discharge Current Models

In this section we will estimate the total discharge current and the Lorentz force acting on the plasma using two different circuit models. The first model assumes fixed circuit elements and a constant propellant mass. It will be used to compare the performance resulting from various current waveforms (underdamped, critically damped, and overdamped), taking crowbar discharges into account. The second model uses a variable inductance and a uniform mass loading to examine more dynamics of the discharge. Although these models have some limiting assumptions, they will prove useful for interpreting the more complicated, numerical solutions that are presented in Section 3.2.

3.1.1 Constant Element Model

Following previous examples found in the literature [42,80], we desire to decouple the discharge equations by keeping all the circuit elements fixed and the amount of mass in the discharge constant. Taking the derivative of the Kirchhoff equation, Eq. (2.1), we have,

$$\ddot{J}L_0 + \dot{J}R + \frac{J}{C} = 0. \tag{3.1}$$

Solving for $J(t)$ with $J(0) = 0$, $\dot{J}(0) = V_0/L_0$, yields,

$$J = \frac{V_0}{\omega L_0}e^{-(R/2L_0)t}\sin(\omega t), \tag{3.2}$$

where,

$$\omega = \left(\frac{1}{L_0 C} - \frac{R^2}{4L_0^2}\right)^{\frac{1}{2}} = \frac{1}{\sqrt{L_0 C}}\left(1 - \psi^2\right)^{\frac{1}{2}}, \tag{3.3}$$

and,

$$\psi \equiv \frac{R}{2}\sqrt{\frac{C}{L_0}}. \tag{3.4}$$

It is well known that this solution has a different character depending on ψ. If $\psi < 1$, then ω is real and the current and voltage are underdamped and oscillatory. If $\psi = 1$, then ω is zero and the current and voltage are critically damped (note that $\sin(\omega t)/\omega \rightarrow t$ for $\omega = 0$). If $\psi > 1$, then ω is imaginary and the current and voltage are overdamped. Figure (3.1) shows all three cases with common operational parameters for PT9.

The impulse from the Lorentz force is proportional to half the inductance-per-unit-length and the integral of the current squared. If we integrate Eq. (3.2) over a time period lasting until the capacitor is fully discharged, then, *regardless of the nature of the waveform*,

$$I_{bit} = \frac{1}{2}L'\frac{E}{R}, \tag{3.5}$$

and,

$$\eta_t = \frac{1}{4}L'\frac{\bar{u}_e}{R}. \tag{3.6}$$

Using the maximum efficiency, $\eta_t = 1$, it follows that the maximum exhaust velocity, $\bar{u}_{emax}$, is,

$$\bar{u}_{emax} = \frac{4R}{L'} = \frac{8\psi}{L'}\sqrt{\frac{L_0}{C}}. \tag{3.7}$$

These relations would suggest that very small resistance values, hence very underdamped waveforms, are preferred for high efficiency but *not for high exhaust*
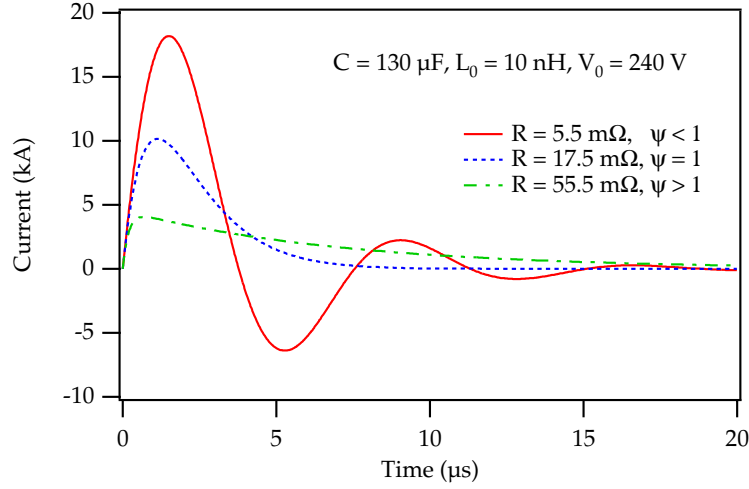
Figure 3.1: Under, Critically, and Over-damped waveforms from the constant-element LRC model with common operational parameters for PT9.

velocity. In fact, if the resistance is close to zero, the efficiency can reach unreasonable values while the exhaust velocity drops to zero. In reality this is not the case for two reasons: 1) In an efficient thruster, the effective "resistance" in the circuit also includes the term uL'. Using a small resistance implies there is small velocity and very little energy is actually transferred to the plasma in any form. 2) Crowbar discharges have been observed experimentally in almost every device when the current waveform reverses, limiting any further energy addition to the discharge from the capacitor.

If we limit our integration up to the time where the current is zero (effectively an infinite time for the critically and underdamped waveforms), then a correction factor, $f_c(\psi)$, is introduced for the underdamped case,

$$I_{bit} = \frac{1}{2}L'\int_0^{\frac{\pi}{\omega}} J^2 dt = \frac{1}{4}L'\sqrt{\frac{C}{L_0}}E\frac{f_c(\psi)}{\psi}, \tag{3.8}$$

$$f_c(\psi) = \begin{cases} 1 - e^{\left(-2\pi\sqrt{\frac{\psi^2}{1-\psi^2}}\right)} & : \quad \psi < 1 \\ 1 & : \quad \psi \geq 1. \end{cases}$$

The functions $f_c(\psi)$ and $f_c(\psi)/\psi$ are shown graphically in Fig. (3.2). If we assume that there is no ohmic heating or other loss mechanism that would contribute to R, we can replace the resistance by a constant inductance change based on an average velocity of the current sheet, $R \approx L' <u> /2$. The efficiency becomes,

$$\eta_t = \frac{1}{8}L'\sqrt{\frac{C}{L_0}}\bar{u}_e\frac{f_c(\psi)}{\psi} = \frac{\bar{u}_e}{\bar{u}_{emax}}f_c(\psi) \approx \frac{1}{2}\frac{\bar{u}_e}{<u>}f_c(\psi) \approx f_c(\psi). \tag{3.9}$$
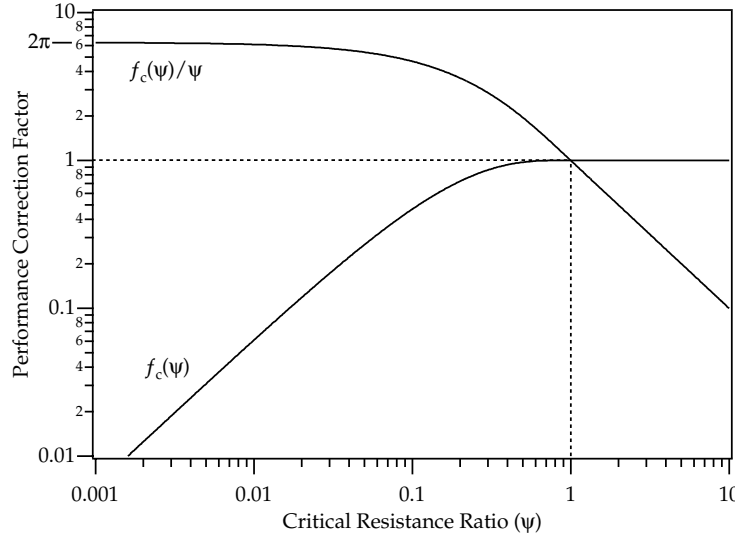
Figure 3.2: Performance correction function (see Eq. (3.8)) for the fixed-element model. ψ is defined in Eq. (3.4).

This approximation simply states that the thruster efficiency (or energy transfer efficiency) is close to unity as it should be when there are no other energy sinks aside from the directed kinetic energy of the plasma, and thus $\bar{u}_e = \bar{u}_{emax}$. If there is a crowbar discharge, however, energy can be left stored in the capacitor or trapped in the magnetic fields and a correction factor is required. This would suggest that it is possible to have 100% energy conversion in either critically or underdamped cases, but not, if a crowbar discharge occurs, with an underdamped waveform. Also note that as the resistance goes to zero, the exhaust velocity and ψ drop to zero, however, $f_c(\psi)/\psi \rightarrow 2\pi$. Instead of an unbounded efficiency as in Eq. (3.6), this relation provides an efficiency that is finite and very small for very small values of resistance and velocity.

Achieving the highest energy conversion efficiency then simply equates to reaching the highest velocity possible and/or *reducing* the maximum obtainable velocity by *increasing* L' and C. One must also realize, however, that large velocities and long current pulses (overdamped waveforms) require very long electrodes to transfer the entire energy stored in the capacitor. Because of wall losses and the cumbersome weight of very long electrodes, very overdamped waveforms may not be as beneficial as close to critically damped waveforms in real devices.

Although this model is a reasonable approximation and useful for examining the best *type* of waveform, using constant elements limits its application to real GFPPTs. In real GFPPT discharges, the changing inductance continually modifies the current waveform away from these fixed-element solutions. In the next section

we will be able to remove the fixed constraints by focusing on nearly critically damped current waveforms.

3.1.2 Variable Element Model

For GFPPTs used in this dissertation, the current waveform is essentially critically damped due to the low inductance ($<$ 10 nH) and large capacitance ($>$ 100 μF) of the energy storage bank. Current waveforms measured with higher mass bits can have a slight underdamped quality while lower mass bits can produce slightly overdamped waveforms. With this understanding, we can focus on ψ values near unity. As will be shown, this allows us to relax the assumptions of fixed inductance and mass used in the previous model and derive useful, analytical scaling relations for a more realistic model.

First, we expand Kirchhoff's equation,

$$V_0 = \frac{1}{C} \int_0^t J dt^* + (R + \dot{L})J + L\dot{J}. \tag{3.10}$$

Solutions to this equation yield current waveforms that have a similar character to those in the first model except that the total resistance term now includes the changing magnetic field due to the motion of the current sheet, $\dot{L}$, and the total inductance, L, increases during the pulse. In this model the resistance, R, includes only the effective plasma resistance as well as the resistance in the capacitor bank and electrodes.

Next, we split the discharge into two segments: before the peak current is reached at $t = t_{peak}$, and from that time until the current changes sign or reaches zero, $t = t_{final}$. During each segment, we will approximate the current with a relation that is linearly proportional to time.

First Segment

In the first segment, the slope of the current is determined by the initial values of the inductance, L_0, and voltage, V_0, along with the fixed values of capacitance, C, and resistance, R. The exact relation is derived from some simple approximations of the solutions to the fixed element case. As shown in Fig. (3.1) and from Eq. (3.2), the peak current and the time it occurs are both functions of ψ,

$$J_{peak} = V_0 \sqrt{\frac{C}{L_0}} e^{-\left(\frac{\psi}{\sqrt{1-\psi^2}} \sin^{-1}(\sqrt{1-\psi^2})\right)} = V_0 \sqrt{\frac{C}{L_0}} f_J(\psi), \tag{3.11}$$

$$t_{peak} = \sqrt{L_0 C} \left(\frac{1}{\sqrt{1-\psi^2}} \sin^{-1}(\sqrt{1-\psi^2})\right) = \sqrt{L_0 C} f_t(\psi), \tag{3.12}$$
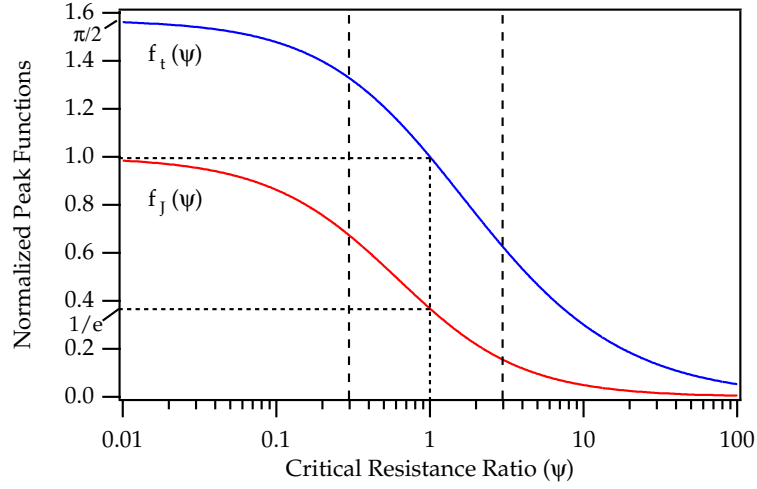
Figure 3.3: Normalized peak functions for the peak current and peak current time as a function of ψ. Values of the correction factors at $\psi = 1$ are shown by horizontal dotted lines. The range of this model is $0.3 \leq \psi \leq 3$ as shown by the vertical dashed lines.

where $f_J(\psi)$ and $f_t(\psi)$ are designated as the "normalized peak functions." These two relations are shown as functions of ψ in Fig. (3.3) with exact values of the functions at $\psi = 1$ marked by dotted lines. The slope of the current in the first segment of the discharge is then simply J_{peak}/t_{peak},

$$J(t)\big|_0^{t_{peak}} = \frac{V_0}{L_0} \frac{f_J(\psi)}{f_t(\psi)} t. \tag{3.13}$$

Second Segment

In the second segment, our assumption of a nearly critically damped waveform is very important in determining the correct slope of the current. For the critically damped case, the slope is related to the increasing inductance and exponential nature of the actual current waveform. For that reason, we will assume that the final slope is related to the total change in inductance, ΔL, by a factor Λ,

$$\Lambda \equiv \frac{L_f}{L_0} = 1 + \frac{\Delta L}{L_0}, \tag{3.14}$$

so that the second half of the current waveform is given by,

$$J(t)\big|_{t_{peak}}^{t_{final}} = \frac{V_0}{\Lambda} \sqrt{\frac{C}{L_0}} f_J(\psi) \left[\Lambda + f_J(\psi) f_t(\psi) - f_J(\psi) \frac{t}{\sqrt{L_0 C}} \right]. \tag{3.15}$$
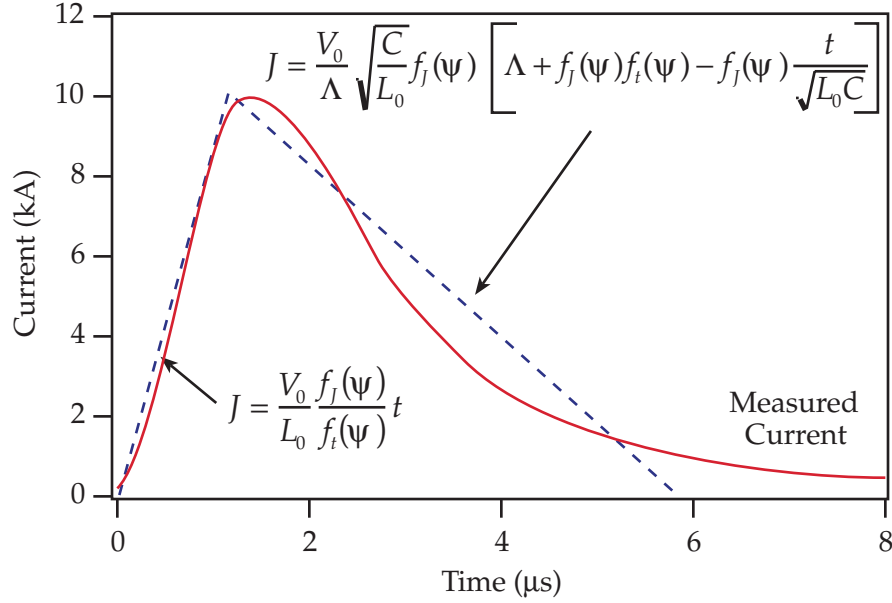
Figure 3.4: Variable element model for the current of a GFPPT discharge compared to a measured current trace from PT9: 4 J per pulse, 2.0 μg argon, 130 μF, 1″ $\times$ 1″ electrodes.

Performance Scaling Relations

The entire current model is shown with a measured current waveform from PT9 in Fig. (3.4) using the measured parameters $L_0 = 10$ nH, $C = 130$ μF, and $V_0 = 242$ V. The approximate value of the inductance change, $\Lambda \approx 1.5$, is found by assuming that the current sheet reaches the end of the electrodes when the capacitor is fully drained. The model is shown to agree reasonably well with this current trace and the thruster parameters assuming $\psi \approx 1$. Although at some times the model appears to over or under predict the current, since the impulse is related to the *integral* of J^2, the model should still predict the performance reasonably well.

As long as the effective resistance does not change significantly during the discharge, i.e. ψ is constant, the integral of J^2 can be evaluated in a straightforward manner,

$$\int_0^{t_{final}} J^2 dt = \frac{2}{3} E \sqrt{\frac{C}{L_0}} \left[f_J^2(\psi) f_t(\psi) + \Lambda f_J(\psi) \right]. \tag{3.16}$$

Using Eqns. (3.11) and (3.12) to estimate the normalized peak functions for $0.3 \leq \psi \leq 3$, we have,

$$\int_0^{t_{final}} J^2 dt = \frac{2}{3} E \sqrt{\frac{C}{L_0}} \left[\frac{\pi}{2} e^{-\sqrt{6\psi}} + \Lambda e^{-\sqrt{\psi}} \right]. \tag{3.17}$$
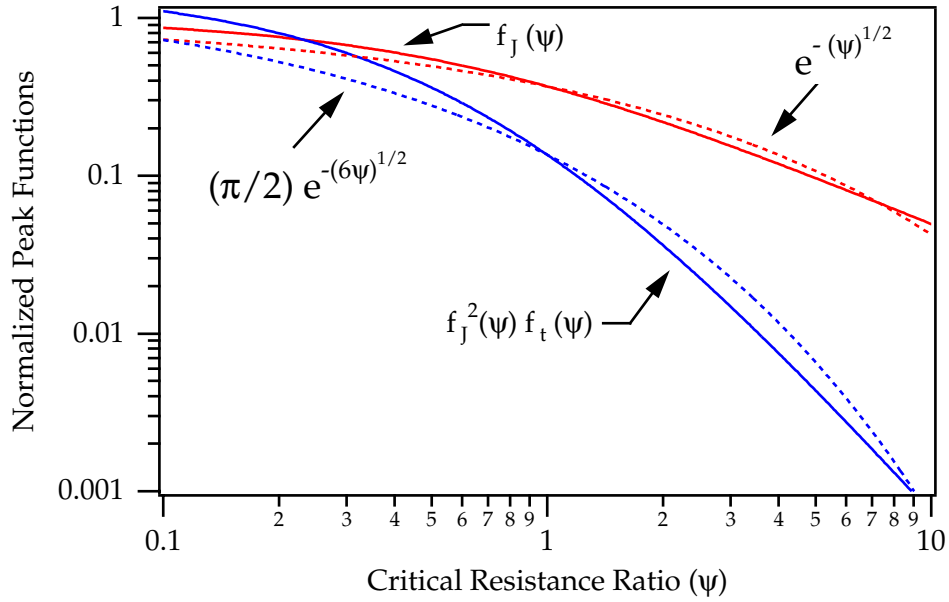
Figure 3.5: Approximations (dashed lines) to the normalized peak functions $f_J(\psi)$ and $f_J^2(\psi)$ (solid lines).

These approximations are shown in Fig. (3.5) to be in good order of magnitude agreement with the actual values of the normalized peak functions over the intended range of ψ, especially near $\psi = 1$. Now using this approximation to determine the impulse, we integrate the momentum equation (Eq. (2.5)) to get the impulse bit, I_{bit},

$$I_{bit} = \int_0^{t_{final}} \left[\frac{d}{dt}(mu) \right] dt, \tag{3.18}$$

$$= \frac{1}{2} L' \int_0^{t_{final}} J^2 dt, \tag{3.19}$$

$$= \frac{1}{3} E L' \sqrt{\frac{C}{L_0}} \left[\frac{\pi}{2} e^{-\sqrt{6\psi}} + \Lambda e^{-\sqrt{\psi}} \right]. \tag{3.20}$$

Note that the *impulse* does not depend on the mass distribution or how the propellant was accumulated. At this point, we only know the exit conditions of the discharge, and the trajectory of the current sheet during the discharge cannot be found without knowing the mass distribution. Although the mass distribution does not determine the impulse, it does determine the amount of *energy* required to accelerate the entire mass down the length of the electrodes to the exit velocity. This, in turn, affects the efficiency.

There is still one unknown in Eq. (3.18): Λ. To determine Λ, we add another

constraint that the integral of the current over the discharge time simply equal the initial charge on the capacitor, CV_0. This implies that the capacitor voltage at the end of the discharge is zero and that current no longer flows after t_{final}. Once again, we use Eqns. (3.13) and (3.15) to model the discharge current waveform and we find that,

$$\Lambda = 2 - f_t(\psi)f_J(\psi). \tag{3.21}$$

Using this relation, we can simplify the expression for the impulse bit,

$$I_{bit} = \frac{2}{3}EL'\sqrt{\frac{C}{L_0}}\,e^{-\sqrt{\psi}}. \tag{3.22}$$

The thruster efficiency is then,

$$\eta_t \equiv \frac{I_{bit}^2}{2m_{bit}E}, \tag{3.23}$$

$$= \frac{1}{3}L'\sqrt{\frac{C}{L_0}}\,\bar{u}_e\,e^{-\sqrt{\psi}}, \tag{3.24}$$

$$= \frac{\bar{u}_e}{\mathcal{U}}\,e^{-\sqrt{\psi}}, \tag{3.25}$$

where we have introduced the GFPPT characteristic velocity, $\mathcal{U}$, as,

$$\mathcal{U} \equiv \frac{3}{L'}\sqrt{\frac{L_0}{C}}. \tag{3.26}$$

Note that this is very similar to the definition of $\bar{u}_{emax}$ found in Eq. (3.7), except that $\mathcal{U}$ is *independent* of ψ. In this model, if the total resistance in the circuit is zero ($\psi = 0$), the maximum efficiency is reached when $\bar{u}_e = \mathcal{U}$. In this respect, the GFPPT characteristic velocity is the maximum obtainable exhaust velocity if there are no resistive losses in the complete discharge circuit. If $\psi > 0$, then the maximum exhaust velocity can be larger than $\mathcal{U}$.

The GFPPT characteristic velocity is only a function of the driving circuit and the electrode geometry making it *uniquely determined for each GFPPT design*. This model predicts that the efficiency is linearly dependent on the exhaust velocity, the inductance-per-unit-length, and the square root of the capacitance-to-initial-inductance ratio.

Effects of Propellant Distribution

As we mentioned before, the efficiency (and hence the exhaust velocity) should depend on how the propellant is accumulated in the discharge. To determine the exhaust velocity and the efficiency explicitly, we must assume a functional form

for the mass distribution. For simplicity, we assume a linear form where the propellant is uniformly distributed before the pulse, and the total mass swept up by the current sheet, m, depends only on the location of the discharge,

$$m = m'z + m_0, \tag{3.27}$$

where m' is a constant "density" and m_0 is the initial mass taken up by the current sheet formation. For a slug mass distribution (where the initial mass is large, $m'z_{final} \ll m_0$) the exhaust velocity becomes,

$$\bar{u}_e = \frac{2}{3}\frac{E}{m_{bit}}L'\sqrt{\frac{C}{L_0}}\,e^{-\sqrt{\psi}} = \frac{2}{\mathcal{U}}\frac{E}{m_{bit}}\,e^{-\sqrt{\psi}}, \tag{3.28}$$

and the efficiency is,

$$\eta_t = \frac{2}{9}\frac{E}{m_{bit}}L'^2\frac{C}{L_0}\,e^{-2\sqrt{\psi}} = \frac{2}{\mathcal{U}^2}\frac{E}{m_{bit}}\,e^{-2\sqrt{\psi}}. \tag{3.29}$$

We would expect this kind of scaling for a GFPPT with a short amount of time between pulses so that the propellant mass does not have a chance to expand much beyond the backplate before the discharge.

If $m'z_{final} \gg m_0$ then the exhaust velocity is,

$$\bar{u}_e = \sqrt{\frac{4EL'}{3m'L_0}}\;e^{-\sqrt{\psi}}, \tag{3.30}$$

and the efficiency is,

$$\eta_t = \sqrt{\frac{2L'^3C^2V_0^2}{27L_0^2m'}}\,e^{-2\sqrt{\psi}} = \frac{L'CV_0}{3L_0}\sqrt{\frac{2L'}{3m'}}\,e^{-2\sqrt{\psi}} = \frac{V_0}{\mathcal{U}^2}\sqrt{\frac{6}{L'm'}}\,e^{-2\sqrt{\psi}}. \tag{3.31}$$

We would expect this kind of scaling for a thruster with a large mass bit value, or a long time between pulses to allow the propellant to evenly distribute itself. In the next section, we will see that this prediction also follows from a non-dimensional approach to the problem.

The performance relations have a different character depending on the mass distribution which should be expected from the discussion of dynamic efficiency in Section 2.3.5. Yet, for the mass and velocity profiles we have used, the dynamic efficiency is fixed and is exactly 5/7 (71.4%) regardless of the value of m_{bit}. This implies that the scaling of the *energy transfer efficiency* (See Eq. (2.11)) also depends on *how* the mass is accumulated. The propellant distribution changes the current sheet trajectory, thus modifying the current waveform itself.

At this point, improving our models further would require lifting our most important assumption that the critical resistance ratio remains relatively constant

and near unity over the course of the discharge. Perhaps the most efficient current waveform would start out as underdamped, reach a high peak current, and then gradually become critically or overdamped as the result of an increasing velocity and $\dot{L}$ with no current reversals. Of course, if the propellant mass is swept up earlier in the discharge, the thruster efficiency will also be greater through an increase in the dynamic efficiency. So far we have constrained the mass distribution to be either fixed or uniform when in reality it may be somewhere in between. Modeling this kind of dynamic system completely requires numerical integration as explained in more detail in the next section. As we will see, however, the simplified models are very useful to explain some trends present in the numerical results.

3.2 Non-Dimensional Model and Numerical Solutions

As demonstrated by the previous models, there are many parameters that must be specified *a priori* such as the main capacitance, initial inductance, mass loading, charging voltage, plasma resistance, etc., to determine a unique outcome for the discharge. This variety of adjustable parameters can preclude the usefulness of a complex model for predicting performance scaling over a wide range of conditions. A correct non-dimensional scheme, however, reduces the number of free parameters allowing a more reasonable approach for finding overall performance scaling laws. This model was first presented by Ziemer et al. in Ref. [73] and follows from similar schemes with linear mass distributions and parallel electrodes in Ref. [2]. The most important points from Ref. [73] as well as some new studies on the dynamic and energy transfer efficiencies will be presented here.

Compared to previous models, this model adds both an exponential mass distribution and a contoured electrode geometry to simulate real GFPPTs more effectively over a wide range of operational conditions. It removes all the fixed-value constraints except for the plasma resistance and capacitor bank internal impedance which are combined and left as a parameter, the total resistance, R. Keeping the total resistance constant is valid when the fixed capacitor bank impedance is on the same order as the somewhat variable plasma resistance or for an efficient device where $\dot{L} \gg R$. This model relies on its simplicity (a modern desktop computer can numerically solve the equations in less than ten seconds) to thoroughly explore various thruster configurations with a total of over 10,000 cases examined to date. The results will be presented here in terms of two possible electrode lengths. One length is based on the maximum efficiency that can be achieved during the discharge, and the other is based on a realistic limit of the total inductance change for typical geometries of interest. Although this model was originally developed for a coaxial geometry GFPPT, only slight modifications which do not change the nature of the results will be required for modeling a parallel-plate geometry.

This section is organized in the following manner. First, the model will be

summarized including the outer electrode contour relation and the mass distribution equation. Next, all of the equations will be non-dimensionalized reducing the number of free parameters from ten to five. This small number of parameters together with the two methods for determining the final integration time will allow the non-dimensional parameter space to be explored in terms of performance scaling. It will be shown that particular values of the five parameters exist that maximize thruster performance. Performance scaling relations similar to those found in the previous sections will also be developed from the study of a large number of solutions to the dynamic equations.

3.2.1 Quasi-One-Dimensional Equations

This quasi-one-dimensional model uses an outer electrode profile, $r_{outer}(z)$, that expands slightly, a constant inner electrode radius, and a non-uniform mass distribution, $m(z)$. The current sheet itself is assumed to be planar, and all forces are considered to act only in the axial direction with no recovery of electrothermal energy. The equation describing the outer electrode contour is taken as exponential in nature to model a variety of potential geometries, especially PT5,

$$r_{outer}(z) = r_{out}e^{z/d}, \tag{3.32}$$

where d is a constant determined by the shape of the electrodes. Due to the exponential nature of the equation, as d increases the outer electrode expands less and less as a function of z. This equation is shown schematically in Fig. (3.6).

The mass distribution equation used in this model is derived from a kinetic description of a gas column expanding into a vacuum. In the ideal one-dimensional case, a barrier, such as a valve, exists at $z = 0$ between a plenum of gas with density $2m'$ and an infinite vacuum. At time $t = 0$, the barrier is removed and the gas expands. The overall density profile is then given by an error function whose exponential nature begins at $z = 0$ some time later,

$$n_{prop} = m'e^{-z^2/b^2}, \quad (z \geq 0, t \geq 0). \tag{3.33}$$

The mass distribution constant in the exponent, b, is related to the product of the molecular speed of the gas and the expansion time, $b = \tau_p\sqrt{2T_pk/m_w}$. Assuming that the density profile is fixed during the discharge (pulse durations are $< 1\%$ of the propellant fill time), the total mass collected by the current sheet at any point along the channel is,

$$m(z) = \int_0^z m'e^{-z^{*2}/b^2}dz^* + m_0. \tag{3.34}$$

Again, the exponential nature of the equation allows a uniform mass distribution for a large value of b and a slug mass for a small mass distribution constant. These
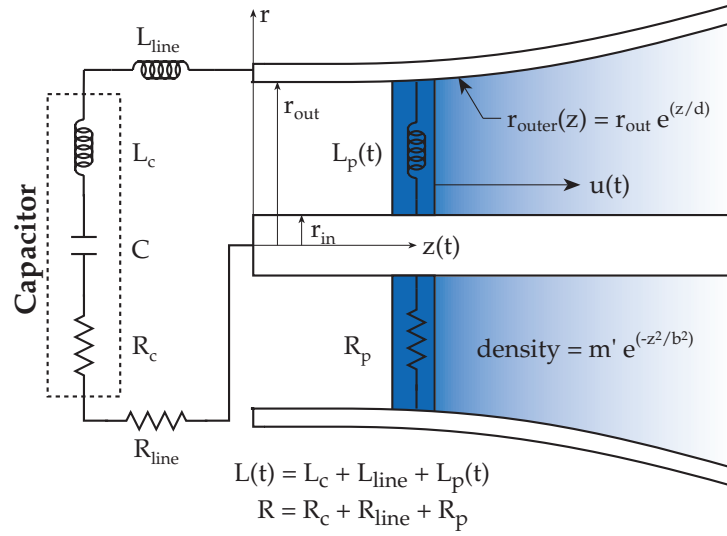
Figure 3.6: Schematic of quasi-one-dimensional GFPPT discharge model.

values can be achieved by adjusting the time between the pulses and choosing an appropriate propellant and plenum temperature. In real GFPPTs, the most effective control of the mass distribution comes from changing the time between pulses as, for many missions, the propellant type and plenum temperatures are fixed.

The inductance for this circuit increases as the current sheet expands down the electrodes. From the outer electrode profile, Eq. (3.32), the inductance can be calculated as a function of z for coaxial electrodes with a planar current sheet,

$$L = \frac{\mu_0}{2\pi} \left[\frac{1}{2d}z^2 + z \ln\left(\frac{r_{out}}{r_{in}}\right) \right] + L_0. \tag{3.35}$$

It is important to note that this inductance is quadratically increasing over z rather than linearly as in previous models due to the exponential nature of the outer electrode profile. At this point it is convenient to express the inductance-per-unit-length for a parallel, coaxial set of electrodes:

$$L' = \frac{\mu_0}{2\pi} \ln\left(\frac{r_{out}}{r_{in}}\right). \tag{3.36}$$

This expression will be used in future sections to non-dimensionalize the total circuit inductance for any outer electrode contour. Again, after the non-dimensional scheme is presented it will be shown that these relations can be modified for parallel-plate geometries with the appropriate L' and with $1/d = 0$.

The circuit equation with all the necessary derivatives can now be expressed

as,

$$J\left[\frac{1}{C} + \frac{dL}{dz}\frac{d^2z}{dt^2} + \frac{d^2L}{dz^2}\left(\frac{dz}{dt}\right)^2\right] + \frac{dJ}{dt}\left[R + 2\frac{dL}{dz}\frac{dz}{dt}\right] + \frac{d^2J}{dt^2}[L] = 0. \qquad (3.37)$$

Note that there is a second spatial derivative of the inductance that will not be zero for the case of a contoured outer electrode.

The full momentum equation can be expressed as,

$$\frac{dm}{dz}\left(\frac{dz}{dt}\right)^2 + m\frac{d^2z}{dt^2} - \frac{\mu_0}{4\pi}J^2\left[\ln\left(\frac{r_{out}}{r_{in}}\right) + \frac{dL}{dz}\right] = 0. \qquad (3.38)$$

To solve these equations, a total of ten parameters ($r_{out}, r_{in}, d, m_0, m', b, V_0, C, R,$ and L_0) must be specified along with an integration period or propagation distance (electrode length) to generate a unique solution. Clearly with this many parameters and a choice of discharge duration, it would be difficult to determine an optimal thruster design or discover any universal trends in performance related to one particular dimensional parameter verses another. In the next section, a non-dimensionalization scheme will reduce the number of parameters in half allowing the parameter space to be spanned in a more reasonable manner.

3.2.2 Non-Dimensional Variables and Parameters

For this non-dimensional scheme, we will normalize by the critically damped current waveform for an appropriate non-dimensional scheme. In a critically damped LRC circuit, the maximum current is reached at $t = \sqrt{L_0C}$ with a value, $J_{peak} \approx 1/3\, V_0\sqrt{C/L_0}$. For the moving current sheet, we are concerned with the characteristic length it will take to match the initial inductance. With this in mind, we can now define the primary non-dimensional variables for time, length, current, and mass in the discharge as follows:

$$\tau = \frac{t}{\sqrt{L_0C}}, \qquad (3.39)$$

$$\delta = \frac{L'}{L_0}z, \qquad (3.40)$$

$$\zeta = \frac{3}{V_0}\sqrt{\frac{C}{L_0}}J, \qquad (3.41)$$

$$\rho = \frac{L'}{m'L_0}m. \qquad (3.42)$$

In order to non-dimensionalize the full equation set, five non-dimensional parameters are required:

$$\alpha = \frac{L'^3V_0^2C^2}{18L_0^2m'}, \qquad (3.43)$$

$$\psi \;=\; \frac{R}{2}\sqrt{\frac{C}{L_0}}, \tag{3.44}$$

$$\rho_0 \;=\; \frac{m_0 L^{'}}{m^{'} L_0}, \tag{3.45}$$

$$\gamma \;=\; \frac{L_0}{L' b}, \tag{3.46}$$

$$\lambda \;=\; \frac{\mu_0}{2\pi}\frac{L_0}{L'^2}\frac{1}{d}. \tag{3.47}$$

The first three parameters have been defined in a similar fashion in previous works (see Refs. [2, 80].) The last two are introduced here and determine the exponential nature of the mass distribution and the flare of the outer electrode, respectively. All of these parameters will be discussed in more detail in Section 3.2.3.

Using these definitions, the mass accumulation can be derived in terms of ρ,

$$\rho = \int_0^\delta e^{(-\gamma^2 \delta^{*2})} d\delta^* + \rho_0. \tag{3.48}$$

The non-dimensional inductance is now a function of δ and λ,

$$\frac{L}{L_0} = \frac{1}{2}\lambda\delta^2 + \delta + 1. \tag{3.49}$$

For parallel-plate geometry, we simply set λ to zero and use the appropriate value of $L^{'}$ from Section 4.2.3 in the next chapter. With all the primary variables and parameters defined, we can express the two main equations for energy and mass conservation non-dimensionally with the following initial conditions,

$$\delta(0), \dot{\delta}(0), \ddot{\delta}(0), \zeta(0) \;=\; 0 \tag{3.50}$$

$$\dot{\zeta}(0) \;=\; 3 \tag{3.51}$$

$$\ddot{\zeta}(0) \;=\; -6\psi \tag{3.52}$$

$$\rho(0) \;=\; \rho_0 \tag{3.53}$$

$$\rho^{'}(0) \;=\; 1 \tag{3.54}$$

The Circuit Energy Equation

The circuit equation, Eq. (3.37), becomes:

$$\zeta\left[1 + \lambda\left(\frac{d\delta}{d\tau}\right)^2 + (1 + \lambda\delta)\left(\frac{d^2\delta}{d\tau^2}\right)\right] \;+\; 2\frac{d\zeta}{d\tau}\left[\psi + (1 + \lambda\delta)\frac{d\delta}{d\tau}\right]$$

$$+\; \frac{d^2\zeta}{d\tau^2}\left[\frac{1}{2}\lambda\delta^2 + \delta + 1\right] = 0. \tag{3.55}$$

There are many terms in this equation related to the curvature of the outer electrode that are not present in previous models. As the quantity $\lambda\delta$ approaches unity, these terms dominate over the normal parallel electrode configuration.

Mass Addition and Momentum Conservation

Under this non-dimensionalization scheme, the momentum equation becomes:

$$\frac{d\rho}{d\delta}\left(\frac{d\delta}{d\tau}\right)^2 + \rho\frac{d^2\delta}{d\tau^2} - \alpha(1+\lambda\delta)\zeta^2 = 0. \tag{3.56}$$

Again, there are terms here that are present due to the contoured nature of the outer electrodes and the exponential mass distribution function. Overall this equation shows that the current sheet acceleration, $d^2\delta/d\tau^2$, is due to the driving electromagnetic force, $\alpha(1+\lambda\delta)\zeta^2$, minus the energy required to bring the mass just in front of the current sheet up to speed, $d\rho/d\delta(d\delta/d\tau)^2$. This energy is lost to internal thermal energy of the plasma and is not recovered. This relates to the dynamic efficiency of the sweeping process and we should expect α and γ to play a strong role in determining that quantity.

3.2.3 Physical Meaning of Non-Dimensional Parameters

This section will go into more detail regarding the five non-dimensional parameters now classified as follows: the dynamic impedance parameter α, the critical resistance ratio ψ, the initial mass parameter ρ_0, the mass distribution parameter γ, and the geometry parameter λ. The parameters are depicted graphically at the end of this section in Fig. (3.7).

The Dynamic Impedance Parameter, α

The dynamic impedance parameter is the most complicated of the non-dimensional parameters. It has appeared before in the previous section from the variable element current model and in previous work (see Section A.1 and Refs. [2, 42, 53]) under a different name. In Eqns. (3.30) and (3.31) it was found that the exhaust velocity and efficiency scaled as the square root of this parameter for a uniform mass distribution. To further understand its value and importance, α can be broken down further into a combination of ratios,

$$\alpha = \frac{L'^3 V_0^2 C^2}{18 L_0^2 m'} = \frac{2}{9}\frac{\Delta L}{L_0}\left(\frac{\dot{L}_f}{R}\right)^2 \frac{1}{\eta_t} \quad \psi^2 \tag{3.57}$$

$$= \frac{8}{9}\frac{L'^3 V_0^2}{R^4 m'}\psi^4. \tag{3.58}$$

The terms in the first equation include:

1. The ratio of the change in inductance to the initial inductance, $\Delta L/L_0$, typically a measure of PPT efficiency with a value greater than or near unity for a discharge dominated by *electromagnetic* acceleration.

2. The ratio of the dynamic impedance to the circuit resistance, $\dot{L}_f/R$, which should be greater than one for GFPPTs that are electromagnetic in nature.

3. The inverse of the thruster efficiency, $1/\eta_t$, which will be greater than one.

4. The critical resistance ratio squared, ψ^2, which is typically one or less.

Together with the $2/9$ coefficient, α should be close to unity for most GFPPTs. The second relation shows that α is proportional to ψ to the fourth power. This formulation presents α without any direct dependence on the capacitance or initial inductance. In Section 3.3, this formulation will prove to describe thruster performance scaling near $\psi = 1$ over a wide range of α and ψ values.

For a slug mass, $m' = 0$, the dynamic impedance parameter takes on a slightly different form,

$$\alpha_{slug} = \frac{L'^2 V_0^2 C^2}{18 L_0 m_{bit}} = \frac{4}{9} \frac{L'^2 E}{m_{bit} R^2} \psi^2. \tag{3.59}$$

From the previous section on the variable element model (see Eq. (3.29)), the efficiency for a slug-mass is expected to scale linearly with this version of α.

The Critical Resistance Ratio, ψ

This ratio describes the oscillatory nature of the current waveform. Together with the changing inductance, $\dot{L}$, this parameter determines if the circuit response is over, under, or critically damped, as described in Section 3.1.1. This parameter includes the internal resistance from the capacitor bank as well as the effective resistance of the plasma including finite conductivity, radiation, and ionization losses. Typical values of ψ for SRL-EPPDyL GFPPTs have been measured to be slightly larger than one. Prior to this work, GFPPTs operated at higher energy and current levels. They also had potentially different values of ψ because of different amounts of radiation and ionization during the discharge as well as a change in plasma conductivity due to higher voltage and current levels. In those experiments, the measured value of the plasma resistance was $< 10m\Omega$ with a slightly larger value during the initial 100 ns of the discharge [46, 47, 58].

The Initial Mass Parameter, ρ_0

The initial mass parameter is simply a ratio of the initial mass taken up during the current sheet initiation to the total mass accumulated after traveling to $\delta = 1$ with a uniform mass distribution. For most gas-fed PPTs, this parameter is small, close to 0.5 or less and does not influence the performance significantly.

The Mass Distribution Parameter, γ

This parameter describes the distribution of mass in the thruster. As seen from Eq. (3.48), large values of γ lead to mass distributions concentrated near the breech of the electrodes. As γ approaches zero, the mass is distributed uniformly with a linear density of m'. This parameter should have a large impact on the dynamic efficiency with little influence over the energy transfer efficiency for $\gamma > 0.2$.

The Geometry Parameter, λ

This parameter describes the contour of the outer electrode. Large values of λ lead to severely expanded outer electrodes that in some extreme cases can be considered unrealistic. In addition, large values of λ can bring the quasi-one-dimensional assumption of the planar current sheet into question. Values of λ less than one, therefore, should provide a slight flare that will be enough to indicate the benefits of using an expanding outer electrode without violating the 1-D assumption. For example, the flared outer electrode of PT5 is modeled well by $\lambda \approx 0.2$. Notice that if λ is set to zero, the electrode set becomes parallel, and the circuit and momentum equations (Eqns. (3.55) and (3.56)) used in previous works (Ref. [2] for example) are recovered.

3.2.4 Performance Benchmarks: Efficiency, Exhaust Velocity, and Impulse-to-Energy Ratio

Before discussing the solution methodology and results, it is important to define our objectives. The performance of a GFPPT is defined by three related quantities: thruster efficiency, exhaust velocity, and the impulse-to-energy ratio. In terms of non-dimensional parameters,

$$\eta_t = \frac{1}{18} \frac{\rho_f \dot{\delta}_f^2}{\alpha}, \tag{3.60}$$

where the subscript "f" refers to their final value at the end of the integration. As shown in the previous chapter, this efficiency can be broken down into the product of the energy transfer and dynamic efficiencies with the profile and sweeping efficiencies having a value of 100%,

$$\eta_t = \eta_{energy} \quad \eta_{dynamic} = \left(\frac{1}{9} \int_0^{\tau_f} \dot{\delta}\zeta^2 d\tau \right) \left(\frac{1}{1 + \frac{1}{\rho_f \dot{\delta}^2} \int_0^{\tau_f} \rho' \dot{\delta}^3 d\tau} \right). \tag{3.61}$$

With the dimensional nature of the exhaust velocity and impulse-to-energy ratio, we must now define two new metrics that can easily be related to particular

0.1   **Dynamic Impedance Parameter**   100

Large m_{bit}
Small Energy
Small C, L'
$$\alpha = \frac{L'^3 V_0^2 C^2}{18 L_0^2 m'}$$
Small m_{bit}
Large Energy
Large C, L'

0.01   **Critical Resistance Ratio**   10

Underdamped
Small C
Large L_0
$$\psi = \frac{R}{2}\sqrt{\frac{C}{L_0}}$$
Overdamped
Large C
Small L_0

0.01   **Initial Mass Parameter**   1

Gradual Mass
Accumulation
$$\rho_0 = \frac{m_0 L'}{m' L_0}$$
Slug Mass

0   **Mass Distribution Parameter**   1

Uniform Density
Distribution
$$\gamma = \frac{L_0}{L'b}$$
Exponential Density
Distribution

0   **Geometry Parameter**   1

Parallel Outer
Electrode
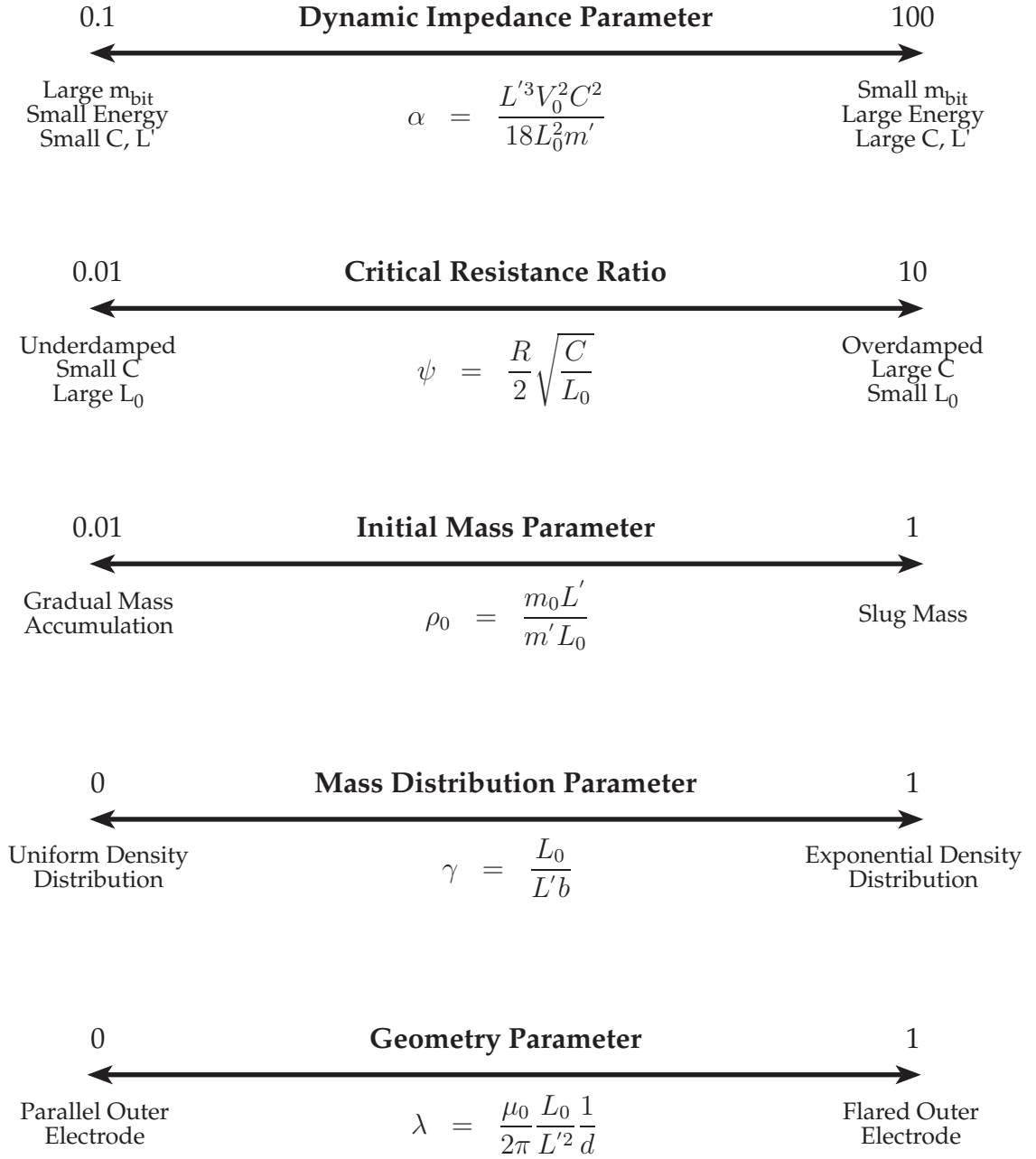$$\lambda = \frac{\mu_0}{2\pi}\frac{L_0}{L'^2}\frac{1}{d}$$
Flared Outer
Electrode

Figure 3.7: Graphic summary of the non-dimensional parameters.

thruster designs. The "non-dimensional exhaust velocity," $(\bar{u}_e)^*$, is simply,

$$(\bar{u}_e)^* \equiv \dot{\delta}_f = \bar{u}_e L' \sqrt{\frac{C}{L_0}} = 3\frac{\bar{u}_e}{\mathcal{U}}. \tag{3.62}$$

Similarly, the "non-dimensional impulse-to-energy ratio," $(I/E)^*$, can be expressed as a function of the model's non-dimensional parameters,

$$\left(\frac{I}{E}\right)^* = \frac{1}{9}\frac{\rho_f \dot{\delta}_f}{\alpha} = \frac{I_{bit}}{E}\frac{1}{L'}\sqrt{\frac{L_0}{C}} = \frac{I_{bit}}{E}\frac{\mathcal{U}}{3}. \tag{3.63}$$

Performance optimization is often a trade-off between high efficiency and a large impulse-to-energy ratio. In general, a thruster should be configured to satisfy the requirements of a specific mission. Without a particular mission in mind, however, we will explore the sensitivity of both η and $(I/E)^*$ to the relevant non-dimensional parameters of the model.

3.2.5 Numerical Solution of Non-Dimensional Equations with Varying Parameters

After specifying the five non-dimensional parameters as well as the initial conditions, the equations can be integrated over an arbitrary number of characteristic time constants ($\sqrt{L_0 C}$) until the capacitor is discharged or another termination condition has been imposed. From the output waveforms, the thrust efficiency and the non-dimensional impulse-to-energy ratio can be calculated at any time during the discharge. The exact numerical integration scheme and verification of the model have been presented in Ref. [73] and will not be discussed further here. As the termination conditions determine the nature of solutions, however, they will be discussed before the results.

A unique solution of Eqns. (3.55) and (3.56) requires the final integration time to be specified. Theoretically, this occurs when the capacitor is fully discharged, but for some parameter sets, this can be a very long time. For discharges that last longer then twenty $\sqrt{L_0 C}$ time constants, the requirement to fully drain the capacitor usually results in very long and unrealistic electrode geometries. In addition, with mass accumulation being specified as a function of z, long integration times can result in heavily loaded current sheets traveling very slowly. Although the thrust typically continues to build, the product of the mass and velocity squared, and thus the efficiency, *decreases*. The choice of the integration duration is critical to evaluating thruster performance. For this model, the period was specified according to one of the following four prescriptions, in order of application:

1. Until the end of the first discharge cycle when and if the current reverses.
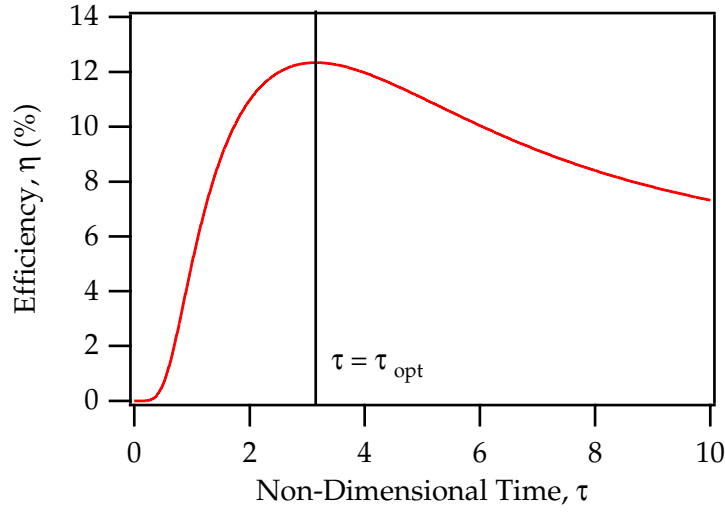
Figure 3.8: The optimal integration time, τ_{opt}, is set when efficiency reaches its maximum value during the discharge.

2. Until the maximum efficiency is reached.

3. Until a limited number of characteristic lengths corresponding to a change in inductance of $10L_0$ ($\Lambda = \delta_f = 10$).

4. If none of the other conditions are met, then until $\tau = 20$.

The second and third conditions are not mutually exclusive, that is, the optimal efficiency point could occur after the inductance has increased by a factor of ten. To understand these two termination conditions in more detail, they will be described in the following subsections.

3.2.6 Optimal Efficiency Electrode Length

For almost every non-dimensional parameter configuration, an integration duration exists that maximizes efficiency. This point will be defined as τ_{opt} and is shown graphically in Fig. (3.8). The optimum electrode length definition follows,

$$(\ell_{elec})_{\eta opt} = \delta(\tau_{opt}). \tag{3.64}$$

Except for the cases with large exponential mass distributions ($\gamma > 0.2$), the efficiency will have a maximum occurring *before* the discharge has fully drained the capacitor. Although current is still flowing after τ_{opt}, the current sheet *slows down* because the Lorentz force is less than "drag" from the accumulation of mass. At

this point it becomes more profitable, in terms of directed kinetic energy, to terminate the discharge and reduce the length of the electrodes to match the position of the current sheet at τ_{opt}. This will have the effect of ending the mass accumulation as well as any more energy addition. In terms of overall efficiency, it becomes more beneficial to let this energy be: a) recovered by some switching technology between the capacitors and the electrodes, or b) lost to a highly resistive "crowbar" discharge at the breech of the thruster. This conclusion is based on the non-recovery of thermal energy in the momentum equation which has been shown to be a good assumption for many low density plasma flows [83, 85].

Although it may seem counterproductive to waste the remaining energy rather than apply it to the discharge, it is advantageous to do so from an efficiency stand point. Long electrodes allow the energy transfer between the capacitor and the current sheet to continue, however, they also allow stationary propellant to be trapped in front of the oncoming current sheet. After τ_{opt} the dynamic efficiency decreases rapidly, canceling out any extra energy (mainly internal) the current sheet might gain from propagating further down the electrodes.

3.2.7   Fixed Electrode Length

For more realistic cases that can be applied to a particular GFPPT geometry, the electrode length (total inductance change) should limit the integration. In this case, the optimal electrode length for the best efficiency may be shorter or longer than the one set in the simulation, in this case $\delta_f = 10$. This is also more realistic in terms of mass loading. In a real thruster, the available propellant mass, m_{avail}, is set by the propellant type, time between pulses, and the electrode length. If the discharge is completed before reaching the end of the electrodes, it may run into unaccelerated propellant and slow down, reducing the efficiency. If the discharge reaches the end of the electrodes before the capacitor has fully discharged, the efficiency might decrease as well. Both the "optimal" and finite electrode lengths will be studied in the following section.

3.3   Results from the Non-Dimensional Model

The results will be presented in the following format. First, we will concentrate on the effects of changing ψ, α, and γ on the efficiency, exhaust velocity, and impulse-to-energy ratio. We will examine the two cases of a slug mass and uniform fill in depth and compare the numerical results to the previous analytical relations. Next, we will examine the efficiency, exhaust velocity, and impulse-to-energy ratio from a typical exponential mass distribution with $\gamma = 0.3$. Finally, we will study the effects of an exponential mass distribution and flared electrodes on the energy transfer and dynamic efficiency, in general.

3.3.1   Case I: Slug mass, $\rho_0 = 1$, $\gamma = 0$, $\lambda = 0$

The main purpose for this case is to examine the general character of the results with minimal influence from the mass distribution and geometry. From the previous analytical models, we should expect the efficiency to vary linearly with the exhaust velocity and α_{slug} from Eq. (3.59).

In the first pair of graphs, Fig. (3.9), the efficiency is seen to depend strongly on both the dynamic impedance parameter and the critical resistance ratio. As predicted from the analytical models, for values of $\psi > 0.3$, the current does not reverse during the discharge. For these solutions, the efficiency is indeed linearly proportional to α_{slug} for $0.1 \leq \alpha \leq 10$ and also dependent on ψ. In general, the efficiency increases for decreasing values of ψ. The best scaling relation is given by the dashed line in the top graph where $\psi \propto \sqrt{\alpha/\eta}$ and from Eq. (3.59),

$$\psi = \sqrt{\frac{9}{4}\frac{m_{bit}R^2}{L'^2 E}\alpha_{slug}}, \tag{3.65}$$

which yields,

$$\eta \propto \frac{4}{9}\frac{L'^2 E}{m_{bit}R^2}. \tag{3.66}$$

This is in almost exact agreement with the asymptotic slug scaling relations found in Ref. [42], indicating that the simulation is functioning correctly. For $\psi < 0.3$, there is a maximum in the efficiency curves near $\alpha_{slug} = 10$. Below this value, the current reverses and the overall efficiency decreases. Above this value of α_{slug}, the velocity is very large and the current waveform is very overdamped. As the integration is limited to $\tau_f = 20$, there may be a significant amount of energy still stored on the capacitor for these solutions. The electrode length, however, can be extremely large, in many cases requiring inductance changes on the order of $100L_0$. This is clearly visible from the decrease in efficiency that comes from fixing the electrode length to $10L_0$.

The second pair of graphs, Fig. (3.10), shows that the efficiency is linearly proportional to the exhaust velocity for $(\bar{u}_e)^* < 10$ as expected,

$$\eta \propto (\bar{u}_e)^* = 3\frac{\bar{u}_e}{\mathcal{U}} = L'\sqrt{\frac{C}{L_0}}\ \bar{u}_e. \tag{3.67}$$

Again, the maximum efficiency value depends on ψ and the electrode length. The exhaust velocity is close to linearly proportional to α_{slug} and not a strong function of ψ except at the lowest values of α_{slug}. For larger values of α_{slug} the exhaust velocity increases more proportionally to the square root of alpha.

The final pair of graphs, Fig. (3.11), shows the non-dimensional impulse-to-energy ratio as a function of α_{slug} and ψ. For large values of ψ, the impulse-to-energy ratio is relatively constant over a wide range of α_{slug} and proportional to

$1/\psi$. On the other hand, at small values of ψ, the impulse-to-energy ratio *decreases* with increasing α_{slug} to the one-half power and is relatively constant with ψ. This is unfortunate as large values of α_{slug} yield the highest efficiency. The fixed electrode length case slightly decreases the impulse-to-energy ratio, to a larger extent for large values of α_{slug}.
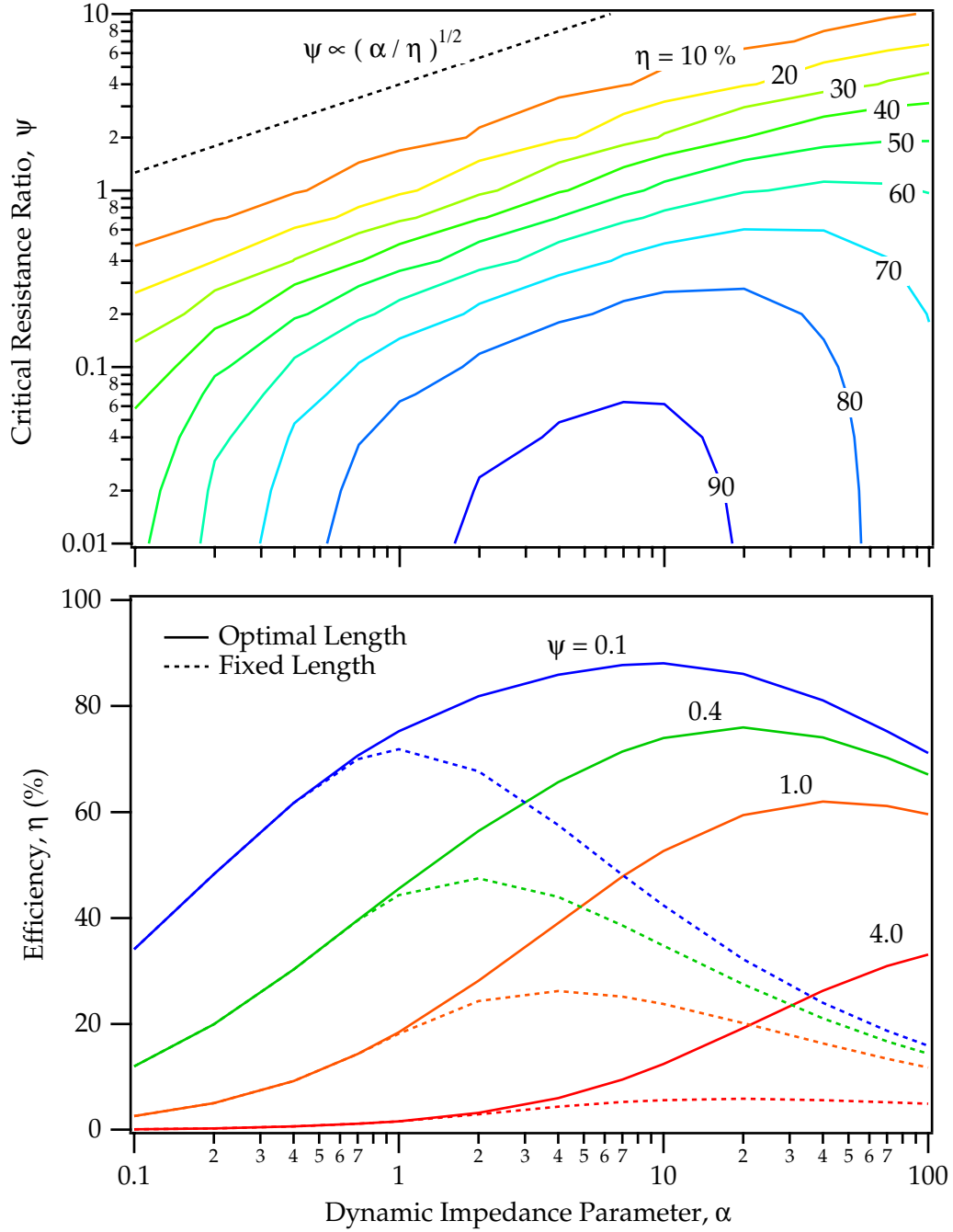
Figure 3.9: Efficiency as a function of ψ and α_{slug} for a slug mass distribution. The top graph shows efficiency contours and a relation between ψ and α_{slug} which matches the efficiency very closely. The bottom graph demonstrates the effect of fixing the electrode length to $10L_0$.
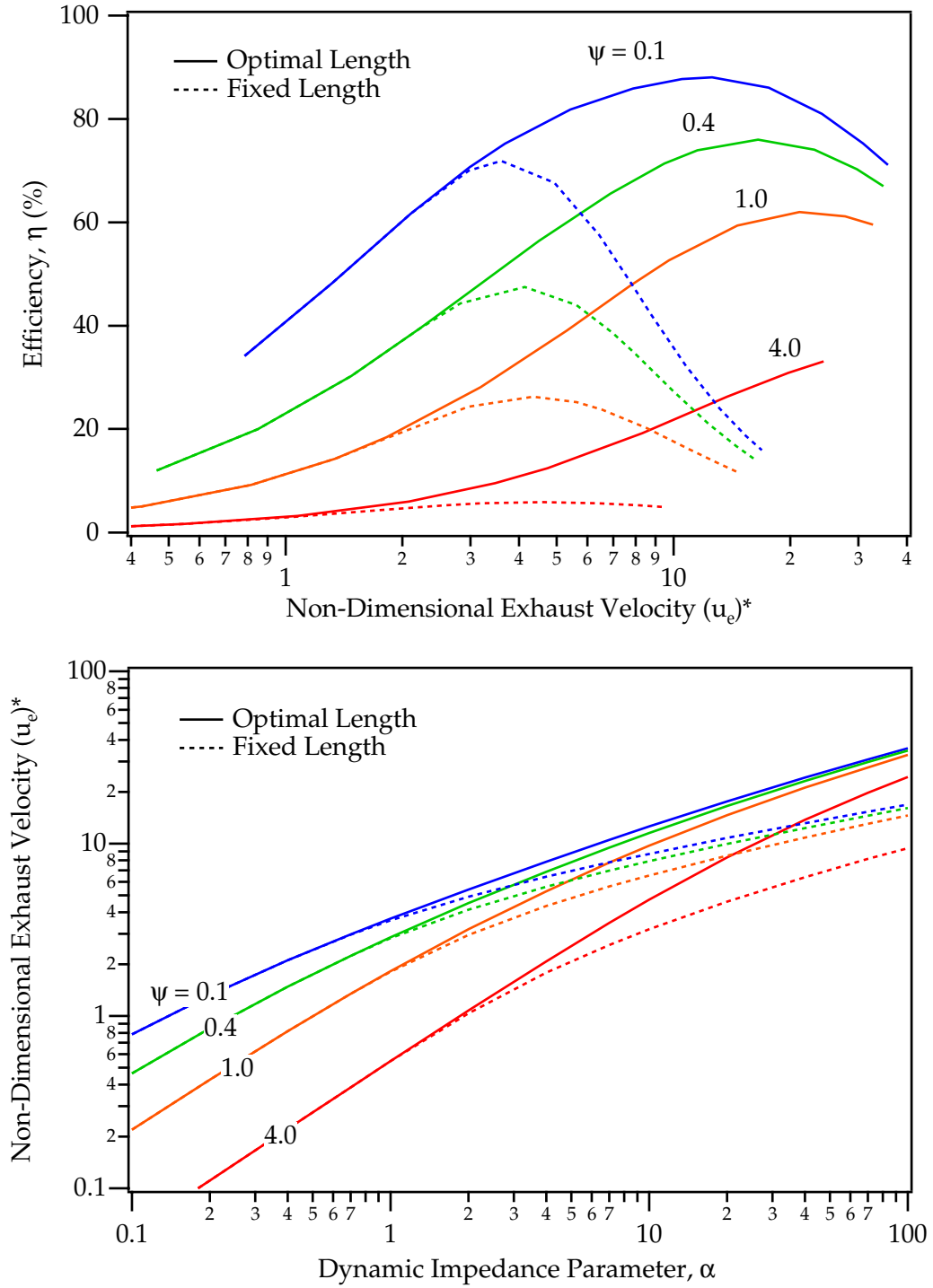
Figure 3.10: Efficiency as a function of the non-dimensional exhaust velocity and the non-dimensional exhaust velocity as a function of α_{slug} for different values of ψ with a slug mass distribution. The length of the electrodes determines the maximum efficiency but does not strongly influence the exhaust velocity.
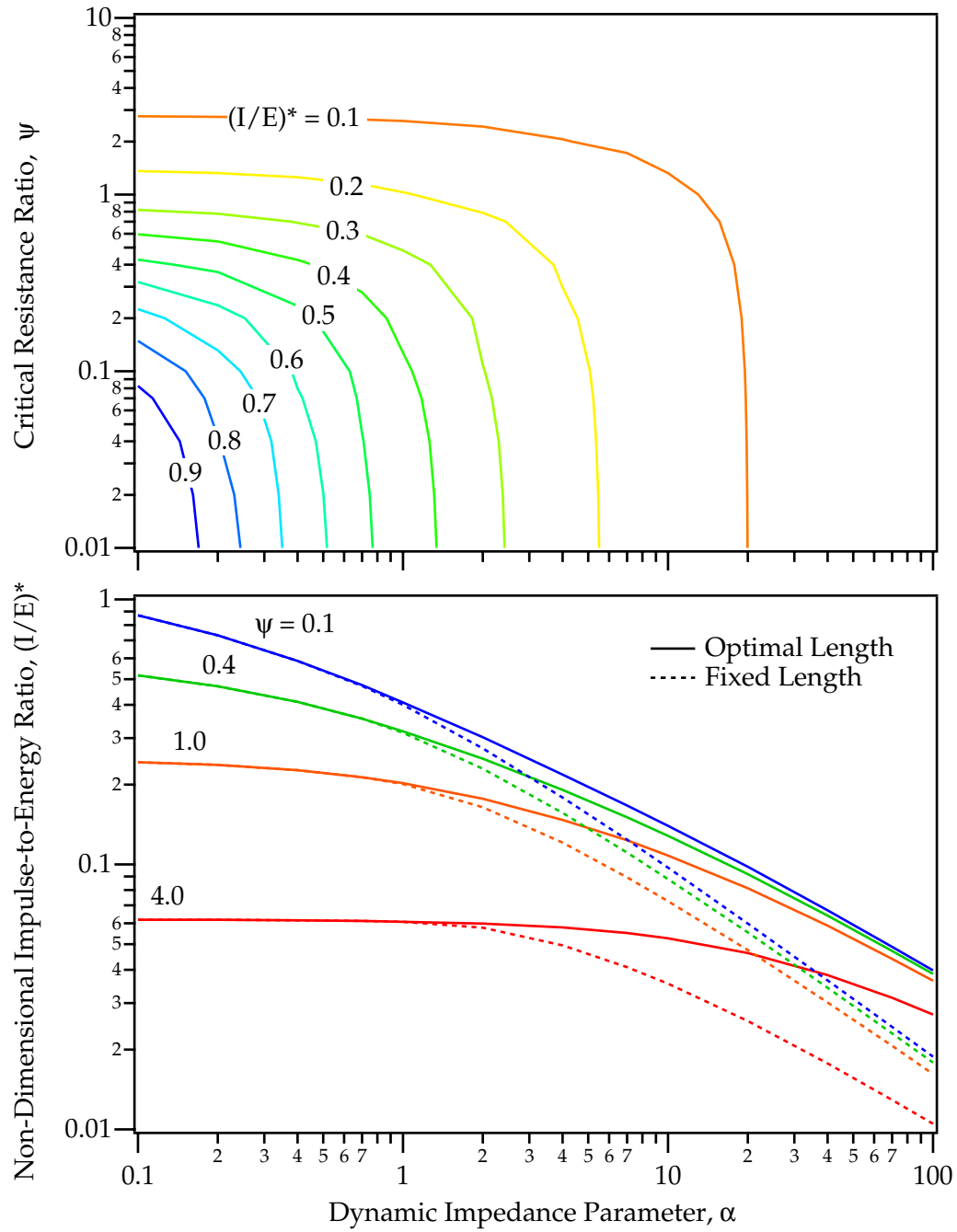
Figure 3.11: Non-dimensional impulse-to-energy ratio as a function of α_{slug} and ψ for a slug mass distribution.

3.3.2 Case II: Uniform Distribution, $\rho_0 = 0.2$, $\gamma = 0$, $\lambda = 0$

The results for the uniform distribution are very similar in character to the slug mass. In general, however, the efficiency and exhaust velocity values are much smaller. From the first pair of graphs, Fig. (3.12), it is clear that there is no longer a strong maximum in efficiency at a particular dynamic impedance parameter. Instead, the efficiency generally increases with α. For values of $\psi \approx 1$, the efficiency scales with the square root of α as predicted from the analytical models, Eq. (3.31). Once again, the efficiency follows a general trend with α and ψ (although to a different power),

$$\eta \propto \frac{\alpha}{\psi^4} = \frac{8}{9} \frac{L'^3 V_0^2}{R^4 m'}. \tag{3.68}$$

Fixing the electrode length has a strong influence on efficiency and brings back the existence of a maximum efficiency near $\alpha = 10$. Below this value, the electrodes are too long, the discharge ends before it reaches the full extent of the electrodes, and there is a large amount of propellant remaining ahead of the accelerated gas. At values of α greater than one, the discharge reaches the end of the electrodes, but the efficiency is still not optimal. Near $\alpha = 10$, the electrode length and discharge duration are perfectly matched for the maximum energy transfer. It should be noted that for all the optimal electrode length solutions, the dynamic efficiency is very close to 50% for a uniform mass distribution.

In the next pair of graphs, Fig. (3.13), the efficiency is seen to be linearly related to the exhaust velocity in the following cases: 1) both fixed and optimal electrode lengths for $\psi > 0.3$, and 2) for fixed electrode lengths (before the maximum point) for $\psi < 0.3$. Also note the "hook" feature in the fixed electrode length, $\psi = 0.1$ case at small value of exhaust velocity. As we will see in Chapter 5, this feature of a finite electrode length is present in the experimental data. Also note, once again, that the exhaust velocity is not a strong function of ψ except at small values of α and generally scales with the square root of α.

The most important feature to note in the final pair of graphs, Fig. (3.14), is that the impulse-to-energy ratio has a similar character and only a slightly smaller value as the impulse-to-energy ratio in the slug mass distribution, Fig. (3.11). This is simply because the impulse does not strongly depend on how the mass was accumulated (although the efficiency does). For the uniform mass distribution, the impulse-to-energy ratio does not decrease as quickly for increasing values of α unless a fixed electrode length is imposed. Note that the impulse-to-energy ratio is actually slightly larger for the cases with the fixed electrode length below $\alpha \approx 10$. Again, this is due to the product of $m \times u$ (impulse) being larger for the fixed electrodes while $m \times u^2$ (kinetic energy) is smaller.
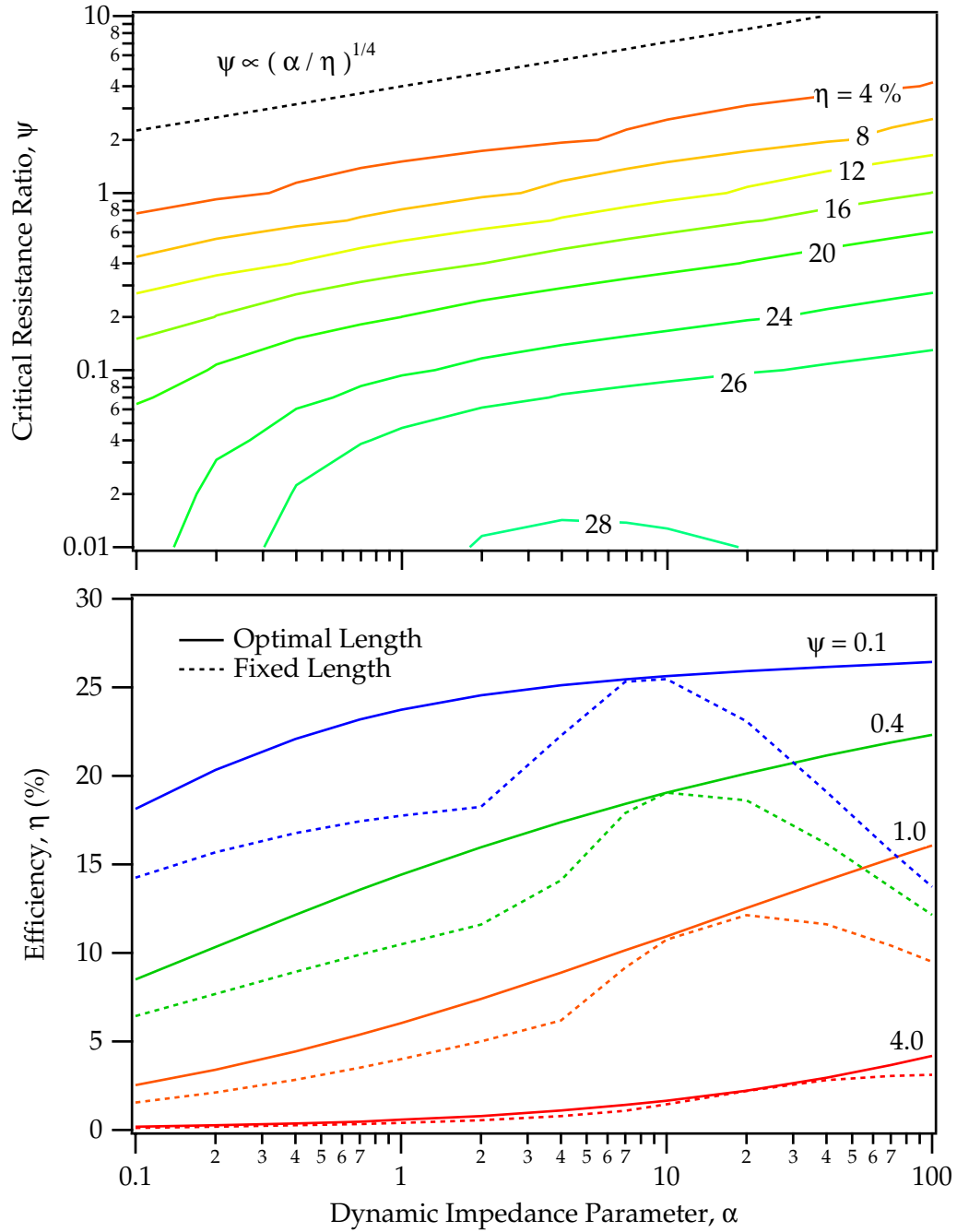
Figure 3.12: Efficiency as a function of ψ and α for a uniform mass distribution. The top graph shows efficiency contours and a relation between ψ and α which matches the efficiency very closely at large ψ. The bottom graph demonstrates the effect of fixing the electrode length to $10L_0$ with a maximum in the efficiency near $\alpha = 10$.
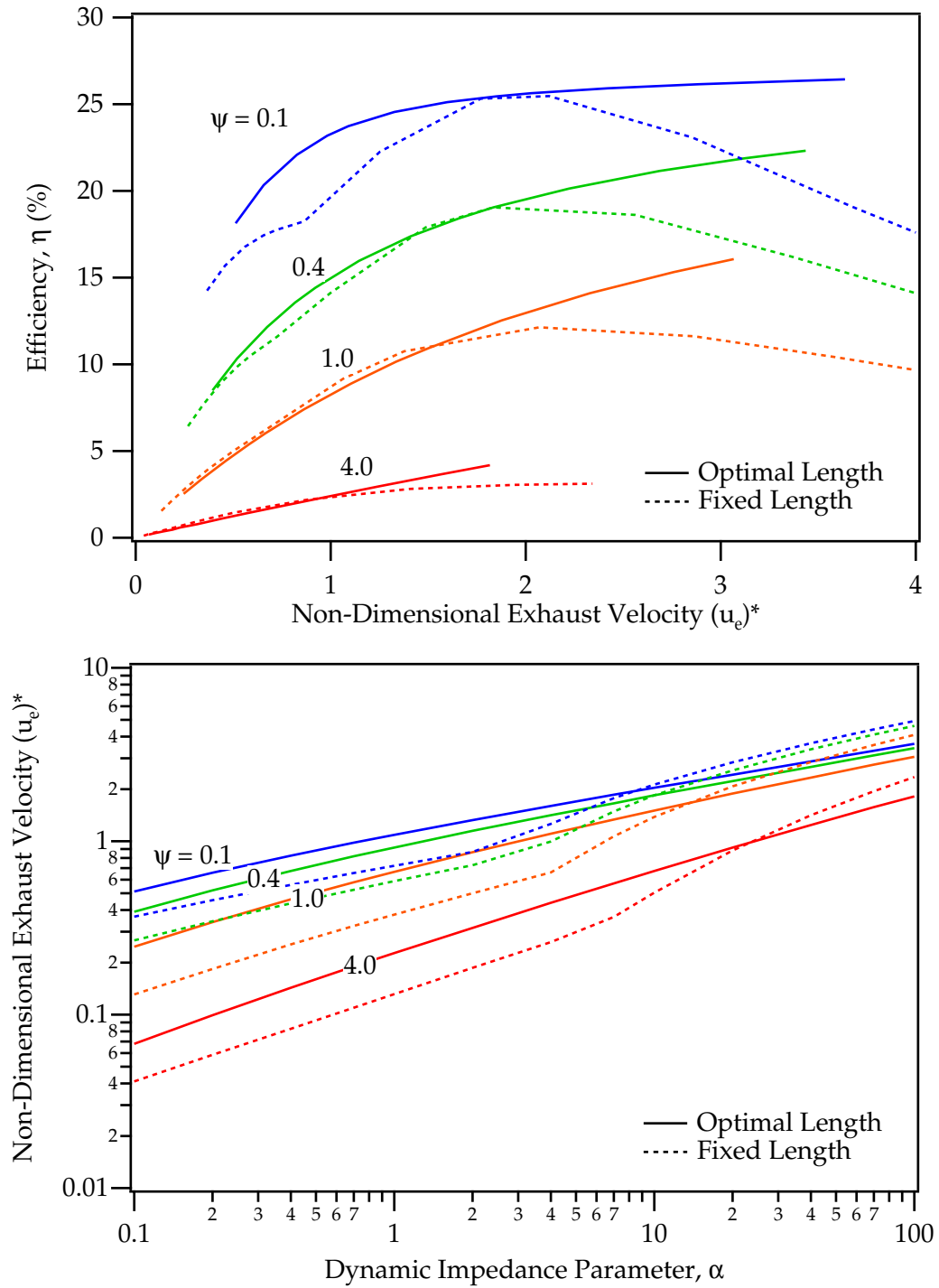
Figure 3.13: Efficiency as a function of the non-dimensional exhaust velocity and the non-dimensional exhaust velocity as a function of α for different values of ψ with a uniform mass distribution.
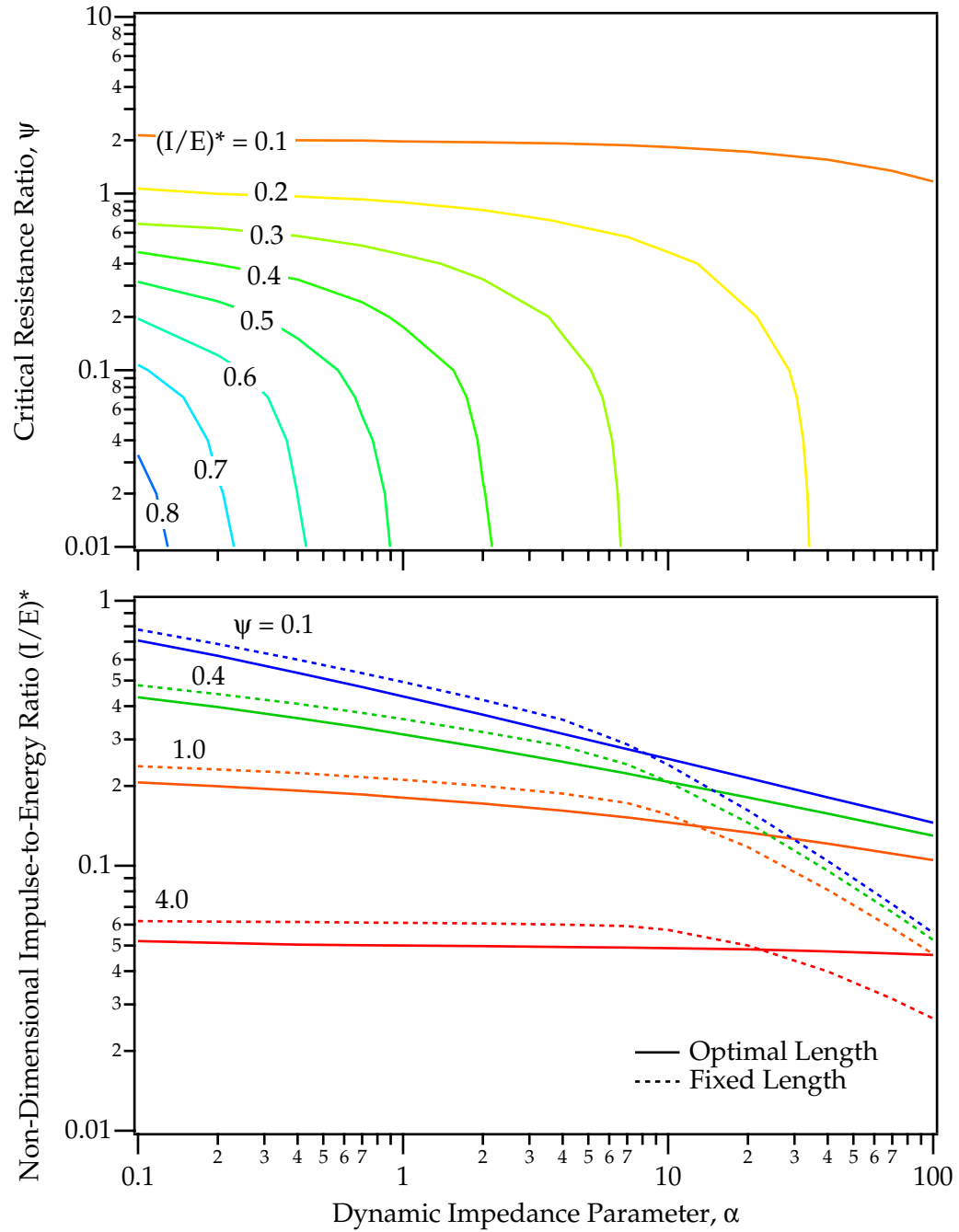
Figure 3.14: Non-dimensional impulse-to-energy ratio as a function of α and ψ for a uniform mass distribution.

3.3.3 Case III: Exponential Distribution, $\rho_0 = 0.2$, $\gamma = 0.3$, $\lambda = 0$

In this case, we examine a situation that is closer to reality in GFPPTs with injected propellant (For PT9, using argon propellant and $\tau_p = 250\mu$s, $\gamma \approx 0.3$). The bulk of the propellant mass is near the breech of the thruster and the density decreases exponentially as the discharge progresses. This should have an impact on the dynamic efficiency, especially at high exhaust velocity values. Indeed, as shown in Fig. (3.15), the efficiency is larger at larger values of α than for the uniform mass case. In fact, the efficiency contours, and the effects of a fixed electrode length are somewhere between the slug and uniform cases. Below $\alpha = 1$, the efficiency is more like the uniform case with the dynamics of the sweeping process dominating the acceleration. Above $\alpha = 1$, the efficiency scales closest to the slug mass distribution. Determining the exact efficiency scaling with α and ψ, therefore, is no longer a simple task as it was presented in Eqns. (3.66) and (3.68).

As seen in the next pair of graphs, Fig. (3.16), however, the efficiency is still linearly proportional to the non-dimensional exhaust velocity for a wide range of α values near one, especially at ψ values close to one. In addition, the exhaust velocity itself is not a strong function of ψ except at very small values of α. Similarly, as shown in Fig. (3.17), the impulse-to-energy ratio has not changed significantly between the slug, uniform, or exponential distribution.

To understand the scaling in this case, we split the thruster efficiency between the energy transfer efficiency and the dynamic efficiency. As shown in Fig. (3.18), the energy transfer efficiency scales almost exactly as the thrust efficiency did for the slug distribution, Fig. (3.9). Of course, the dynamic efficiency for the slug case is exactly 100%, indicating that the energy transfer efficiency is similar for both a slug and exponential mass distribution. As there is indeed some mass ahead of the discharge, however, the dynamic efficiency is not 100% in an exponential distribution. As expected, the dynamic efficiency is a strong function of α and not of ψ. For $\alpha < 1$, as before, the dynamic efficiency is 50% and very similar to the uniform distribution. Above $\alpha = 1$, the dynamic efficiency increases with increasing α (large inductance-per-unit-length, capacitance, and voltage; small initial inductance and mass). Before we go into the exact scaling of the dynamic efficiency with the dynamic impedance parameter, we will also examine the effects of changing the exponential mass distribution, γ, over a broader range of values.
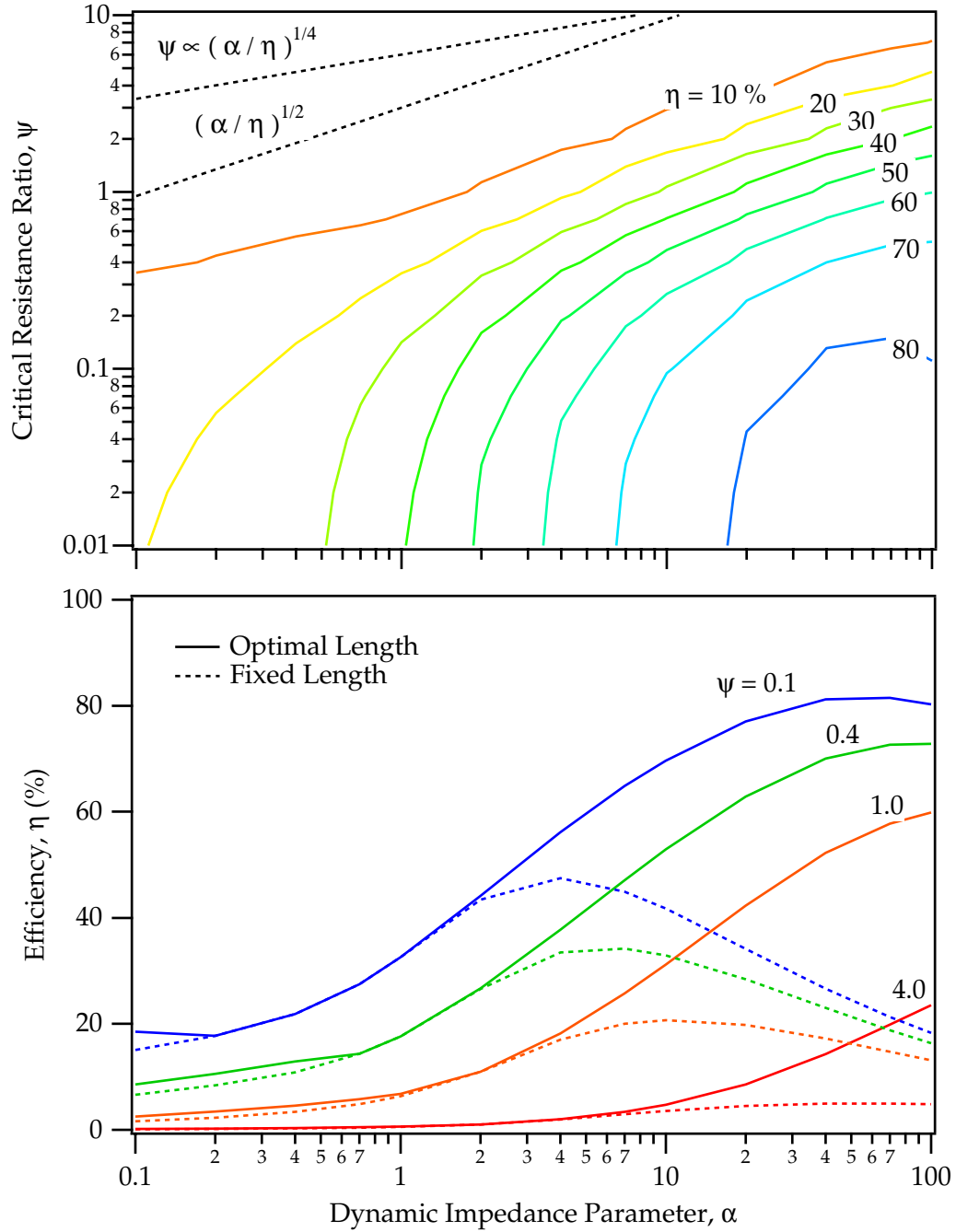
Figure 3.15: Efficiency as a function of ψ and α for an exponential mass distribution, $\gamma = 0.3$. The top graph shows efficiency contours that have a character similar to either the uniform or slug distributions depending on α. The bottom graph demonstrates the effect of fixing the electrode length to $10L_0$.
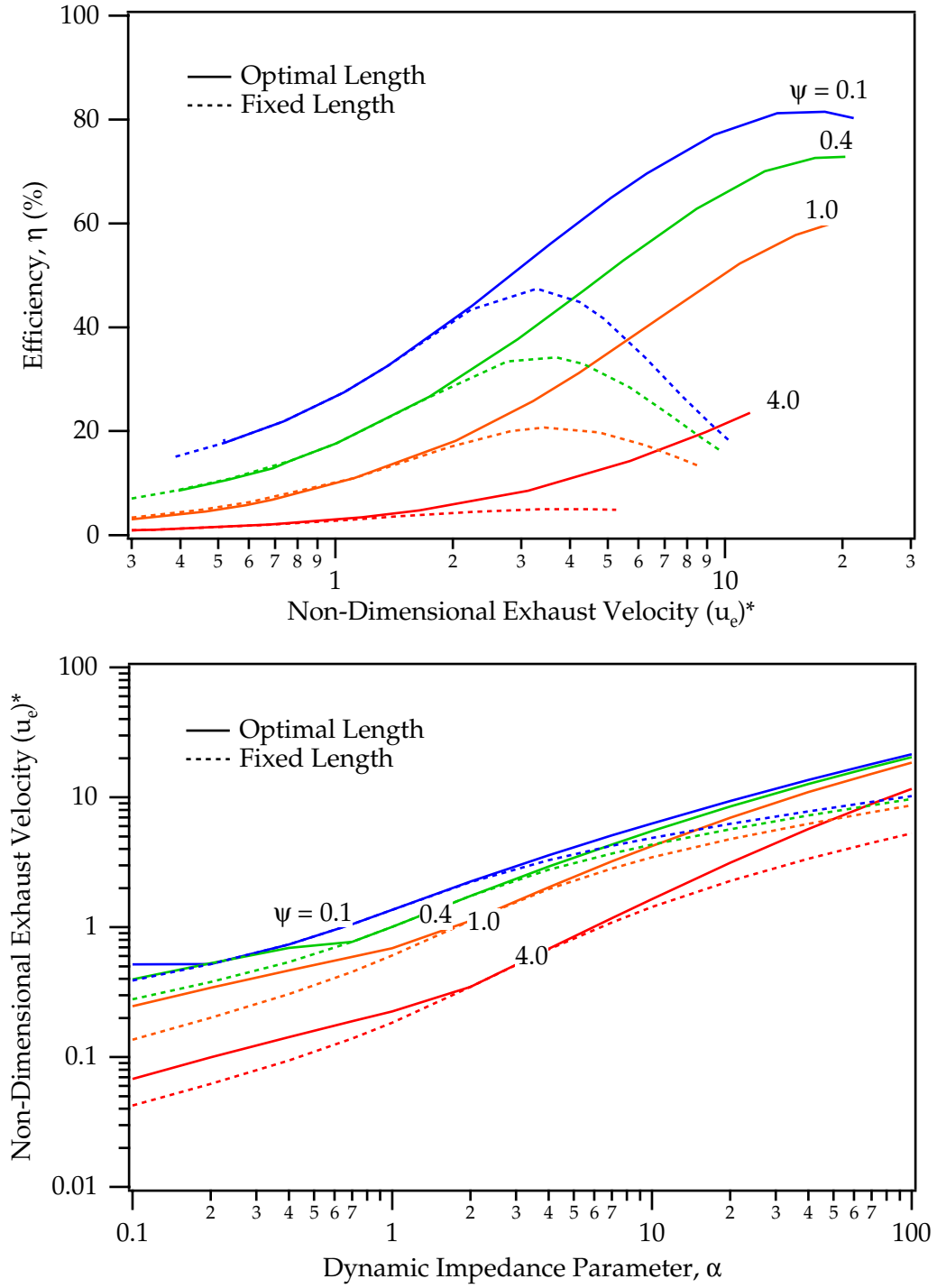
Figure 3.16: Efficiency as a function of the non-dimensional exhaust velocity and the non-dimensional exhaust velocity as a function of α for different values of ψ with an exponential mass distribution, $\gamma = 0.3$.
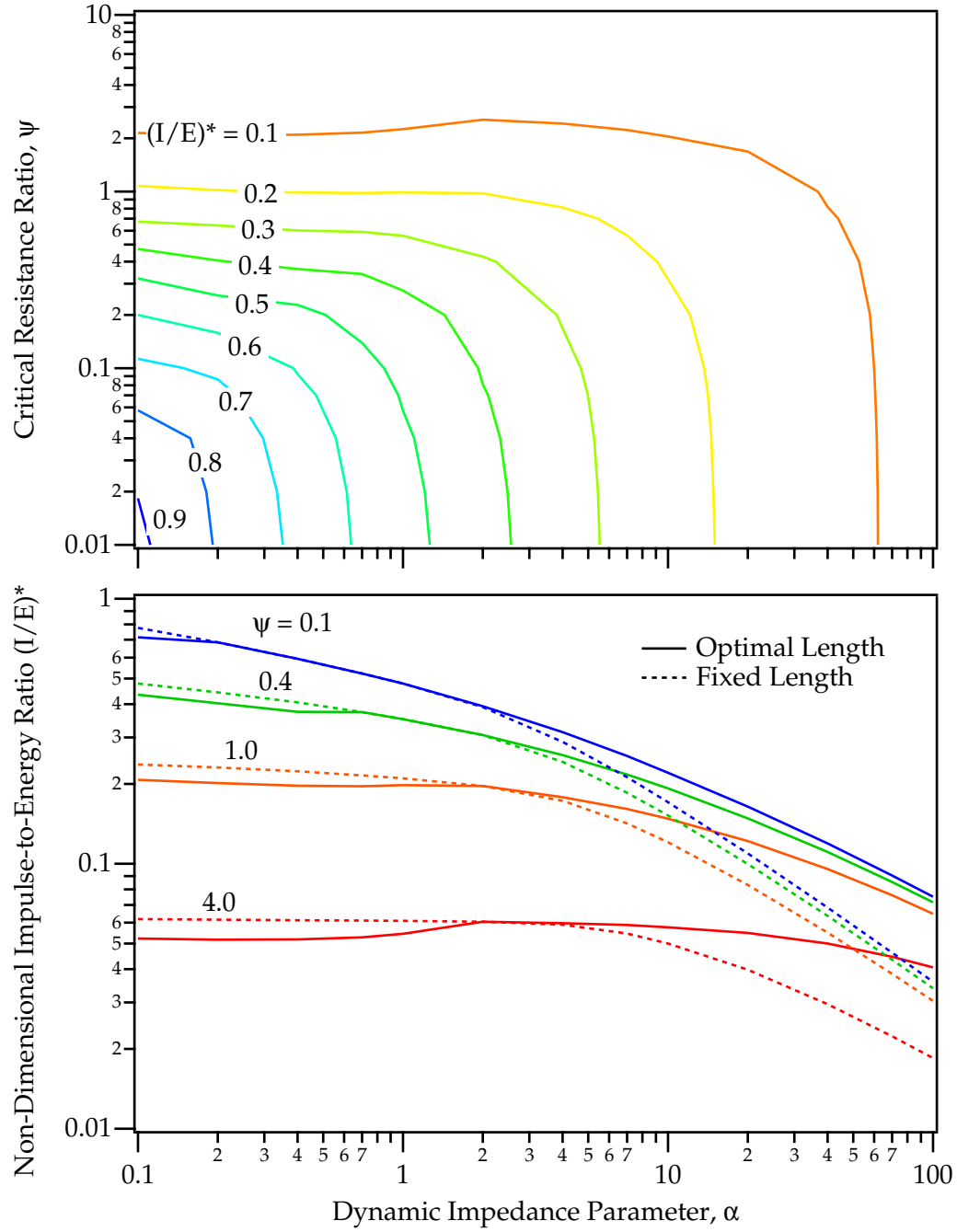
Figure 3.17: Non-dimensional impulse-to-energy ratio as a function of α and ψ for an exponential mass distribution, $\gamma = 0.3$.

Figure 3.18: Contour plots of energy transfer and dynamic efficiencies for an exponential mass distribution, $\gamma = 0.3$. The energy transfer efficiency is very similar to the efficiency of the slug mass distribution, Fig. (3.9). The dynamic efficiency is a strong function of α but not of ψ.

3.3.4 Effects of Varying Mass Distribution and Geometry

Besides testing a wide range of conditions, this model adds two critical features to other models found previously in the literature: using an exponent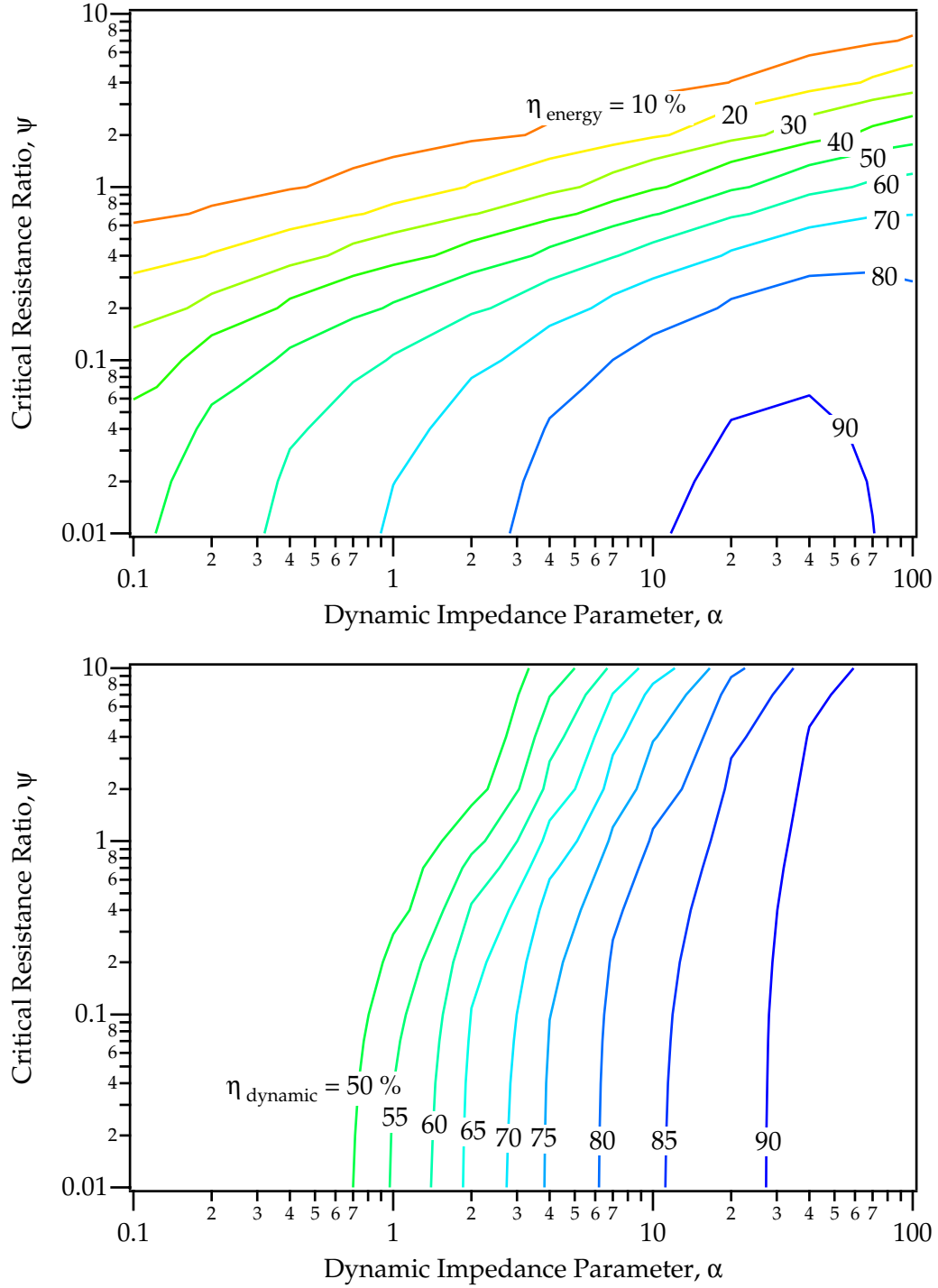ial mass distribution and a flared electrode geometry. First, we will examine the effects of the exponential mass distribution keeping $\psi = 0.3$ and varying α with the hope of understanding the dynamic efficiency scaling completely. Next we will examine the effects of having a flared outer electrode for $\psi = 0.3$ to see if there is any benefit from increasing the effective inductance-per-unit-length in the later portion of the discharge. The critical resistance ratio is set to 0.3 for both studies because this value is near the middle of the range for ψ used in the previous cases.

Exponential Mass Distribution, $0.1 \leq \gamma \leq 1.0, \lambda = 0$

In this study, the mass distribution parameter, γ, is changed between 0.1 and 1.0. Below 0.1, the mass distribution is nearly uniform, while above 1.0 it is slug-like. It follows, then, that the efficiency should increase with increasing γ mainly through an increase in the dynamic efficiency. Figure (3.19) shows the thruster efficiency as a function of the mass distribution parameter and the dynamic impedance parameter. As expected, the efficiency increases with large values of γ and α. For the larger values of γ (slug mass), once again there is a maximum in efficiency at a particular α value. This peak dies off for smaller values of γ as it did in the uniform mass distribution. Notice that between $1 \leq \alpha \leq 10$, the efficiency increases in proportion to γ. Also note, as shown in Fig. (3.20), that the impulse-to-energy ratio (and efficiency vs. exhaust velocity) is not a strong function of γ and that the efficiency is still close to linearly proportional to exhaust velocity below $(\bar{u}_e)^* = 10$.

To understand the performance scaling with γ, we now split the efficiency between the energy transfer and dynamic efficiencies. As shown in Fig. (3.21), the energy transfer efficiency is not a strong function of γ although it does increase slightly as the propellant distribution becomes more slug-like. The dynamic efficiency, however, shows a very strong and well-formed dependence on both γ and α. To examine this further, we plot both the energy transfer and dynamic efficiency as a function of γ in Fig. (3.22). From these plots it is obvious that 1) the energy transfer efficiency is relatively constant over the gamma values of interest (especially for the finite electrode case), and 2) that the dynamic efficiency follows a very simple relation above $\eta_{dynamic} = 50\%$,

$$\eta_{dynamic} \approx \left(1 - \frac{0.16}{\gamma\sqrt{\alpha}}\right) \qquad \left(\eta_{dynamic} \geq 0.5, \quad \gamma\sqrt{\alpha} \geq 0.32\right). \qquad (3.69)$$
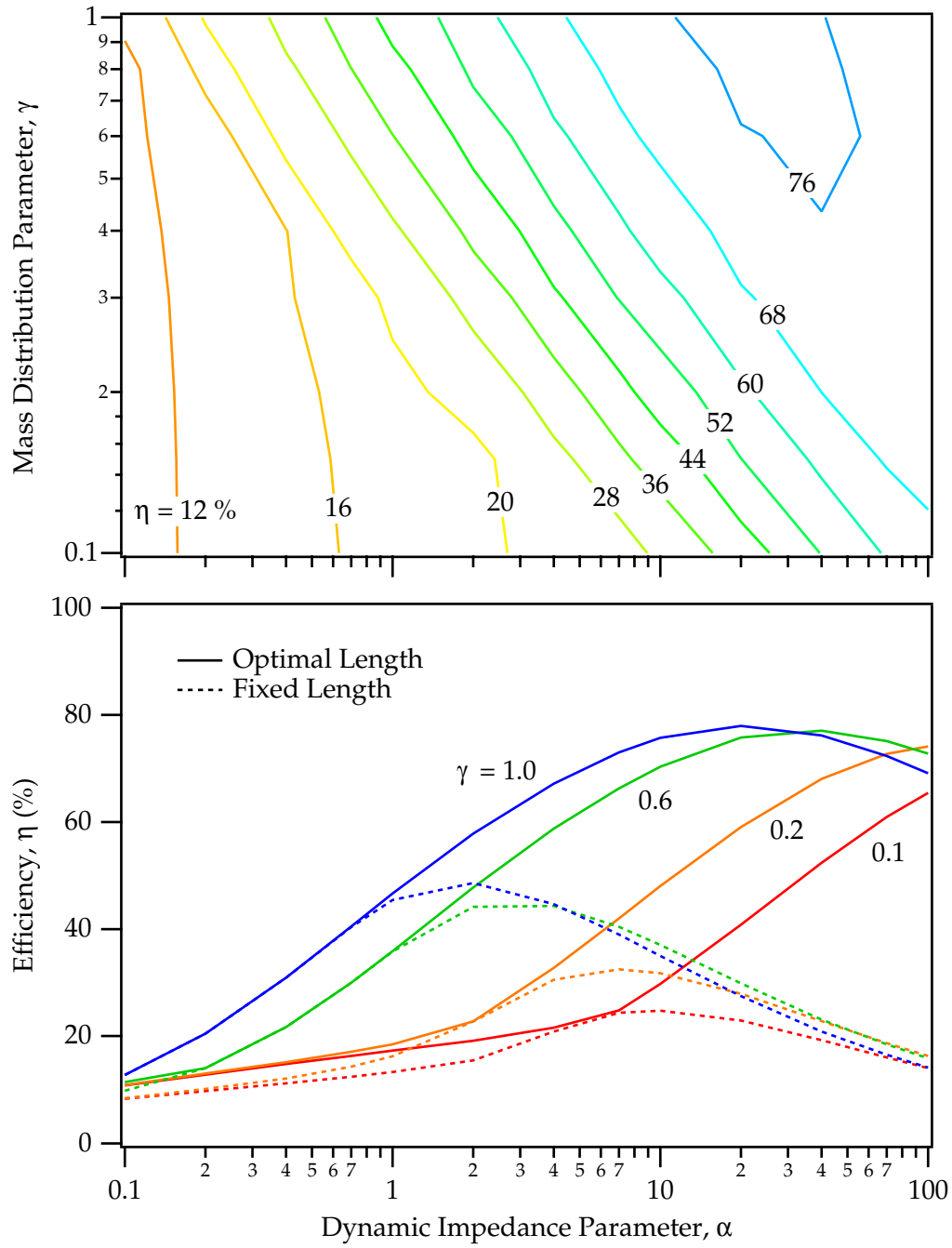
Figure 3.19: Efficiency contours as a function of γ and α with $\psi = 0.3$. The efficiency follows similar trends to the uniform mass distribution at $\gamma = 0.1$ and to the slug distribution for $\gamma = 1.0$.
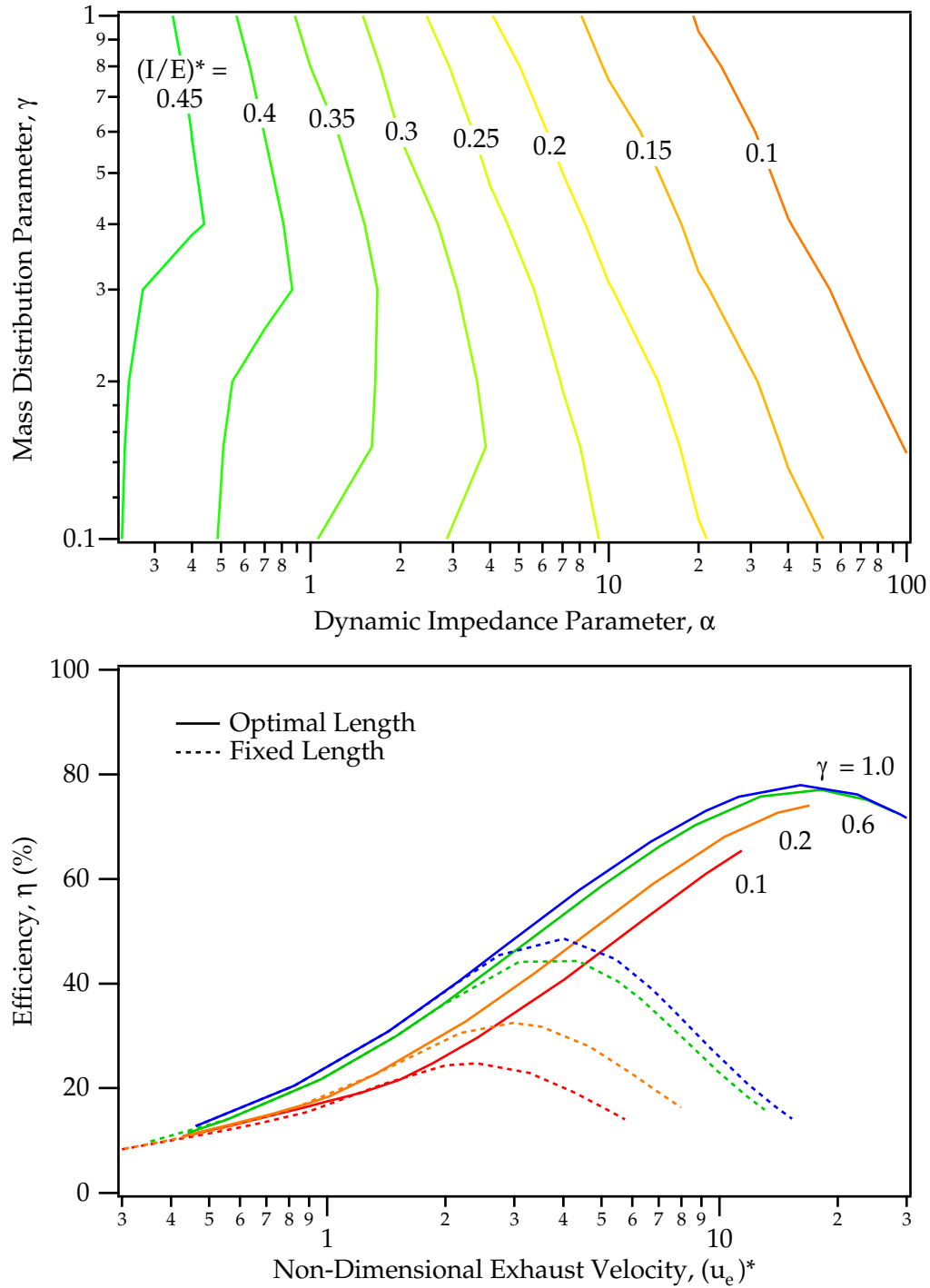
Figure 3.20: Contour plot of the impulse-to-energy ratio as a function of γ and α for $\psi = 0.3$. The impulse-to-energy ratio is not a strong function of γ except at the largest values of α. The efficiency as a function of exhaust velocity is also shown not to be a strong function of γ.

Figure 3.21: Contour plots of the energy transfer and dynamic efficiency over a wide range of γ and α values for $\psi = 0.3$.
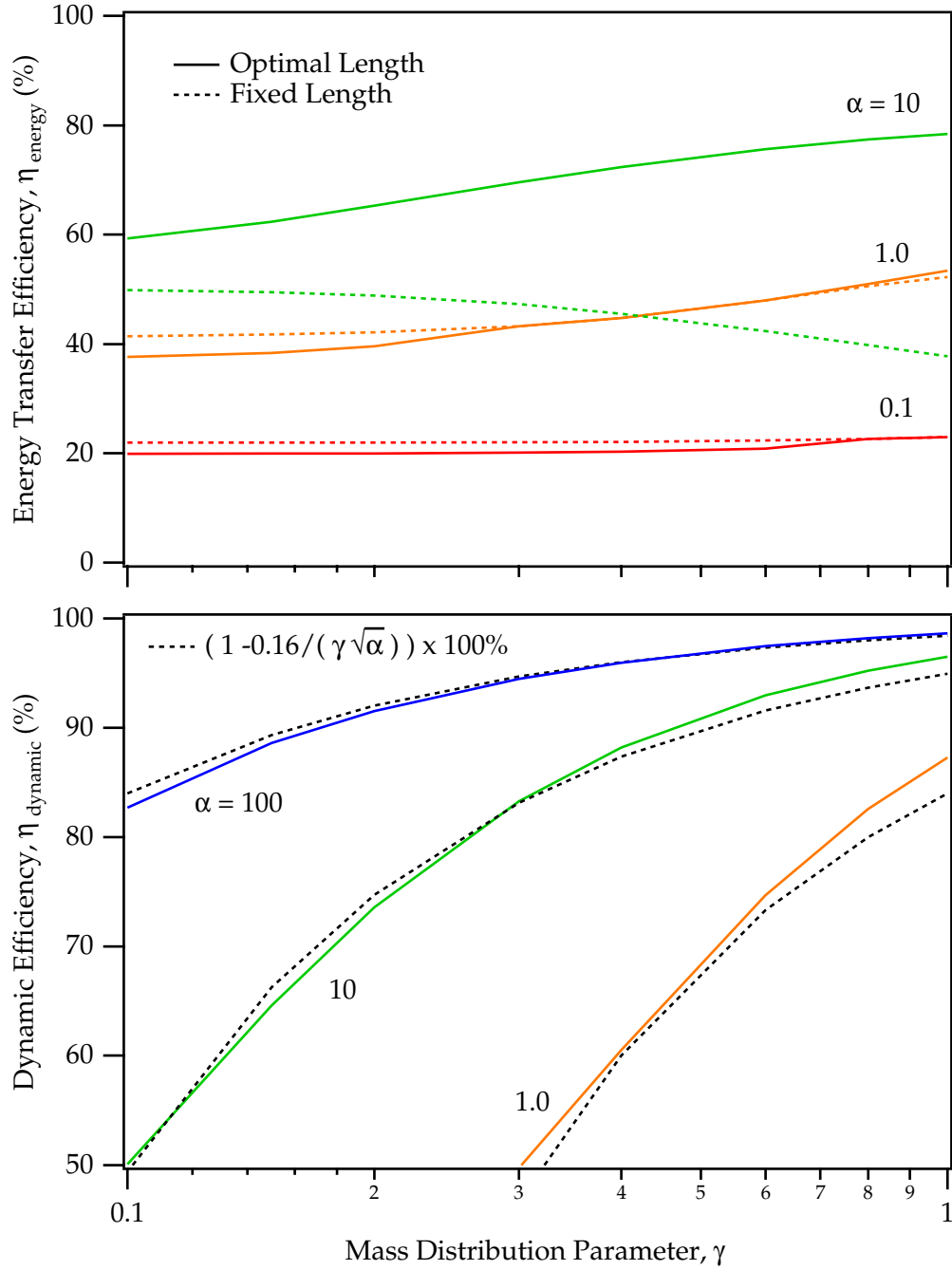
Figure 3.22: Energy transfer and dynamic efficiency as a function of γ with α as a parameter. The plot of dynamic efficiency also shows three curve fits with the functional form given by the legend and Eq. (3.69).

Flared Electrode Geometry, $0.01 \leq \lambda \leq 1.0, \gamma = 0 \, or \, 0.3$

Putting an expanding flare in the electrodes is perhaps desirable for the increase in inductance-per-unit-length as the discharge progresses. Although any attempt to create a nozzle for electrothermal recovery has been shown to either have none or a detrimental effect (see Appendix C), an expansion (or contraction) might be beneficial for the inductance profile. As seen in Figs. (3.23) and (3.24), however, it does not generally seem to be the case. In fact, the nature of the effect changes depending on the value of dynamic impedance parameter. For large α, a flare actually decreases the efficiency for both a uniform and $\gamma = 0.3$ mass distribution. In fact, with very large expansions and uniform fills, the dynamic efficiency becomes very poor for high values of α where the sheet velocity is large. For smaller values of α there is a benefit from a flare, although very slight except for extremely large expansions. In the case of an exponential mass distribution, $\gamma = 0.3$, the dynamic efficiency is mainly a function of α. Although not shown here, the energy transfer efficiency is not a strong function of λ and increases only slightly with increasing expansion.

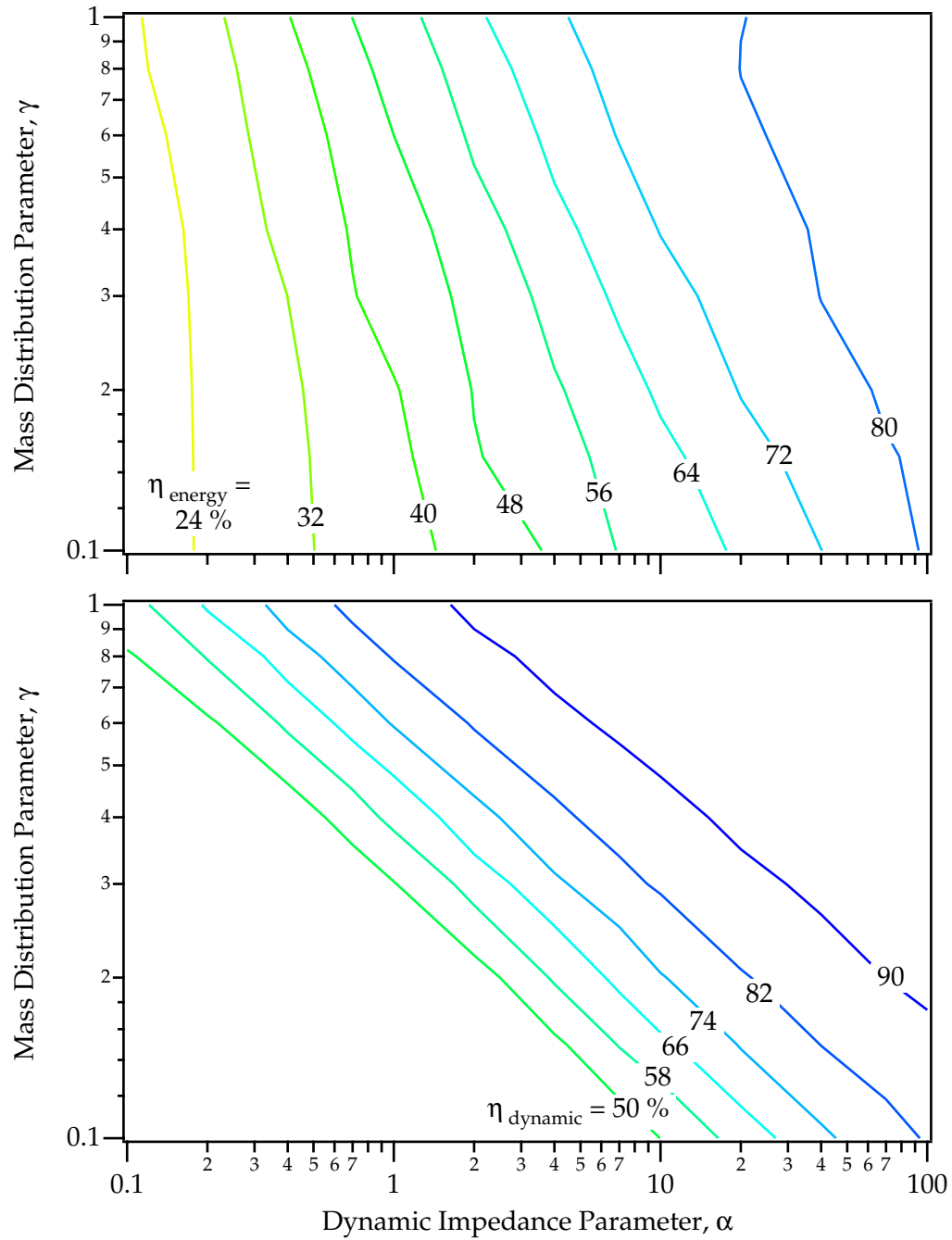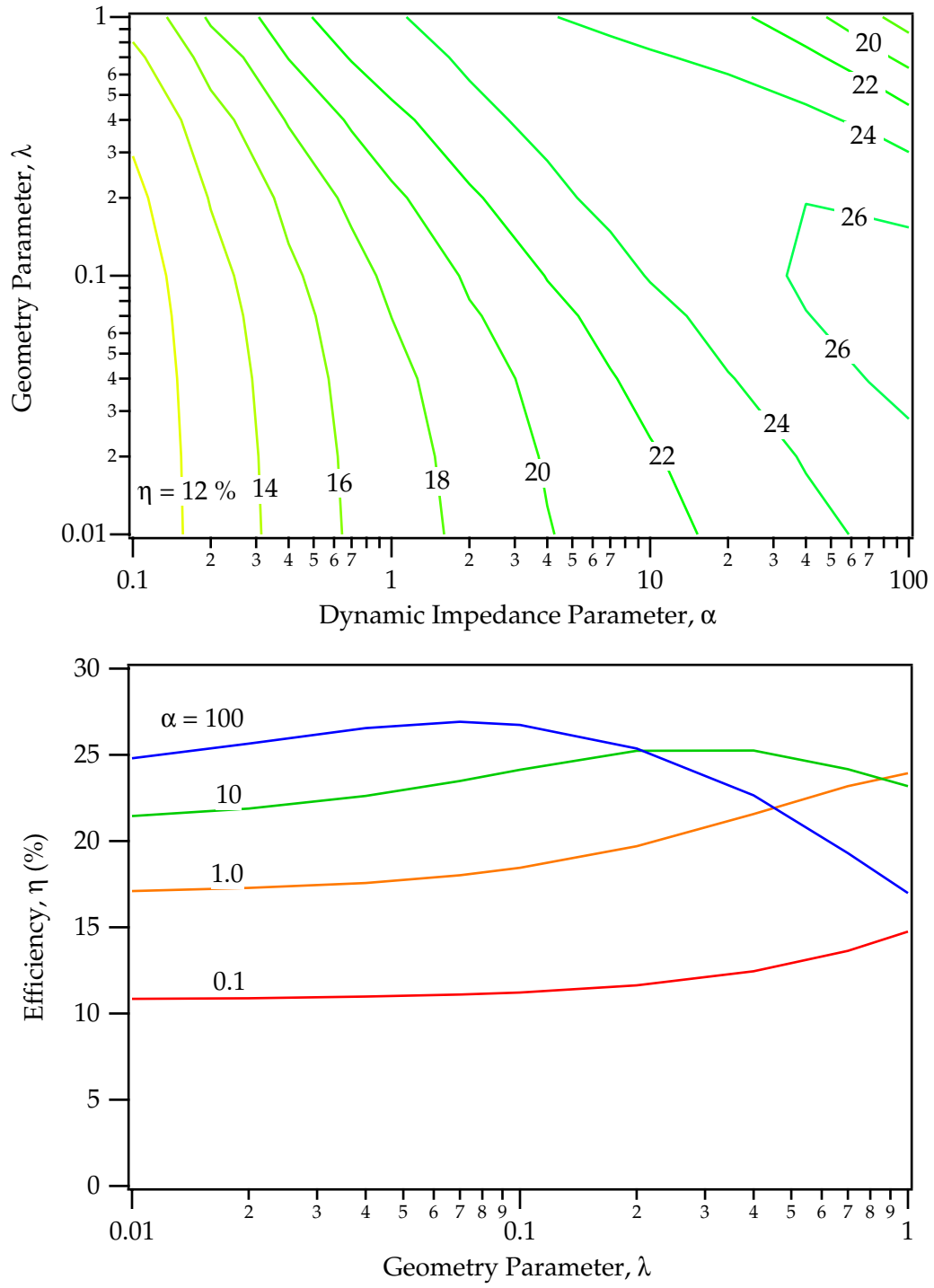Figure 3.23: Graphs of efficiency as a function of λ and α for $\psi = 0.3$ and $\gamma = 0$.

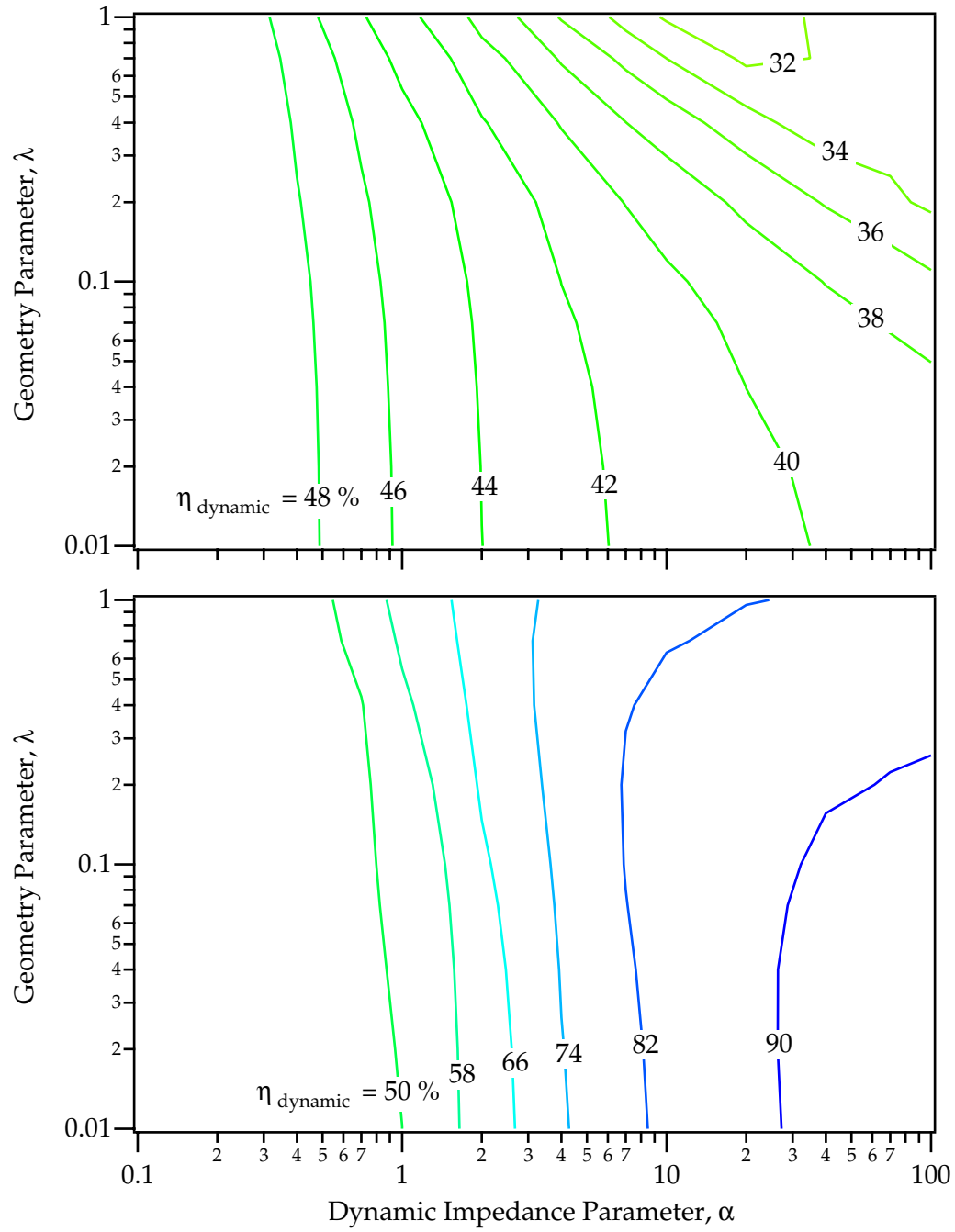Figure 3.24: Contour plots of dynamic efficiency as a function of λ and α for $\psi = 0.3$. The top plot shows a uniform distribution with $\gamma = 0$ and the bottom plot shows an exponential distribution with $\gamma = 0.3$.

3.4 Summary and Comments

This chapter has presented three models for predicting the performance of GF-PPTs. The simplest model used fixed elements and predicted that close to critically damped current waveforms have the highest energy transfer efficiency. The next model estimated the impulse of such a current waveform with a variable inductance and a uniform mass distribution. The efficiency was predicted to scale linearly with the exhaust velocity,

$$\eta_t = \frac{\bar{u}_e}{\mathcal{U}} e^{-\sqrt{\psi}} = \frac{1}{3} L' \sqrt{\frac{C}{L_0}} \bar{u}_e e^{-\sqrt{\psi}}, \tag{3.70}$$

indicating a constant impulse-to-energy ratio proportional to $1/\mathcal{U}$. For the variable element model, the exhaust velocity scaling depended on the mass distribution. For a slug mass, $\bar{u}_e \propto \mathcal{U}\alpha_{slug}$, and for a uniform distribution, $\bar{u}_e \propto \mathcal{U}\sqrt{\alpha}$ which can be easily used to determine the efficiency in Eq. (3.70).

The numerical model produced very similar results to the variable element model in the appropriate range of $0.3 \leq \psi \leq 3$. Outside of that range, and in general, the non-dimensional model gave the following results:

- Small values of ψ had the highest values of efficiency and the non-dimensional impulse-to-energy ratio.

- In general, increasing α increased the efficiency and decreased the non-dimensional impulse-to-energy ratio; however, unrealistically large electrode geometries can be required for larger values of α.

- As in the variable element model, for $\alpha < 10$, the efficiency was found to be linearly *proportional* to the non-dimensional exhaust velocity, $\bar{u}_e/\mathcal{U}$, and $(\bar{u}_e)^*$ was found not to be a strong function of ψ or the electrode length.

- The energy transfer efficiency was found to depend on the mass distribution and ψ. For $\psi > 0.3$, the slug mass efficiency scales as,

$$(\eta_{energy})_{slug} \propto \frac{L'^2 C V_0^2}{R^2 m_{bit}}, \tag{3.71}$$

  while the uniform distribution efficiency scales as,

$$(\eta_{energy})_{uniform} \propto \frac{L'^3 V_0^2}{R^4 m'}, \tag{3.72}$$

  and the exponential mass distribution is somewhere between these relations, closer to the slug mass scaling. For $\psi < 0.3$, there is an optimum efficiency between $1 \leq \alpha \leq 10$.

- The dynamic efficiency with an exponential mass distribution was found to be related to the dynamic impedance parameter, α, and the mass distribution parameter, γ, through the following relation for $\gamma\sqrt{\alpha} > 0.32$,

$$\eta_{dynamic} \propto \left(1 - \frac{0.16}{\gamma\sqrt{\alpha}}\right). \qquad (3.73)$$

- Using a finite electrode length changes the exact value of the efficiency, but the scaling relations remained generally intact.

- Using a flared outer electrode had mixed and only slight benefits, depending on α.

The scaling trends reported in this chapter provide a framework for experimental study described in the next chapter.

Chapter 4

The SRL-EPPDyL Family of GFPPTs

This chapter will describe the two SRL-EPPDyL GFPPT designs used in this dissertation primarily to examine performance scaling. First, the high-repetition rate scheme will be discussed in terms of its benefits and improvements over previous GFPPT systems. Next, the power conditioning and propellant delivery systems will be described in detail. Finally, both PT5 with its modular capacitor bank and PT9 with its modular electrodes will be documented.

4.1   System Description

Over the last five years, the Electric Propulsion and Plasma Dynamics Lab (EP-PDyL) has teamed up with Science Research Laboratory, Inc. (SRL) to design and test nine generations of GFPPTs. SRL-EPPDyL GFPPTs use a capacitively driven arc discharge that is accelerated by a self-induced magnetic field and the resulting $J \times B$ Lorentz force. Typical operational parameters for one pulse include charging voltages close to 250 V, peak discharge currents near 10 kA, peak magnetic fields near 0.5 T, and discharge durations of less than 10 μs with nearly critically damped current waveforms. During the pulse, instantaneous power is on the order of a megawatt; however, the duration is short enough that only 1-10 J of stored energy is necessary for each pulse. With modern, solid-state, pulsed-power conditioning technology, a space qualified SRL-EPPDyL GFPPT is expected to have a mass less than 2 kg (1 kg capacitor bank and 1 kg control modulator), pulse rates as high as 10 kHz, and a 10^8 pulse lifetime. A picture showing PT5 (described in more detail in Section 4.2.1) mounted to a thrust stand is shown in Fig. (4.1). A typical voltage history of multiple pulses and a typical current waveform for a single pulse is shown in Fig. (4.2).

All of the GFPPTs described in this dissertation operate in a *burst* mode (a series of discharges are grouped together to form a "burst" of pulses) for four important reasons: 1) to maximize propellant utilization, 2) to reduce overall power require-
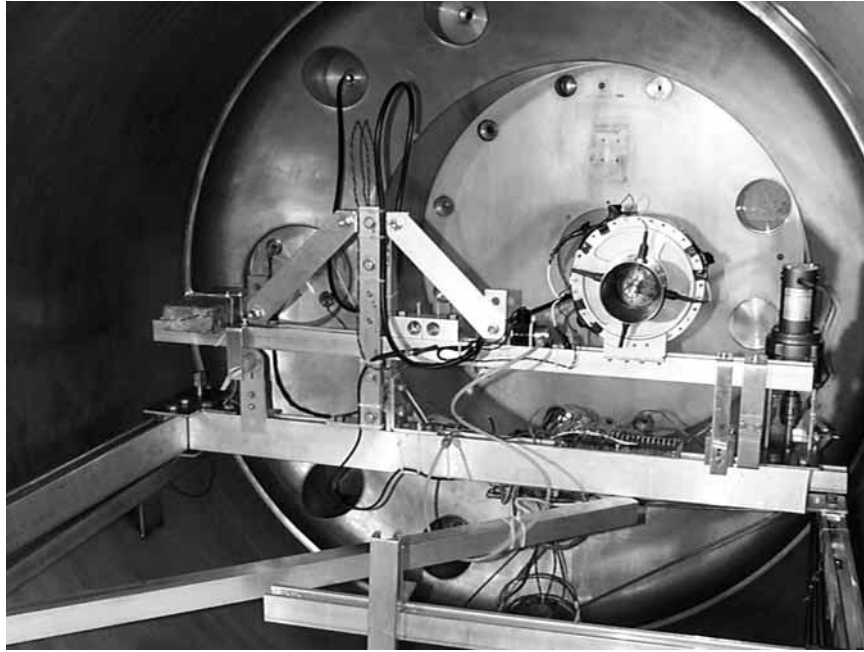
Figure 4.1: Picture of PT5 mounted on a thrust stand at NASA JPL.
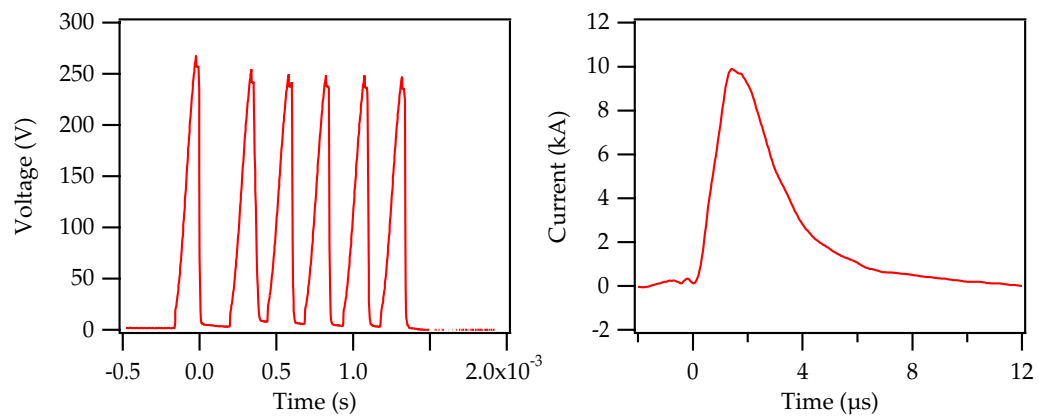

Figure 4.2: Typical voltage history during a burst and typical current waveform for one pulse. Taken with PT9, 4 J per pulse, 2.0 μg argon, 130 μF, 1" $\times$ 1" electrodes.
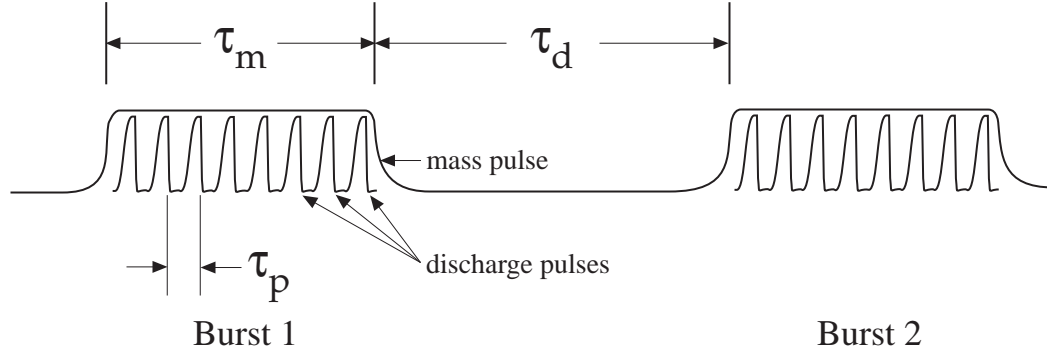
Figure 4.3: Schematic drawing showing two bursts each containing 10 pulses. τ_p is the time between single pulses in a burst, τ_m is the time during which propellant mass flows, and τ_d is the delay between bursts.

ments, 3) to reduce the total number of valve cycles over the lifetime of the device, and 4) to allow throttling between high-thrust slew maneuvers and fine low-thrust pointing maneuvers *without* affecting performance. The first two reasons relate to keeping the mass of the propellant and power supply to a minimum. The last two reasons relate to thruster lifetime and the convenience of using a single thruster for a variety of maneuvers, respectively. These reasons are fully explained below.

Examining Fig. (4.3), during a burst the propellant flows at a steady rate and the time between the pulses, τ_p, is chosen to preclude any propellant from flowing beyond the electrode volume. Therefore, the time between the pulses is set regardless of power or thrust level, and is determined by the molecular speed of the gas and the length of the electrodes as described in more detail in Section 4.1.3. The "mass bit" for each pulse is the product of the steady-state mass flow rate, $\dot{m}_{ss}$, and the time between pulses,

$$m_{bit} \equiv \dot{m}_{ss}\tau_p. \tag{4.1}$$

The average power, P_{avg}, consumed by the thruster from the modulator is,

$$P_{avg} = \frac{N_{pb}E}{N_{pb}\tau_p + \tau_d}, \tag{4.2}$$

where N_{pb} is the number of pulses per burst. The average thrust is similarly,

$$T = \frac{N_{pb}I_{bit}}{N_{pb}\tau_p + \tau_d}, \tag{4.3}$$

where I_{bit} is the impulse provided by a single pulse in the burst. Both the average power and thrust can be throttled by changing the delay between bursts, τ_d, as shown schematically in Fig. (4.3). The number of pulses per burst is set
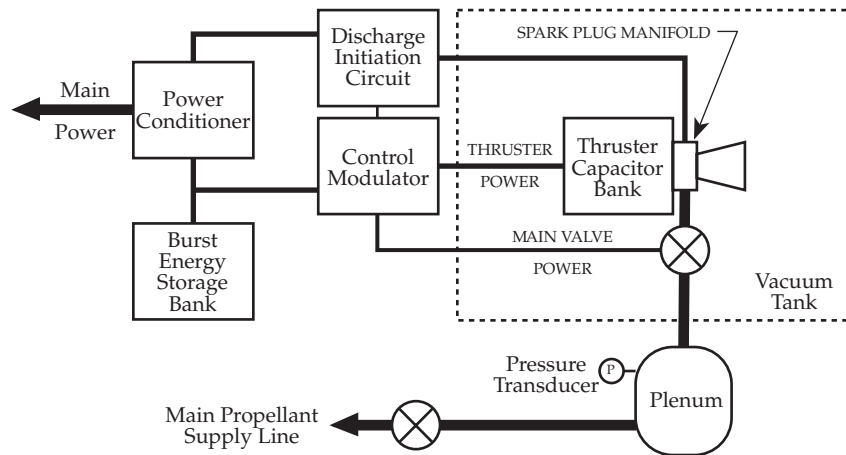
Figure 4.4: SRL-EPPDyL GFPPT system schematic showing the power conditioner, control modulator, discharge initiation circuitry, and thruster connections.

for optimal propellant delivery as described in Section 4.1.3. Energy for all the pulses in the burst is processed by the thruster modulator which contains the charging control and discharge initiation circuitry. The main GFPPT capacitors are mounted directly behind the electrodes and are designed to have the lowest parasitic inductance possible (see Section 4.1.2 for measurements of the capacitor bank impedance) for the best overall performance.

The rest of this section will describe the sequence of events during a burst, the new power conditioning technology for the SRL-GFPPTs, and the related propellant feed system efficiency.

4.1.1   Sequence of Events

During a burst of pulses, the propellant control, power conditioning, capacitor charging, and discharge initiation must be controlled with micro-second timing. A schematic of the SRL-EPPDyL GFPPT system is shown in Fig. (4.4). The following is a sequence of events that would occur during a space-based maneuver:

1. Before firing, the plenum is filled to provide enough propellant for the entire maneuver and the control modulator is put in "stand-by" mode. This mode includes charging the capacitors that store the total energy required for one burst as well as charging the high-voltage discharge initiation capacitor.

2. When the command to fire a burst is received, the control modulator checks to see that the burst capacitors are fully charged and that the thruster electrodes are not electrically shorted.

3. The main propellant valve is opened, and the propellant flow rapidly approaches steady-state conditions in a time that depends on the propellant type, plenum conditions, valve response time, and length of tubing between the valve and propellant injection ports. Typically for our experiments, this time is on the order of 1 ms.

4. The main discharge capacitors are charged quickly, in typically 100-200 μs, to a voltage near 250 V which is less than the Paschen breakdown condition for any of the geometries and propellant distributions tested in this dissertation.

5. The modulator waits a prescribed amount of time, τ_p minus the charging time, that is just long enough to allow the propellant to fill the electrode volume.

6. The modulator sends a command to the discharge initiation circuit to fire.

7. The discharge initiation circuit discharges its high voltage (typically between 400-1000 V) capacitors through a pulse transformer and one or more spark plugs near the back of the cathode in less than 100 nanoseconds.

8. Along with the applied voltage on the electrodes, the spark helps to breakdown the gas between the electrodes. The main capacitors are discharged through the arc in less than ten microseconds.

9. After a short pause, typically 50 μs, the process starts at Step 4 and repeats until all the pulses in the burst have been fired.

10. After the burst is complete, the modulator quickly closes the main propellant valve.

11. A delay, τ_d, that depends on the spacecraft power supply and mission requirements is initiated to allow the burst energy capacitor bank in the modulator to recharge before the next burst.

12. The process repeats from Step 2 until the maneuver is complete and the GFPPT system is shut down.

A similar testing procedure is followed in the laboratory. During performance measurements, the time between bursts is set to approximately 50 s requiring <1 W from a power supply that simulates the spacecraft bus. In the laboratory experiments, a rather slow (20 ms) solenoid valve is used with a sonic orifice to control the mass flow rate of propellant approximately 20 cm upstream of the propellant injection ports. Because of the slow response time of the valve and extra tubing length, the valve is opened 40 ms before the burst and a large amount of propellant is wasted. As described in Chapter 5, however, this extra propellant mass is

measured and subtracted from the impulse measurement. In addition, as shown in Eq. (4.1), the mass bit is calculated from the steady-state mass flow rate and the time between pulses. Since in a space-qualified system a much faster valve would be placed closer to the injection ports, the wasted mass was not included in any of our laboratory performance calculations (see Section 4.1.3).

4.1.2   Power Conditioning and the Control Modulator

A simple and compact DC-DC converter modifies the spacecraft bus or laboratory power supply voltage to the charging voltage required by the main discharge capacitors. As shown in Fig. (4.4) there are actually *two* capacitor banks. One capacitor bank is kept in parallel with the power supply to store enough energy for all the pulses in the burst. This reduces the instantaneous current demand on the power supply during a burst. The other capacitor bank (called the "main" or "discharge" capacitor bank) is located inside the thruster casing and stores the energy for only one pulse at a time. The power conditioning circuitry also steps up the voltage to charge the discharge initiation capacitors to between 400-1000 V. The discharge initiation capacitors are switched through an SCR into a 10:1 pulse transformer. The secondary side of the pulse transformer is connected to between one and four spark plugs which are described in more detail in Section 4.2.4. The pulse transformer helps increase the voltage on the spark plugs to breakdown conditions and isolates them from the main GFPPT discharge circuitry.

The efficiency of the power conditioner is defined as the ratio of the power supplied by the spacecraft or laboratory supply to the average power supplied to the main GFPPT capacitors by the modulator,

$$\eta_{pc} \equiv \frac{P_{avg}}{P} = \frac{f_p \frac{1}{2} C V_0^2}{P},$$
(4.4)

where C is the total capacitance of the main GFPPT capacitor bank, V_0 is the initial voltage before each pulse, and f_p is the pulse frequency, $1/\tau_p$. It also follows that,

$$\frac{T}{P} = \eta_{pc} \frac{I_{bit}}{E}.$$
(4.5)

The overall efficiency of the GFPPT system is related to the power conditioner efficiency, thruster efficiency, and propellant feed system efficiency as described at the end of the next subsection.

Main Capacitor Bank

The main capacitors in the SRL-EPPDyL GFPPT are charged and controlled by a solid-state modulator using modern IGBT commutation techniques that provide

a discharge pulse frequency up to 10 kHz. The energy per pulse is variable over a range of 1-10 J per pulse depending on charging voltage and main discharge capacitance. This capacitor bank consists of between one and six 45 μF boards each made up of thirty WIMA 1.5 μF capacitors connected in parallel. The capacitors (typically used in pulsed laser power supplies) are designed for quick pulses, have a low internal impedance, and an advertised lifetime of 10^9 pulses at their rated voltage of 250 V. The parallel construction using a thin, two-layer circuit board reduces the internal inductance and resistance to minimum levels. The mass and volume, however, are slightly larger than a single capacitor would be with the same energy storage capability. The 45 μF boards are also connected in parallel with aluminum coaxial rings separated by a 10 micron Kapton sheet. The coaxial rings connect directly to the thruster electrodes creating a minimum inductance path.

The internal impedance of the capacitor bank has been measured by simulating a discharge through an electrical short and monitoring the bank voltage. The experiment consisted of charging one capacitor board ($C = 46.7\mu F$) to approximately 25 V and discharging it through a small short. A typical voltage trace is shown in Fig. (4.5). The voltage can be modeled using the fixed-element LRC circuit equations presented in Chapter 3. The natural frequency, ω, and critical resistance ratio, ψ, can be found from a damped sine curve fit (see Eq. (3.2)) of the voltage trace. Knowing the capacitance from a separate measurement allows the internal inductance and resistance to be determined. Based on the measurement, on average, one capacitor board has an internal inductance of 28 nH and a resistance of 8.5 mΩ. Similar measurements using the assembled capacitor banks (three or six boards connected in parallel) of PT5 and PT9 showed that the internal inductance was close to 10 nH for both thrusters. This indicates that the inductance of the leads between the capacitors and the electrodes (which are common to both thrusters) dominates over the internal inductance of the capacitor boards.
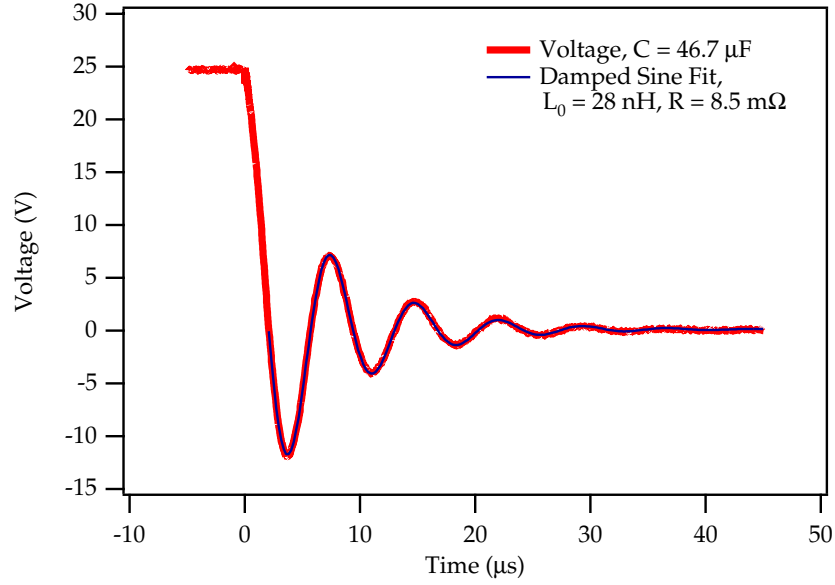
Figure 4.5: Voltage trace and damped sine curve fit from a measurement of the internal impedance of one capacitor board.

4.1.3 Propellant Delivery

Propellant utilization is an important concern that directly affects the performance of any propulsion device, especially one such as the GFPPT that is pulsed as many as 10^8 times over its lifetime. As described in Chapter 1, previous GFPPT designs used ultra-fast (100 μs) valves that cycled each time the thruster was fired and limited the system lifetime. In the modern GFPPT design, a low-energy valve that has a slightly slower response time, 1 ms, can be used instead. This system is expected to have a longer lifetime as only one valve cycle is required *per burst*. Therefore, in SRL-EPPDyL GFPPT designs, the valve is no longer considered the lifetime-limiting component. Using a slower valve does have its disadvantages. Before and after each burst, a small amount of propellant is wasted, m_{waste}, as the valve opens and closes. The time the valve is being actuated is greater than the time the propellant flows at a steady rate, τ_m, during which the pulses occur. The average mass flow rate supplied to the GFPPT by the feed system, $\dot{m}_{avg}$, is then slightly greater than the steady mass flow rate during pulsing, $\dot{m}_{ss}$, both found using τ_m as the time base. If we describe the amount of wasted mass as some variable fraction, κ, of a mass bit,

$$\kappa \equiv \frac{m_{waste}}{m_{bit}}, \tag{4.6}$$

then the feed system efficiency, η_{fs}, can be defined as,

$$\eta_{fs} \equiv \frac{\dot{m}_{ss}}{\dot{m}_{avg}} = \frac{N_{pb}m_{bit}}{N_{pb}m_{bit} + m_{waste}} = \frac{1}{1 + \frac{\kappa}{N_{pb}}}. \tag{4.7}$$

As expected, the feed system efficiency improves as the number of pulses per burst is increased and the valve cycle time is decreased. The number of pulses per burst is limited, however, by the power conditioning circuitry. An optimum number of pulses per burst exists for the lowest system mass including the wasted propellant.

Optimal Number of Pulses per Burst

The optimal number of pulses in a burst comes from the trade-off between having a higher feed system efficiency (increasing N_{pb}) and requiring a more massive *burst* energy storage device, $\alpha_e N_{pb} E$. By examining the sum of this mass and the total wasted propellant mass over the lifetime of the device, $m_{waste}N_{ptot}/N_{pb}$, the optimal number of pulses is,

$$(N_{pb})_{opt} = \sqrt{\kappa}\frac{\tilde{V}}{\bar{u}_e}, \tag{4.8}$$

where again we see the PEP velocity, $\tilde{V}$, from Eq. (1.11). With a 1 ms valve ($\kappa \approx 4$) and using an appropriate, usually smaller, value of α_e, the optimal number of pulses per burst is close to six for the GFPPTs studied here. A lower value for α_e is justified because this energy storage device does not have to be configured for low inductance and will have a much lower specific mass then the main discharge capacitors. The PEP velocity is set about three times larger than a typical exhaust velocity of 25 km/s. This analysis assumes that the total number of pulses is independent of the number of pulses per burst. That is, it assumes that the system lifetime is not dictated by the valve lifetime.

It should be noted that since valve technology is not the prime focus of this dissertation, the mass wasted on each burst is not included in any performance measurement (impulse bit, mass bit, etc.) or calculation (overall efficiency, specific impulse, etc.) effectively assuming that $\kappa = 0$. The specific experimental procedure for measuring and calculating performance will be discussed further in Chapter 5. Six pulses per burst will be used for performance measurements, however, as a representation of what could be used by a space-qualified SRL-EPPDyL GFPPT.

Relation of Thruster Efficiency to Overall Efficiency

Now that the feed system efficiency is defined, the overall efficiency of a GFPPT, discussed in Section 2.3, can be related to the thruster efficiency. Including Eq. (4.4), the overall efficiency is,

Thruster		Geometry	Cap. (μF)	$L^{'}$ (nH/cm)	m_{bit} (μg)	Energy (J)
PT5	(a)	Coaxial	130	~ 2.8	0.2-2.0	2
	(b)	Coaxial	130	~ 2.8	0.2-2.0	4
	(c)	Coaxial	270	~ 2.8	0.2-2.0	4
	(d)	Coaxial	270	~ 2.8	0.2-2.0	6
PT9	(a)	P-Plate	130	2.8	0.2-2.0	4
	(b)	P-Plate	130	3.9	0.2-2.0	4
	(c)	P-Plate	130	5.7	0.2-2.0	4

Table 4.1: Thruster test configurations using argon propellant. Because PT5 has slightly flared electrodes the inductance-per-unit-length value, $L^{'}$, shown here is the average value.

$$\eta = \eta_{fs} \qquad \eta_{pc} \qquad \eta_t \qquad\qquad (4.9)$$

$$= \left(\frac{\dot{m}_{ss}}{\dot{m}_{avg}}\right) \left(\frac{f_p C V_0^2}{2P}\right) \left(\frac{I_{bit}^2}{2m_{bit}E}\right). \qquad\qquad (4.10)$$

Although power conditioning and valve technology are critical to the overall performance of a GFPPT system, their development will be left to the experts in their respective fields. Characterizing the thruster efficiency, η_t, and its scaling are the main subjects of this dissertation.

4.2 SRL-EPPDyL GFPPT Designs

Nine generations of SRL-EPPDyL GFPPTs have been designed and tested as part of the research project related to this dissertation. Two of these designs, PT5 and PT9, were built specifically to test the effects of capacitance and inductance-per-unit-length over a wide range of energy and mass bit values. While the other generations (see Appendix C) were used to explore the effects of propellant injection location, even lower energy (1 J) operation, and propellant type, PT5 and PT9 provided tightly controlled test-beds for experiments on performance scaling. The two thruster designs are summarized in Table (4.1). A method for evaluating the inductance-per-unit-length of various electrode geometries and a description of the discharge initiation system will be presented in this section.
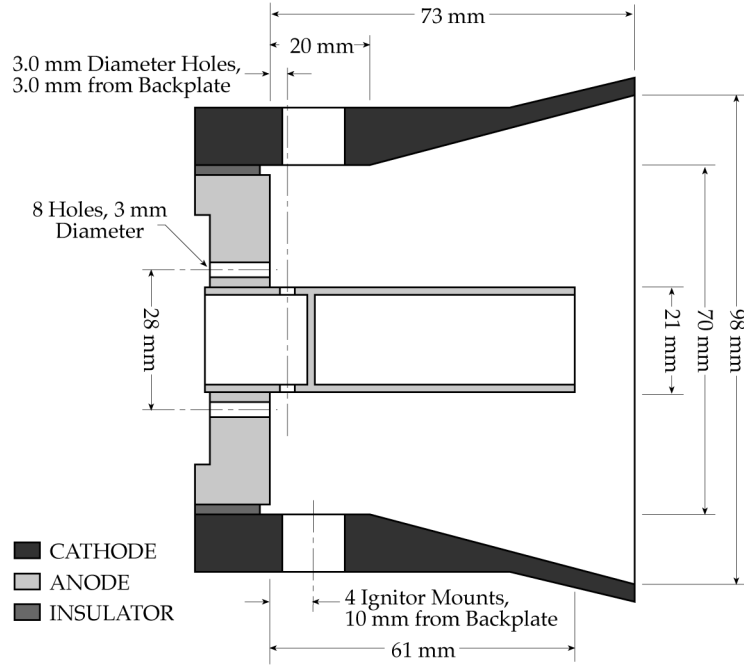
Figure 4.6: Schematic of SRL-GFPPT PT5.

4.2.1 The Coaxial PT5 Design

The fifth-generation SRL-EPPDyL GFPPT is designated PT5 and has undergone many modifications since its original conception, including changes to its discharge initiation system and propellant distribution [74]. A schematic of PT5 is shown in Fig. (4.6). PT5 has a relatively large, stainless-steel, coaxial set of electrodes with an outer to inner electrode radius ratio of approximately four and a total volume of 350 cm^3. It uses four semi-conductor-type spark plugs mounted on the inside of the outer electrode (cathode) at 90 degree azimuthal intervals to initiate the discharge uniformly. The main discharge is driven by a low-inductance (10 nH) 130 or 270 μF capacitor bank which is capable of being charged to 250 V giving a maximum energy per pulse of 4 or 8 J, respectively. The entire thruster has a mass of approximately 6 or 8 kg (depending on the capacitance level), including the electrode mass as well as the thruster housing mass. The latest design includes a new discharge initiation circuit that provides reliable, simultaneous activation of all four spark plugs at the beginning of the discharge as described in Section 4.2.4.

PT5 was designed to test the effects of capacitance on the performance over a wide range of mass bits *without* significantly changing the applied voltage. Changing the capacitance changes the characteristic time of the discharge ($\sqrt{LC}$) and energy in the discharge. Although only two capacitance values were tested, they

were chosen as ultimate limits of the typical values that would be used in these devices. At a similar voltage level, larger values of capacitance lead to longer charging times, τ_p, or higher current levels in the modulator. Along with the larger mass that comes with more capacitors and the associated hardware, both of these trends have adverse effects on performance. Longer charging times can lead to a decrease in propellant utilization (See Eq. (2.16)), and higher charging currents can lead to a decrease in power conditioning efficiency along with possibly a shorter lifetime from the high-current IGBT switch. At the same time, lower values of capacitance simply do not provide enough energy to the discharge at these relatively low voltage values. Furthermore, the characteristic time of the discharge is reduced below the time it takes for the current sheet to reach the end of the electrodes, possibly causing detrimental crowbar discharges. Highly underdamped current waveforms have also been shown to be less effective for acceleration in Chapter 3.

Before this research, reference [39] provided the only controlled study of the effect of capacitance on performance. The experimental data showed that the thrust-to-power ratio increased with the *square root* of capacitance from 45-200 μF at a constant specific impulse of 5000 s. Keeping the specific impulse constant led to many different energy levels and mass bit values in the study. Unfortunately, this does not provide enough information for a more global scaling relation over a wider variety of conditions. Furthermore, these performance measurements have been put into question (see Refs. [17,79]) as there is no evidence that they conditioned the electrode surfaces before taking measurements. Without proper conditioning, it has been shown by this author [75] and others [88] that the impulse can be significantly greater due to the addition of adsorbed gas and organic monolayers (pump oil) to the discharge. In our experiments with PT5, we will be able to study the scaling in a carefully controlled environment due to changing the capacitance without the possible effects of electrode contamination.

4.2.2   The Parallel-Plate PT9 Design

PT9 uses the 130 μF capacitor bank and thruster casing from PT5 with a modular set of parallel-plate electrodes for testing various values of inductance-per-unit-length. All the electrodes are made of 1/8″ thick 70% tungsten, 30% copper plates, with dimensions of 1″ x 4″ (width x length) or 1/2″ x 4″. There are two places to mount the electrodes at distances of either 1″ or 1/2″ apart. The mountings include one (1/2″ gap) or two (1″ gap) propellant injection ports that direct the propellant flow axially. This gives four different electrode configurations and three different inductance-per-unit-length or aspect ratio values. Three of the four configurations were tested for this study including the smallest, PT9a (H/W = 0.5, L' = 2.83 nH/cm), middle, PT9b (H/W = 1, L' = 3.92 nH/cm), and the largest, PT9c
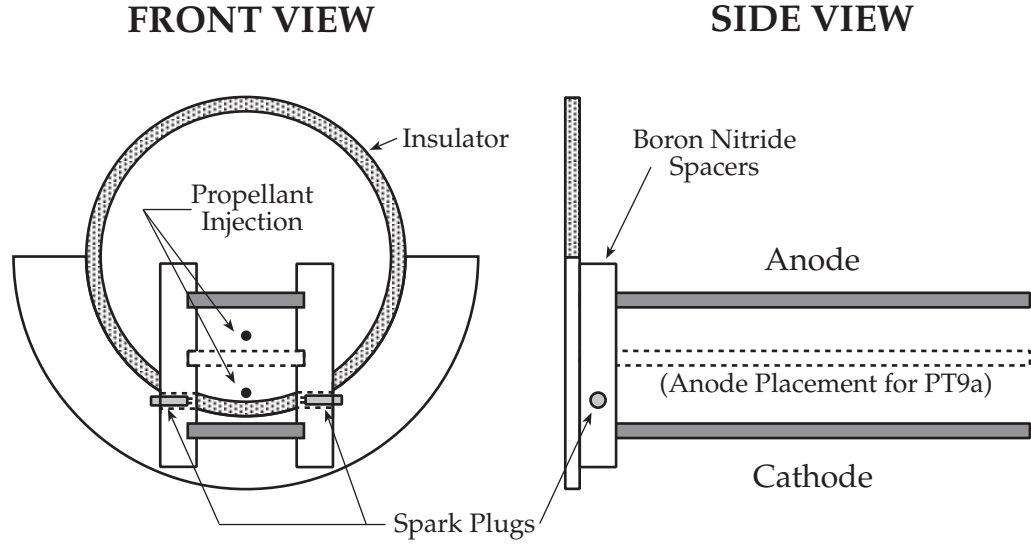
FRONT VIEW   **SIDE VIEW**

Figure 4.7: Drawing of PT9b with 1" x 1" electrodes as well as the anode placement for PT9a. PT9c uses 1/2" wide electrodes with the same vertical 1" placement as PT9b.

(H/W = 2, $L^{'}$ = 5.68 nH/cm) values of inductance-per-unit-length. A schematic of PT9 is shown in Fig. (4.7).

PT9 has been tested with and without pyrex sidewalls to contain the discharge. As discussed in Section 5.4.1, although the sidewalls were successful in containing the discharge, the efficiency was unexpectedly low. Removal of the sidewalls actually led to better performance, especially at the lower mass bit conditions with argon propellant. PT9 uses the 130 μF capacitor bank because of this open nature of the electrode volume. Using the smaller capacitor bank reduces the charging time and, therefore, the time between pulses. With smaller values of τ_p, the amount of injected propellant mass that can escape out of the electrode volume before the discharge is reduced to a minimum.

The main purpose of PT9 is to test different inductance-per-unit-length configurations at similar operational conditions to those tested with PT5. In PT5, the coaxial set of electrodes has roughly the same value of $L^{'}$ as PT9a. The inductance-per-unit-length is directly related to the strength of the Lorentz force (see Eq. (2.5)) and also influences the effective circuit load, $L^{'}u$. Only one study by Hart [41] tried to systematically investigate the effects of inductance-per-unit-length by changing the radius ratio of a coaxial GFPPT. Unfortunately, as described in detail in Appendix A, the insulating backplate Hart used was made of Teflon, a material known to ablate very well in these type of discharges. By changing the radius ratio, he exposed more Teflon surface area and changed the mass loading. Other in-
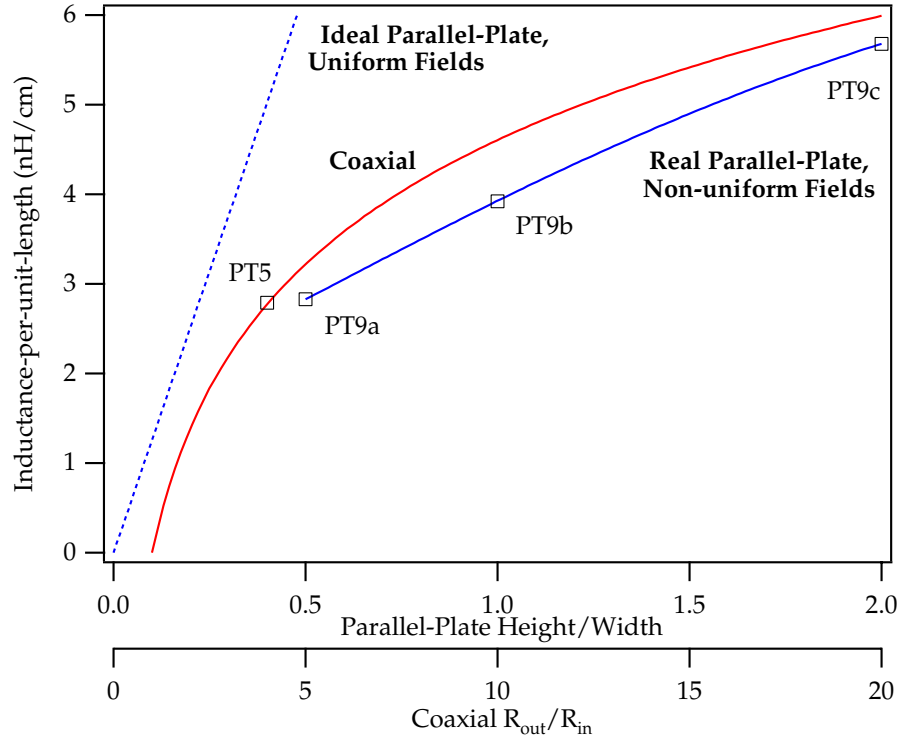
Figure 4.8: Normalized inductance gradient as a function of geometry for parallel-plate and coaxial electrodes. The relation for the inductance-per-unit-length of an ideal (infinite width) set of parallel-plates is given in Eq. (4.11).

vestigators have, in general, found a monotonically increasing performance trend with increasing values of L' [17,78], although the exact scaling relation remains unclear.

4.2.3 Determining Inductance-per-unit-length

The magnitude of the inductance-per-unit-length, L', is one of the most important differences between parallel-plate and coaxial electrode geometries. It is calculated by integrating the magnetic flux through the volume enclosed by the discharge.

The inductance-per-unit-length for a parallel-plate thruster can be estimated by treating the electrodes as an infinite single-turn current loop with a *uniform* field,

$$L'_{pp} \approx \mu_0 \frac{h}{w}, \tag{4.11}$$

where h is the height (separation) and w is the width of the electrodes. As other

authors [89] have pointed out, however, most commonly designed parallel-plate thrusters produce very non-uniform fields, and the fringing effects of finite-width electrodes must be taken into account. Using a conformal mapping technique to determine the electromagnetic fields in a parallel rail launcher, Ref. [90] provides the necessary tabular data to determine the actual value of the inductance-per-unit-length for a given electrode aspect ratio.

For a coaxial GFPPT, the calculation can be carried out directly and no approximation is necessary assuming a planar current sheet,

$$L'_{coax} = \frac{\mu_0}{2\pi} \ln \left(\frac{r_{out}}{r_{in}} \right). \tag{4.12}$$

The graph in Fig. (4.8) shows the L' values for both the parallel-plate and coaxial geometries which are used in this study. The graph also provides a comparison of the L' values for all the GFPPTs tested here and shows that the inductance-per-unit-length for a coaxial thruster and a parallel-plate thruster is similar if the former has a radius-ratio about ten times the height-to-width ratio of the latter. This is the case when comparing PT5 with PT9a which have similar values of inductance-per-unit-length. In general, however, reasonable dimensions (in terms of electrode mass) for parallel-plate thrusters have a higher value of L'.

4.2.4 Discharge Initiation and Stability

The design of the discharge initiation (DI) system for multiple initiation-point GFPPTs has undergone many revisions at EPPDyL to improve repeatability, spark plug lifetime, and discharge symmetry. In the final design of PT5, the same Bendix semi-conductor type spark plugs used in the LES 8/9 ablative pulsed plasma thruster (APPT) were adopted for their low breakdown voltage characteristics [91] and demonstrated long-lifetime. Firing four or more spark plugs *simultaneously* to create a uniform and symmetric discharge, however, was found to be a difficult task due to the configuration of the spark plugs and the polarity of the electrodes. In the case of PT5, the spark plugs shared a common cathode (ground potential) with the thruster which dictated parallel electrical connections. Discharge asymmetry due to one or more spark plugs not firing at all was shown by fast-framing camera images of coaxial GFPPT discharges over many different operating conditions (see Chapter 5 and Ref. [74]). In addition, as described in the next chapter and Ref. [77], performance measurements conducted at NASA JPL showed that the impulse bit was reduced by as much as 40% when only one spark plug fired instead of four.

Following a design similar to the Fairchild DI circuit in the LES 8/9 APPT, the secondary side of the original pulse transformer was modified to include a high-voltage, 20 nF mylar capacitor in parallel with the spark plug, as shown in Fig. (4.9). In addition, a high-current, fast-switching diode (International Rectifier
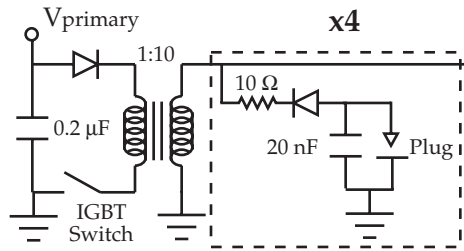
Figure 4.9: Schematic of the new discharge initiation circuit. The portion of the circuit surrounded by the dashed box is repeated four times in parallel, one for each spark plug.

part HFA15TB60) and a 10 Ω resistor in series with the spark plug were used to insure that each capacitor did not lose its charge to another spark plug already in the process of breaking down. This is important as the first spark plug to fire provides the lowest impedance path for draining the other spark plug capacitors before they have the chance to discharge. A different discharge initiation scheme developed at EPPDyL places the spark plugs in *series* insuring that all the spark plugs fire simultaneously. Unfortunately, this scheme could not used in PT5 with the Bendix spark plugs due to the common ground connections.

As shown in Fig. (4.7), PT9 uses two smaller surface-flashover spark plugs that are insulated from the discharge by a boron-nitride mounting block near the breech of the cathode. Erosion rate measurements have shown that less than 0.1 μg of ignitor material is lost per pulse. These plugs use the same parallel DI circuitry from PT5 with a required breakdown voltage of 500 V at normal operating conditions with argon propellant. These plugs are used instead of the previous design for their smaller size and because they can be isolated from the electrical ground of the main discharge. In the future, these type of spark plugs can also be connected in series with each other to insure multiple initiation points.

Now that both of the GFPPT designs are completely described, the performance measurements over a wide range of operating conditions will be presented in the following chapter.

Chapter 5

GFPPT Performance Measurements

This chapter explains the procedures for measuring performance and documents the results of testing PT5 and PT9 over a wide range of operational conditions. It includes descriptions of the vacuum facility and techniques for measuring the impulse, mass bit, energy, and current of a GFPPT discharge. The performance measurements from PT5 with variable capacitance and PT9 with variable inductance-per-unit-length, both over a wide range of argon mass bits, will also be presented. A more in-depth discussion of the results and a comparison with the models developed in Chapter 3 will be left to the next chapter.

5.1   Performance Measurement Techniques

Performance indicators such as the thruster efficiency, the impulse-to-energy ratio, and the exhaust velocity are derived from direct measurements of the impulse bit, capacitance, initial voltage, mass flow rate, and the time between pulses in a burst. Since the GFPPTs studied here operate in a burst mode, the performance measurements are based on average, per pulse, quantities. In a single series, at least twenty trials (120 pulses) are conducted at the same operating conditions in order to reduce the standard deviation of these average measurements.

The testing facility and methods for measuring performance will be described in detail in this section. The calibration and data reduction procedures as well as a discussion of the potential sources of error in the measurements are presented in Appendix B. Briefly, each of the performance variables will be defined in terms of measurable quantities.

The efficiency used here is the conventional thruster efficiency,

$$\eta_t = \frac{I_{bit}^2}{m_{bit}CV_0^2},\tag{5.1}$$
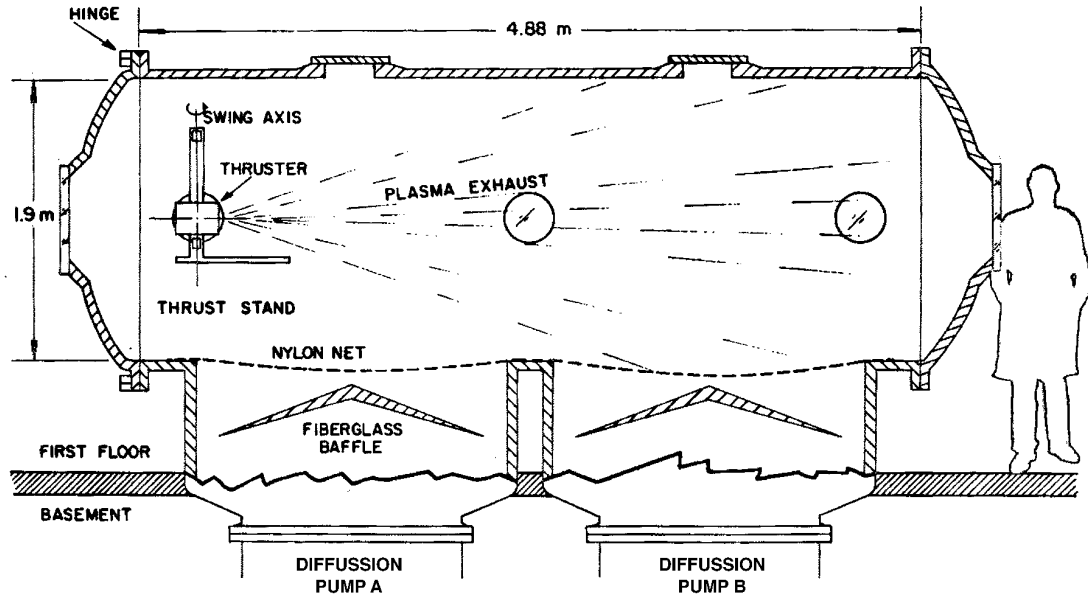
Figure 5.1: The Pulsed Performance Facility at EPPDyL.

where the mass bit is $m_{bit} = \dot{m}_{ss}\tau_p$. The impulse-to-energy ratio is simply,

$$\frac{I_{bit}}{E} = \frac{I_{bit}}{\frac{1}{2}CV_0^2},$$ (5.2)

and the mass average exhaust velocity is,

$$\bar{u}_e = \frac{I_{bit}}{m_{bit}} = \frac{I_{bit}}{\dot{m}_{ss}\tau_p}.$$ (5.3)

Again, I_{bit}, C, V_0, τ_p, and $\dot{m}_{ss}$ are all measurable quantities discussed in the following sections after the facility description.

5.1.1 Performance Measurement Facility

The vacuum vessel used for this study, shown in Fig. (5.1), is approximately 2 m in diameter, 5 m in length, has eight optical access ports, and is made of fiberglass. Originally designated the Pulsed High-Power Performance Facility for its heritage of quasi-steady MPD work, this facility has been renovated (see Appendix B) to measure very low impulses ($< 20\mu$Ns) from low-energy (< 10 J) unsteady GFPPTs. A vacuum level of 5×10^{-5} torr or less is maintained by two 1.2 m oil-vapor (DC-704) diffusion pumps. Each pump has a capacity of 95 m^3/s and is backed by a

roots blower (1340 cfm) and a mechanical pump (150 cfm) that also provide rough vacuum during initial evacuation. Two liquid nitrogen cooled baffles positioned directly above each diffusion pump prevent backstreaming oil from entering the tank. A nylon mesh net covers the traps and intakes to the diffusion pumps providing another layer of protection from contamination, although slightly reducing the pumping speed. For low-energy GFPPTs, the propellant mass flow rates are always below 30 mg/s and the valve is only opened for 45 ms. The effect of mass injection on the background pressure (and backstreaming rates) during the experiments was barely detectable from both pressure and residual gas analyzer (RGA) measurements.

Some performance measurements reported in this dissertation were also conducted by this author at NASA JPL in the Advanced Propulsion Technology facilities. These experiments used a similar set-up, including a thrust stand developed by EPPDyL that is completely documented in Refs. [77, 84]. The vacuum tank itself, however, uses cryo-pumps to reach an operating pressure of 2×10^{-6} Torr. Although mechanical pumps are used for the initial evacuation, the cryo-pumps provide a clean high-vacuum environment.

As pointed out in Refs. [75, 88], adsorbed gases and pump oil monolayers on the electrode surfaces can influence the performance of GFPPTs that have not been properly conditioned before testing. Consequently, a substantial effort has been invested in cleaning the vacuum facility at Princeton and modifying the existing baffle system to accept liquid nitrogen which should reduce backstreaming as much as possible. These activities are described in detail in Appendix B, with the results summarized here.

Unlike previous pulsed thrust measurements at EPPDyL where impulse bits $> 280 \ \mu \mathrm{Ns}$[1] were measured consistently, lower impulse bit measurements have shown signs of magnitude decay that seem to implicate pump-oil and adsorbed gas contamination effects. In these performance measurement experiments, the magnitude of the impulse bit has been seen to decrease as the total number of pulses increases. As shown in Fig. (5.2), the impulse measurements from both facilities at EPPDyL and JPL show approximately a 30% decline in impulse after removing adsorbed gases off the electrodes during the first 10-100 pulses. After 100 pulses, both measurements show the same impulse within the systematic error, <5%. In addition, at EPPDyL, measurements with and without the liquid nitrogen baffles have shown that the thruster has a slightly higher performance with the baffles off. This is now believed to be due to the accumulation of diffusion pump oil on the surface of the electrodes between pulses. New experimental procedures for cleaning the thruster under vacuum before performance measurements are described in Section 5.2.1. Care has been taken to ensure that none of the performance

---

[1]This number corresponds to the impulse bit of an LES8/9 APPT measured at EPPDyL [92] that agrees with measurements from other laboratories, for example [93].
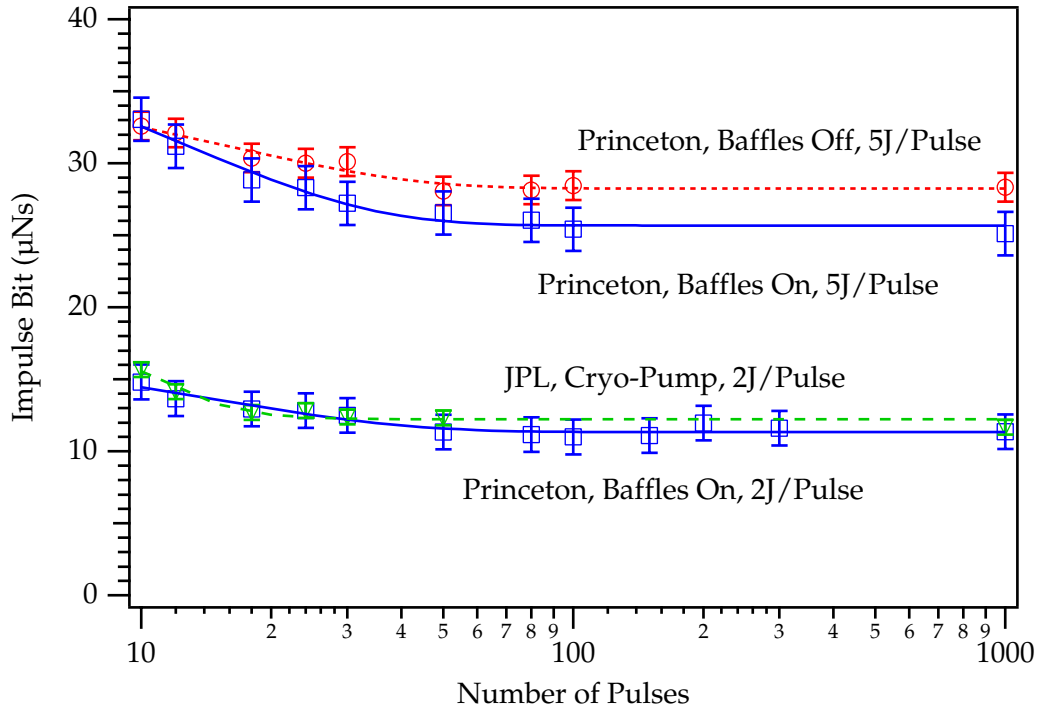
Figure 5.2: Impulse bit decay as a function of the number of pulses at two different energies and two different facilities.

measurements presented here are influenced by contamination products.

All the diagnostic tools for measuring performance in EPPDyL's facility will now be described in separate subsections.

5.1.2 Impulse Bit

The typical impulse produced by a GFPPT operating near 5 J per pulse is about the same as the impact of a pin dropped from 1 cm. In our experiments, this minute level of impulse is measured accurately by monitoring the position of the thruster mounted at the end of a swinging gate type thrust stand, as shown in Fig. (5.3). The thrust stand has a vertical rotational axis through two flexural pivots that allows relatively friction-free rotational motion in the horizontal plane. Knowing the position of the thruster at all times during an experiment allows the thrust force to be determined based on calibrated thrust stand dynamics. In the case of very short duration accelerations, as with most unsteady pulsed plasma thrusters, the force can be considered impulsive and observing the change in velocity of the effective thruster mass is enough to determine the impulse magnitude.

Originally designed for testing quasi-steady MPD thrusters [94, 95], the thrust

Figure 5.3: Swinging gate impulsive thrust stand.

stand has undergone many modifications to measure very small impulses ($< 20\mu$Ns) accurately. Electrical connections including thruster and valve power are supplied through coaxial cables attached to the thrust st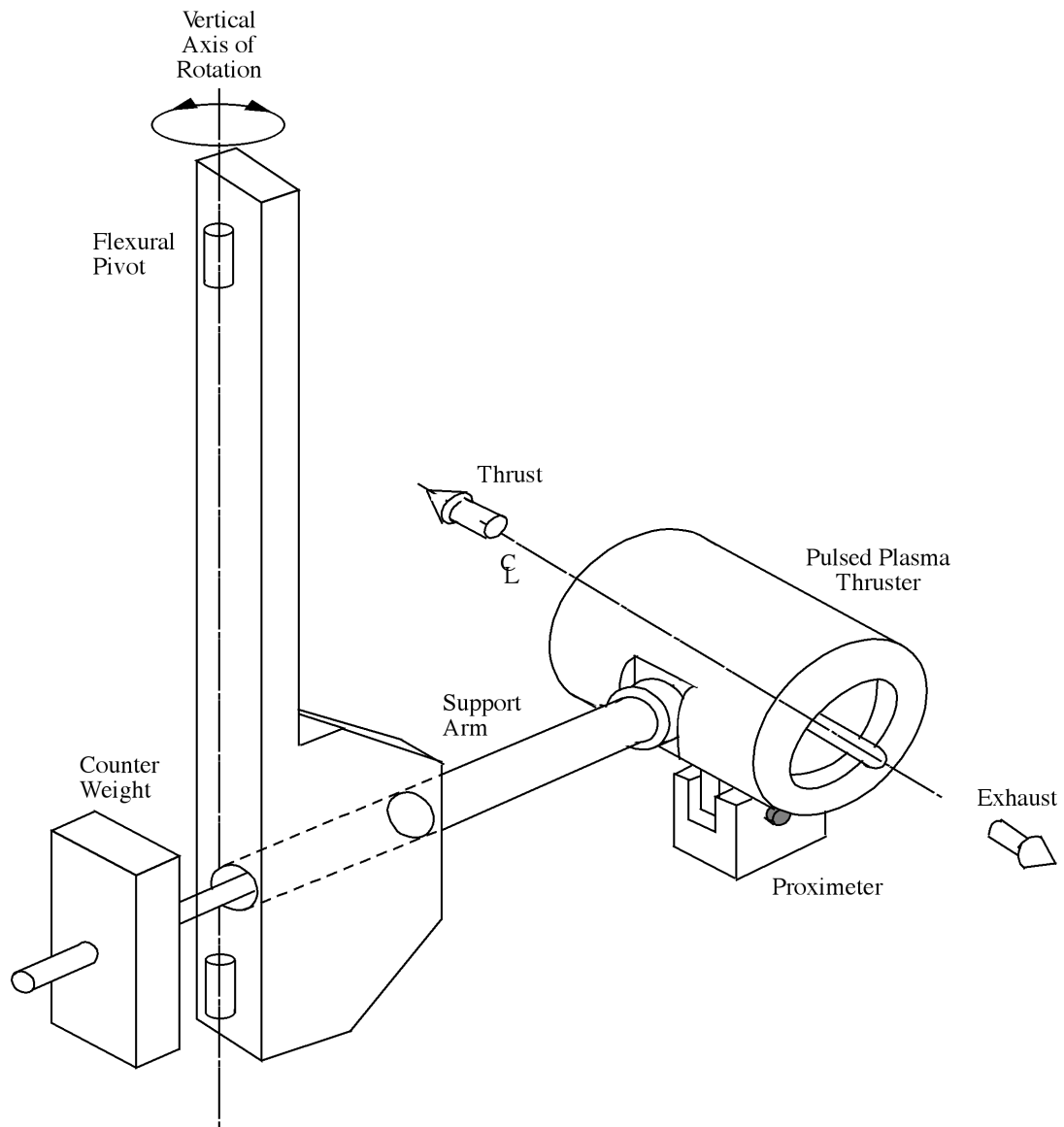and arm and support structure through cable clamps. Gas propellant is fed through polyvinyl tubes also mounted between the arm and the support frame. Care has been taken to ensure that the cables do not touch each other or drift in any way that would change the neutral position of the thrust stand. Along with a small contribution from the cables and propellant lines, the flexural pivots provide the restoring force and a small amount of damping to the almost exclusively horizontal motion of the thruster. A slight tilt in the horizontal plane of the thrust arm permits a stable neutral position without allowing gravity to play a significant role in the restoring force. The tilt and stability of the thrust stand are controlled by two screw-jacks that can be actuated under vacuum.

The dynamics of this slightly damped spring-mass system are well understood. Since the thruster is mounted well away from the rotational axis, its motion can be described accurately as a linear displacement over a small angle. In response to an impulsive force, I_{bit}, the position of the thruster, $x(t)$, initially at rest is given by,

$$x(t) = \frac{I_{bit}}{m_{eff}} \frac{1}{\omega_n \sqrt{1 - \varsigma^2}} \ e^{-\varsigma\omega_n t} \sin\left(\omega_n t \sqrt{1 - \varsigma^2}\right), \tag{5.4}$$

where ς is the damping coefficient, ω_n is the natural frequency, and m_{eff} is the effective mass of the thrust stand. The natural frequency and damping coefficient can be determined from the position history and are independent of the impulse value. If the arm is moving before the impulse occurs, then the post-impulse sine wave could be offset by a phase angle. In this case, a change in the velocity must be considered and $I_{bit} = m_{eff}\Delta\dot{x}$. The velocity is the derivative of position with the added phase offset,

$$\dot{x}(t) = \frac{I_{bit}}{m_{eff}} \ e^{-\varsigma\omega_n t} \left[\cos\left(\omega_n t \sqrt{1 - \varsigma^2} + \phi\right) - \frac{\varsigma}{\sqrt{1 - \varsigma^2}} \sin\left(\omega_n t \sqrt{1 - \varsigma^2} + \phi\right)\right]. \tag{5.5}$$

Using the coefficients from the position relation (including the phase offset) and the calibrated value of the effective mass, the velocity change can be found without actually taking the derivative of the measured position signal. In comparison, numerically differentiating a digitally stored position trace would lead to large errors without extensive filtering that could adversely affect the results. For the impulse measurements described in this dissertation, a damped sinusoid function is numerically fit by a least squares method to the position history before and after the impulse to determine all the coefficients ($I_{bit}, \omega_n, \varsigma,$ and ϕ) except the effective mass. The effective mass and the error of the impulse measurement are largely determined by the calibration procedure as described in Section B.5. Before

the work associated with this dissertation, the change in velocity was found by fitting a line to the position history and measuring the slope of proximeter data after the pulse. The procedure outlined here improves on that process significantly and allows very small impulses to be measured accurately by reducing the error in the curve fitting operation.

In all the experimental trials (a "trial" is one *burst*), the impulse is actually measured for one burst of pulses, and the impulse bit of a particular trial is the average impulse per pulse. In addition, since the propellant flows for much longer than the burst time (typically 65 ms of effective gas flow compared to about 2 ms of pulses) the unaccelerated gas contribution to the impulse is completely subtracted before any performance calculations are made. The *cold gas* impulse is determined for each mass bit by firing the thruster "cold" (without charging the main capacitors) 5 times before and 5 times after the "hot pulses" at the same plenum pressure. All the impulse data presented in this dissertation are found by averaging the hot impulse values from the last 20-25 of 30 hot trials with the cold gas impulse subtracted out. The first five hot trials (30 pulses) at any condition are discarded to ensure that electrode contamination does not influence the measurement. Other trials may also be discarded if problems (such as shorting or other spurious arc attachment) occur during the burst causing the modulator to shut down prematurely. Typically, there are no more than five of these events in a series of thirty trials, thus leaving at least twenty trials for averaging.

Two devices for measuring the position of the thruster have been used in this dissertation work. The interferometric proximeter system (IPS) is used for the accurate resolution of small impulses including very small cold gas pulses. A radio frequency position transducer (or proximeter) is also used to measure the position of the thrust arm due to its linear output (1.27e-4 m/V). Both systems can be used to measure any magnitude of impulse considered in this dissertation. Although the IPS is slightly more precise, the RF proximeter was used more commonly to reduce the data processing requirements over a large number of trials.

Interferometric Proximeter System

The interferometric proximeter system has been described in detail in Ref. [92] and in a masters thesis, Ref. [96]. The IPS measures position by monitoring the intensity of an interference pattern produced by a Michelson type interferometer, as shown in Fig. (5.4). In our application, the corner cubes which form the two legs of the interferometer are both mounted on the arm of the thrust stand near the thruster mount. In this case, the position measured is the *relative* displacement between the two corner cubes. This configuration is necessary to reduce the sampling frequency required for long duration (> 10 second) position measurement [92]. More sensitive arrangements can be made but are not required for any measurement described in this dissertation. Using the IPS for position measurement is only re-
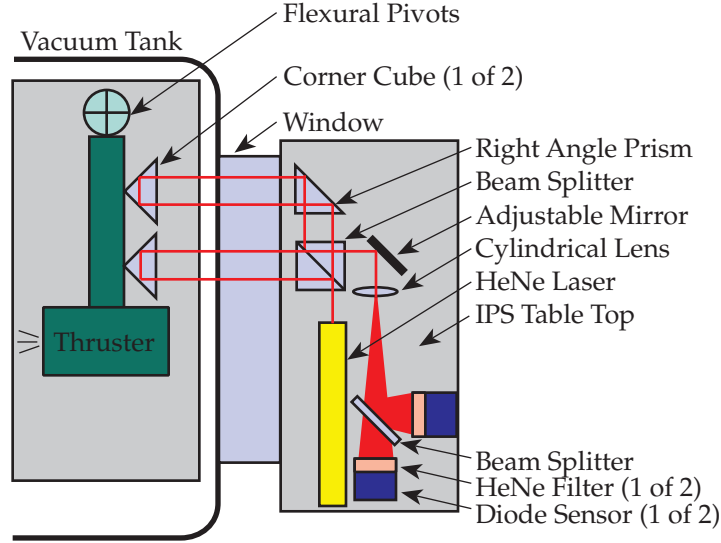
Figure 5.4: Thrust stand set-up with the Interferometric Proximeter System (IPS). Taken from Ref. [96].

quired for very high accuracy, low impulse applications such as cold gas pulses at very small mass bits. Although the position resolution is very high, facility vibrational noise limits the accuracy to about 1 μm of displacement for both the IPS and RF proximeter.

Radio Frequency Proximeter

A Bently Nevada position transducer has been used at EPPDyL for many years to measure the impulse from high power gas fed pulsed plasma thrusters [94]. The proximeter measures the *absolute* linear displacement of a steel target mounted directly below the thruster. The proximeter is useful for positioning the arm in a stable configuration and for its simple operation. Although the proximeter is ultimately not as precise as the IPS, it was able to perform all of the impulse measurements presented in this dissertation with $< 3\%$ error. When compared with the IPS using an appropriate scaling factor, both position measurement systems agreed to within less than a percent.

5.1.3 Mass Bit

Propellant, in most cases argon, is supplied to the GFPPT through a solenoid valve, choking orifice, and plenum arrangement as shown in Fig. (5.5). The valve is located approximately 20 cm upstream from the thruster propellant injection ports.

Figure 5.5: Experimental set-up for performance measurements of GFPPTs.

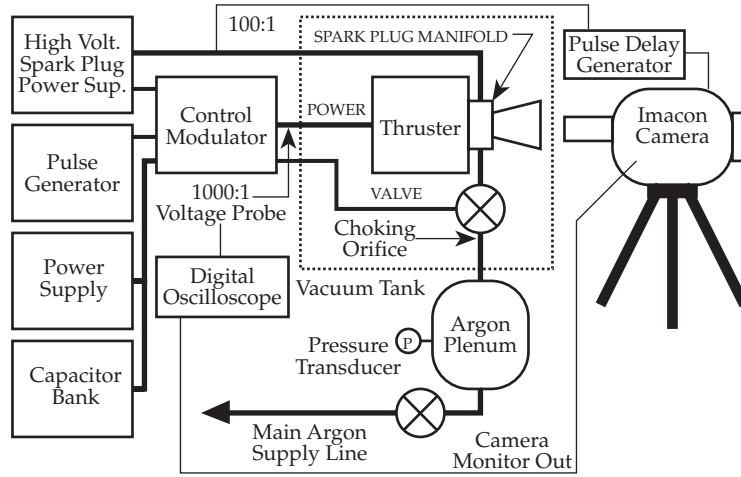It is opened and closed by the control module and timed by a Stanford DG535 pulse signal generator. For these experiments, the valve was open for 45 ms and the thruster was set to fire 40 ms after the valve opened to allow sufficient time for the gas to reach a steady flow rate. This time could be greatly reduced with a faster acting gas valve located closer to the electrodes. The mass flow rate is controlled by changing the pressure in the plenum upstream of the sonic orifice. Approximately 10 ms after the valve is open, the flow is choked at a sonic orifice made from a copper plate with a 0.36 mm diameter hole. Using a pressure transducer located downstream of the sonic orifice, the mass flow rate was seen to reach a steady-state condition within 20 ms of the valve opening at relatively high mass flow rates. Integrating the pressure history waveform gives an effective valve time of 65 ms for the calculation of the effective cold gas exhaust velocity, near 400 m/s for argon propellant.

The mass bit value itself comes from the timing of the pulses within a burst, τ_p, and the steady-state mass flow rate, $\dot{m}_{ss}$. In these tests, the pulses are either spaced every 274 μs for PT5 or 250 μs for PT9 as measured from the voltage trace taken during the burst. The difference between these two values is related to the fixed, lower value of capacitance and subsequent faster charging time for PT9 as explained in Chapter 4. To obtain the mass bit, the time between pulses is multiplied by the steady-state mass flow rate which is a function of plenum pressure. The calibration between mass flow rate and plenum pressure is described in Section B.5. From the kinetic model presented in Chapter 3 and using argon propellant, less than 5% of the propellant is expected to reach beyond the boundaries of the electrodes before each pulse.

5.1.4 Energy

The primary capacitor voltage is measured at the charging supply through a passively compensated 1000:1 P6015 Tektronix voltage probe with a calibrated frequency response up to 100 MHz. For each set of pulses, a voltage trace was captured on a Tektronix 460A digital oscilloscope showing the charging cycle of the capacitor for the entire burst. The scope has an expanded memory to allow a sampling rate of 50 million samples per second (20 ns/sample) for 2 ms, the full duration of the burst. The voltage trace is squared and multiplied by the measured capacitance for each thruster, resulting in a plot of energy during the pulse train accurate to within 1.5 %. The peak energy before every pulse was averaged over the number of pulses in the burst to determine the energy per pulse. The standard deviation of that average is used as the error in this measurement, typically $\sigma < 4\%$.

5.1.5 Current

The current flowing out of a capacitor is simply related to the derivative of the potential across its terminals, $-CdV/dt$. This measurement is independent of the load on the capacitor although it requires a highly time-accurate voltage measurement. With a passive voltage probe, this requires compensation for the parasitic impedance between the capacitor bank and the probe. In comparison, including a Regowski coil or other current transformer for a more direct measurement would necessarily add volume between the anode and cathode electrical leads. For any conventional GFPPT design, this would increase the inductance of the driving circuit, a parameter known to influence performance. The internal inductance of the most recent capacitor bank design used in both PT5 and PT9 has a measured inductance value of only 4.7 nH; therefore, even a minor change would significantly alter L_0. As shown in Chapter 2, Fig. (2.3), the product of the voltage and *inferred* current does, in fact, match the expected power and energy for a low-energy GFPPT discharge suggesting that this method is fairly accurate. Furthermore, for the data presented here, we will use the *integral* of the current squared which should be less susceptible to electronic noise. In any case, the current will only be used to discuss *trends* in the expected impulse and energy transfer efficiency.

5.1.6 Imacon Fast Framing Camera

The Imacon fast framing camera (Hadland Photonics model 792LC) has been used previously at EPPDyL to document the effects of initiation on discharge symmetry [74]. It produces up to 14 multiple black and white (grayscale) images on one exposure of a 3.25″ by 4.25″ polaroid photograph. Each *frame* can be taken at rates of either 2×10^7 or 5×10^5 frames per second depending on the selected oscillator
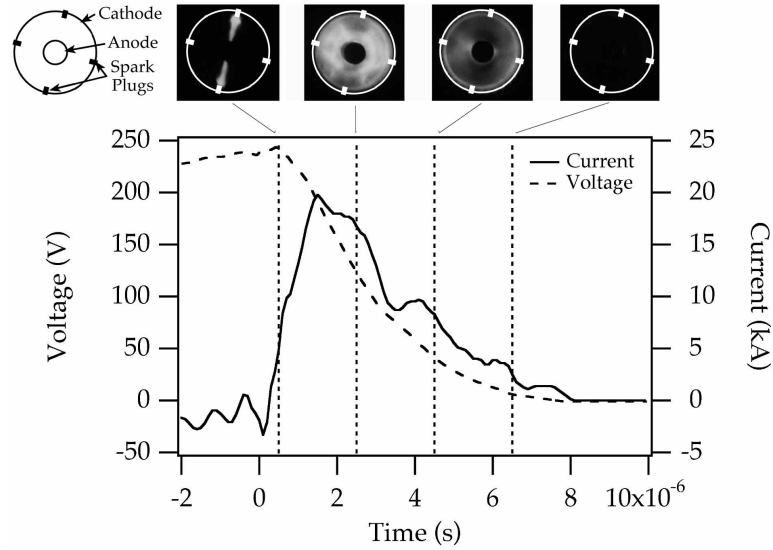
Figure 5.6: Frames from an Imacon picture (5×10^5 frames per second, 0.5 μs delay) coordinated with the voltage and current traces of the discharge. The head-on images show the initiation occurring at two of four spark plugs with PT5 firing at 5 J/pulse and a 0.5 μg argon mass bit.

module. The camera is timed and triggered by a digital delay generator (DDG), which is in turn triggered off the high voltage leads to the spark plugs. Since there is a slight delay between the applied voltage to the spark plugs and the actual breakdown, the DDG can be set to activate the camera just before the discharge begins or at any time later. In all references to time in this dissertation, $t = 0$ occurs when the breakdown actually begins and current begins to flow. To correctly match the timing of the Imacon pictures with the discharge, the camera has an electrical monitor line that pulses when the camera exposes each frame. In coordination with voltage traces saved on the Tektronix 460A digital oscilloscope (see Fig. (5.6)), the pictures can be placed at the correct time with regard to the discharge.

In this dissertation work, the Imacon camera was used to examine the symmetry of the discharge in PT5 and the profile of the discharge in PT9. At the highest mass bits, the plasma emission from the discharge was bright enough so that a 10 nm band-pass filter centered at 488 nm (corresponding to an argon ion electronic transition) could be used to identify the location of the plasma. At lower mass bits, filtering was not possible because there was not enough light to expose the film after filtering. Since at higher mass bit values filtered and unfiltered pictures looked very similar, we expect this to be the case at lower mass bit values as

well. Similar filtering techniques involving higher energy GFPPTs in the past have shown that the location of the plasma emission corresponds well to the front of the current sheet [53].

5.2 Influence of Background Gases and Erosion Products on Performance

Now that the diagnostics have been explained in detail, we will discuss the effects of background gases in the vacuum chamber and erosion products in the discharge. These two effects provide potentially the largest sources of error in the performance measurements. A separate discussion of the error involved with each of the diagnostic tools described in the previous section can be found in Appendix B.

5.2.1 Thruster Conditioning Prior to Performance Measurements

As mentioned in Chapter 1, the performance of low-energy GFPPTs can be effected by diffusion pump oil vapor condensing on the electrode surfaces. As described in detail in Appendix B, both spectroscopic studies of silicon line emission (DC-704 is a silicon-based diffusion pump oil) and impulse measurements have shown that background oil and measured performance levels reach an asymptote after approximately 100 consecutive pulses with less than one minute between each discharge. This indicates that the high current GFPPT discharge can effectively remove potential contaminants and adsorbed gases off the electrode surfaces on every pulse. Although the oil backstreaming flux has been reduced at least 50% by the activation of liquid nitrogen baffles, a significant amount of oil may still accumulate between testing runs or pauses greater than a certain duration. By experimenting with various delays between bursts, impulse bit increases above 5% were only noticed for pauses longer than 10 minutes. Some time (typically less than a minute) is required between impulse measurements to allow the thrust arm to relax back to its neutral position. For the performance measurements presented in this dissertation, a period of exactly 50 seconds was used between all bursts. This is considered a short enough time to ensure that an insignificant amount of oil has been deposited on the electrodes between trials and a long enough time to ensure the arm is nearly at rest before each measurement. In addition, the first five bursts (30 pulses) of hot trials in each series are discarded as cold gas measurements taken between each series of hot trials may allow a slight amount of oil to build up on the electrodes.

Using an RGA, measurements of partial pressures have also been collected after the electrodes have been cleaned by many discharges. Although the RGA data showed a tenfold increase in DC 704 oil levels *immediately* after each burst, the in-

crease in the argon levels due to the propellant flow were measured to be 1000 times larger than the oil levels. This suggests that the oil makes up a very small portion of the mass in the discharge. Although oil level increases were much larger on the first few bursts after long delay without firing, the levels returned to their lower, steady values after only four or five bursts (20-30 pulses). From these observations, we can conclude that after the electrodes have been properly cleaned, the amount of oil residue in the discharge is minimal.

A protocol for performance measurements that are free of contamination effects was developed in light of the above described experiments. It includes the following three guidelines:

1. The LN_2 baffles must be activated for at least 60 minutes before testing in order to reach the correct operating temperature. This ensures that the impulse reaches the correct asymptote.

2. After initial evacuation of the facility or extended times between hot pulses, 1000 pulses should be fired to ensure that the thruster electrodes are clean and the impulse magnitude has reached an asymptote level.

3. Because of the 8 minute break between hot pulses caused by routine cold gas impulse measurements, the first 5 bursts (30 pulses) of a series of 30 bursts should be ignored to ensure uncontaminated impulse measurement.

This protocol was followed for every performance data point reported here and has been verified by comparing similar performance measurements in a cryo-pumped facility (see Appendix B).

5.2.2 Influence of Erosion Products on Performance

Erosion rate measurements conducted at JPL (see Appendix D) have shown that the electrodes, specifically the cathode and spark plug, can erode a significant amount of mass, approximately 0.1-0.2 μg, per discharge. The amount of mass has been shown to be relatively independent of pulse energy and mass bit for the conditions tested here. From pictures taken before and after a 1 million pulse test (see Appendix D), we believe that most of the erosion comes from the stainless-steel spark plug cathode. Unfortunately, during the test the spark plug was effectively welded to the thruster cathode, and an independent measurement of the mass lost during the test could not be made. In many cases, Imacon pictures taken immediately after the capacitors are fully drained show a plume of material being emitted from regions near the spark plug locations. It is very possible that a large fraction of the erosion products do not get swept up in the discharge and, therefore, do not significantly contribute to the impulse.

In PT5, some of spark plug material was observed to be deposited on the anode in locations geometrically opposite from the spark plugs. Due to the large initial mass of the anode, the deposited mass (on the order of micrograms) remained difficult to quantify. The fact that this deposition occurs at all further suggests that the spark plug erosion products may not contribute significantly to the dynamics of the discharge. For PT9, where the spark plugs are slightly smaller and isolated from the thruster circuitry, the measured erosion rates were about half that of the larger Bendix plugs in PT5. For both thrusters the impulse produced by discharging the spark plugs alone was found to be on the same order as the error associated with operating the thrust stand. Still, the erosion of electrode material plays, as yet, an unknown role in GFPPT performance. For that reason and the others mentioned above, the mass of the eroded electrode material was not added to the mass bit for performance calculations. Although including the eroded mass would reduce the efficiency and exhaust velocity by the same amount, the *trends* in performance should remain similar and the calculation of the impulse-to-energy ratio will be unaffected. Experiments are just beginning at EPPDyL that are designed to investigate (and hopefully reduce) the effects of erosion by developing a completely new type of "spark-less" UV photon initiation system.

Now that potentially the largest sources of error have been discussed and procedures for reducing their influence have been developed, we will present the measured performance from PT5 and PT9.

5.3 Measured Performance of PT5

The fifth-generation SRL-EPPDyL GFPPT, PT5, has been described in Section 4.2.1. Although it has gone through many modifications to date, the most important change relates to the discharge initiation circuitry. The effects of an asymmetric discharge on performance, therefore, will be documented before the final database with *symmetric* discharges is presented. The final database includes performance measurements over a wide range of operational parameters including a change in capacitance from 130 to 270 μF.

5.3.1 Effects of Asymmetric Discharge Initiation

Before the final modification to the discharge initiation circuit which solved the asymmetry problem, PT5 exhibited erratic operation where only one, two, or three spark plugs operated simultaneously. This affected the discharge symmetry and, consequently, the impulse. In fact, impulse bit levels are as much as 40% higher when all four spark plugs operate in a symmetric fashion compared to single-plug, asymmetric discharges, as shown from performance measurements taken at JPL in Fig. (5.7).
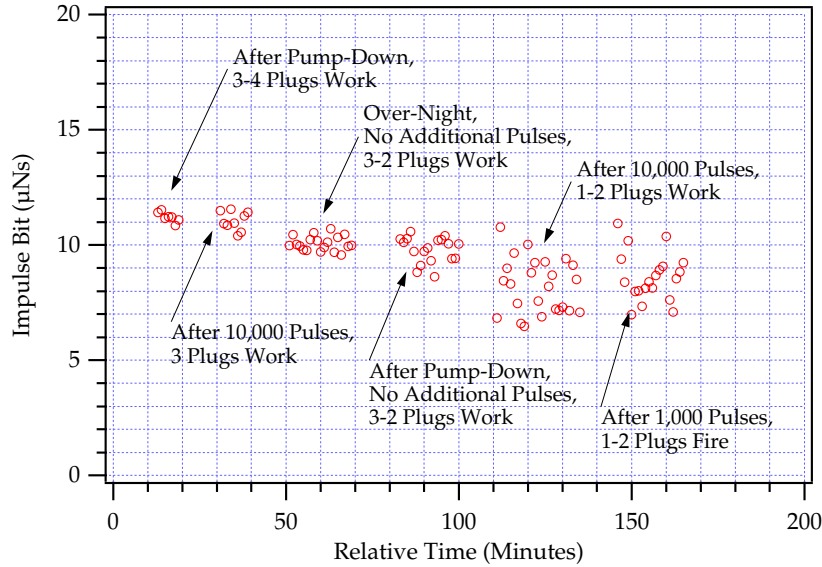
Figure 5.7: Six series of impulse bit measurements from PT5 at constant operating conditions, although the number of operating spark plugs decreases as time goes on. In some cases, the series are also separated by longer breaks as stated.

The Imacon camera with the 500 kHz module was used to photograph the full development of a single discharge. Due to the fast timing of the pulses in a burst, only the first pulse could be captured during one full exposure. It should also be noted that no optical filters were used in these Imacon photographs due to the relatively low intensity of the discharge light. Recent work at EPPDyL has shown that an argon ion band-pass filter allows the current sheet to be seen more sharply in brighter discharges [60]. For all of these trials (except where noted), the pulses were visually very repeatable and a single exposure or a compilation of multiple exposures is a good representation of what is occurring during each discharge at those operating conditions.

PT5 was photographed head-on with the Imacon camera at JPL as shown in Figs. (5.8) through (5.11). As shown schematically in Fig. (5.8), all the pictures show an end view of the anode (center electrode) and the cathode (outer electrode) looking into the discharge chamber. The four spark plugs are mounted orthogonally on the top, bottom, right, and left sections of the cathode to provide a uniform discharge initiation.

Compared to pictures taken at Princeton in Ref. [74], pictures taken during testing at NASA JPL in a cryo-pumped facility showed erratic spark plug operation with three, two, or sometimes only one spark plug firing on each pulse. While both set-ups use the same exact semi-conductor-type spark plugs and propellant
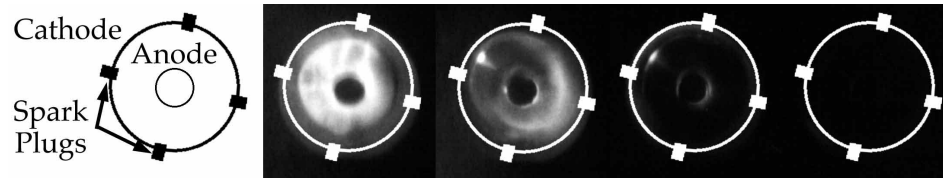
Figure 5.8: Head on Imacon photographs of a PT5 discharge with three spark plugs (top, left, and bottom) working effectively. Each picture progresses 2 μs in time from left to right showing the entire history of one discharge. A white outline is provided to indicate the location of the cathode and spark plugs.

feed systems, data from Princeton showed three spark plugs (top, bottom, and left plugs in this thruster orientation) working consistently. Potentially the cleaner vacuum environment at JPL led to the spark plugs failing as the semi-conductor material between the anode and the cathode was eroded away on each pulse. From tests conducted at EPPDyL, even small amounts of graphite placed between the anode and the cathode of the spark plug led to more frequent breakdowns. It is possible that in the diffusion pumped facility at EPPDyL a small amount of oil vapor condensed on the spark plugs which then helped them break down more easily and consistently.

Figure (5.8) shows the PT5 firing with three spark plugs working. This photograph is from one pulse and shows three important aspects of the discharge dynamics. First, with three out of four spark plugs firing, the discharge is asymmetric and the luminous region moves from the upper-left to lower-right region of the discharge chamber as it evolves downstream. Second, the luminous region appears to have reached the end of the anode by approximately 4 μs after the discharge is initiated, possibly even earlier. This is evident because light is being emitted from *inside* the hollow anode. In this case, the discharge is complete after 6 μs. Third, there is a luminous region near the left spark plug that is glowing very brightly away from the main part of the discharge. This is also seen in other photographs of all the PT5 designs and could be a luminous ejection of hot electrode or spark plug material. The spark plugs were the largest noticeable source of erosion products as mentioned in the previous section.

Figures (5.9) and (5.10) show two diametrically apposed spark plugs firing and two adjacent spark plugs firing, respectively. Although neither initiation pattern produces a completely *uniform* discharge, the discharges are symmetric and asymmetric, respectively. Figure (5.9) is the interlaced combination of two pictures from two different PT5 discharges temporally spaced slightly less than 1 μs apart from each other. In these photos, the discharge reaches the end of the anode 4 μs after the spark plug fired, and the discharge is basically complete after 5 μs. Figure (5.10) also shows the discharge reaching the end of the anode and extinguishing at nearly

Figure 5.9: PT5 thruster discharge with only two spark plugs (top and bottom) working effectively. Each picture progresses 1 μs in time from left to right with 1 μs between the right-most top row picture and the left-most bottom row picture. A white outline is provided to indicate the location of the cathode and spark plugs.

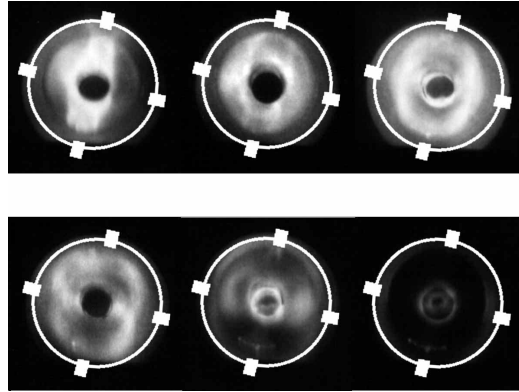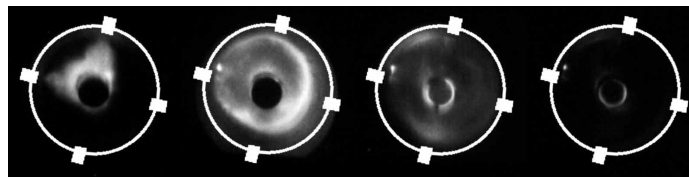

Figure 5.10: PT5 thruster discharge with only two spark plugs (top and left) working effectively. Each picture progresses 2 μs in time from left to right. A white outline is provided to indicate the location of the cathode and spark plugs.

Figure 5.11: PT5 thruster discharge with only one spark plug (top) working effectively. Each picture progresses 2 μs in time from left to right. A white outline is provided to indicate the location of the cathode and spark plugs.
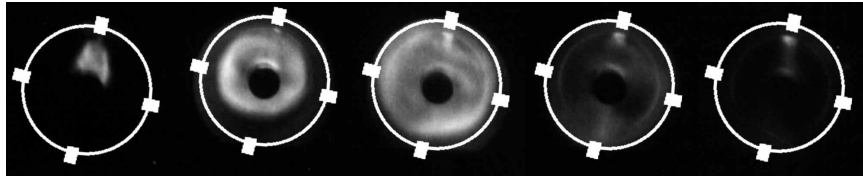
the same time as in the case of a discharge with three spark plugs working effectively. There is also the indication of hot electrode material being emitted after the discharge near the left spark plug.

The photograph in Fig. (5.11) has two major differences compared to those of the other non-uniform discharges. First, the discharge does not appear to reach the end of the anode before it is extinguished because there is no light emitted from inside the anode. This would indicate a reduced current sheet speed in the axial direction. Second, the discharge illumination lasts longer as the final frame at 8 μs after initiation still shows a slight glow. This indicates a slower discharge of the capacitor which could be caused by a higher resistive load on the circuit. This picture also shows a glowing region well into the discharge although it is near the top spark plug instead of the left spark plug.

During testing at JPL, the discharge initiation pattern and the number of working spark plugs were visible to the naked eye during performance measurements. These observations, when combined with impulse data, imply that one-plug and some two-plug initiations provide a reduced performance than those initiations occurring with three or four spark plugs working effectively, as shown in Fig. (5.7). This trend also agrees with asymmetric discharge performance data taken at Princeton.

This problem has subsequently been corrected with a new design of the discharge initiation circuit that distributes the power to the spark plugs more effectively [75]. As discussed in Section 4.2.4, each spark plug now has its own local energy source that is protected by a diode. When one plug fires, it is no longer allowed to drain the energy away from the other spark plugs. The new circuit has demonstrated its ability to consistently produce a symmetric discharge in tests at Princeton. A series of Imacon photographs of PT5 with the new DI circuitry are shown in Fig. (5.12) with the resulting discharge symmetry. The pictures also show that the discharge reaches the end of the anode uniformly between 3-4 μs, and that all the spark plugs continue to glow after the pulse is over, possibly indicating spark plug erosion after the discharge.

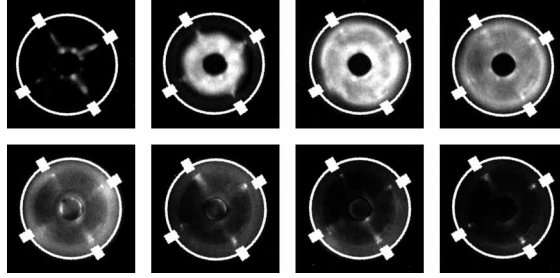New methods for initiating GFPPT discharges without spark plugs are cur-

Figure 5.12: Unfiltered Imacon Fast-Framing Camera photos of a typical PT5 discharge looking straight into the discharge chamber using 0.5 μg argon and 4 J of energy per pulse. The photos seen here are spaced by 1 μs going from left to right and then top-right to bottom-left. A white outline is provided to indicate the location of the cathode and spark plugs.

rently under development at EPPDyL. In all the performance measurements shown in the next section, however, the current configuration where all four spark plugs fire simultaneously will be used as an effective discharge initiator.

5.3.2   Effects of Varying Mass Bit, Energy and Capacitance

Two energy levels for each of two capacitance values were tested over ten different mass bits yielding a 40-point GFPPT performance database. Six graphs in Figs. (5.13), (5.14) and (5.15) show PT5 performance as a function of mass bit and exhaust velocity with the capacitance and the initial stored energy level as parameters. The lines between the data points are simple fourth order polynomial curve fits meant to show overall trends apparent in the data. This representation, however, is not necessarily the correct functional form to the data. The coefficients for the curve fits are not shown here for that reason.

The graphs in Fig. (5.13) show the impulse bit and exhaust velocity as a function of mass bit for each configuration of PT5. In general, the exhaust velocity decreases monotonically with increasing mass bit while the impulse bit shows nearly the opposite trend. At a given mass bit, both the impulse bit and exhaust velocity increase as the capacitance and discharge energy increase. Near 0.5 μg there appears to be a transition between a region where the impulse bit is nearly constant and the exhaust velocity decreases rapidly to a region where the impulse bit increases and the exhaust velocity only slightly decreases.

From the graphs in Fig. (5.14), the same transition is seen to exist in the efficiency and impulse-to-energy ratio data. As the mass bit increases, the efficiency decreases to an asymptote level that depends both on energy and capacitance. For the larger capacitance configurations, the efficiency levels off at a mass bit near

Figure 5.13: PT5 performance with argon propellant at various capacitance, energy, and mass bit values. The dotted vertical lines show the boundary between Mode I and Mode II operation, as discussed in Section 5.3.3.

Figure 5.14: PT5 performance with argon propellant at various capacitance, energy, and mass bit values. The dotted vertical lines show the boundary between Mode I and Mode II operation, as discussed in Section 5.3.3.
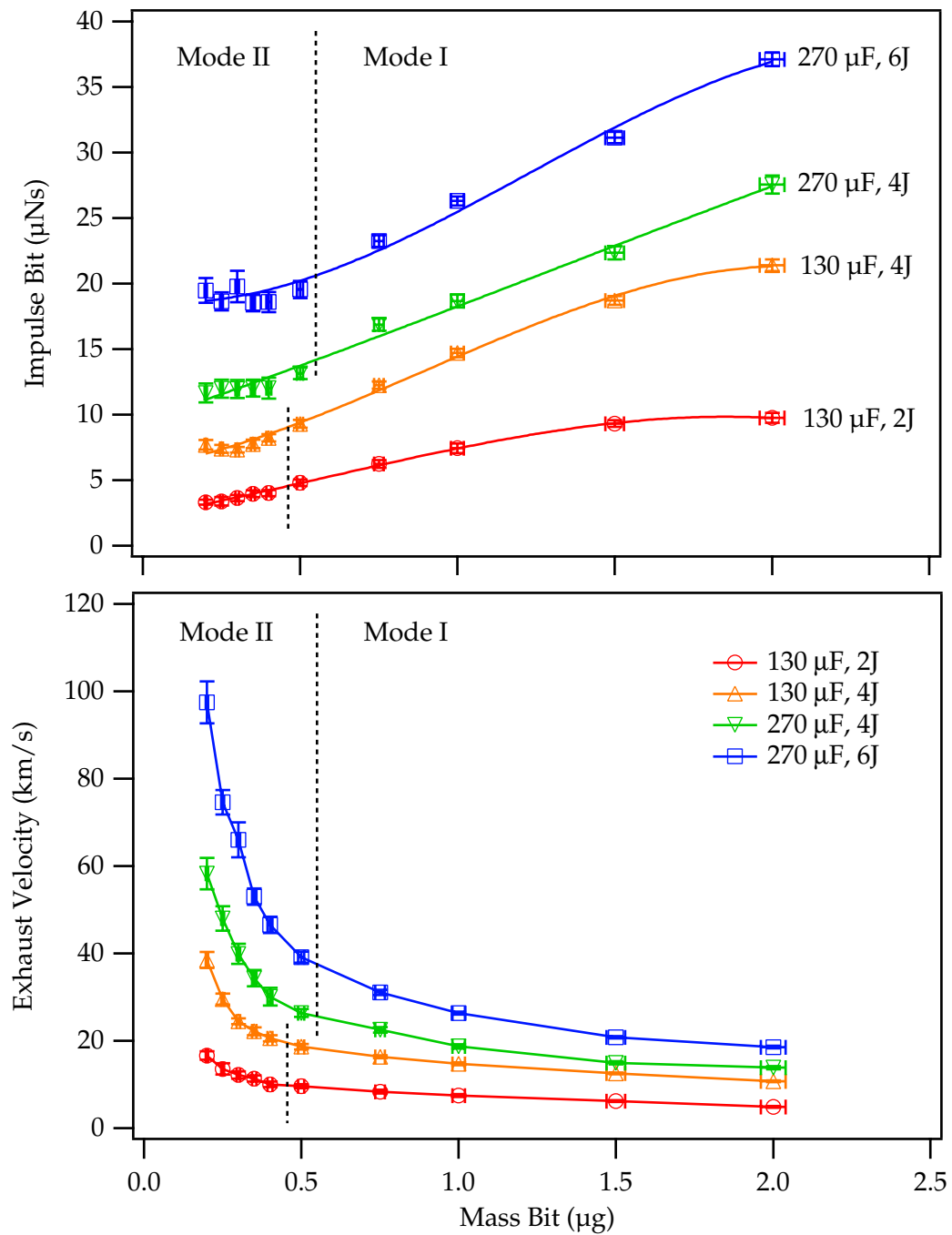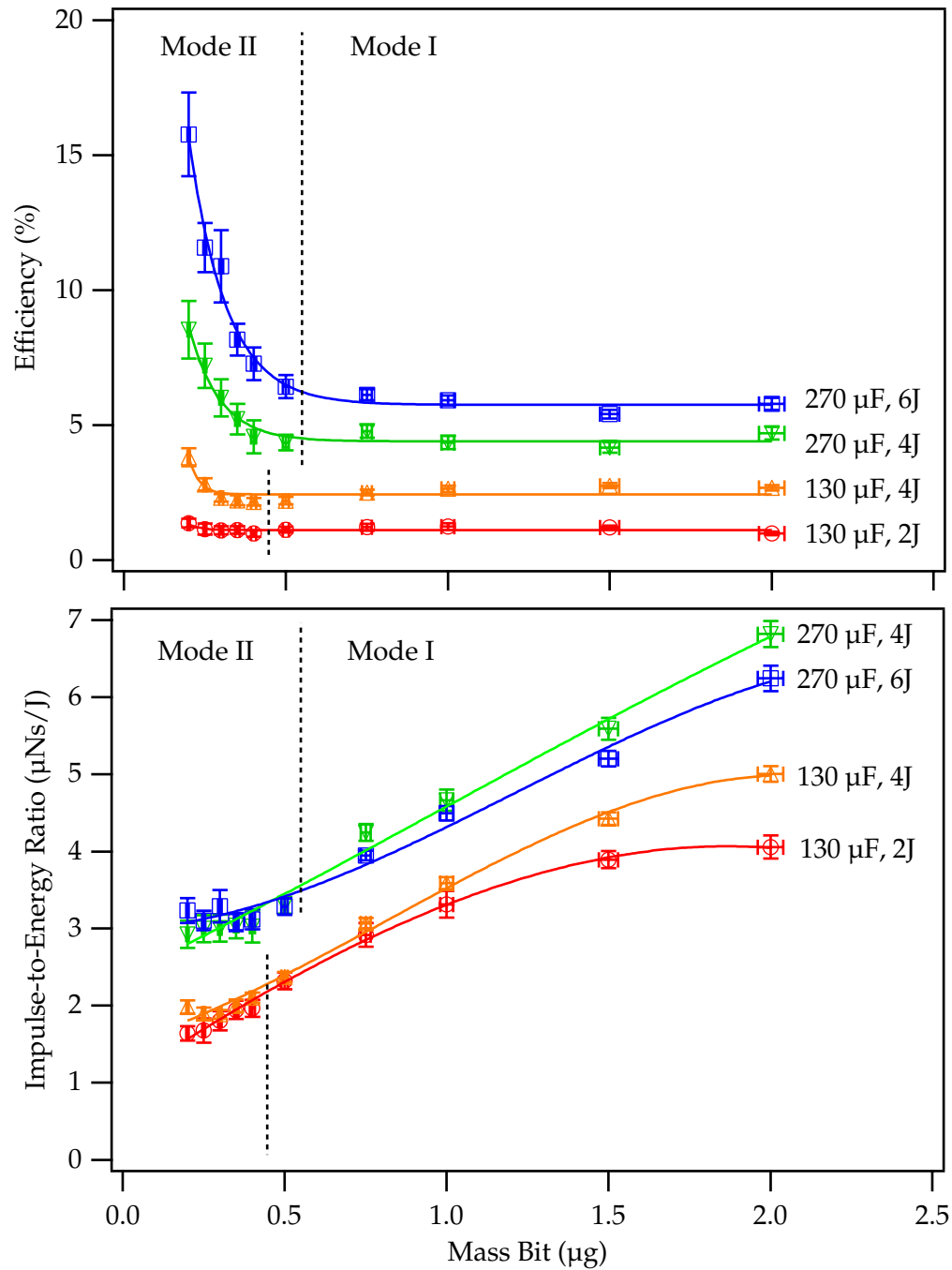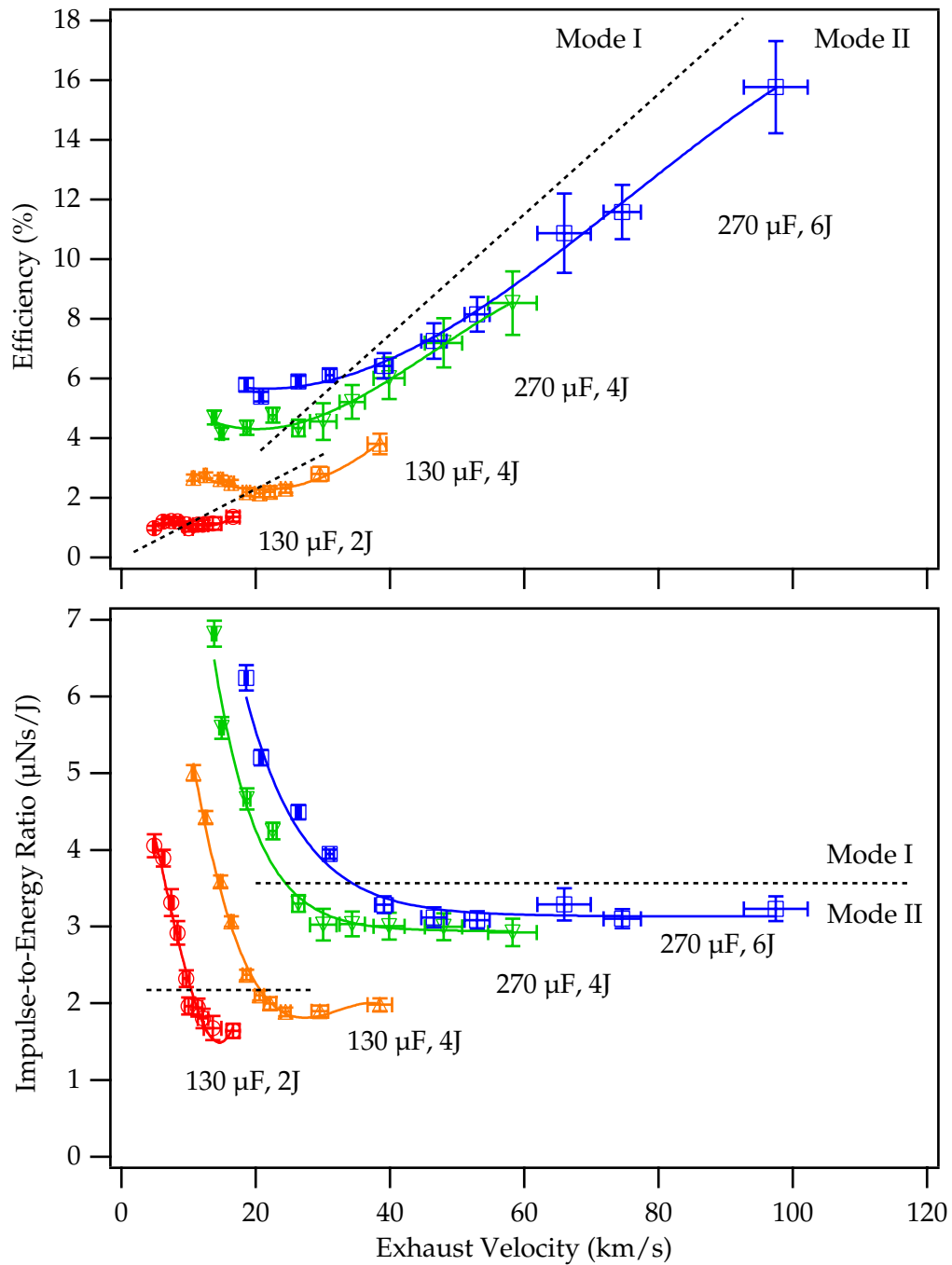
Figure 5.15: PT5 performance with argon propellant at various capacitance, energy, and exhaust velocity values. The dotted vertical lines show the boundary between Mode I and Mode II operation, as discussed in Section 5.3.3.

0.5 μg per shot. For the lowest energy and capacitance, 2 J and 130 μF, the efficiency is almost constant over all mass bit values. For the highest energy and capacitance, 6 J and 270 μF, the efficiency increases very rapidly as the mass bit decreases below 0.5 μg. The highest energy, highest capacitance, and lowest mass bit have the highest thruster efficiency.

The impulse-to-energy ratio is fairly constant and *independent* of energy within the error bars below about 0.5 μg. The impulse-to-energy ratio increases by a factor of approximately 1.4 for a slightly more than doubled value of capacitance. At the higher mass bit values the impulse-to-energy ratio increases with increasing mass bit and is dependent on both the capacitance and energy level. When plotted versus exhaust velocity in Fig. (5.15), the largest mass bit value corresponds to the smallest value of exhaust velocity. As the exhaust velocity decreases, the impulse-to-energy ratio is seen to increase rapidly after some transition point that appears to change slightly with capacitance and energy.

The opposite trend is true from the plot of efficiency versus exhaust velocity: *above* a certain exhaust velocity value the efficiency increases rapidly. From both plots, when the efficiency is increasing rapidly, the impulse-to-energy ratio is fairly constant and vice versa. In the 130 μF data sets, the efficiency is seen to increase, decrease, and then increase again as the exhaust velocity is increased. The second inflection point in the data, once again, marks the transition between two trends in this data set. These two operational modes of PT5 that are apparent in all the plots of performance will be explored further in the next section.

5.3.3 Operational Modes in PT5

We will distinguish the two operational modes of PT5 identified in the previous section as simply Mode I and Mode II. Mode I includes the larger mass bit values and is characterized by a relatively constant efficiency that is independent of mass bit and exhaust velocity. The impulse bit and impulse-to-energy ratio in Mode I are monotonically increasing functions of mass bit. Mode II includes the smaller mass bit values and is characterized by an increasing efficiency with decreasing mass bit. The impulse bit and impulse-to-energy ratio in Mode II are relatively independent of mass bit and exhaust velocity. The characteristics of Mode I and II are summarized in Table (5.1). It should be noted from all the PT5 performance data that the transition between Mode I and Mode II is somewhat gradual. In this section, we will examine the operational modes in more detail using experimental data and try to determine a more specific criteria for the transition point.

To investigate the dependence of the transition point on energy, four experiments with two values of mass bit and capacitance were performed over a range of energy levels. The mass bit values, 1.0 and 0.3 μg, were chosen to fall in the middle of Mode I and Mode II operation, respectively. As shown in the top graph of

Performance	Mode I		Mode II	
Indicator	$\uparrow m_{bit}$	$\uparrow \bar{u}_e$	$\uparrow m_{bit}$	$\uparrow \bar{u}_e$
I_{bit}	$\uparrow$	$\downarrow$	const.	const.
$\bar{u}_e$	$\downarrow$	$\uparrow$	$\downarrow$	$\uparrow$
η_t	const.	const.	$\downarrow$	$\uparrow$
I_{bit}/E	$\uparrow$	$\downarrow$	const.	const.

Table 5.1: Characteristics of Mode I and II as a function of increasing mass bit and exhaust velocity.

Fig. (5.16), in all four cases the impulse bit varies linearly with the energy suggesting a constant impulse-to-energy ratio. When this data set is combined with the rest of the PT5 performance database as shown in the bottom graph of Fig. (5.16), some important trends can be observed:

1. The impulse-to-energy ratio is nearly constant over different energy levels *regardless* of mass bit, capacitance, or the operational mode.

2. In Mode I, the impulse-to-energy ratio increases with mass bit, while in Mode II, it is fixed. The mode of operation does not change significantly with energy.

3. The impulse-to-energy ratio for the 270 μF configurations is higher than the 130 μF configurations by nearly a factor of $\sqrt{2}$ over *all* conditions.

It is also interesting to note that the range of mass bit values for the two modes changes with capacitance. For the 130 μF configuration, the impulse-to-energy ratio clusters around a single value ($\approx 2\mu$Ns/J) from 0.2-0.4 μg. For the 270 μF configuration, the impulse-to-energy ratio clusters around a single value ($\approx 3\mu$Ns/J) over a slightly larger range of mass bit values from 0.2-0.5 μg.

This clustering trend can also been seen in a graph of impulse bit plotted as a function of $\int J^2 dt$ as shown in Fig. (5.17). In each configuration, at the lower mass bit values (Mode II) the impulse bit and $\int J^2 dt$ are nearly constant within the error of the measurements. As the mass bit increases to Mode I operation, *both* the impulse bit and $\int J^2 dt$ increase linearly together. The peak current in the discharge also increases a large amount (nearly a factor of three in many cases) as the mass bit is increased in Mode I operation. Although the general trend of $\int J^2 dt$ monotonically increasing with peak current should be expected, the duration of the discharge must be getting shorter since the $\int J^2 dt$ increases only *linearly* with the peak current. In any case, the clustering in the data from Mode II operation is apparent and can be used to determine the transition between the two modes.

In a more objective approach to determining the transition point, we examine the $\int J^2 dt$ and peak current as functions of mass bit. As shown in Fig. (5.18), in
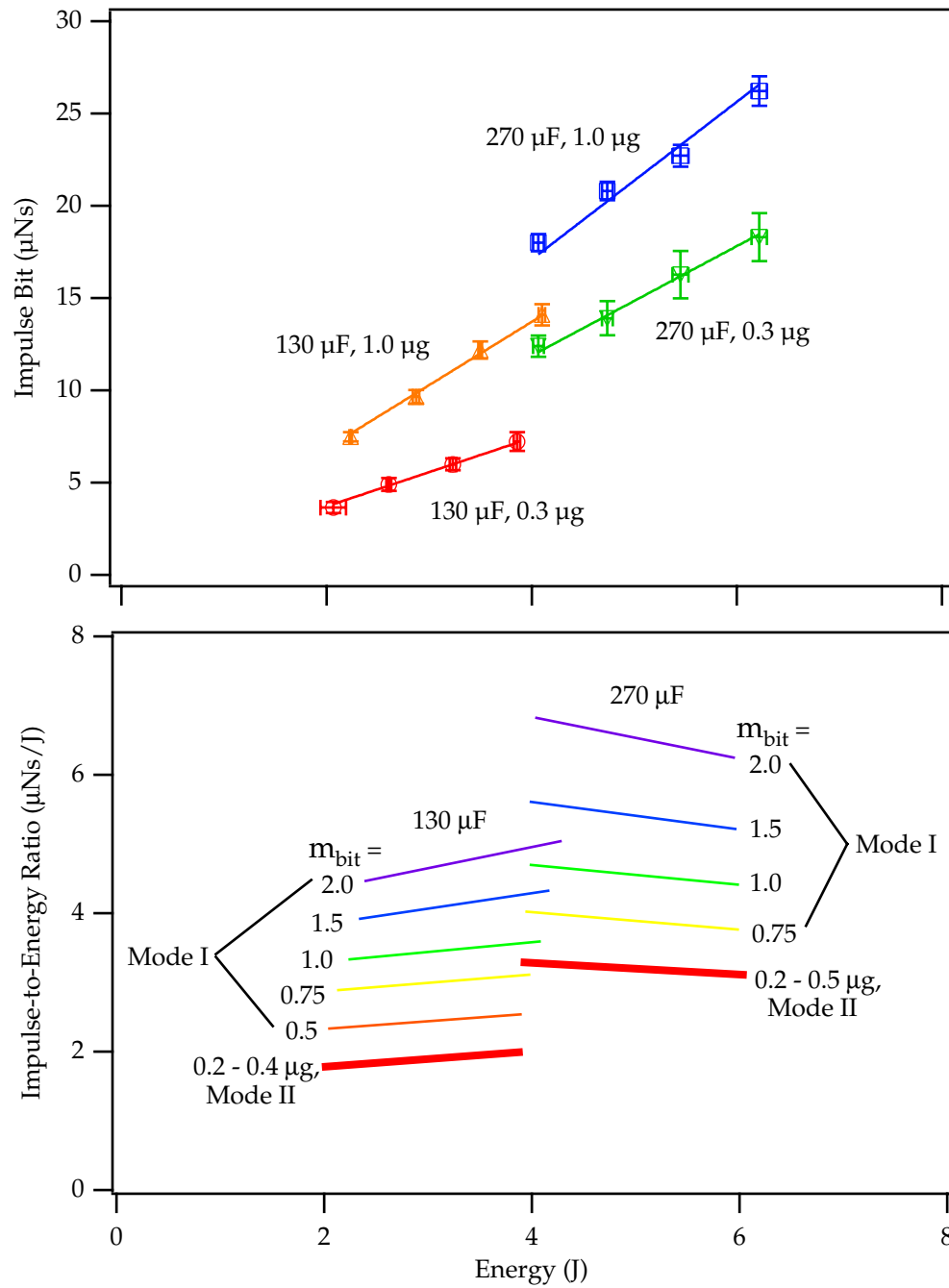
Figure 5.16: PT5 impulse bit as a function of energy per pulse and peak current as a function of mass bit with argon propellant.
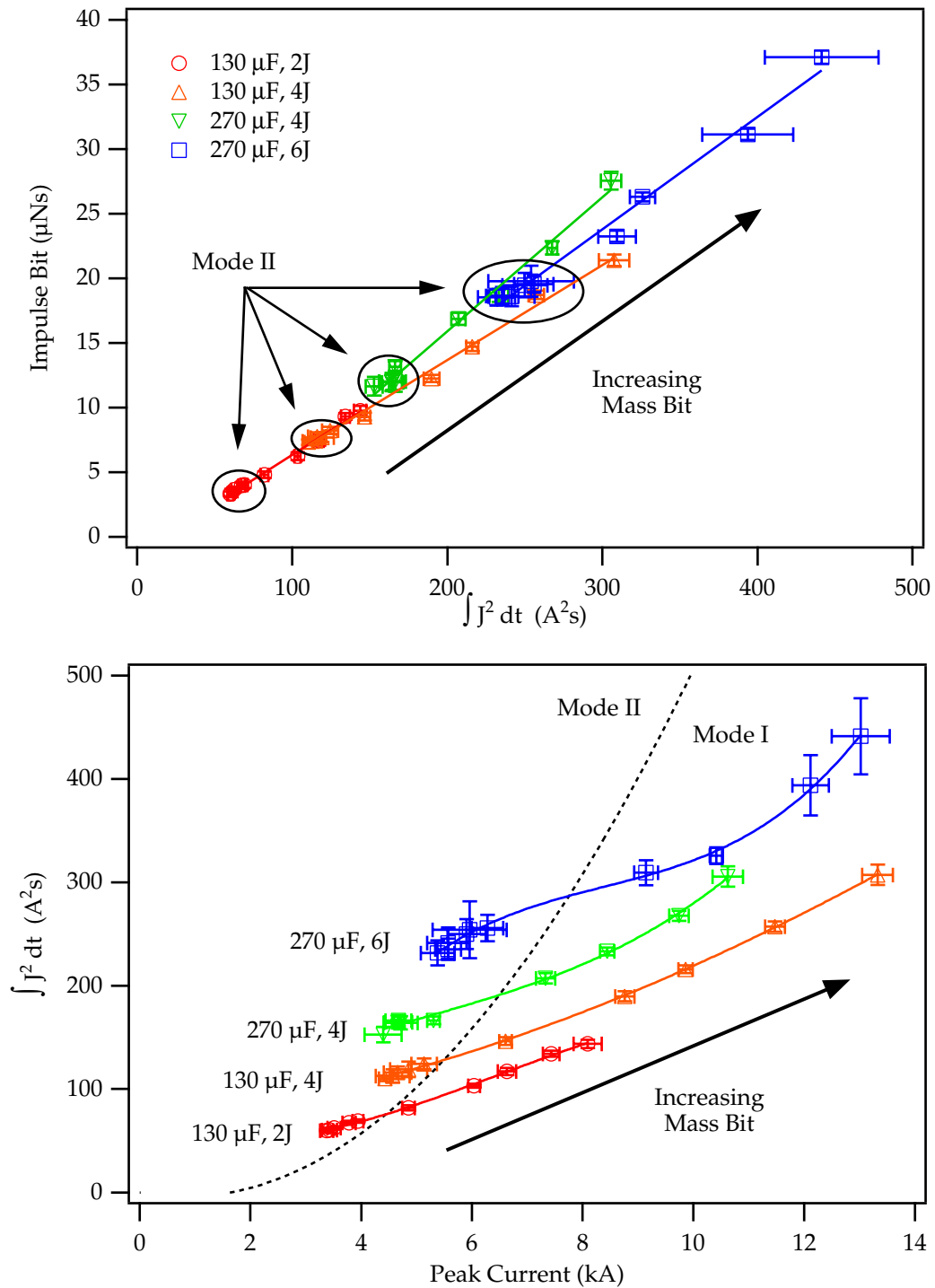
Figure 5.17: Graphs of the impulse bit as a function of the integral of the current squared and the same integral as a function of peak current. The data for all configurations clusters together in Mode II operation. A line on each graph shows the trend of increasing mass bit.
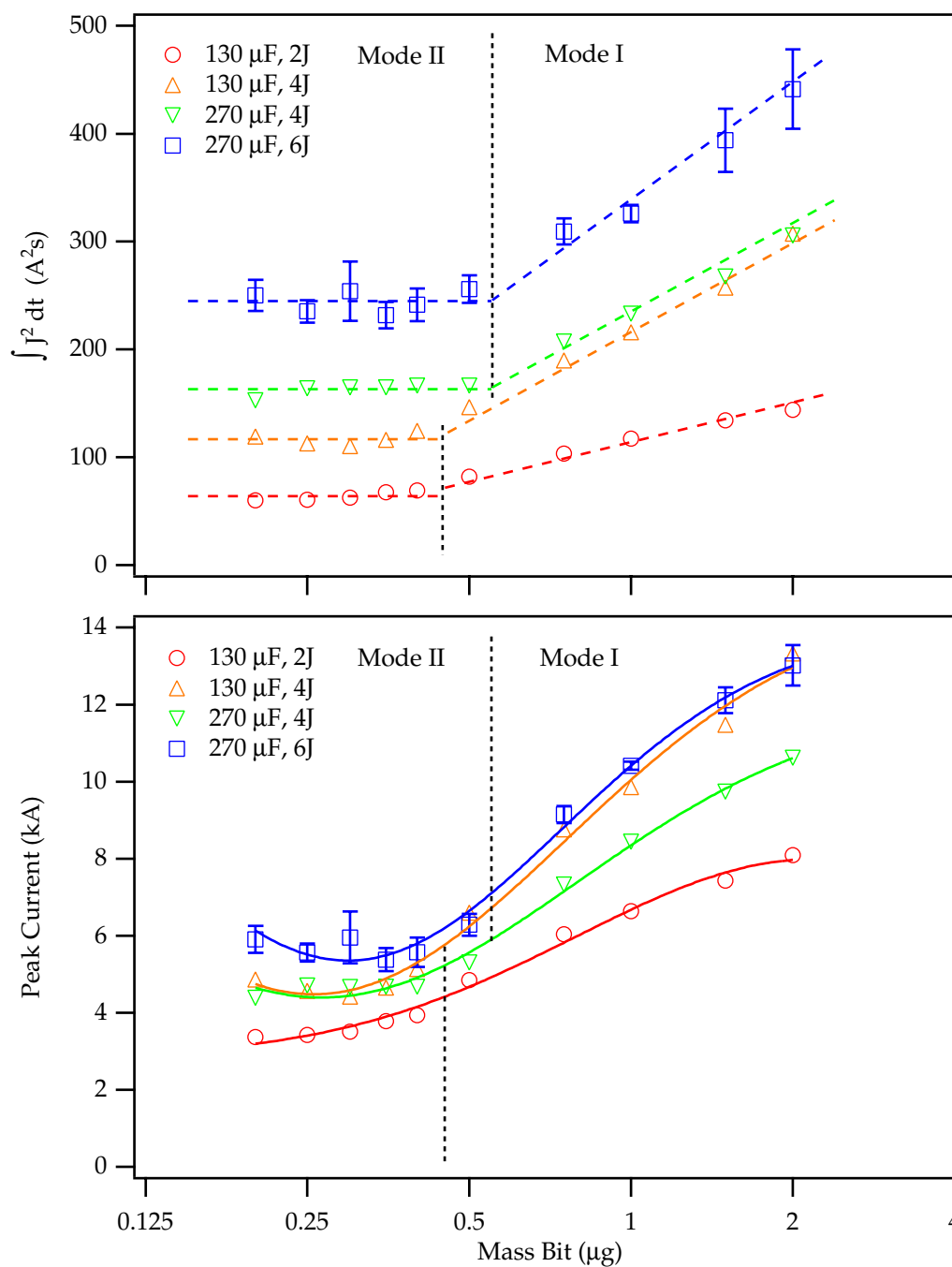
Figure 5.18: Graphs of the integral of the current squared and the peak current as functions of mass bit. The error bars for each point are approximately the same size as the marker except where noted.

Mode II all the data points fit (within the error of the measurement) to a single average value of $\int J^2 dt$ that increases with both capacitance and energy. The next higher mass bit value does not conform to this average value, instead showing a larger $\int J^2 dt$ that scales linearly with mass bit. In Mode I operation, the integral of the current squared appears to be more dependent on the energy and not the capacitance since the two 4 J cases have nearly similar values.

The peak current also remains nearly constant in Mode II and increases monotonically with increasing mass bit in Mode I. Although the peak current should increase as the mass bit increases due to the reduction in discharge velocity, the rate at which the peak current increases is not consistent with the rest of the data set. As shown in Fig. (5.13) the exhaust velocity decreases only slightly in Mode I operation. Therefore, we would expect that the dynamic load on the circuit from the changing impedance of the current sheet would not change to a large extent in Mode I. Certainly it should not change nearly as much as would be expected in Mode II where the exhaust velocity increases rapidly with decreasing mass bit. Also, it appears the peak current does not depend on capacitance in Mode II, but it does depend on the energy. In Mode I operation the peak current increases with increasing mass bit and depends on both the capacitance and energy. In fact, the 130 μF, 4 J configuration has a *higher* peak current than the 270 μF, 4 J configuration. Since the initial voltage on the capacitor bank is much higher for the 130 μF case, this suggests that the effective circuit impedance is decreasing significantly in Mode I. More discussion of the operational mode transition point as well as how the performance scaling compares to the models developed in Chapter 3 will be presented in the next chapter. We now turn to experiments with PT9 where we test the effects of a variable inductance-per-unit-length.

5.4   Measured Performance of PT9

The ninth-generation SRL-EPPDyL GFPPT, PT9, has been described in Section 4.2.2. PT9 uses 10 cm long parallel plates with various widths and gaps to change the inductance-per-unit-length which should affect the performance as described in Chapter 3. Originally PT9 used pyrex sidewalls to provide optical access and contain the discharge between the electrodes. It was soon discovered, however, that the performance with the sidewalls was not as high as expected and, in fact, showed almost no effect from changing the inductance-per-unit-length. Tests were conducted using both helium and argon propellants to determine the influence of molecular weight with and without the sidewalls. It was found that for argon, especially at low mass bits, the performance dramatically improved when the sidewalls were *removed*. The final database includes performance measurements from PT9 without sidewalls with argon propellant over a wide range of operational parameters including changes in inductance-per-unit length.

5.4.1 Effects of Sidewalls on Parallel Plate Performance

At first thought, the idea of using sidewalls to contain the discharge and direct the plasma seemed appropriate. Performance measurements with and without sidewalls, however, show that the impulse bit and exhaust velocity are *reduced* by the presence of sidewalls. This is especially true for the lowest mass bits where the sheet velocity is the highest. Conversely, and more so with helium, the performance at higher mass bits improves with sidewalls.

First, we begin by showing performance of PT9 with pyrex sidewalls using argon propellant at 4 J per pulse in Fig. (5.19). In these graphs the behavior is very similar to that seen in PT5 with two modes of operation and a transition near 0.5 μg per pulse. This transition, however, is at a much lower exhaust velocity (about 5 km/s) than the 130 μF, 4 J case from PT5 (about 18 km/s). Once again there is an inflection point in the efficiency curve occurring at an exhaust velocity value near 8 km/s. Below this point the efficiency increases linearly with the exhaust velocity at a relatively large impulse-to-energy ratio of 3.8 μNs/J. Then at larger exhaust velocities, it also increases linearly with exhaust velocity, but at a lower value of impulse-to-energy, 1.5 μNs/J. Another important point to notice is that the efficiency *does not change* with a two-fold increase in inductance-per-unit-length as would be expected from the performance scaling relations developed in Chapter 3. In fact, in both cases of PT9 (130 μF, 4 J), the performance is very similar to the 130 μF, 4 J configuration of PT5. As this performance level was much lower than expected, many possibilities were investigated including using a different propellant and not using sidewalls at all.

Figure (5.20) shows the impulse bit measured from PT9b (1″ by 1″, 3.9 nH/cm) with and without sidewalls using both argon and helium. It is clear that using helium propellant with the sidewalls gives a higher impulse than using argon with the sidewalls. This trend is reversed in the impulse measurements without the sidewalls. The amount of the difference depends on the mass bit and propellant type. For argon, there is a very large ($>$ 150%) benefit at the smallest mass bits (highest exhaust velocities) from removing the sidewalls. At the largest argon mass bits there is less of a benefit. For helium there is a small benefit from removing the sidewalls at the lowest mass bit; however, the impulse bit actually increases for helium when the sidewalls are added above 0.5 μg per shot.

Figure (5.21) shows the efficiency and impulse-to-energy ratio of PT9b with and without sidewalls, again using both argon and helium for propellant. The *trends* in the data depend more on the presence or absence of sidewalls rather than the propellant type. With sidewalls, the trends are very similar in character to those measured with PT5. At lower exhaust velocities, the efficiency is constant and the impulse-to-energy ratio decreases with increasing exhaust velocity. At higher exhaust velocities the efficiency increases linearly and the impulse-to-energy begins to reach an asymptote. Compared to argon, helium has a larger efficiency
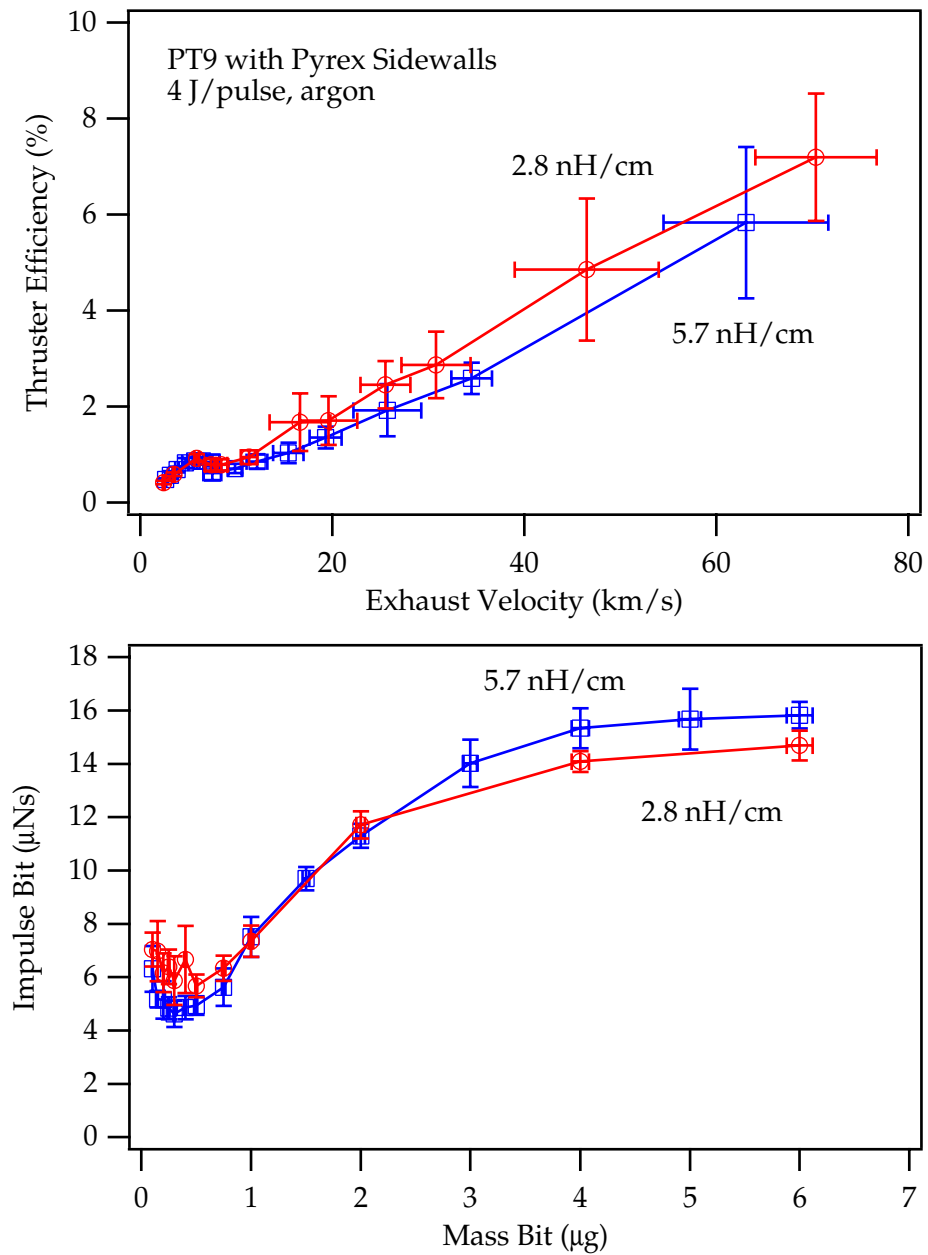
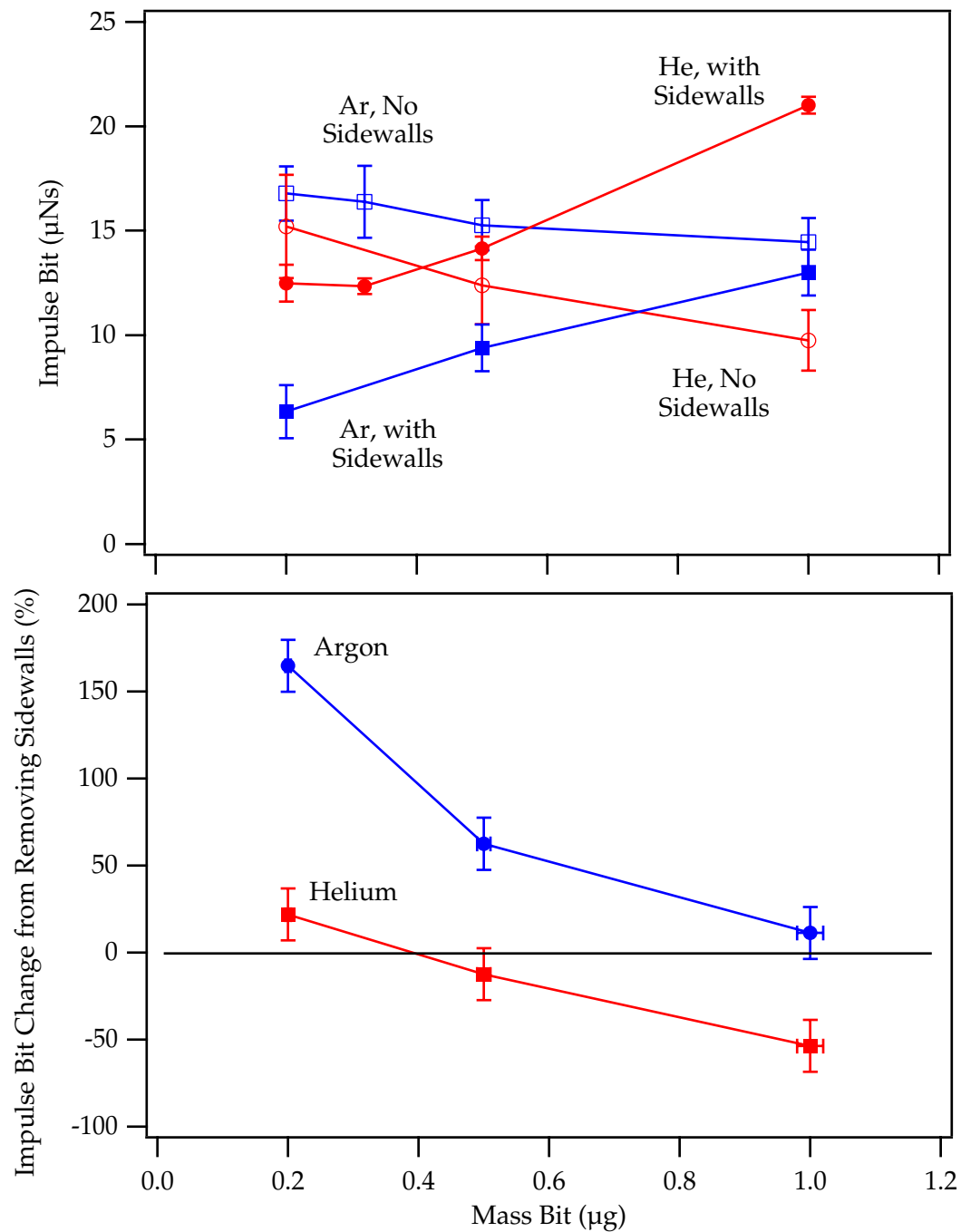Figure 5.19: PT9 performance with pyrex sidewalls and two different aspect ratios.

Figure 5.20: A comparison of PT9b impulse bit measurements with and without sidewalls using both argon and helium for propellant.
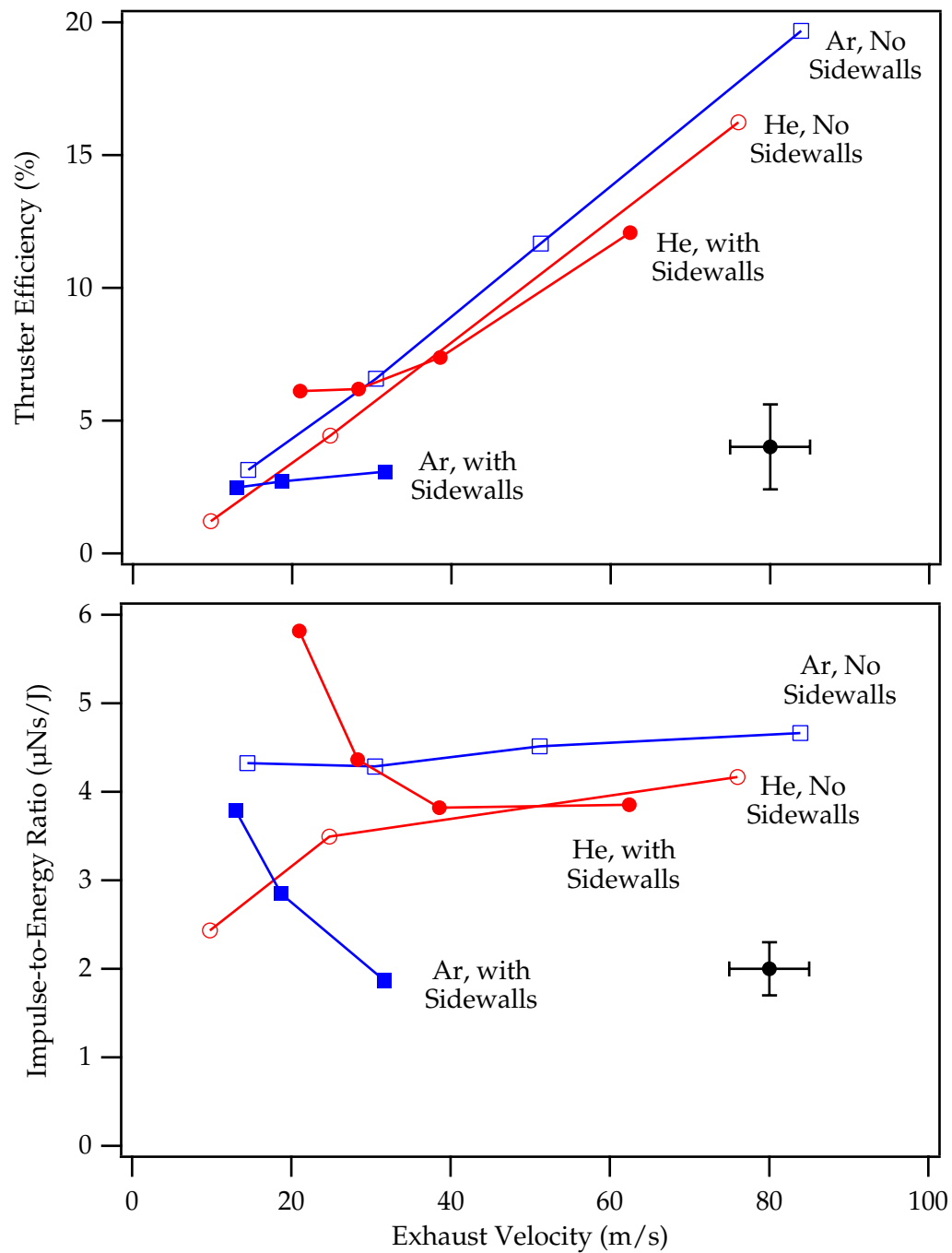
Figure 5.21: PT9b performance with and without sidewalls using both argon and helium for propellant. A characteristic error bar is shown for each plot.

and impulse-to-energy ratio by close to a factor of 2.5 at the same exhaust velocity. Without sidewalls, the performance shows different trends. With both argon and helium the efficiency increases linearly with exhaust velocity and the impulse-to-energy ratio remains relatively constant. In this case, the argon performance is consistently higher than the helium performance. Furthermore, the argon performance without the sidewalls is significantly better than with the sidewalls over all exhaust velocity values. This is not the case for helium where the performance is similar at higher exhaust velocities and actually better *with* the sidewalls at lower exhaust velocities.

These results suggest that two trends are competing depending on the mass bit and molecular weight. It appears that for both argon and helium, as the mass bit (and pressure) increases, the sidewalls may actually help to focus the exhaust stream and the performance improves. This is more the case for helium which has a larger thermal velocity for the same plenum temperature. Since the pulse rate was kept constant with both propellants, the propellant utilization efficiency may be much lower with helium, especially without the sidewalls. In that case, a significant amount of helium may escape out of the electrode volume and not be accelerated by the discharge at all. For argon, the time between pulses is not long enough for a significant fraction of the propellant mass to escape the discharge chamber. Without the sidewalls, the current sheet is not slowed down by the interaction with an insulator surface, and the performance improves. With the sidewalls, some of the ions moving at sheet speed will diffuse to the surface and recombine, effectively slowing to a much smaller thermal velocity determined by the sidewall temperature. This kind of interaction would have the greatest influence at the highest sheet velocities, which agrees with our data set.

Ion diffusion to the walls has been suspected before as a significant loss mechanism in magnetic shock tubes [87] and plasma guns [97]. Furthermore, if the current is carried at all by the ions in these kind of discharges, then the cathode surface could also be retarding the bulk motion of the current sheet. Regardless of the physical nature of the retarding force, the negative effect for argon of having any extra surface area[2] exposed to the discharge is extremely apparent. For that reason, it was decided that the performance of PT9 was best measured again *without* sidewalls.

5.4.2 Effects of Varying Mass Bit and Inductance-per-unit-length

Without sidewalls, PT9 behaves very differently. First, the propellant utilization is slightly less than unity because a small fraction of the propellant escapes from the *sides* during propellant injection. Second, although the tops of the electrodes are

---

[2]It is interesting to note that in the cases with sidewalls (performance shown in Fig. (5.19)), both PT9 with 2.8 nH/cm and PT9 with 5.9 nH/cm have the *same* surface area.

insulated by pyrex, the sides of the electrodes are not due to the likely contact with the discharge and the possibility of erosion. This open geometry can sometimes allow spurious arcs, and, in general, more electromagnetic interference (EMI) that can influence the performance and decrease the repeatability of the measurements. Since the error in a given measurement is mainly based on the repeatability, the errors in the PT9 performance measurements are larger than those found in PT5 data. In addition, current measurements from the derivative of the voltage trace proved to be especially prone to EMI and had >25% error in some cases.

Changing the inductance-per-unit-length had a very noticeable effect on performance. In Fig. (5.23) thruster performance is shown as a function of mass bit. No sharply distinct modes of operation are apparent as in the data from PT5. Instead, as seen from Fig. (5.24), the efficiency increases monotonically with exhaust velocity and the impulse-to-energy ratio remains relatively constant. At the lowest mass bits, the trend in both efficiency and impulse-to-energy ratio appears to be in a linear relation to the inductance-per-unit-length values presented in Section 4.2.3 for PT9. Perhaps the configuration with the highest surface area to volume ratio, PT9a, has a slight "two mode" character as seen in PT5. The increase in impulse-to-energy ratio at lower exhaust velocity, however, is not as pronounced as in PT5. Again, the error bars in this plot are relatively large, but trends in the average performance (as shown by the curve fits) are significant.

In the next chapter, we will examine the entire performance database with both PT5 and PT9 in more detail. We will compare the measurements to the previously developed models in order to obtain experimentally verified scaling laws.
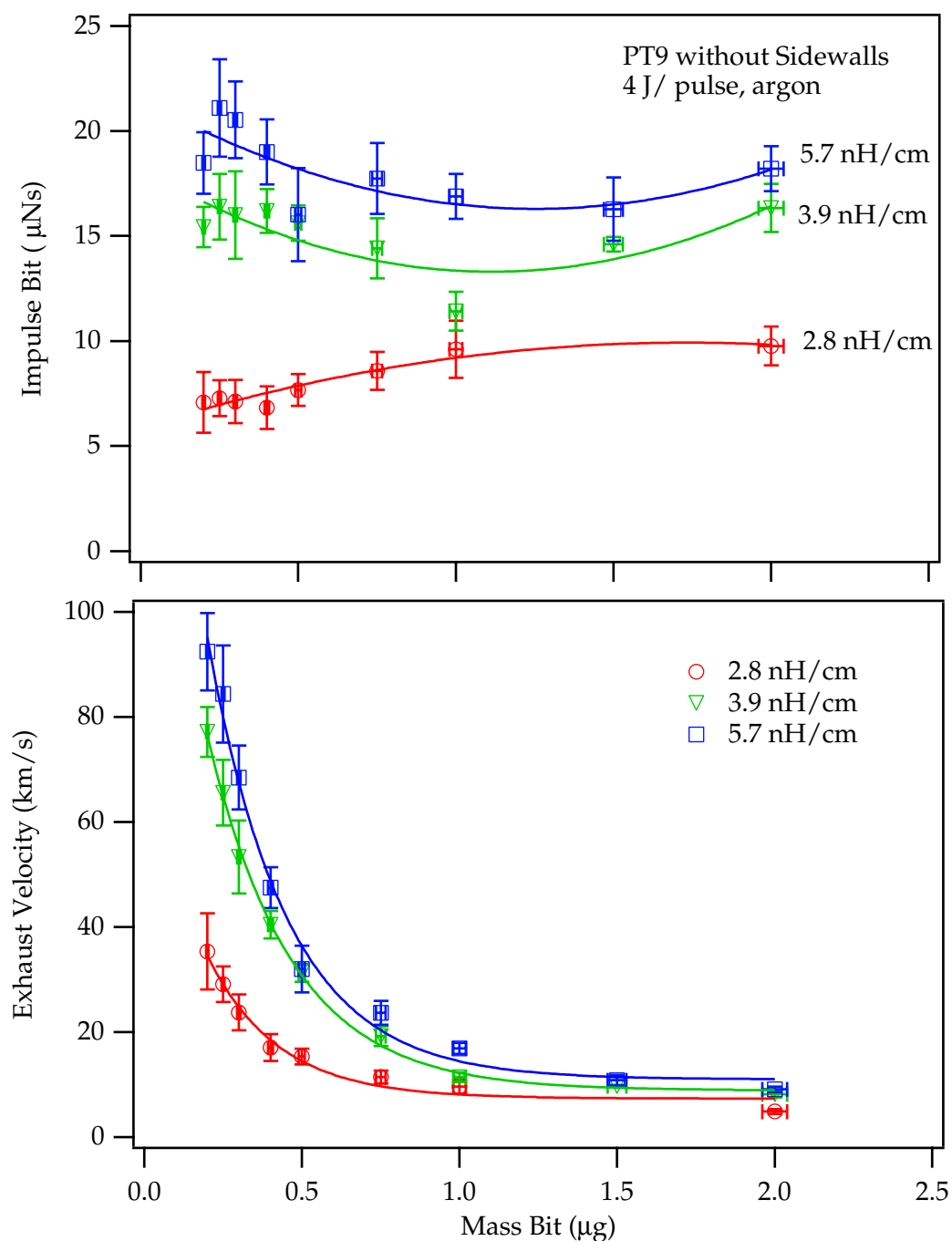
Figure 5.22: Thruster impulse bit and exhaust velocity as a function of mass bit for PT9, 130 μF, 4 J, and with three different inductance-per-unit-length values.
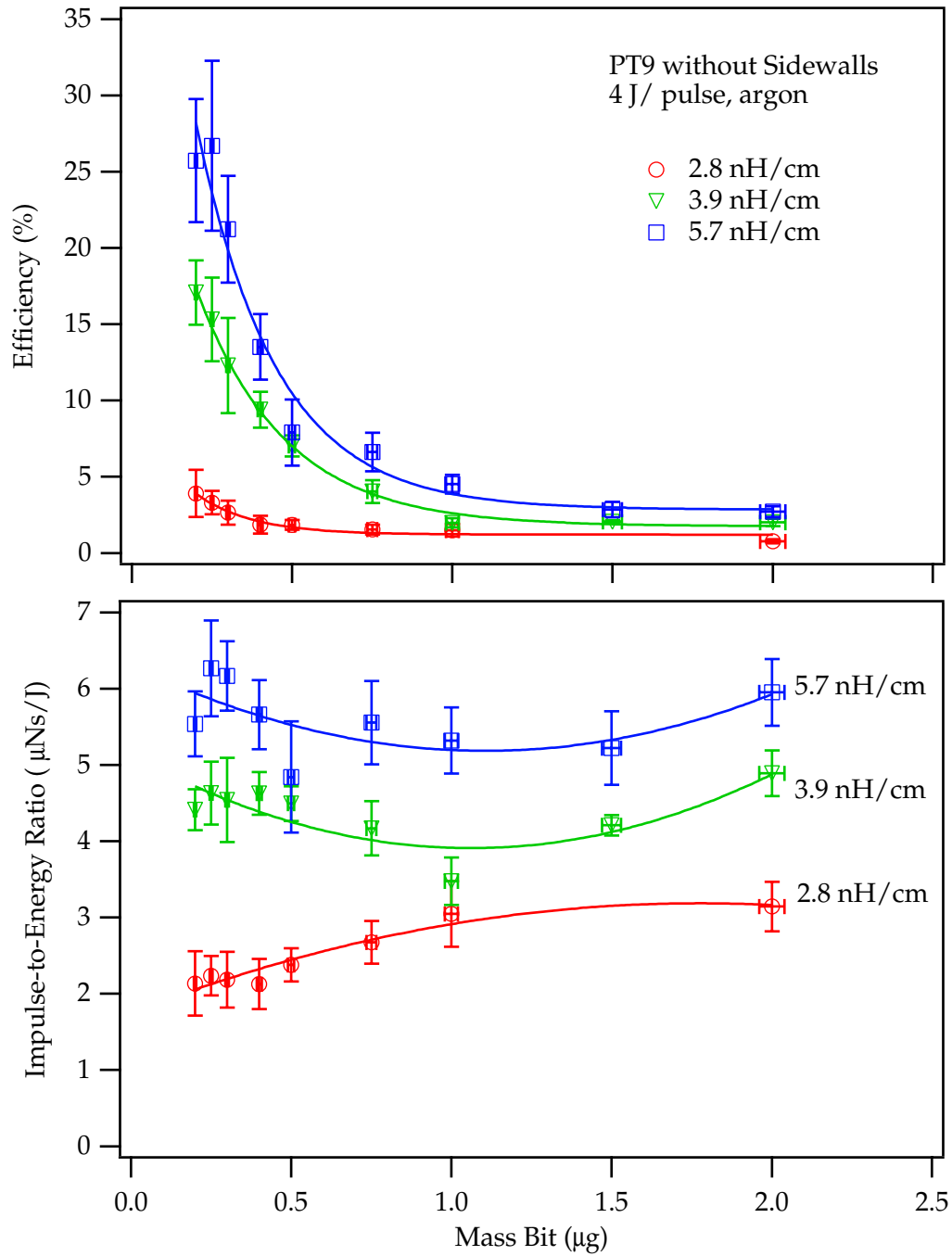
Figure 5.23: Thruster efficiency and impulse-to-energy ratio as a function of mass bit for PT9, 130 μF, 4 J, and with three different inductance-per-unit-length values.
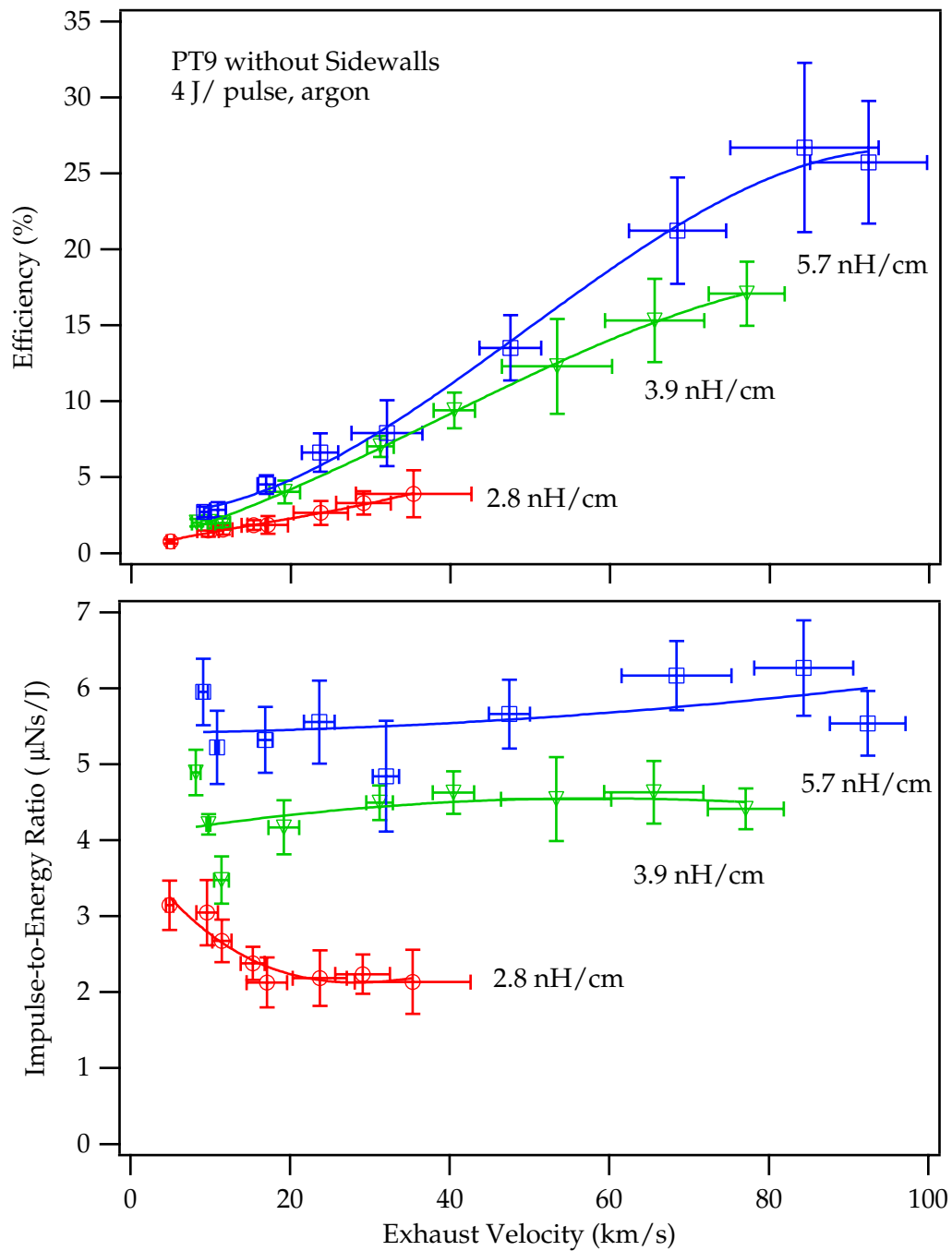
Figure 5.24: Thruster efficiency and impulse-to-energy ratio as a function of exhaust velocity for PT9, 130 μF, 4 J, and with three different inductance-per-unit-length values.

Chapter 6

GFPPT Performance Scaling

This chapter compares the models and measurements from Chapters 3 and 5. The characteristic velocity, $\mathcal{U}$, and non-dimensional performance indicators, $(\bar{u}_e)^*$ and $(I/E)^*$, will be calculated for all the thruster designs to determine performance scaling relations. The performance measurements will also be compared to the results of the non-dimensional model. Finally, the important findings will be summarized and the cause of the Mode I operation in PT5 will be investigated.

6.1   Evaluating Characteristic Parameters

The main design parameters for each SRL-EPPDyL GFPPT are the energy per pulse, capacitance, initial inductance, inductance-per-unit-length, and mass bit. All of these parameters can be condensed into just two that can effectively be used to predict performance: the PPT Characteristic Velocity, $\mathcal{U}$, defined in Eq. (3.26), and the non-dimensional dynamic impedance parameter, α, defined in Eq. (3.43). Note that they are related in the following manner,

$$\alpha = \frac{1}{9}\frac{L'^3 EC}{L_0^2 m'} = \frac{16}{9}\frac{L'}{L_0}\frac{E}{m'}\frac{1}{\mathcal{U}^2}. \tag{6.1}$$

Both of these characteristic parameters are derived from easily measurable quantities. The results of these measurements, along with values taken from Table (4.1), are listed in Table (6.1). Note that larger values of $\mathcal{U}$ correspond to small capacitance and inductance-per-unit-length values. Larger values of α correspond to larger values of capacitance, inductance-per-unit-length and energy as well as smaller values of mass bit.

Thruster		C (μF)	$L^{'}(nH/cm)$	$\mathcal{U}$ (km/s)	α
PT5	(a)	130	2.8	94	0.33 - 2.8
	(b)	130	2.8	94	0.58 - 5.3
	(c)	270	2.8	65	1.1 - 11.0
	(d)	270	2.8	65	1.7 - 17.0
PT9	(a)	130	2.8	94	0.77 - 4.1
	(b)	130	3.9	67	1.5 - 12.0
	(c)	130	5.7	46	4.3 - 35.0

Table 6.1: Characteristic parameters $\mathcal{U}$ and α for each of the seven variants of PT5 and PT9.

6.2 Results of Predictions and Measurements

The scaling trends identified in all three of the models have been summarized in Chapter 3, Section 3.4. It is expected that the impulse bit should scale linearly with the integral of the current squared, the impulse-to-energy should be independent of the exhaust velocity, and the thruster efficiency should be linearly proportional to the non-dimensional exhaust velocity. We will now evaluate these three predictions one at a time.

6.2.1 Impulse Bit Scaling with $\int J^2 dt$

For a pulsed electromagnetic accelerator, the impulse bit should scale with the time integral of the Lorentz force. Because the magnetic field is self-induced, the impulse bit is predicted to scale linearly with the integral of the discharge current squared. The proportionality constant should be related to the inductance-per-unit-length.

Figure (6.1) shows the measured impulse bit as a function of the integral of the discharge current squared for both PT5 and PT9. As mentioned previously, with the open electrode design of PT9, deriving the current from the voltage waveform was difficult due to EMI effects, and, consequently, the errors are large for that measurement. All the data from PT5 shows a linear trend as expected, while only parts of the data from PT9 follow a linear relationship. Also note that for PT5 the integral of the current squared and the impulse bit increase as the mass bit decreases while both values stay relatively fixed for PT9. For PT5, the inductance-per-unit-length is fixed and the slope of a line going through the data for each configuration is very similar as expected. In PT9, the inductance-per-unit length changes depending on the electrode set and there is a corresponding increase in the impulse bit for the same value of $\int J^2 dt$. From Eq. (3.8) and Eq. (3.16) the impulse
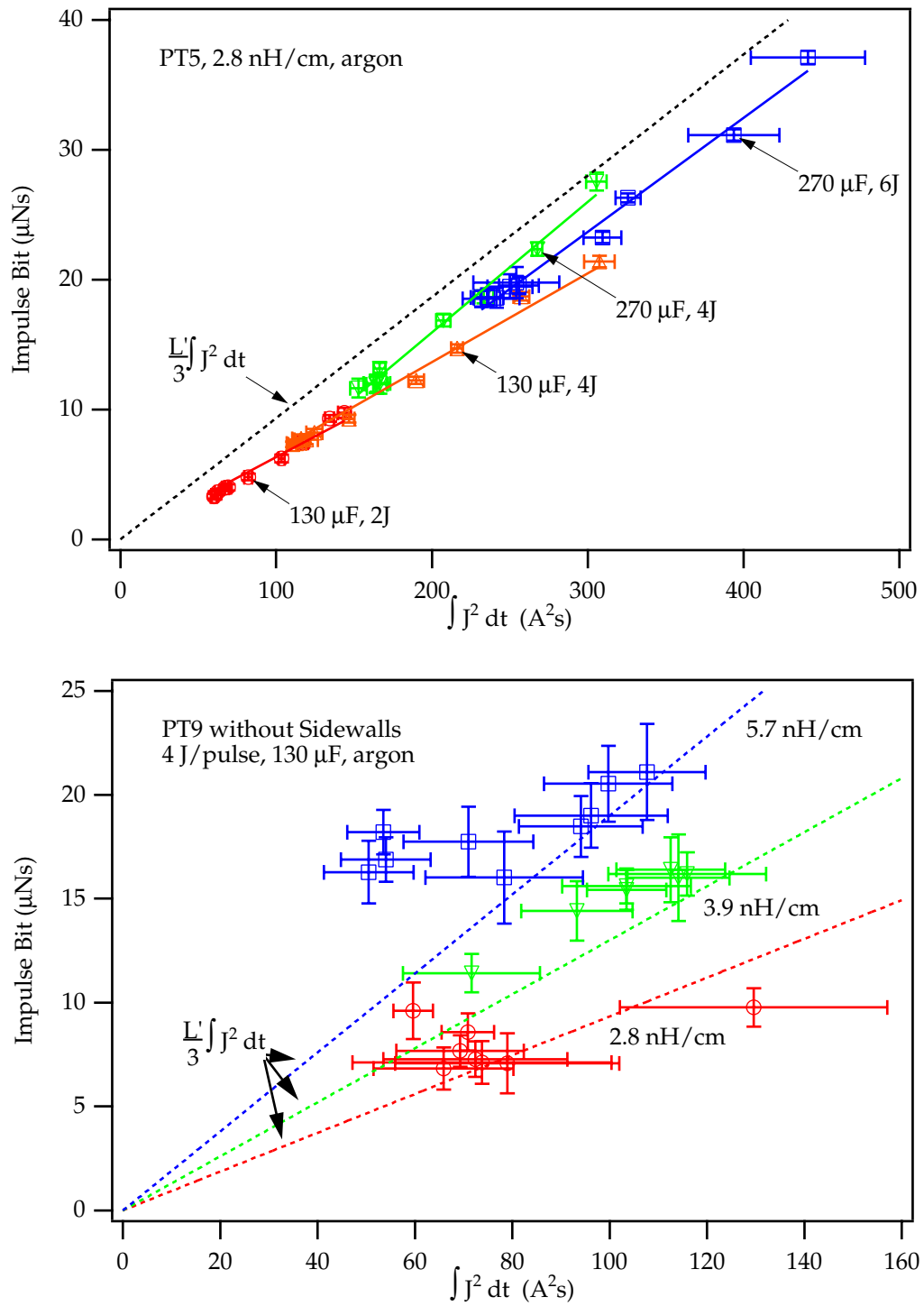
Figure 6.1: Impulse bit as a function of the integral of the current squared for both PT5 and PT9 over a wide range of operational conditions.

bit should be proportional to $L' \int J^2 dt$. This relation, with a coefficient of 1/3, has been added as a dashed line to each graph. The data from PT5, again, follows a similar linear trend, and most of the data from PT9 comes within the error bars to the lines.

6.2.2 Energy-to-Impulse Ratio Scaling with Mass Bit

Graphs of the impulse-to-energy ratio as a function of mass bit for each thruster have already been shown in Figs. (5.14) and (5.23). Here we begin by showing the impulse bit as a function of mass bit for both thrusters in Figs. (6.2) and (6.3). Notice that the impulse bit varies by a large amount depending on the capacitance, inductance-per-unit length, energy, and mass bit. While PT5 shows the dual modes of operation that were first pointed out in Chapter 5, PT9 does not. For PT5, the impulse bit (and impulse-to-energy ratio) is not constant above about 0.5 μg, however, for PT9 it is almost constant over all the mass bits within the error of the measurement.

Normalizing the impulse bit by the discharge energy and the PPT Characteristic Velocity, $\mathcal{U}$, yields the non-dimensional impulse-to-energy ratio as defined in Eq. (3.63). Using this relation to display the data collapses all the curves with varying capacitance, inductance-per-unit-length, and energy effectively onto a single curve for each thruster. In general, the trend of the impulse bit scaling with the energy level, the square root of the capacitance, and the inductance-per-unit length is present throughout the data from both thrusters. Both thrusters have approximately the same value of $(I/E)^*$ near 0.08 at the low mass bit values, but PT5 has higher values at higher mass bit values. This trend will be examined in more detail in Section 6.4, but for now it is important to notice that although there is an increase, it is similar for all four cases. In PT9, the curves of $(I/E)^*$ have more points in common at higher mass bits. The 1" x 1" configuration of PT9b seems to have the highest value of $(I/E)^*$ at the lower mass bits, possibly because it has slightly more propellant to accelerate than in the case of PT9c with 1/2" wide electrodes. As defined in Chapter 2, the propellant utilization efficiency for the 1" wide electrode sets of PT9a and PT9b might be larger than that for PT9c. PT9b also has a better electrode surface to volume ratio than PT9a or PT9c.

6.2.3 Efficiency Scaling with $\bar{u}_e/\mathcal{U}$

Perhaps the most important prediction for the performance scaling of GFPPTs is that the efficiency is expected to scale linearly with the exhaust velocity. This trend was predicted by both the variable element model, Eq. (3.25), and the non-dimensional model, Section 3.4. Except for Mode I operation in PT5, this is generally true from measured performance, as shown in Fig. (6.4). These graphs show
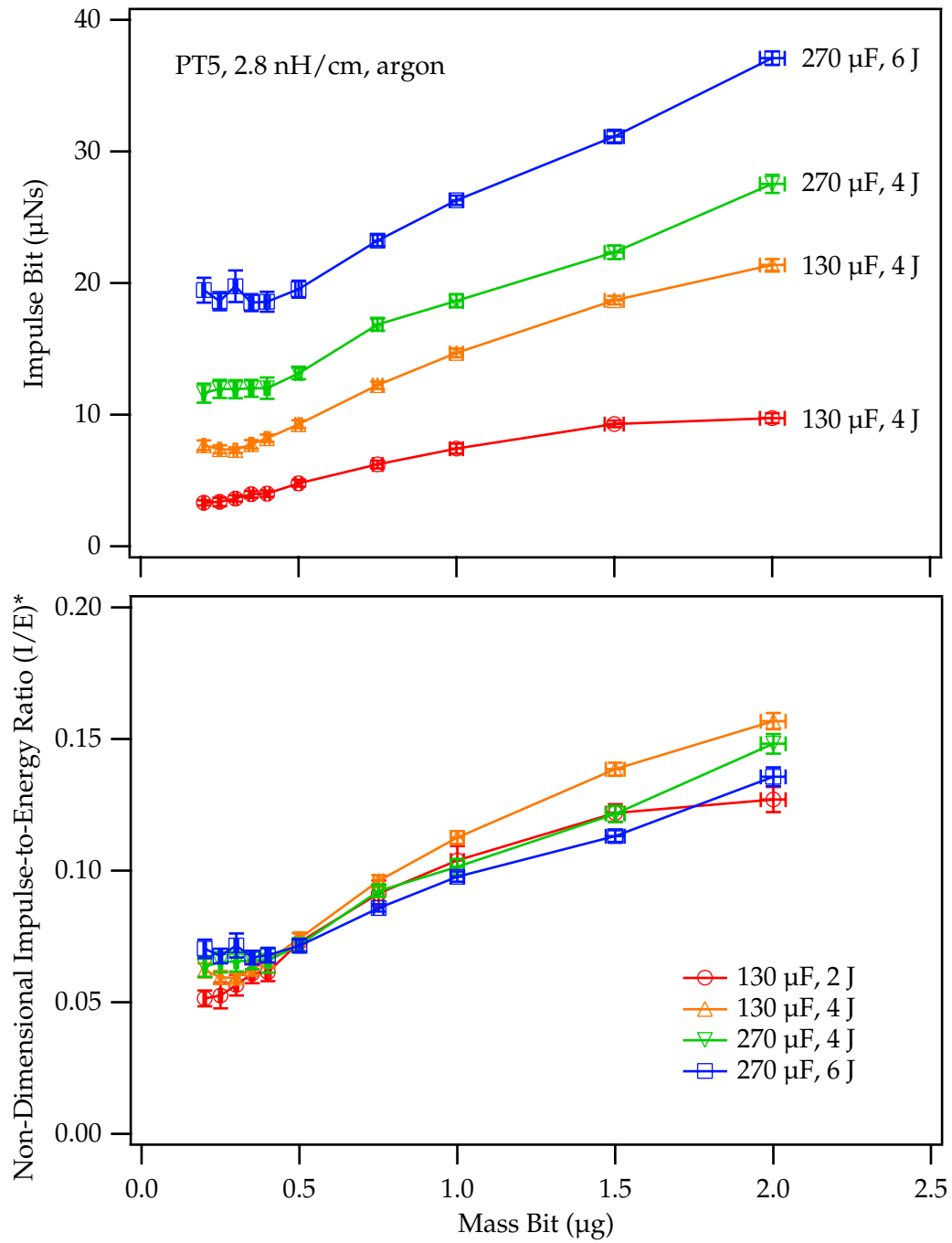
Figure 6.2: Impulse bit and non-dimensional impulse-to-energy ratio as a function of mass bit for PT5. The top graph is similar to one found in Fig. (5.14) and is repeated here for clarity.
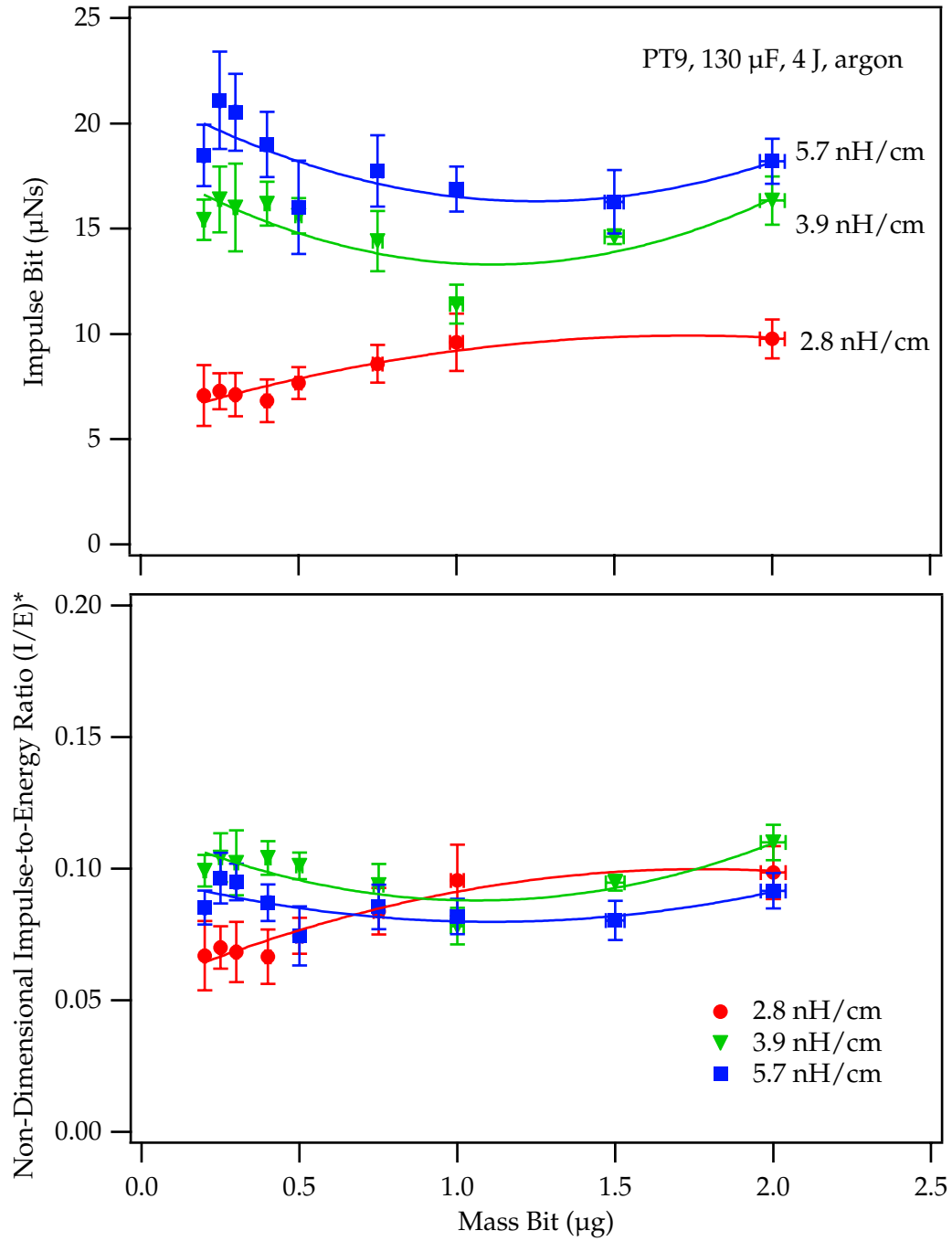
Figure 6.3: Impulse bit and non-dimensional impulse-to-energy ratio as a function of mass bit for PT9. The top graph is similar to one found in Fig. (5.23) and is repeated here for clarity.

the combined measurements for all seven configurations of the two GFPPT designs. In the top graph, the curves are spread out depending on capacitance, inductance-per-unit-length, and energy as the thruster efficiency is plotted versus the measured exhaust velocity. In the bottom graph, the thruster efficiency is plotted versus the non-dimensional exhaust velocity, $(\bar{u}_e)^* = 3\bar{u}_e/\mathcal{U}$. In that graph, much of the data collapses within 10% of a *single line*. The implications of this are simple: for the SRL-EPPDyL low-energy GFPPTs, the efficiency is almost always related to the non-dimensional exhaust velocity *regardless* of capacitance, inductance-per-unit-length, or energy. The largest deviations from this trend are at high mass bit values in PT5, Mode I operation. There are also some slight deviations in PT9 at higher mass bit values, especially for the 1″ wide cases, PT9a and PT9b.
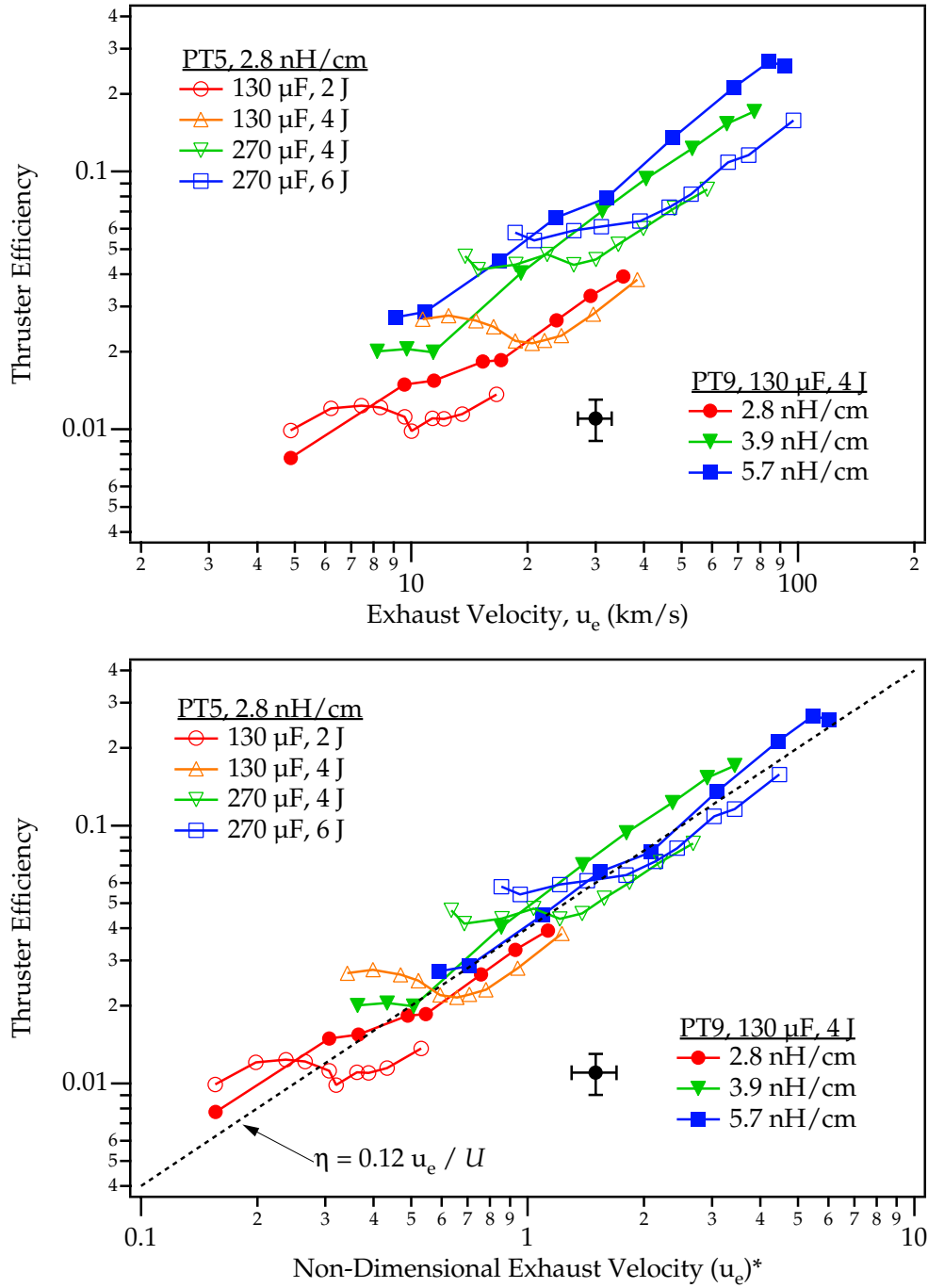
Figure 6.4: Thruster efficiency as a function of exhaust velocity and the non-dimensional exhaust velocity, $\bar{u}_e/\mathcal{U}$ with a typical error bar shown near the legend. Using the PPT characteristic velocity, $\mathcal{U}$, allows almost all the data to fall close to one line, $\eta_t = 0.12\bar{u}_e/\mathcal{U}$.

6.3 Comparing Non-Dimensional Model Results and Measurements

The non-dimensional model developed in Chapter 3 showed that the thruster efficiency, non-dimensional exhaust velocity, and non-dimensional impulse-to-energy ratio depended mainly of the values of three parameters: the dynamic impedance parameter, α, the critical resistance ratio, ψ, and the mass distribution parameter, γ, all defined in Section 3.2.3. For PT5 and PT9, α can be measured directly (see Table (6.1)) and γ can be estimated based on the propellant type, plenum temperature, and the time between pulses (roughly $\gamma = 0.3$ for many of the configurations tested here). The critical resistance ratio, however, is difficult to measure accurately due to the unknown value of the effective plasma resistance in the circuit. Although attempts were made to measure this quantity in PT9, once again the open nature of the electrodes and the plasma itself interfered with the accuracy. In a slightly easier measurement, the internal impedance of the 130 μF capacitor bank has been measured near 3 mΩ (see Section 4.1.2) which would yield a value of $\psi \approx 0.2$. As shown in the next three subsections, however, values of ψ slightly greater than unity match the performance measurements more closely. This would imply that the total resistance of the circuit is greater than the internal impedance of the capacitor bank, and that the effective plasma resistance plays an important role in determining ψ. If $\psi \geq 1$, the effective plasma resistance must be at least 15 mΩ. This value seems plausible, especially considering that the peak current does not reach above 10 kA in most tests of both PT5 and PT9. This may also be related to the low-voltage nature of these GFPPT discharges. More discussion on the impact of the effective plasma resistance is given in Section 6.4.4.

Besides a large plasma resistance, another possibility is that the profile and sweeping efficiencies (which are not included in these models) are significantly less than unity. In that case, the *linear scaling* of the thruster efficiency with exhaust velocity would still be present, but the magnitude of the slope may be much less. For now, we will leave the critical resistance ratio as a free parameter and use our measured performance and measured values of the dynamic impedance parameter, α, to examine the performance scaling. We will find that although the measured performance and the model predictions do not match exactly, many of the measured trends are apparent and agree with theoretical predictions.

6.3.1 Thruster Efficiency

Thruster efficiency as a function of the dynamic impedance parameter is shown in Fig. (6.5) for both PT5 and PT9. For almost all the conditions except Mode I operation in the PT5 data, both graphs show general agreement with the expected trends (shown by the dashed lines for various values of ψ) with a critical resistance

ratio value somewhere between one and four.

In the PT5 data set, Mode I operation (constant efficiency at *small* values of α) does not follow the predicted trend. This higher than expected performance could be a result of a decreasing ψ value as explored further in Section 6.4.4. In Mode II operation, the efficiency follows the predicted trend fairly well, although it has a slightly steeper slope than that for the $\psi = 4.0$ prediction. The steepness of the prediction curve is due mainly to the value of the mass distribution parameter. As seen in Chapter 3, Figs. (3.9), (3.12), and (3.15), slightly different mass distributions with more mass located towards the breech of the thruster could lead to a slightly steeper slope. The disparity could also be a result of a slight sweeping or profile loss that is not accounted for in this model.

For the PT9 data set, there is more deviation from the predicted trends. Again, much of the data falls between within a range of the dynamic impedance parameter, $1 \leq \psi \leq 4$. At lower mass bit values, the configurations with larger values of inductance-per-unit-length (PT9b and PT9c) have a slightly steeper slope than the predicted curves. Again, this could be due to a slightly different mass distribution at different mass bit levels or due to a changing value of ψ.

6.3.2   Non-Dimensional Exhaust Velocity

The non-dimensional exhaust velocity (shown in Fig. (6.6)) shows a similar behavior to that found in the thruster efficiency comparison. There is reasonably close agreement between predicted and measured trends (within a factor of less than two) for PT5 Mode II and most of the PT9 data. For PT5 Mode I operation, once again, the measured exhaust velocity is slightly higher than the predicted trends with a constant value of $\psi \approx 4$. Although the predicted curves of $(\bar{u}_e)^*$ show a slight decrease in slope at lower values of α, this change in the slope is not exactly reflected by what is found in the measurements. This effect is possibly due to the finite length of the electrodes or a variable plasma resistance as a function of mass bit as explored further in Section 6.4. Still, considering the simplified nature of the model, the trends between the predictions and measured values are in relatively good agreement.

6.3.3   Non-Dimensional Impulse-to-Energy Ratio

Here again, as expected, we observe a very similar situation to what was found previously for the thruster efficiency and non-dimensional exhaust velocity (see Fig. (6.7)). Both the data from PT5 in Mode II and the majority of PT9 data match well with the predicted trends for ψ values between one and four. In this case, perhaps more than the others, Mode I operation for PT5 seems to be a result of a decreasing ψ value as α decreases (mass bit increases.)
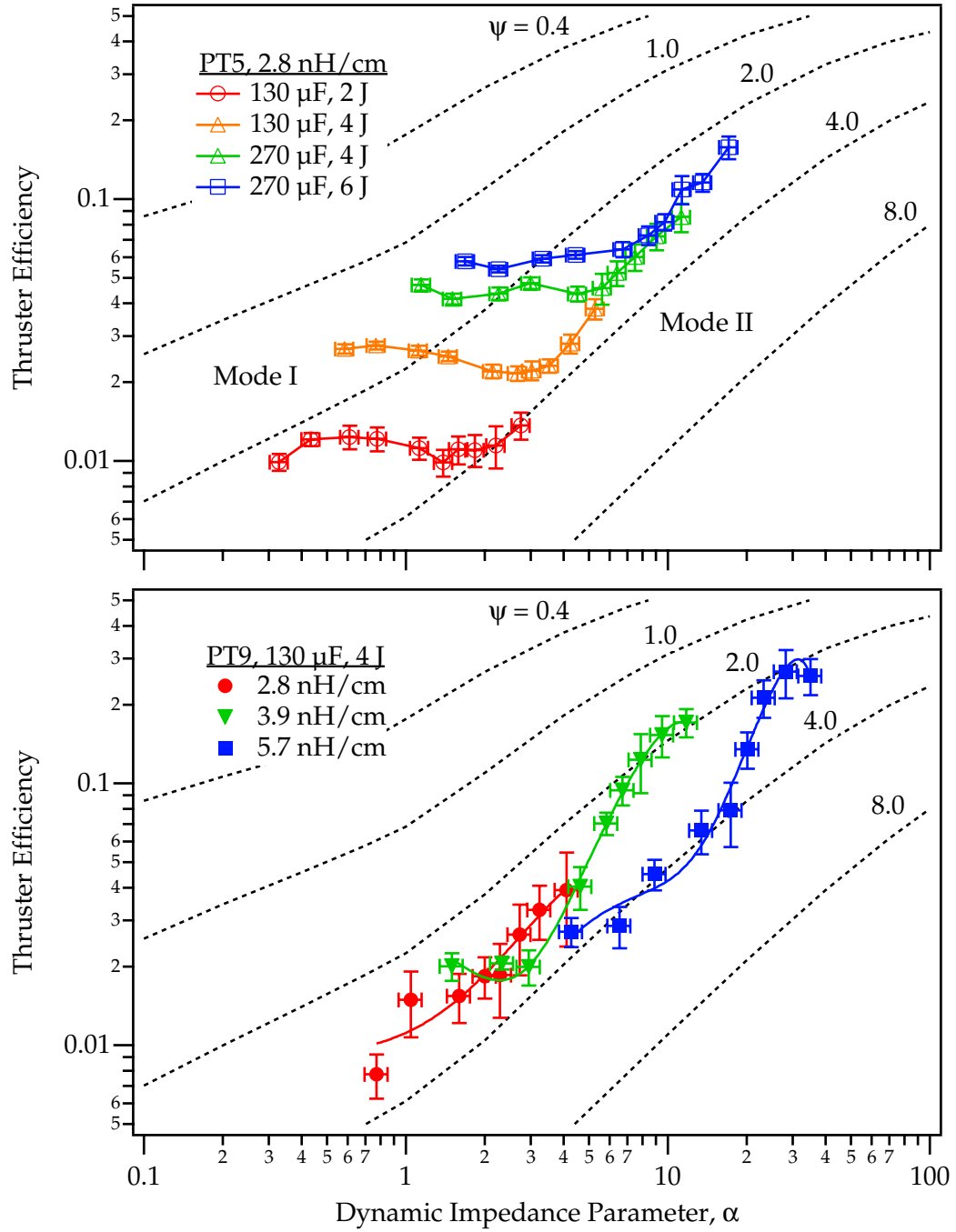
Figure 6.5: Thruster efficiency, η_t, as a function of the dynamic impedance parameter, α. The measured results are shown with error bars while the predicted level-curves are shown as dashed lines with the critical resistance ratio, ψ, as a parameter.
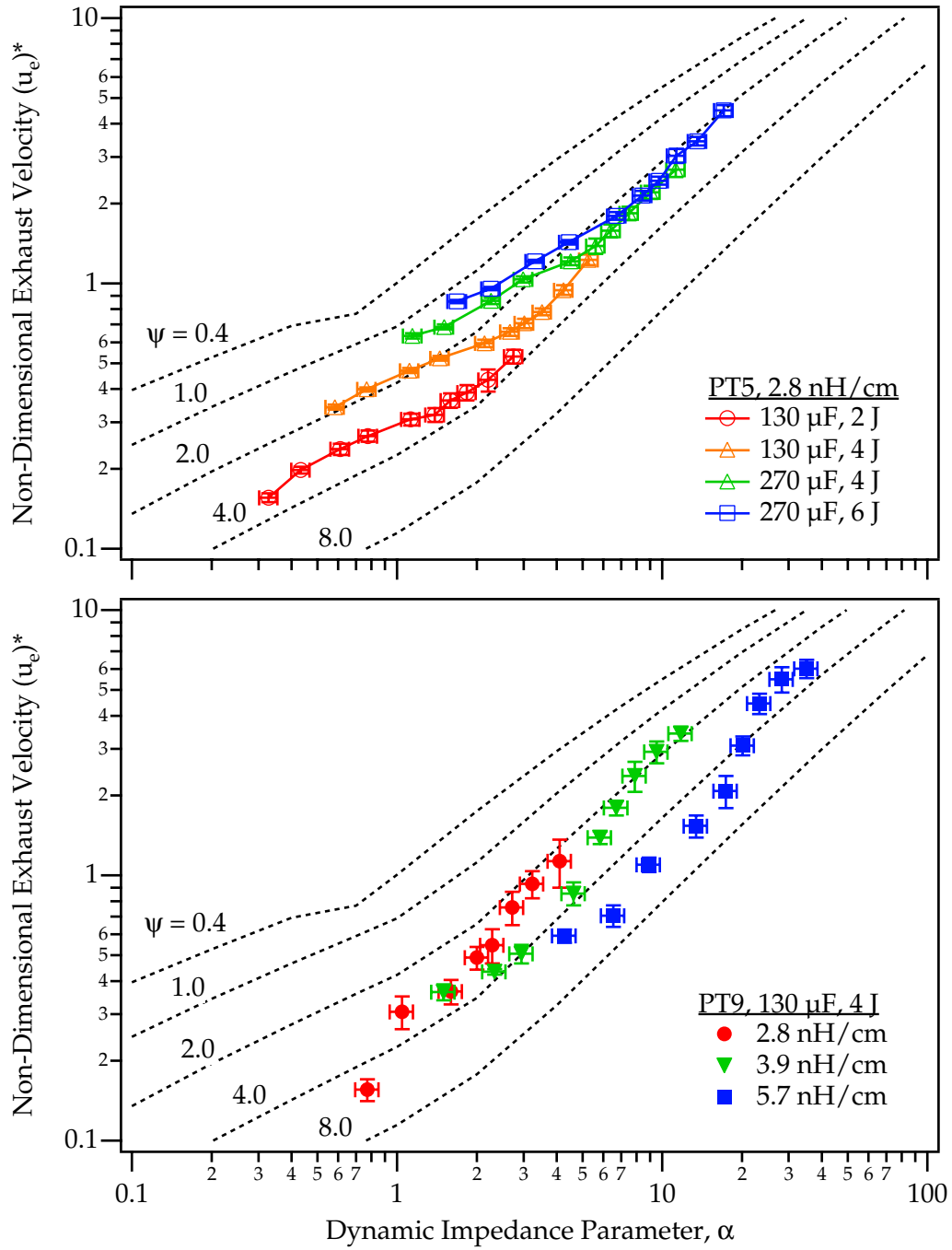
Figure 6.6: Non-dimensional exhaust velocity, $(\bar{u}_e)^*$, as a function of the dynamic impedance parameter, α. The measured results are shown with error bars while the predicted level-curves are shown as dashed lines with the critical resistance ratio, ψ, as a parameter.

Figure 6.7: Non-dimensional impulse-to-energy ratio, $(I/E)^*$, as a function of the dynamic impedance parameter, α. The measured results are shown with error bars while the predicted level-curves are shown as dashed lines with the critical resistance ratio, ψ, as a parameter.
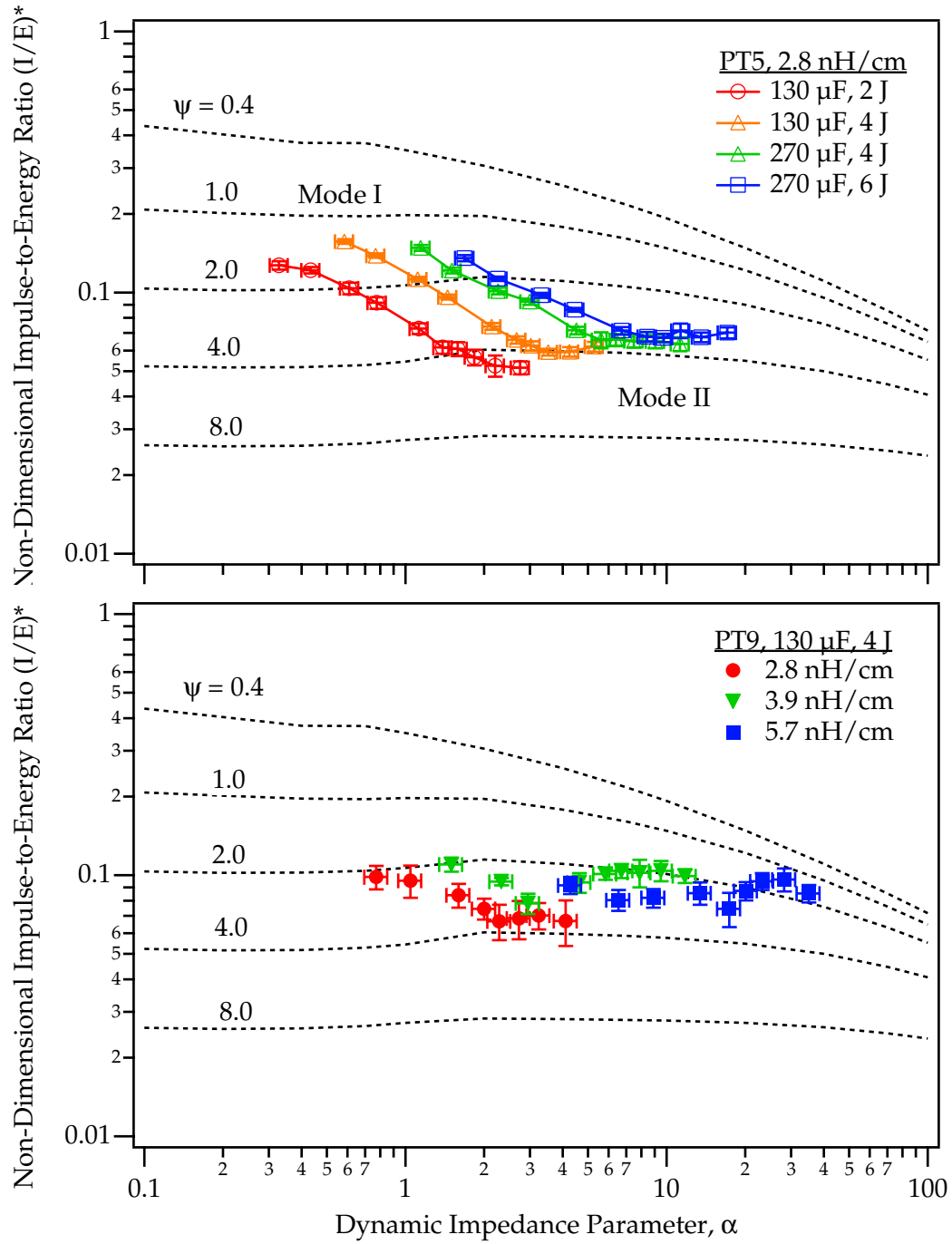
6.4 Possible Explanations for Mode I

As seen in almost all the comparisons between measurements and models, the largest discrepancies occur for PT5 in Mode I operation. In this mode, the efficiency is relatively constant with exhaust velocity and the impulse-to-energy ratio increases with increasing mass bit value. We will consider four different explanations for the higher than predicted performance: 1) electrothermal energy recovery, 2) finite electrode length effects, 3) increased profile or sweeping efficiency, and/or 4) a decrease in the effective plasma resistance at higher mass bit values. The real explanation could be a combination of these effects which we will now explore one at a time.

6.4.1 Electrothermal Energy Recovery

At higher mass bit values, the number density and pressure are higher and the mean free path is correspondingly lower compared to Mode II operation. If any electrothermal energy is to be recovered at all, it would be at these conditions. The scaling relations suggested for a thruster where electrothermal acceleration is dominant, however, are quite different (see Ref. [64] for example). In such a case, the impulse bit would be expected to scale with the *square root* of the discharge energy-to-mass bit ratio and not to depend directly on capacitance or inductance change. This is a result of the proportional relationship between the energy deposited in the plasma and the integral of RJ^2. Furthermore, the *efficiency* of a pure electrothermal accelerator is expected to be constant over wide range of energy, exhaust velocity, and mass bit values. While the efficiency for PT5 is indeed independent of mass bit and exhaust velocity at high mass bit values (i.e. Mode I), it does show a dependence on energy.

More evidence that is contrary to this explanation is the relation between the impulse bit and integral of the current squared, as shown in Fig. (6.1). For an electrothermal thruster, the exhaust velocity and hence the impulse bit should scale as the square root of the integral of the current squared. Clearly this is not the case with the measured trends having more of a linear character as would be expected from electromagnetic acceleration. In addition, even at mass bit values that clearly fall into Mode I operation, the impulse-to-energy ratio was *constant* over a wide range of energy values as shown in Fig. (5.16). This is characteristic of an electromagnetic accelerator, not an electrothermal one. Therefore, although some electrothermal energy may very well be recovered in these discharges at higher mass bits, the amount is believed to be minor and not enough to completely explain Mode I operation.

6.4.2 Finite Electrode Length Effects

Chapter 3 described and predicted the effects due to the electrodes having a finite length. At high mass bit values in Mode I operation, the discharge may not reach the end of the electrodes by the time the capacitor is fully drained. As the mass bit value increases, the discharge is not able to propagate as far down the electrodes before the discharge is complete. As shown in Fig. (3.12), for a uniform mass distribution the efficiency stays relatively constant until the point where the discharge finally begins to reach the end of the electrodes. It then increases sharply until the actual electrode length is near the predicted optimal length. Although this trend is apparent in Fig. (6.5), the value of α which marks the transition from Mode I to Mode II is variable. This is *not* predicted by the model, where the transition would have to occur at a single value of α for a set value of ψ. In addition, the actual mass distribution in PT5 is far from uniform. For a more likely mass distribution, as seen in Fig. (3.15) for $\gamma = 0.3$, the effect of finite length electrodes is much less pronounced. This is due to most of the mass being swept up at the beginning of the discharge, near the breech of the thruster, which would occur for all but the smallest sheet velocities. Indeed, at velocities below 20 km/s, the discharge may not reach the end of the electrodes before the capacitor is fully drained. With an exponential mass distribution, however, the effect should be minor.

6.4.3 Increased Sweeping and Profile Efficiencies

Since the profile and sweeping efficiencies have not been measured directly, it is difficult to determine if an increase in one or the other is indeed the cause for the higher than expected performance. In previous studies of current sheet structure in argon discharges, it has been noticed that the sweeping efficiency increases with increasing current rise rates [2, 53]. An empirical rule of thumb is that 10^{10} A/cm-s over the span of the current sheet is required for 100% sweeping efficiency [2]. Most of the low-energy SRL-EPPDyL GFPPT discharges presented here fall just *below* this 10^{10} A/cm-s cut-off. As seen in Fig. (5.18) the peak current does indeed increase as the mass bit value increases which could imply that the sweeping efficiency is improving. Still, as found in Chapter 3, the *impulse* should not depend on how the mass was swept up at a fixed energy. In other words, although the thruster efficiency should be sensitive to the sweeping efficiency, the impulse-to-energy ratio should not. In addition, both Ref. [53] and Ref. [58] showed that the sweeping efficiency *decreased* for higher mass bit values.

As far as the possibility of an improvement in the profile efficiency in Mode I, once again the literature points toward the opposite trend from one that is observed with mass bit and pressure. Using an inverse z-pinch device, Johansson found that the tilting of the current sheet *increased* for higher mass bit values Ref. [58]. Although the profile efficiency should effect both the thruster efficiency and the

impulse-to-energy ratio, it appears to have the opposite trend. This suggests against the possibility of an increased sweeping or profile efficiency.

6.4.4 Decrease in Effective Plasma Resistance

Another possibility is based on the potentially changing value of ψ with the mass bit (which is related to the initial propellant density). As apparent in all the comparisons between predicted and measured performance, as the mass bit increases, the measured performance moves closer to values that are predicted by smaller critical resistance ratios. As the initial inductance and capacitance are fixed, this would imply that the effective resistance in the circuit (capacitor internal impedance plus plasma resistance) is decreasing as the mass bit (and density) is increasing. Once again we turn to Fig. (5.18) to see that the peak current also increases at higher mass bit values. In fact, the mass bit cut-off between a constant peak current value and where the peak current values begin to increase agrees well with the transition points found in the comparison graphs presented in the previous section. As expected, and found in previous experiments (Refs. [87, 98]), as the energy and current increases, the effective plasma resistance drops. A decreasing value of ψ for the observed increasing performance of PT5 in Mode I operation is, therefore, the most consistent explanation with all the observed trends presented here and in the literature.

6.5 Summary of Chapter 6

This section has used performance models and measurements to examine the performance scaling of low-energy GFPPTs over a wide range of operating conditions. The following summary and conclusions can be drawn from this study:

- The thruster efficiency is proportional to the exhaust velocity and PPT characteristic velocity for the mass bit and α values tested here,

$$\eta_t \propto \frac{\bar{u}_e}{\mathcal{U}} = \frac{1}{3}L'\sqrt{\frac{C}{L_0}} \quad \bar{u}_e. \tag{6.2}$$

- The exhaust velocity is proportional to the dynamic impedance parameter, α^n, where $0.5 \leq n \leq 1$, depending on the mass distribution prior to the discharge and the dynamic efficiency.

- The non-dimensional impulse-to-energy ratio, $(I/E)^*$, is relatively constant for α values of practical interest and for a fixed value of the critical resistance ratio, ψ.

- For the low-energy SRL-EPPDyL GFPPTs studied here, the effective plasma resistance seems to be significant. Values of ψ between one and four provide predictions from a non-dimensional model that closely match performance measurements within a factor of two.

Perhaps the largest remaining question to be answered about GFPPT performance scaling is how the thruster performs at higher energy levels and with different propellant types. The effect of these parameters on the value of ψ and the corresponding values of the performance would be important to study in future work on GFPPTs. This and other conclusions are presented in the next chapter.

Chapter 7

Conclusions

This chapter comprises the conclusions based on the work presented in Chapters 1-6. First, we restate the need for the development of GFPPT performance scaling relations and outline the goals of this research work. Next, we summarize the important findings from each chapter, and, finally, suggest future GFPPT design considerations and research topics.

7.1 Determining Experimentally Verified Performance Scaling Relations

To design and optimize a GFPPT for a particular mission or maneuver, its efficiency, exhaust velocity (specific impulse), and impulse-to-energy ratio must be predictable over a wide range of operating conditions. This implies that the influence of the mass bit, discharge voltage, capacitance, energy, initial inductance, and electrode geometry on performance is known with some certainty. The difficulty of developing such performance scaling relations is due to the complex nature of the GFPPT discharge dynamics, the large number of variable parameters that could influence the performance, and the lack of a previously measured performance database that spans over a wide range of operating conditions. To be of any benefit, a set of performance scaling relations must be developed from a model that is based on the fundamental acceleration processes and subsequently verified empirically. Completing this task is the main topic of this dissertation work.

7.2 Research Goals and Activities

The goal of this research has been two-fold: 1) to derive useful performance scaling laws for low-energy GFPPTs, and 2) to experimentally verify them with performance measurements over a wide range of operational conditions. In order to

derive a complete set of performance scaling relations, a series of theoretical models have been developed with the following qualities:

1. Consecutive models were developed with increasing complexity so that the results of the most intricate model can be understood in terms of the more elementary relations.

2. The dynamics of the discharge have been modeled in detail while the more complex plasma physics including the conductivity, radiation, and internal mode losses have been condensed into a single effective resistance term.

3. The number of free parameters has been reduced to a minimum by a non-dimensional approach to the problem.

4. The non-dimensional model has been explored over a wide range of input parameters to identify global scaling trends.

To test the validity of the models, the performance of two specially designed GFPPTs has been measured in carefully controlled experiments. The performance measurements and GFPPTs have been designed so that:

1. Contamination from background gases in the vacuum facility did not affect the measured performance of the GFPPTs.

2. The discharge initiation was symmetric and nearly uniform for each test.

3. PT5 and PT9 tested the effects of changing capacitance and inductance-per-unit-length, respectively.

4. Each time a single operational condition ($C, L^{'}, m_{bit}, V_0$, etc.) was changed, the others remained fixed so that the experiment is controlled.

5. The performance of each operational condition was measured at least twenty times to insure accuracy.

The results from the models and the performance measurements will now be summarized in the next section.

7.3 Summary of Findings

In this section we summarize the results of this dissertation work by dividing them into three categories: 1) predictions from models, 2) performance measurements from PT5 and PT9, and 3) a comparison of the models and the measurements.

7.3.1 Derivation of Scaling Relations

Three models with increasing complexity were developed to provide performance scaling relations in Chapter 3. The first model used an effective circuit relation with fixed elements to show that the highest energy transfer efficiency comes from using a nearly-critically damped current waveform. This was explored further in the second model where the inductance and mass were allowed to vary throughout the pulse, and the critical resistance ratio, ψ, was constrained between 0.3 and 3.0. The results from the second analytical model are as follows:

- The efficiency is expected to scale linearly with the ratio of the exhaust velocity to the GFPPT characteristic velocity, $\mathcal{U}$,

$$\eta_t = \frac{\bar{u}_e}{\mathcal{U}} e^{-\sqrt{\psi}}, \tag{7.1}$$

  where,

$$\mathcal{U} \equiv \frac{3}{L'}\sqrt{\frac{L_0}{C}}, \qquad \psi \equiv \frac{R}{2}\sqrt{\frac{C}{L_0}}. \tag{7.2}$$

- The exhaust velocity is expected to scale with a set of parameters that depends on the mass distribution. These parameters are also found in the non-dimensional model as the dynamic impedance parameter, α. For a slug mass distribution, the expected scaling is,

$$\bar{u}_e = \frac{2}{\mathcal{U}}\frac{E}{m_{bit}} e^{-\sqrt{\psi}} = 2\mathcal{U}\alpha_{slug}\, e^{-\sqrt{\psi}}, \tag{7.3}$$

  and for a uniform mass distribution, the expected scaling is,

$$\bar{u}_e = \sqrt{\frac{4EL'}{3m'L_0}}\, e^{-\sqrt{\psi}} = 2\mathcal{U}\sqrt{\frac{\alpha}{3}}\, e^{-\sqrt{\psi}}, \tag{7.4}$$

  where,

$$\alpha_{slug} \equiv \frac{L'^2 V_0^2 C^2}{18 L_0 m_{bit}}, \qquad \alpha \equiv \frac{L'^3 V_0^2 C^2}{18 L_0^2 m'}. \tag{7.5}$$

The third model used a non-dimensional approach to reduce the number of free parameters by half. Furthermore, as compared to the previous model, no assumptions where made about the current waveform type or the inductance profile, an exponential mass distribution was used to simulate the conditions more accurately, and the electrodes were allowed to have a flared geometry. The consequent set of coupled, non-linear differential equations was solved numerically and yielded the following results (taken from Section 3.4):

- Small values of ψ have the highest values of efficiency and the non-dimensional impulse-to-energy ratio, $(I/E)^*$.

- As in the variable element model, for $\alpha < 10$, the efficiency is linearly *proportional* to the non-dimensional exhaust velocity, $(\bar{u}_e)^* = 3\bar{u}_e/\mathcal{U}$, which is not a strong function of ψ or the electrode length.

- For $\psi < 0.3$, there is an optimum efficiency between $1 \leq \alpha \leq 10$.

- Using a finite electrode length changes the exact value of the efficiency, but the scaling relations are generally intact.

- Using a flared outer electrode has mixed, and only slight benefits, depending on α.

7.3.2 Performance Measurements

The performances of PT5 with variable capacitance and PT9 with variable inductance-per-unit-length were measured over a wide range of argon mass bits. For PT5, four cases with different capacitance and energy levels were examined: a) 130 μF, 2 J, b) 130 μF, 4 J, c) 270 μF, 4 J, and d) 270 μF, 6 J. The inductance-per-unit-length, L', for PT5 was kept constant at 2.8 nH/cm. For PT9, three cases with different values of L' were evaluated: a) 2.8 nH/cm, b) 3.9 nH/cm, and c) 5.7 nH/cm. The capacitance and energy per pulse for PT9 were fixed at 130 μF and 4 J. In all seven cases, 10 mass bit values between $0.2 - 2.0\mu$g were used to span over a large range of exhaust velocity values.

For PT5, two modes of operation were identified. Mode II operation occurs at the lowest values of mass bit and highest values of exhaust velocity. In this mode, the efficiency scaled linearly with exhaust velocity, as expected. Mode I operation occurs at the highest values of mass bit and the lowest values of exhaust velocity. In this mode, the efficiency remained *constant* with exhaust velocity, providing *better* than expected performance. The increase in performance is suspected to be caused by a decrease in the effective plasma resistance, and consequently a smaller ψ value. The transition point between the modes is determined by the current level in the discharge. In Mode II, the current level remained relatively fixed and was determined solely by the energy per pulse. In Mode I, the current increased with increasing mass bit. In both modes, the performance increased with the square-root of capacitance, and the impulse-to-energy ratio remained nearly constant over different energy levels.

For PT9, a large increase in performance was observed when the insulating sidewalls were removed. With the sidewalls in place, the performance did not depend on the inductance-per-unit-length. Without the sidewalls, the performance scaled linearly with the inductance-per-unit-length as expected. The two modes of

operation that occurred in PT5 were not observed in PT9. PT9c, which had 1/2″ wide electrodes separated by a 1″ gap and an $L' = 5.7$ nH/cm, had the best overall performance with an efficiency of 25% at an exhaust velocity of 85 km/s (8700 s I_{sp}) and an impulse-to-energy ratio of 6 μNs/J.

7.3.3   Comparison of Measurements and Models

The following trends were noticed when the performance measurements were compared to the theoretical models:

1. The thruster efficiency is indeed proportional to the ratio of the exhaust velocity to the PPT characteristic velocity for both PT9 and PT5 in Mode II operation (See Fig. (7.1)).

2. The thruster efficiency also increases gradually with α. The measured performance trends for PT9 and PT5 in Mode II operation match the predicted trends for $2 \leq \psi \leq 4$ (See Fig. (7.2)).

3. The exhaust velocity is proportional to the dynamic impedance parameter, α^n, where $0.5 \leq n \leq 1$, depending on the mass distribution prior to the discharge and the dynamic efficiency.

4. The non-dimensional impulse-to-energy ratio, $(I/E)^*$, is relatively constant (near 0.1) for α values of practical interest (between 1-10) and for a fixed value of the critical resistance ratio, ψ.

5. For the low-energy SRL-EPPDyL GFPPTs studied here, the effective plasma resistance plays an important role in determining performance. Values of ψ between one and four provide predictions from the non-dimensional model that match measured performance trends within a factor of two.

Although there is generally good agreement between the models and the performance measurements over certain ranges of operation, the critical resistance ratio, ψ, remains difficult to determine from a measurement of the internal impedance of the capacitor bank alone. As discussed further in the last section of this chapter on the future directions of GFPPT research, understanding the effective resistance of the plasma is paramount to determining and reducing ψ which should improve performance.

7.4   The Next Generation GFPPT Design

The performance scaling relations found in this dissertation suggest that a GFPPT should be designed with the largest inductance-per-unit-length and capacitance

Figure 7.1: Plot of measured thruster efficiency versus measured non-dimensional exhaust velocity for both PT5 (Mode II operation only) and PT9. Almost all the data points fall within the error bars of a linear relationship, $\eta = 0.12\bar{u}_e/\mathcal{U}$.

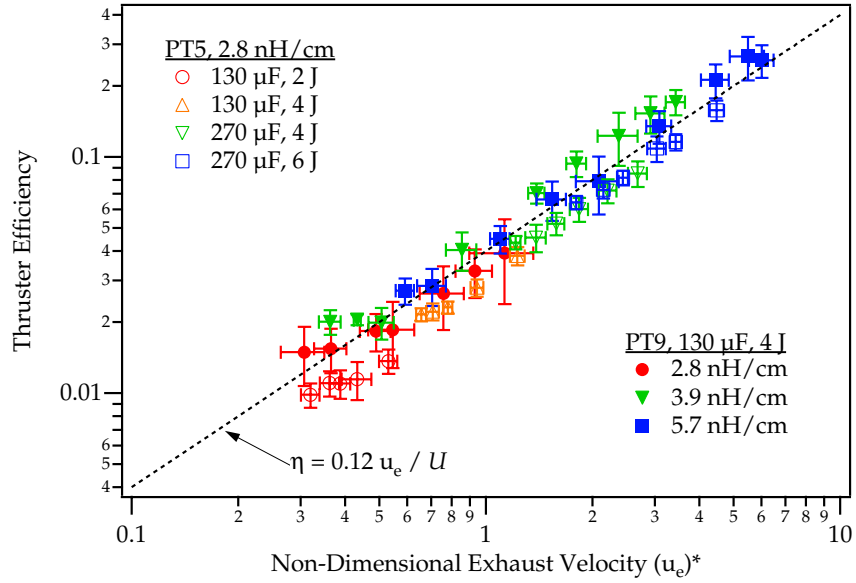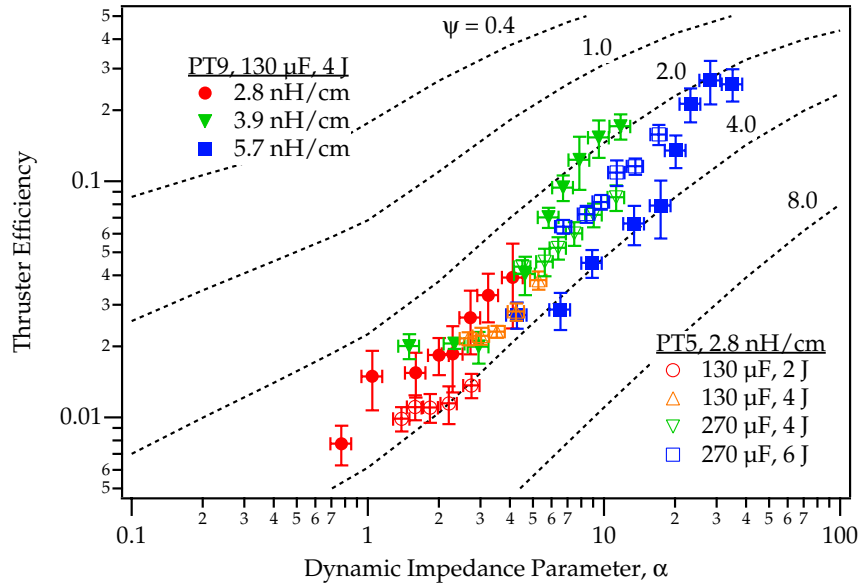Figure 7.2: Plot of measured thruster efficiency versus measured dynamic impedance parameter for both PT5 (Mode II operation only) and PT9. Almost all the data points fall within the error bars of $2 \leq \psi \leq 4$.

possible. Both of these parameters, however, cannot extend beyond some reasonable limits whereby other effects such as a reduced propellant utilization efficiency, profile losses, or increased power conditioner mass, for example, start to have a greater influence. We will now examine the maximum limits of the inductance-per-unit-length and capacitance in the next two sections.

7.4.1 Parallel-Plate vs. Coaxial Electrodes

As shown in Fig. (4.8), for coaxial electrodes to have a value of L' equal to that of a parallel-plate electrode set, its outer-to-inner radius ratio must be approximately ten times larger than the corresponding height-to-width ratio. For example, to have $L' = 5.7$ nH/cm, as in the PT9c configuration, a coaxial electrode set would have to have a radius ratio of 18. Unless the inner electrode is very slim, the outer electrode, in many cases, would have to be quite large and possibly massive. The radius of the inner electrode also has a lower limit due to the probability that large current densities can cause a significant amount of erosion. Initiating the discharge uniformly with a large outer electrode could also be a problem. Finally, because the Lorentz force is proportional to $1/r^2$ in a coaxial thruster, a slim inner electrode could cause a significant non-uniform acceleration that would tilt the current sheet. Although other effects such as canting (see Ref. [60]) can also influence the current sheet profile, a slim inner electrode could lead to large profile losses.

A coaxial set of electrodes has the advantage that all the propellant injected before the discharge is contained. This is not the case, however, for a parallel-plate set of electrodes. As the height-to-width ratio increases, more and more of the propellant escapes the discharge volume before the pulse. Although sidewalls can contain the propellant before the discharge, they have been shown to significantly reduce the performance. If the electrodes are made wide enough to capture almost all of the propellant, the height of the gap between them could make uniform discharge initiation difficult. Furthermore, the profile of the current sheet in parallel-plate thrusters has been shown, in many cases, to be non-planar. The cause of the canting is currently under investigation, but the impact on performance is obviously detrimental. Finally, the open nature of the parallel-plate design allows the plasma to escape outside the intended discharge volume. Extreme care must be taken to insulate nearby electrically conducting surfaces to prevent the arc from attaching to undesirable locations.

For many of the reasons mentioned above, we believe that a *coaxial* set of electrodes could be the most desirable from a system point of view. First, coaxial electrodes contain the discharge and magnetic fields, and, although a uniform initiation may be difficult to accomplish, it is not impossible. Second, the profile losses from a non-uniform Lorentz force may be combated by the canting effects that have been noticed in GFPPTs. If the inner electrode is designed to be the cathode,

it could be made quite slim (to the limit where current density and erosion are still tolerable) with the overall profile losses not being as important as the performance gain from a higher inductance-per-unit-length. Obviously, more experiments with coaxial electrodes testing various inner electrode radii need to be conducted. In any case, we believe this is the direction for future GFPPT designs.

7.4.2 The Optimal Value of Capacitance

Besides the performance scaling, the value of capacitance mainly effects the mass of the thruster and power conditioning hardware. This is because larger capacitance values lead to a more massive energy storage device and larger charging currents unless the charging time is increased. Larger values of charging current require a more massive power processing modulator. Conversely, longer charging times allow more propellant to escape the discharge volume before each pulse, thus reducing the propellant utilization efficiency. For this reason, larger values of capacitance dictate longer (and potentially wider electrodes for parallel-plate thrusters), more massive electrodes. Although the axial extent of the propellant column before the discharge also depends on the molecular weight and the plenum temperature, long electrodes may also be required because the duration of the discharge increases with increasing capacitance. Finally, the capacitance level also effects the critical resistance ratio. Depending of the effective plasma resistance, the capacitance level should not be increased beyond the point where ψ becomes much greater than unity.

The relationship between the capacitance and the mass of the power processing hardware needs to be investigated further before the optimal capacitance level can be determined explicitly. Still, the benefit of a higher capacitance has been shown both theoretically and experimentally. With that in mind, the largest possible capacitance should be used while keeping the propellant utilization efficiency near 100%. For the GFPPTs studied in this dissertation with argon propellant, the maximum capacitance is close to 270 μF.

7.4.3 Additional Design Guidelines

In Section 1.3.1, we found that the optimal exhaust velocity is often close in value to the PEP velocity, $\tilde{V}$, a solely technology dependent parameter,

$$\bar{u}_{eopt} \approx \tilde{V} = \sqrt{\frac{2\eta_t N_{ptot}}{\alpha_e}} \propto \sqrt{\frac{2 N_{ptot} \bar{u}_e}{\alpha_e \mathcal{U}}}, \tag{7.6}$$

$$\bar{u}_{eopt} \propto \frac{N_{ptot}}{\alpha_e} L' \sqrt{\frac{C}{L_0}}. \tag{7.7}$$

This final relationship should be expected since the payload mass fraction increases with greater performance if the efficiency is linearly proportional to the exhaust velocity. In other words, a larger optimal exhaust velocity leads to more payload mass. For typical values of N_{ptot}, α_e, etc., the optimal exhaust velocity is between 10 and 100 km/s.

It is interesting to note that the lifetime of the device and the specific mass of the capacitors play as important of a role as the GFPPT Characteristic Velocity, $\mathcal{U}$, in determining the optimal mass of the propulsion device. This, along with other trends found in the data, suggest other important guidelines for designing GFPPTs:

- Any change in a GFPPT design which results in higher performance should also be judged on its effect on the lifetime and specific mass of the thruster.

- The fixed masses: electrodes, packaging, etc. should be kept as small as possible, especially for high exhaust velocity values where the propellant mass will be a small fraction of the spacecraft.

- Care must be taken to minimize the surface area of any insulator that is exposed to the discharge to minimize wall losses and erosion.

- Discharge initiation plays a critical role in determining the performance and lifetime of GFPPTs. New low-mass discharge initiation schemes that provide a reliable, uniform, and symmetric breakdown need to be investigated further.

7.5 Future Directions in GFPPT Research

Again, perhaps the largest remaining question to be answered about GFPPT performance scaling is how the thruster performs at higher energy levels and with different propellant types. The effect of these parameters on the value of the critical resistance ratio, ψ, and the corresponding values of the performance will be important to study in future work on GFPPTs. In general, understanding how the effective plasma resistance and ψ scale with mass bit, energy, current level, and geometry is important, and will involve detailed studies of the plasma physics involved in the discharge.

Two other important research areas involving GFPPTs are currently being studied at EPPDyL. They include investigating the scaling of the profile and sweeping efficiencies in parallel-plate thrusters using various propellants [60], and investigating a new discharge initiation scheme that could provide a more uniform, symmetric breakdown with less erosion.

From the scaling relations and performance data presented in this thesis, GF-PPTs could be made useful for a variety of missions. Unfortunately, the ultimate performance of these low-energy GFPPTs is not as good as other electric propulsion systems (such as the Hall or ion thrusters) that operate above 1 kW. Yet in missions where the power is limited or the propellant type is unique, the performance of GFPPTs may be significantly better than other alternatives. Furthermore, its low impulse bit capability may be valuable for missions where fine-pointing maneuvers are critical. Still, with its relatively low impulse-to-energy (or thrust-to-power) ratio and high exhaust velocity (specific impulse), the use of GFPPTs will probably be limited to missions that have large ΔV requirements and maneuvers that do not have short time constraints. With all this in mind, GFPPTs could prove to be very useful for DARPA's Orbital Express mission where water vapor will be available as a propellant, constellations of small satellites such as the Terrestrial Planet Finder that will need to stay in a vary precise formation, and deep space exploration missions such as the Pluto Fly-By or Europa Orbiter that will use low-power nuclear sources because of a lack of solar power.

With more research investigating the nature of the conductivity in the current sheet, the cause of canting and profile loses, and potential alternatives for better discharge initiation, GFPPTs could be made useful for even more missions in the future.

Appendix A

Detailed History of GFPPT Research

This appendix provides a detailed account of the prior research related to GFPPTs, both theoretical and experimental. Although the focus is on performance scaling studies, other, more general research regarding GFPPTs is also included in the last section on current sheet structure.

A.1   Theoretical GFPPT Performance Studies

Researchers in almost every program studying gas-fed pulsed plasma thrusters used an acceleration model that consisted of an effective circuit equation representing the discharge elements, and a momentum equation that usually included a coupling term between the motion of the discharge and the effective driving circuit. It is this driving term that makes the one-dimensional, ordinary differential equation set non-linear. This also makes the equations impossible to solve analytically without making some severe approximations to uncouple the equations. In general, there are two classes of solutions, those using a constant mass (a "slug" mass approximation) and those including the sweeping up of mass as the current sheet progresses like a "snowplow." Whereas much of the previous work has focused on using one or two solutions of the equations that match a particular accelerator configuration, the final approach developed in Chapter 3 encompasses solutions to many different cases. The purpose there was to identify scaling *trends* that can be verified experimentally over a wide range of conditions. In this section, we will review the previous work in more detail.

In one of the first papers presenting an acceleration model for linear plasma thrusters, Mostov and others at Republic Aviation used a non-dimensional slug model for the propellant, thus eliminating any dynamic efficiency effects [42]. As in similar models of this type, they did not include any effects of plasma resistance, wall effects, or radiation, considering them to be insignificant losses. They did include, however, a linearly distributed resistance for the electrodes as their

161

early devices had quite long geometries. They developed two cases depending on the duration of integration, yet they did not require a computer to solve the equations. Their "long time" model used asymptotic analysis to integrate the circuit and momentum equations out to an infinite time later. As any solution to the these equations provides a damped current waveform, the current will be zero and the velocity will be constant at the end of an infinite integration period. Using this technique, the energy stored in the magnetic field and capacitor are also, by definition, non-existent at the end of the integration. At t=∞ the relation given for the efficiency is,

$$\eta_t = 1 - \frac{2}{1 + \sqrt{1 + EL'^2/2m_{bit}R^2}}; \ t \to \infty. \tag{A.1}$$

This "long time" solution includes the effects of changing inductance, but it does not include the effects of crowbar discharges typically found in accelerators with an oscillatory current waveform.

The "short time" model assumed that the sheet motion was weakly coupled to the external circuit, i.e., that the inductance was *constant* over the first half-cycle of the current. This assumption makes the problem linear with separate, analytical solutions to the circuit and momentum equations. Again assuming a slug mass with a constant resistance for the electrodes,

$$\eta_t = \frac{1}{8}L'^2 \frac{E}{m_{bit}} \frac{1}{R^2} \approx \frac{1}{2\sqrt{2}} \frac{L'}{R} \bar{u}_e. \tag{A.2}$$

Solutions including the effects of a linearly increasing electrode resistance introduced only a small correction, and, more importantly, provided an optimal initial inductance for the best performance,

$$(L_0)_{opt} = \frac{R^2C}{9}, \tag{A.3}$$

where L_0 is in Henrys, C is in Farads, and R is in Ohms. Below this value, the performance was seen to be relatively constant or decrease slightly with L_0, while above this value the performance dropped off considerably. It is interesting to note, however, that the initial inductance *does not* enter into either of their efficiency scaling relations, presumably because it has been set at this optimum value. In addition, setting the initial inductance to this value leads to considerably overdamped current waveforms with $\psi = 3/2$. Both Eq. (A.1) and Eq. (A.2) show a monotonic increase in efficiency with increases in inductance-per-unit-length and energy, and decreases in mass bit and external resistance. The relative effect of each of these parameters, however, is slightly different in the two equations.

In a NASA Lewis technical report, Ref. [80], another slug model which was non-dimensional included a slight snowplow-like effect for mass that was eroded

from the electrodes and accumulated as the current sheet progressed. As can be expected, the performance in this model strongly depended on a mass ablation coefficient that determined the ratio of ablated mass to injected propellant mass. The overall trends, however, showed a familiar global result with the highest predicted performance corresponding to large values of inductance-per-unit-length, initial voltage, and capacitance as well as small values of initial inductance,

$$\eta \propto \frac{L'^2 V_0 C}{2kL_0},\tag{A.4}$$

where k is the ratio of the ablated mass to the propellant mass.

The earliest (and perhaps most frequently referenced) work which proposed that the current sheet acts like a "snowplow" can be found in Ref. [81] where Rosenbluth examined an infinitely thin sheet with infinite conductivity in a z-pinch device. In research at Princeton, a similar model was used to investigate the sweeping efficiency and crowbar breakdown timing [53]. There a parameter, β, was found to determine many aspects of the discharge dynamics,

$$\beta = \frac{\mu_0 Q_0^2}{4\pi^2 \rho_0 r_0^4} = \frac{\mu_0 h C E}{2\pi m r_0^2},\tag{A.5}$$

where Q_0 is the initial charge on the main discharge capacitor bank, ρ_0 is the ambient density before the pulse, m is the total propellant mass in the z-pinch chamber before the pulse, r_0 is the outer radius of the z-pinch, and h is the height between the electrodes. In Eq. (A.5), the sign of beta has been reversed to remove the inward (negative radial direction) motion of the current sheet in the z-pinch geometry. Experimental measurements of the pinch time and current showed that the pinch occurred before subsequent crowbar discharges for $|\beta| > 0.2$ over a wide range of ambient density and discharge energy values. The sheet speed was, in general, observed to depend on the square root of the energy-to-mass ratio [52] with all other parameters constant, which implies,

$$\bar{u}_e \propto \sqrt{\frac{2\beta r_0}{\sqrt{L_0 C}}} = \sqrt{\frac{E}{m}\frac{\mu_0 h}{\pi r_0}\sqrt{\frac{C}{L_0}}} \approx \sqrt{2L'\frac{E}{m}\sqrt{\frac{C}{L_0}}},\tag{A.6}$$

$$\eta \propto L'\sqrt{\frac{C}{L_0}}.\tag{A.7}$$

Although this scaling relation was not developed in either reference, and no impulse measurements were made to confirm this efficiency scaling, it does follow from their modeling and experimental results. As discussed in Ref. [53], the β parameter also seemed to effect the sweeping efficiency with higher beta values leading to more effective, snowplow-like behavior.

In 1962, Hart examined both a slug and uniform mass distribution with a variable current sheet thickness and finite conductivity [37]. He used a computer to numerically integrate the equations simultaneously for three cases corresponding to the three thruster geometries he was testing. He showed, as expected, that when compared to uniform distributions, not as much energy goes into internal modes of the plasma for slug-like distributions. Current waveforms predicted from this model were close to critically damped in character, indicating a large rate of inductance change which, in reality, would require long electrodes. In the uniform mass distribution, Hart found very different current waveforms depending on gas density. He also showed that a snowplow model could be modified slightly to account for the finite thickness of the current sheet and the gradually increasing magnetic fields within the sheet. The correction factor turned out to be small unless the thickness of the current sheet was almost on the same order as the thruster electrode length. This is not the case in almost all the capacitively driven thrusters examined experimentally.

In the most advanced "circuit-model" studied before this research work, Michels (again at NASA Lewis) combined a non-dimensional model with a parametrically distributed propellant mass that varied between a uniform fill or a slug mass [43]. As opposed to previous work, this model used the final conditions (inductance, current sheet position, etc.) to normalize the equations, thus removing the difficulty of determining the end of the integration. He included terms for ionization energy losses, radiation losses, wall drag due to ion diffusion, and heat transfer from the plasma to the electrodes by adding a plasma energy equation to the normal circuit and momentum equations. This formulation required the following assumptions:

- The "wall drag" included the loss in forward momentum from ions diffusing to the walls and recombining. The amount of diffusion was based solely on plasma temperature and not current conduction.

- The internal energy of the plasma and all the associated loss mechanisms were only a function of temperature. Energy is transferred to the plasma from the mass accumulation process and ohmic heating. Energy was assumed to be lost from the plasma through heat conduction and ion diffusion to the electrodes, ionization, and radiation[1].

- There were no terms that represented the conversion of electrothermal energy into directed kinetic motion. The plasma energy equation included only internal modes and had no enthalpy term.

---

[1]It was noted by Michels, however, that although ohmic heating, ionization, and radiation losses appeared in the equations, those terms were removed as "small contributions" for the solutions presented in the paper.
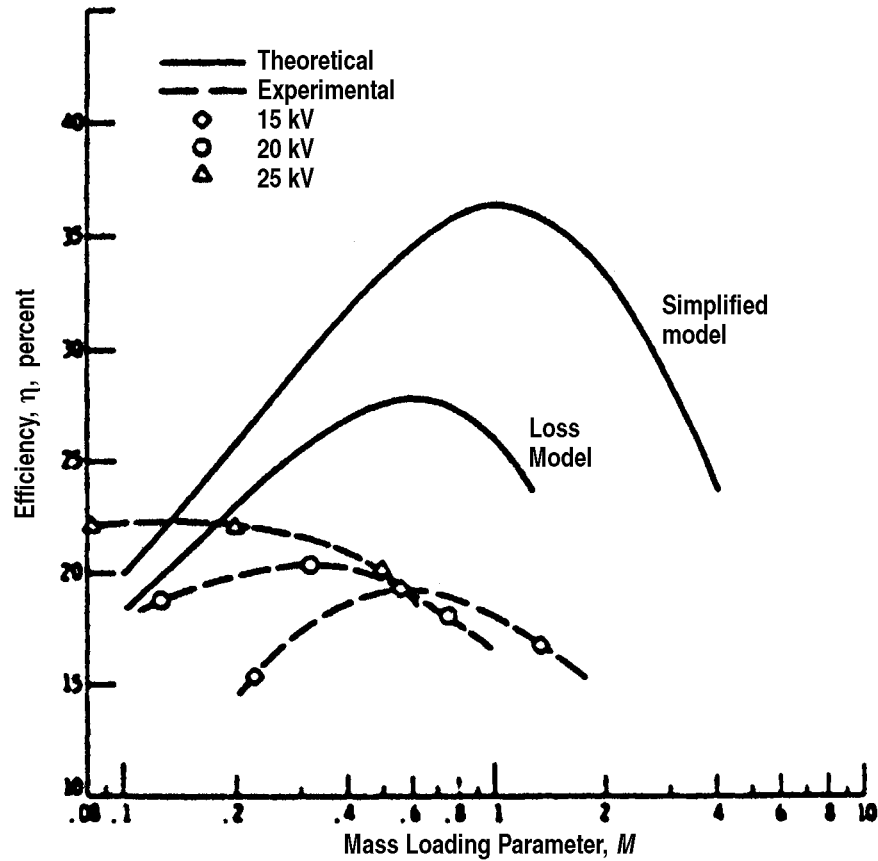
Figure A.1: Graph of efficiency vs. mass loading parameter (see Eq. (A.8)). The graph includes theoretical curves (both simple and advanced) and measured performance data (calorimetry) from "Gun D" using argon at 15, 20, and 25 kV (1.4, 2.4, and 3.8 kJ). Taken from Ref. [43] which describes the NASA Lewis modeling and experimental program.

Unfortunately the initial temperature was not specified explicitly in Ref. [43] and no profiles for plasma temperature were mentioned or displayed to compare with experimental measurements. The effects of introducing the plasma energy equation were present in comparing the results of the more advanced model with one that did not include these losses, as shown in Fig. (A.1). In this graph as well as others in his paper, the "mass loading parameter" was used as the dominant variable parameter,

$$\mathcal{M} \equiv \frac{2\ell_{elec}m_0}{L'Q_0^2} = \frac{\ell_{elec}m_0}{L'CE} \tag{A.8}$$

which includes the mass in the initial discharge, m_0, the initial energy charge on the capacitor, the capacitance, the inductance-per-unit-length, and the length of the electrodes, but interestingly, *not how the mass is distributed before the discharge*. Going back to Fig. (A.1), the efficiency is found, in general, to follow a similar trend in the more complex model, peaking at a different mass loading parameter than that predicted by the simplified model. The relative loss is smallest at small values of the mass loading parameter. Unfortunately the non-dimensional scheme used the electrode length and the final inductance as the scaling parameters which makes it difficult to examine the influence of the initial conditions on performance independently. In addition, with the experimental value of the mass loading parameter strongly dependent on the initial mass taken up by the current sheet, it is a very difficult quantity to determine and control in real GFPPTs.

In comparing the simple and complex models, Michels suggested that the largest loss in the plasma energy equation comes from ion diffusion to the walls. He proposed, based on his results, that radiation losses are negligible, removing them from the solutions entirely. He explains that the true character of the radiation is difficult to determine in these very non-equilibrium plasmas and may be more significant than his model suggests. Although he admits that radiation cooling could play a significant role in determining the plasma temperature, the results did not seem sensitive to it. Without more information on the temperature profile as a function of time, it is hard to say if the plasma energy equation and the associated assumptions were reasonable. Certainly the effects of radiation limiting the plasma temperature are well known in these devices [2, 83]. Adding more complexity, possibly including empirical constants or other experimentally measured loss parameters, has the potential of improving the model. Added complexity, however, may cloud the visible performance scaling trends unless the implementation provides a way to independently examine its effects.

In including the possibility of crowbar discharges, the simplified model was used to examine the effects of crowbarring when the current is zero (no energy is stored in the magnetic fields) and when the current is maximum. In general, the effects of choosing an appropriate crowbar time were very pronounced with up to 40% performance reduction predicted using the "maximum current" crowbar

time. Experimentally, the crowbar time was seen to depend on accelerator geometry, especially near the breech. Later geometries at NASA Lewis included an "inhibitor ring" that delayed the crowbar discharge to a time when the total current was smaller. It should also be noted that the most advanced model at NASA Lewis did not take crowbar discharges into account.

Andrenucci and others in Italy followed almost the same exact non-dimensional scheme as Michels' simplified model in their studies [82]. Their model, however, also assumed infinite conductivity of the plasma and driving circuit leaving the expanding current sheet as the only impedance. This assumption led to underdamped waveforms in almost every solution. A Gaussian propellant distribution was also examined and produced a result similar to the mass-loading distribution used by Lewis. The main contributions from the research were the following: 1.) as the models were developed in 1972, computers were far enough along in their development to provide a large number of solutions over a wide range of parameters, and 2.) a second, quasi-2D model examined the non-uniform Lorentz force in coaxial accelerators and found very different current sheet profiles depending on the *radial* propellant loading. It did not suggest an optimum load, however, and did not make any correction for the anomalous canting effect noticed in many coaxial geometries discussed previously. The results for the one-dimensional model were similar in character to Michels' results with an optimum mass loading parameter.

Other research laboratories have developed sophisticated *numerical* models, mainly for studying APPTs [99–101]. Although these may provide the most accurate simulations of the discharge, they are quite complex and require a significant amount of time to reach a solution. For that reason, these codes have not been used to study performance *scaling* over a wide range of operational parameters.

In summary, very different scaling relations have come from the collected body of GFPPT model research. Depending on the initial conditions and assumptions, the performance has been shown to depend on different powers of the inductance-per-unit-length, capacitance, initial inductance, energy, mass bit, and total circuit resistance. More complex models have shown more complex scaling relations, and some models have been made so complex that they can only simulate very few cases. There is still a need for a clearer understanding of the true scaling relations. A model needs to be developed that effectively shows the correct trends, yet it must not be so complex as to apply only to a limited number of cases.

Jahn included a comprehensive study of acceleration models in Ref. [2]. Based on published work of similar models, he used a non-dimensional approach based on the initial conditions for a parallel-plate accelerator. He examined the current waveforms and resulting current sheet trajectories for both slug and uniform propellant distributions. In the work presented in this dissertation in Chapter 3, we started with this formulation as a base and expanded the application to include an exponential mass distribution based on kinetic theory, flared as well as finite

length electrodes, and crowbarring effects. We used these models to predict the performance scaling of low-energy GFPPTs and compared them to performance measurements in Chapter 6.

A.2 Experimental Performance Scaling Studies

Although many GFPPT experimental performance scaling studies have been completed, most of them, unfortunately, have not been controlled experiments. That is to say that instead of varying only one parameter (capacitance, for example) at a time, most researchers enacted many changes at once, sometimes without even realizing it. For example, Hart began using inner electrodes with smaller and smaller radii to determine the effect of inductance-per-unit-length, but at the same time he exposed more insulator (Teflon) surface area, thereby increasing the ablation and effecting the performance. With these multi-parameter changes, any conclusions cannot be attributed to a specific change in one parameter and the *exact* scaling relation is unclear. In this section, we present the two most carefully designed performance scaling experiments.

At General Electric, Gloersen and Gorowitz made multi-parameter modifications [78] until a final design was completed. In tests with this thruster, the efficiency was shown to be linear with exhaust velocity over a wide range of mass bits (smaller mass bits gave higher efficiency) with a relatively constant thrust-to-power ratio near 20 μN/W at relatively constant capacitance and discharge energy levels [39]. Gloersen and Gorowitz also conducted a performance survey over five different capacitance values from 50 to 200 μF at a constant specific impulse. Although the trend was not identified in Ref. [102], the performance scaled with the square root of the capacitance to within 5-10%. It should be noted, however, that the performance measurements at GE have the possibility of including facility background contamination (See Ref. [79]) which has been shown to increase thrust stand performance by as much as a factor of two [75, 88]. This may add doubt to their *absolute* performance measurements, but perhaps their *relative* scaling trends are more acceptable. In any case, the trends should be re-examined in a clean facility with proper thruster conditioning as was done for the experiments presented in this dissertation.

Hart may have been the first one to realize that a solid-propellant Teflon thruster could have space-flight applications in 1964 (see footnote in Ref. [41]). Although he tested a variety of geometries, capacitance, inductance, and mass bit values, unfortunately all of his experiments were influenced by the ablation of a significant amount of Teflon from the backplate. With gas propellant mass bits between 10 and 500 μg and discharge energy levels being 1 kJ or higher, the majority of the discharge could easily have been made up of Teflon at the lowest, middle, and even highest mass bits for the small inner electrode diameters he used. Although his

computational models are valid (except possibly the modified form of the snow-plow model which was made to fit experimental results in Ref. [41]), the results from streak photos can be questioned. In his configuration with coaxial electrodes, the photographs do not distinguish the *radial* position of the current sheet at the anode and cathode. Hence, the current sheet profile is not included and the experimental results do not provide an adequate comparison or verification of the models [37]. The "Mode II" operation Hart observed showing the fastest sheet speed is probably a result of a canted current sheet leading down the center electrode (anode). In this case, the current sheet would appear to move much faster than the true plasma center-of-mass. Unfortunately, Hart did not use a thrust stand to measure the impulse.

In general, all the models and experimental evidence point to using high-voltage, high-capacitance (hence high-energy), high-inductance-per-unit-length, low-mass discharges with a minimum of parasitic inductance or resistance and short electrodes. Current sheet permeability, propellant utilization efficiency, and the potential problems of crowbar discharges are important to consider when designing the driving circuit as well. Discharge symmetry is probably a result of proper discharge initiation. Yet, with all of these research programs, specific and experimentally verified scaling models that are required to effectively design and optimize GFPPTs remained unavailable prior to this dissertation.

A.3 Investigations of Current Sheet Structure

Although the specific nature of the current sheet has not been the main topic this dissertation, it is important to understand the related acceleration processes. Moreover, many of these measurements have been made in the past using similar higher energy devices. In fact, two laboratories made investigating the current sheet structure their primary task in the 1960's. One was the Atomic Physics Laboratory at General Dynamics headed by Lovberg, and the other was the Electric Propulsion Laboratory at Princeton headed by Jahn. Both projects provided very detailed theories and measurements from which a picture of current sheet structure can be formed. The structure of the discharge in low-energy GFPPTs is believed to be similar to the structure seen in higher-energy GFPPTs as there are similar peak current and *energy-to-mass bit* conditions in both experiments. We will now review the most significant current sheet structure research at the two laboratories.

A.3.1 Current Sheet Structure Research at General Dynamics

In the current sheet studies at General Dynamics, Lovberg used electric and B-dot probes [45, 103] as well as Schlieren photography to investigate the nature of the current sheet and acceleration process in both parallel-plate [46] and coaxial [50]

geometries using mainly hydrogen for propellant. One of the main questions he was trying to answer was if the current sheet behaved as a "magnetic piston" or as more of a strong shock-wave.

In the parallel-plate geometry, he saw a very planar, thin current sheet that had an electron density ten times that of the ambient pre-pulse density. In addition, probe data showed that the arrival of the magnetic field at the probe location agreed well with the visual indications of the front. He concluded that the sheet *did* behave as a piston effectively sweeping up all the gas in front of it. He also found a strong polarization field within the sheet and speculated that the electrons were conducting all of the current, experiencing a Lorentz force which then slightly separated them from the ions. The polarization field that develops as a result of this very slight charge separation was measured to be enough to explain the subsequent ion acceleration. Using gases such as nitrogen and argon, however, he saw the sheet "bifurcate" near the anode with the bulk of the current being carried by a slightly canted sheet, anode leading cathode. He did not study this phenomenon in depth but suggested that it was a result of the higher molecular weight, and subsequent larger gyro-radii, of nitrogen and argon molecules. Regardless of propellant, Lovberg also noticed a thin but strong density gradient in a small layer all along the cathode surface. This suggested that, although most of the propellant mass was being accelerated, some of the ions near the cathode were being left behind.

In the coaxial geometry using hydrogen, nitrogen, and argon, he saw very different features depending on electrode polarity and molecular weight. In some of his earliest papers using hydrogen, Ref. [45, 103], the center electrode was at negative potential (cathode) and the current sheet seemed to be planar from magnetic field probe measurements. With the sheet speed (measured from probe data) being about twice that expected from a snowplow model, and the fact that the current sheet itself was *not* bowed outward as would be expected due to the $1/r^2$ Lorentz force profile typical of a coaxial thruster, he concluded that the sheet behaved more like a strong shock in this case. Electric field data showed a similar polarization field to that seen in the parallel-plate geometry, however, it dropped off towards the outer electrode. Although this might be expected with a non-uniform Lorentz profile, the polarization field was no longer strong enough for the ions to be accelerated to the observed sheet speed near the anode. In another coaxial experiment with the reverse polarity, Lovberg examined the sheet structure using a Schlieren technique with a slotted outer electrode [50]). Here the current sheet was seen to separate into two layers. The thin, leading sheet was seen to bow out along the center electrode as should be expected by the non-uniform Lorentz force in a coaxial accelerator. In a second, more planar and diffuse layer, he observed a small amount of radial current, possibly due to ion conduction at the cathode. Integrating the gradient information from the Schlieren data showed that the electron

density was about the same as the ambient conditions indicating that, again, the current sheet *did not* behave like a piston, rather like a strong shock. A possible explanation for this behavior included a significant ion current which could leave a large number of recombined molecules near the cathode moving much slower than the sheet. The presence of strong radial density gradients near the cathode seemed to agree with that theory.

The coaxial thruster tested by Lovberg showed some interesting features depending on polarity. Although Schlieren photos showed a front that seemed to expand depending on the Lorentz force (bowed outward near the inner electrode) regardless of polarity, electric probe data for the cathode-center configuration showed a very planar current conduction zone. It could be possible that in the negative polarity the non-uniform Lorentz force profile is balanced by some other effect that normally causes canting with the anode leading the cathode. Other researchers have also seen different current sheet structure from changing the polarity of a coaxial geometry [49, 56] although the current sheet speed *was not* found to be a strong function of polarity in Refs. [37, 38, 50]. The performance could still be affected, however, by the non-axial acceleration of the plasma, thus leading to a tilted current sheet.

A.3.2 Previous Current Sheet Structure Research at Princeton

Three Ph.D. theses [54, 104, 105] and three journal publications [47, 48, 106] by Burton, Ellis, and York, respectively, with Jahn as the lead investigator examined the structure of the current sheet through electric and magnetic field probing, microwave interferometry, and fast-response pressure measurements in a linear z-pinch with argon. Reference [48] provides a good summary of the research as it was published after all the work had been completed. All of the measurements discussed here were taken at the midline of the z-pinch apparatus and at a radius half-way between the outer insulator and the center axis. Similar results have also been observed in other pulsed accelerators with different geometries.

First, the authors' use a generalized Ohm's Law in the frame of the moving current sheet (note: the current sheet moves in the *radial* direction in a z-pinch),

$$\vec{j} = \sigma_0 \left(\vec{E} + \vec{v}_i \times \vec{B} + \frac{\nabla P_e}{n_e e} \right) - \frac{\Omega_e}{|B|} \vec{j} \times \vec{B}, \quad (A.9)$$

where $\vec{v}_i$ is with respect to the current sheet velocity, and $\vec{E}$ is the net field including the applied field and the back EMF contribution from the moving sheet (all other symbols have conventional definitions). Note that the Hall conductivity for the electrons (but not the ions) was included because the chamber dimensions were assumed to be much larger than the electron gyro-radius, but smaller than the ion gyro-radius for argon propellant. Also, the effects of ion-slip (sheet permeability) were not included, and an assumption of complete, single ionization
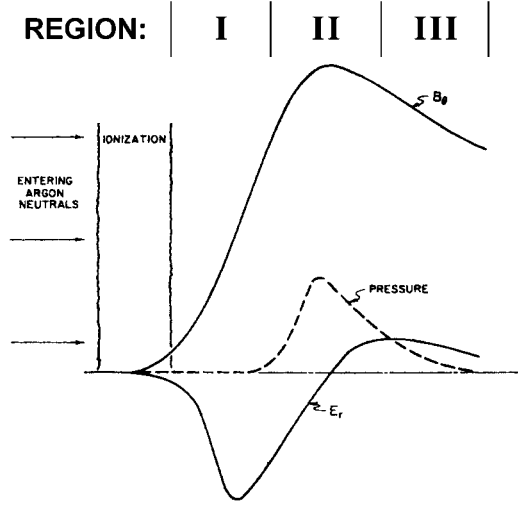
Figure A.2: Radial electric field, azimuthal magnetic field, and heavy species pressure profiles in the current sheet frame. Taken from Ref. [47] with modifications to show regions identified in Refs. [48, 106]. The area of expected pressure increase was confirmed in Ref. [106].

occurring as soon as the molecule enters the sheet was held throughout the publications. The electric and magnetic fields were measured with probes [47] while the scalar plasma conductivity, plasma temperature and density were measured by microwave interferometry [48]. The Hall parameter was inferred from these measurements as was the electron pressure from the kinetic relation, $P_e = n_e k T_e$. Only the azimuthal magnetic field was found to be significant while, similarly, only the radial and axial components of the electric field were found to be important. In the frame of the current sheet, the radial ion velocity was assumed to start at sheet speed (measured from streak and Kerr-cell data as well as probe arrival time data) and slow down to zero, eventually traveling with the current sheet. As the axial current density is known from total current measurements as well as magnetic field probe data, only two unknowns remain: the radial current and the axial ion velocity. Measurements of these parameters as a function of time as the current sheet sweeps by are presented in Fig. (A.2).

It should be noted that the axial electric field is very nearly balanced by the back EMF of the moving current sheet so that the axial electric field actually dominates the conductivity in the current sheet frame of reference. As seen from the measurements in Fig. (A.2), three general regions characterized by the derivative of the *radial* electric field exist within the ≈ 1 cm thick current sheet. In Region I, the radial electric field is in the direction of current sheet propagation and is very large. It is caused by the separation of the electrons caught on an $E_r \times B_\theta$ drift

while the ions have a large momentum and penetrate deeper into the sheet with only a slight deflection towards the cathode. This radial electric field slows down the ions into Region II, however with argon propellant, it *is not* enough to slow the ions down completely to sheet speed. Region I was found to be dominated by axial electron current making up a significant fraction of the total current, but it did *not* account for the *entire* current. Region I was found to be about 5 mm thick for argon. As the separation of the ions and electrons induces a radial polarization field, it also creates a radial current. This radial current, although relatively small, interacts with the azimuthal field enough to cause the ion trajectories to deflect more towards the cathode. In Region II, with the ions now moving slower and slightly deflected, *axial ion current* dominates through ions recombining on the cathode surface to complete the total current. Burton suggested that this produces a $j_{iz} \times B_\theta$ that further decelerates the ions (in the frame of the current sheet) to sheet speed. Region II was also found to be the location of a large heavy species pressure gradient by York. As the radial electric field reverses sign in Region II, the electrons actually try to drift against the current flow. With the greater ion density, however, collisions dominate and they remain relatively stationary with respect to the sheet. In Region III, the axial electric field is still negative, although smaller and returning to zero. As the ion density is low here, there is actually the possibility of a small reverse current being carried by the electrons in the trailing edge of the current sheet. The total sheet was found to be about 1 cm thick at the center line with a slight tilt, anode front leading cathode. At that time, no explanation was given for the tilt besides that it should depend strongly on the propellant molecular weight and possibly the electron Hall parameter. Other, more recent research at Princeton is examining the causes of current sheet canting and permeability in more detail [60].

Appendix B

Facility Improvements and Testing Procedures

This appendix describes the renovation of the Pulsed Performance Measurement Facility (also see Ref. [75] by Ziemer et al) and the techniques used to calibrate the performance measurement diagnostics. The renovations were performed between October 1998 and March 1999 to reduce the contamination from diffusion pump oil during GFPPT testing. The renovations included the following:

- Repairing surface cracks in the fiberglass polyester coating to obtain higher levels of vacuum.

- Modifying existing baffles to accommodate liquid nitrogen cooling.

- Improving the existing thrust stand to increase its resolution.

- Developing new calibration techniques to improve the accuracy of performance measurements.

These modifications and the testing procedures for measuring performance will be described in this appendix.

B.1   Vacuum Chamber Cleaning and Repair

The vacuum vessel used for this study is a 2 m diameter, 5 m long fiberglass tank (shown in Chapter 5, Fig. (5.1)) which is pumped to high vacuum (10^{-5} Torr) by two 48 inch diffusion pumps that are backed by a 1340 cfm roots blower and mechanical pump system. This facility has accumulated over 50,000 hours of operation since it was first evacuated twenty years ago. Experiments performed in this facility have included the use of quasi-steady magnetoplasmadynamic thrusters (MPDTs), ablative pulsed plasma thrusters (APPTs), and many other devices. Over

time, residual mechanical and diffusion pump oil as well as various erosion products from different experiments have built up on the facility walls. During pump down and operation, these contaminants can outgas and affect the performance of low-energy GFPPTs. As part of the facility renovations, the entire interior surface of the tank was cleaned by scrubbing with isopropyl alcohol, effectively eliminating the background contaminants from the walls.

The facility has also experienced some surface fatigue due to pressure cycling. This is apparent from the visual cracks in the gel-coat surface covering the fiberglass flanges and optical ports. The cracks produced numerous small leaks which increased the background pressure and, therefore, the oil back-streaming rate. The cracks were repaired through a process of grinding out the material around each crack and replacing the removed material with three layers of gel-coat epoxy. Care was taken to replace the smooth finish of the flange surfaces, keeping leaks to a minimum. After all repairs were complete, the facility background pressure was reduced by 50% to an operating pressure now normally below 4×10^{-5} Torr.

B.2 Activation of Liquid Nitrogen Cooled Baffles

Further reduction of diffusion pump oil back-streaming and contamination requires active cooling of baffles or traps very near the diffusion pump interface with the facility. The baffles in the fiberglass facility at EPPDyL (shown in Fig. (5.1)) have been in place since its construction, yet they have not been actively cooled until recently. The baffles used here are low-profile fiberglass cones with a copper plate attached on the underside facing towards the diffusion pump. Copper tubing (3/8″ diameter) is attached to the copper plate with small clamps in a spiral configuration. Only two inches separate each turn of the coil, and the total length of the lines is close to 150 ft. for each baffle. Originally designed for a freon-based cooling system, the baffles have been converted for liquid nitrogen cooling by the installation of new cryo-genic feed-throughs and the replacement of all Swagelok fittings with hard-soldered connections. The baffles are connected in parallel for even cooling and have Type T thermocouples mounted to the inlets and outlets of both baffles inside the tank. Liquid nitrogen is supplied for eight hours at a time by a 160 liter portable Dewar that is refilled before each test. Between tests, the baffles are *not* actively cooled requiring a cleaning process before testing as described in Section 5.2.1.

Slightly more than an hour after activation, the baffles reach their lowest operating temperature of at most $-70°$C as measured by the outlet temperature of the baffle cooling lines. The inlet temperature reaches $-180°$C (evaporation temperature of ℓN_2) almost immediately after activation and both baffles generally cool down at the same rate. The background tank pressure typically decreases by 10% due, in large part, to the freezing of water vapor to the baffle surface. The baffle
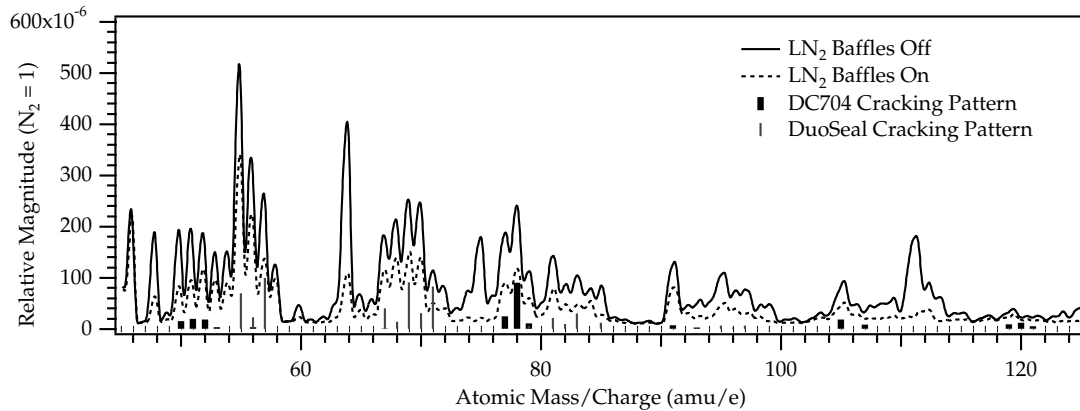
Figure B.1: Mass spectrum of background gases from the RGA with baffles on and off as well as expected DC704 diffusion pump oil and DuoSeal roughing pump oil cracking patterns.

operation and cooling rate are very similar from test to test although the outlet temperature of the baffle is verified to be below $-60°C$ before any testing begins.

B.3 Overall Diffusion Pump Oil Contamination Reduction

To measure the level of background oil vapor, a UTI 100C residual gas analyzer (RGA) was connected to the tank through an isolation valve mounted on one of the optical ports at the end of the tank. The isolation valve was kept closed unless the LN_2 baffles were activated to reduce the possibility of the ionizing filament or faraday cup becoming contaminated. In addition, before making any of the measurements presented in this paper, the entire RGA unit was baked at close to $200°C$ for over 48 hours to remove any contaminants from the gauge walls.

Figure (B.1) shows a typical mass spectrum produced by the RGA just as the baffles were activated and two hours later. This figure also shows the predicted spectra of DC 704 diffusion pump oil and conventional Duo-Seal roughing pump oil both used in the high vacuum facilities at EPPDyL. Many of the peaks shown in Fig. (B.1) match up with those predictions, indicating that diffusion and roughing pump oil vapors exist, albeit at very low levels (partial pressures on the order of 20×10^{-9} Torr) compared to the background nitrogen levels. This data also shows an overall trend of about a 50% reduction in background gases over a wide range of atomic masses. Choosing one atomic mass-to-charge ratio as a representative for diffusion pump oil (78 amu/e) and roughing pump oil (57 amu/e) allows a
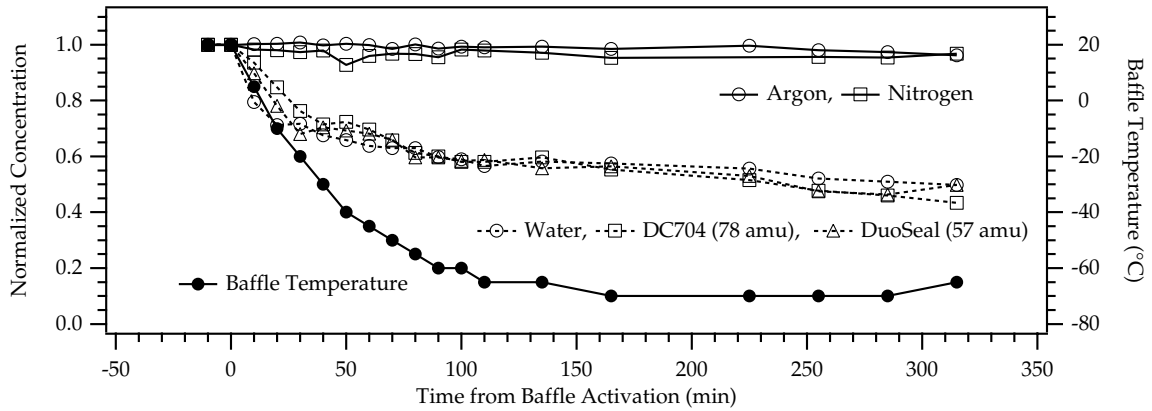
Figure B.2: Baffle temperature and background gases as a function of time from baffle activation.

quantitative assessment of background vapor level during baffle cooling. These two levels were chosen from a list of maximum peaks in various cracking patterns. A graph showing the reduction of oil and water vapor as a function of time and baffle temperature is shown in Fig. (B.2). Again, this shows approximately a 50% reduction of possible contaminants after the baffles have been cooling for over 100 minutes down to a temperature of $-60°C$. This reduction level was confirmed by opening the RGA isolation valve for a short time after the liquid nitrogen cooling was deactivated and the baffles were allowed to completely warm-up. The levels measured by the RGA at that time returned to the previous value before the baffles were activated.

B.4 Modifications to the Thrust Stand

Originally designed for testing quasi-steady MPD thrusters [94, 95], the thrust stand has undergone the following modifications to measure very small impulses ($< 20\mu$Ns) accurately:

1. The main conductor for the MPD cathode has been replaced by a more elastic coaxial cable. This *decreased* the spring constant, allowing larger displacements from smaller impulses.

2. A laser Interferometric Proximeter System (IPS) has been installed to increase position measurement resolution to better than 10 nm. (For more details, see Ref. [92] and the masters dissertation that documents this device completely, Ref. [96])
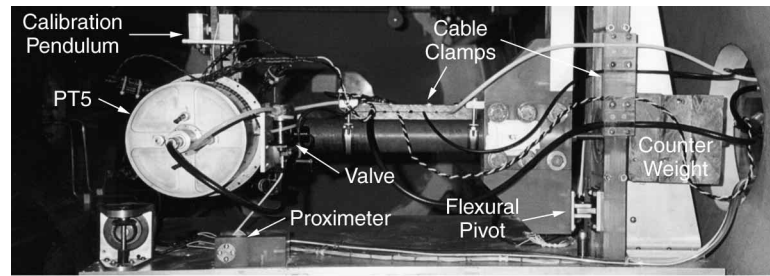
Figure B.3: Picture of the thrust stand from behind and set-up for calibration.

3. Cable clamps have been installed to minimize the neutral position drift and vibrational noise transmittance from the facility during operation.

4. A counter-weight has been installed so that the flexural pivots are located near the center of mass of the thrust arm assembly. This reduces the transmittance of low frequency perturbations from the vacuum pumps and background motion.

5. A variety of materials and vibration isolation schemes have been tested and documented. Currently, the thrust stand is vibrationally isolated from the vacuum tank by thin butyl rubber pads.

6. The calibration and data reduction procedures have been completely revamped and automated to reduce error as described in Section B.5.5.

B.5   Calibration Techniques

This section covers the thrust stand, mass flow rate, and voltage probe calibrations in detail. It provides a discussion of the sources for error in each calibration. As we will see, however, the errors associated with the shot-to-shot repeatability usually dominate over the calibration errors.

B.5.1   Thrust Stand Calibration

A necessary parameter to determine the impulse bit from the position history of the thruster is the effective mass. Supplying *known* impulses to the stand along the thrust axis allows the effective mass to be determined from the dynamic equations, Eqns. (5.4) and (5.5). The known impulse is supplied by a Peziotronics A08 force transducer mounted at the end of a steel pendulum arm. The pendulum is lined up along the thrust axis to impact the thruster electrode perpendicular to the support
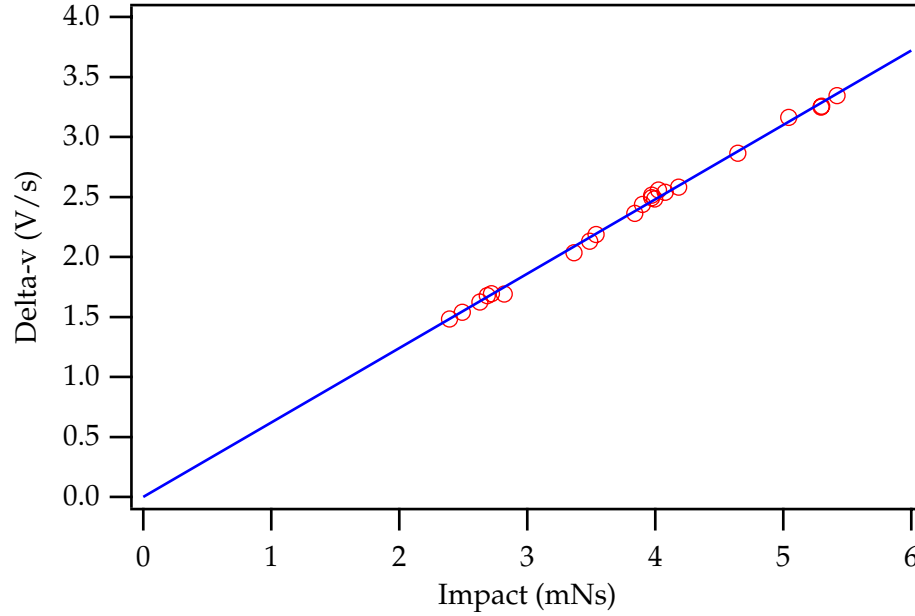
Figure B.4: Effective mass calibration. The effective mass is the slope of the line fit to Impact vs. Thrust Arm Velocity data with a zero intercept.

arm, simulating an impulse from the GFPPT. The pendulum swings so that its tip impacts the center of the thruster electrode to insure the effective mass is calculated correctly. The calibration is conducted at atmospheric pressure and the pendulum is released by an electromagnet triggered from outside of the vacuum tank.

The force transducer has been calibrated at EPPDyL for a force ranging between 0.5 and 100 N (in agreement with the supplied calibration from Peziotronics) and a shows a 87.6±0.6 N/V linear voltage response. The electromagnet can hold the pendulum at a variety of angles to deliver a wide range of impulses to the thrust stand. The force from the transducer is recorded and numerically integrated on a digital oscilloscope. At the same time, the outputs from both the IPS and proximeter are measured and stored on a separate digital oscilloscope with a large enough time base to capture at least three natural periods of thrust stand motion. Dividing the impulse from the force transducer by the velocity change given by the position history yields the effective mass value for that trial. Typically over twenty trials are spread over four different impulse magnitudes to determine m_{eff} within $\leq 2\%$. A graph showing one effective mass calibration with 20 trials is shown in Fig. (B.4).

The effective mass must be determined after any adjustment to the thrust stand has been made. It has the units of kg-m/V and needs to be multiplied by a voltage-to-distance conversion factor (V/m) to produce a *mass* value. This factor is not required for impulse measurements as the delta-v is supplied in units of V/s.

B.5.2   Mass Flow Rate Calibration

The mass flow rate has been calibrated as a function of plenum pressure by measuring the total volume of the plenum and propellant lines, filling them with argon to a pressure of almost 400 torr, and gradually venting them into the vacuum chamber in a controlled fashion. The volume of the plenum was found by filling the plenum with distilled water and measuring the mass and volume of the water. The volume of the propellant lines was found by measuring the length and inner diameter of all the tubing and was < 5% of the total volume; consequently, the errors in this measurement do not contribute significantly to the calibration error. The mass flow rate out of the plenum, through the sonic orifice, and into the vacuum tank is linearly proportional to the plenum pressure for all but the smallest pressure values. During the calibration procedure, the plenum and propellant lines are evacuated in discrete steps by opening the valve in the vacuum tank for a period of 4-20 seconds at a time. The timing of the valve pulses is maintained by using a Stanford DG-535 pulsed signal generator and the SRL pulse modulator. After a short equilibration period, a pressure measurement is taken and the valve is opened again. For this sonic orifice with argon, the mass flow rate for typical operating plenum pressures (between 35 and 350 Torr) is given by $\dot{m} = 28.7 \times P_{torr} - 265$, where the pressure is in torr and the mass flow rate is in milligrams per second. This value is accurate within 1% according to the correlation coefficients for a linear fit of measured pressure vs. calculated mass flow rate, as shown in Fig. (B.5).

The largest source of error in this calibration is from the volume measurement of the plenum and propellant lines. By using a standard volume that can be evacuated, the volume of the propellant lines and plenum was determined in a secondary three step process: 1) the lines and plenum were isolated from the known volume and evacuated, 2) the known volume was filled to half an atmosphere with argon and the pressure was measured with a standard deviation of less than 1%, and 3) the evacuated propellant lines and plenum were then once again exposed to the standard volume, and the new system pressure was recorded. By monitoring the pressure change from filling the plenum and propellant lines, the total volume of the feed system was calculated within 2% of the geometrically measured volume. The final error in the mass flow rate calibration is set at this level, 2%.

Finally, as described in detail in Appendix D, approximately 0.1-0.2 μg of electrode or spark plug material is lost during each pulse in both PT5 and PT9. Although at the lowest mass bit values tested here, 0.2 μg argon, this can be as much as the propellant mass, it is not accounted for in any efficiency calculation. This is done because the erosion rate is thought to be a strong function of the type of discharge initiation and, therefore, not a function of the discharge dynamics. In addition, the amount of the eroded mass actually swept up by the discharge and accelerated is unknown. As described in detail in Appendix D and shown in Section 5.3.1, Imacon photos have demonstrated that much of the erosion may be oc-
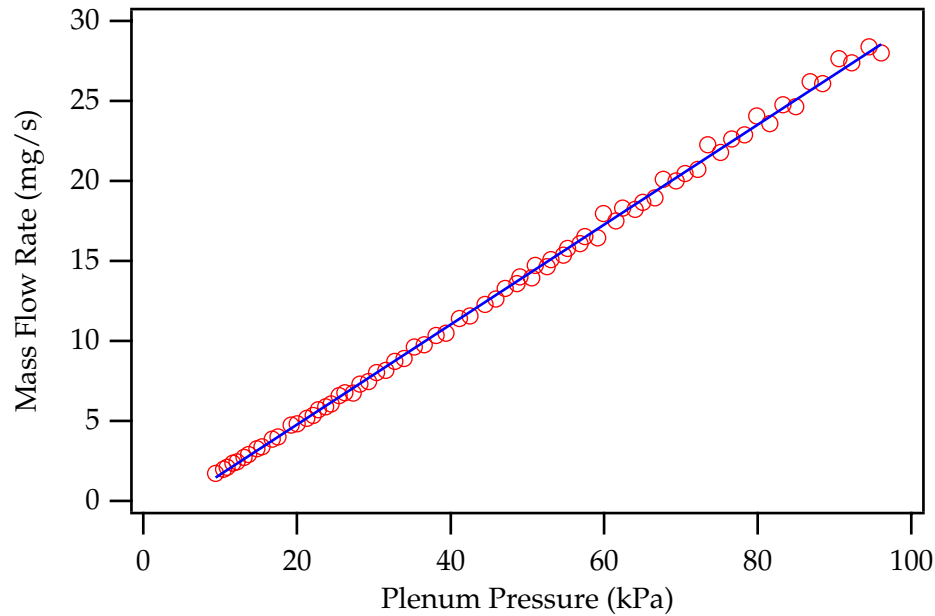
Figure B.5: Sample mass flow rate calibration curve.

curring near the spark plugs well after the discharge is complete. Moreover, even if some of the eroded mass is being accelerated, both the efficiency and exhaust velocity would decrease by a similar fraction. Erosion products, therefore, will not affect the impulse-to-energy ratio because the measured mass bit does not enter into its *calculation*. Once again, the "mass bit" value used in efficiency calculations is only made up of gas propellant.

B.5.3 Voltage Probe Calibration

As pointed out in the section on deducing the current from the voltage waveform, the voltage probe must be carefully compensated for time-accurate data that can be numerically differentiated. Any stray impedances between the capacitor bank terminals and the probe itself could otherwise affect the probe's frequency response. In these measurements, a 1000:1 Tektronix P6015 voltage probe has been calibrated periodically for this application. It is placed at the charging supply outside of the vacuum tank, and the compensator has been calibrated using a 40 V 100 MHz square-wave. Although the current (voltage derivative) is only used to examine trends in the data, the peak value of the voltage before each discharge is important to determine the pulse energy accurately. Because of this, the DC attenuation of the probe is checked routinely with a fixed 250 V power supply. The error in the peak voltage measurement itself (about 4%) actually comes more from electronic

noise in the voltage signal (caused by the spark plugs) than from the probe calibration itself. Care has been taken to supply a common ground to all electrical measurement devices and power supplies without creating "ground loops" that can produce common mode errors.

B.5.4   Automated LabVIEW Data Acquisition

As mentioned at the beginning of this section, all of the performance data presented here are actually average values from a series of trials at the same operational conditions. With the finite time of the liquid nitrogen supply for the baffles (one 160 liter Dewar lasts approximately eight hours), almost the entire performance measurement process was automated to maximize the number of trials in one session. To facilitate this, a LabVIEW virtual instrument (VI) was created that controls the thruster pulsing, the propellant valve timing, and the digital oscilloscopes. The VI can be set-up for hot or cold pulse and will download the appropriate oscilloscope channels accordingly. The energy per pulse and mass bit are set by analog controls that must be actuated manually at the beginning of each series. The VI is designed to store the data in a binary format that can be accessed by a common software package ("Igor") and the data reduction routines as described in the next section. With the automated VI, between 320 and 400 trials (about 8-10 series) can be conducted during one 8 hour session.

B.5.5   Igor Data Reduction Procedures

The digital position and voltage data, as well as the plenum pressure and calibration data, are analyzed by an Igor macro that has been especially written for this application. The program is designed to work with the automated VI described in the previous section in order to keep processing time to a minimum. The user simply enters the directory where the binary data files can be found, inputs the appropriate calibration information, and the macro reduces all of the position and voltage data from one session in approximately an hour. The macro outputs the average impulse bit (both hot and cold), time between pulses, mass bit, exhaust velocity, energy, thruster efficiency, impulse-to-energy ratio, peak current, integral of the current squared, and number of pulses per burst for each trial. After the first five trials in every series have been eliminated (as well as any obvious measurement errors or deviations caused by spurious arc attachments outside of the thruster electrodes), the "gross" average value and the standard deviation of each quantity is determined, saved, and displayed graphically.

Many of the series that will be shown here have been repeated multiple times to ensure that the data are accurate. In addition, the data reduction procedure has been automated to the point where minimal user interaction is required. A

discussion of the errors found in the performance measurements will be presented in the next subsection.

B.5.6 Error Analysis

Individual sources of systematic error have already been discussed in the previous sections on performance requirements and calibrations. Putting these sources together allows the performance measurement error for an individual trial to be calculated.

Impulse Bit

The total error in measuring a particular impulse comes from the effective mass calibration error, the error in measuring the thrust arm velocity just before and after the impulse, and the random low-frequency noise in the position history. Putting these factors together, the average error of an impulse measurement is $< 3\%$ for much of the data presented in this dissertation. The only remaining free variable is the amount of background vibrational noise which can vary slightly from day to day. From numerous measurements, typically the average cold gas impulse from 10 trials has a standard deviation of $\pm 3\mu$Ns out of a typical value of 100 μNs, indicating good shot-to-shot repeatability close to the predicted error value. The standard deviation of the average hot impulse, on the other hand, varies depending on many factors, including the GFPPT itself. This deviation is a result of slight changes in energy, mass loading, and spark plug operation from pulse-to-pulse, as well as the influence of the electrode and insulator surfaces. If the surfaces are dirty, some preferential arc attachment has been noticed to occur at certain locations, especially with the open parallel-plate geometry of PT9. In fact, as the shot-to-shot error is larger than the predicted error on an individual hot impulse measurement (typically 5-8% instead of 3%), it will be conservatively used for further error calculations. It is believed that these larger errors (based on the standard deviation of an average value from a large number of pulses) represent actual shot-to-shot performance more conservatively.

Mass Bit and Energy

As discussed previously, the error in the mass bit (typically about 2%) comes mainly from the mass flow rate calibration as the time between the pulses is fixed. The main source of error in the energy determination (typically about 4%) is finding the peak voltage value just before the discharge. The effects of EMI from the spark plugs are minimized by a digital low pass filter.

Other Performance Parameters

Performance parameters such as efficiency and the impulse-to-energy ratio are calculated from measurements made on *individual* trials before gross averaging at one operating condition. Frequently, when one parameter has a slight deviation, such as the average energy per pulse, there is a strong corollary trend in the others, such as the impulse. Using this correlation reduces the overall error from gross averaging. Shot-to-shot deviations, however, still dominate over systematic error from calibrations and measurement. Therefore, the final error associated with each performance parameter is simply the standard deviation of the average parameter value over at least twenty measurements at the same conditions. Using this method, typical errors for the efficiency, impulse-to-energy ratio, and exhaust velocity are near or less than 10%. Individual error bars have been shown for all performance data where applicable.

Appendix C

Other GFPPT Designs

This appendix describes the other SRL-EPPDyL GFPPT designs, PT6 through PT8 for completeness. They are not, however, used in the performance scaling study due to their complicated electrode geometries. Originally designed for lower-energy (< 2 J) attitude control maneuvers, these designs form the "quad thruster" family as they have four sets of orthogonally mounted electrodes. All performance measurements reported here were conducted at NASA JPL in the Advanced Propulsion Technology Facilities (see Refs. [76,77,84] also by Ziemer, et al.)

C.1   The Quad Thrusters

The quad configuration has the smallest mass of any generation of SRL-EPPDyL GFPPTs to date. Combining four sets of electrodes mounted orthogonally on one 63 μF capacitor storage unit, the latest quad thruster has a mass of 1.6 kg. With an expected control modulator mass of 1 kg, the total mass for the current system would be 2.6 kg (not including valves or propellant tanks) with possibly more mass savings attainable in future generations. PT6 and PT7 are almost identical and can use the same electrode sets with either parallel-plate or coaxial geometry made of either titanium or stainless steel. PT8 uses parallel-plate electrodes specially designed to increase the inductance-per-unit-length. All the quad thrusters have the same capacitance and initial inductance. The mass savings in the latest quad design comes from a reduction in the packaging of the main discharge capacitors. PT6 was used mainly for performance studies while, in parallel, PT7 was used for the erosion rate experiments, as described in Appendix D.

PT8 was used to test the effect of propellant type on performance including tests with argon and water vapor. Compared to the first quad designs, PT8 has three major modifications: it uses a new lower-energy RF system to initiate the discharge, it uses a non-axial propellant injection scheme to reduce the axial cold gas velocity and improve propellant utilization, and it has a set of ferrite blocks
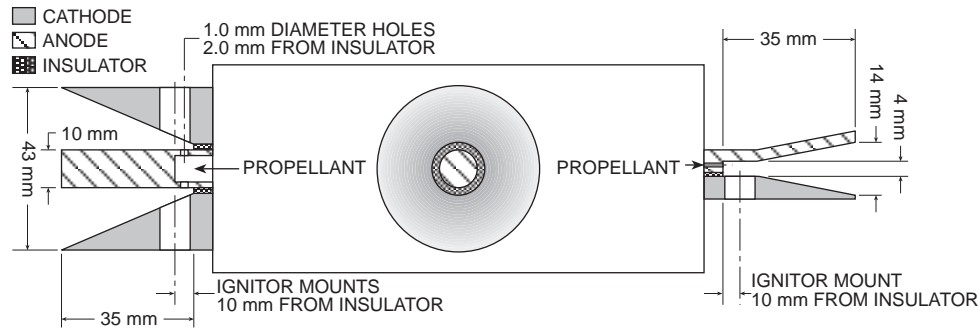
Figure C.1: The quad thruster has three coaxial and one parallel-plate electrode set. In this drawing, the coaxial set of electrodes is mounted on the front, left, and back side, while the parallel-plate set of electrodes mounted on the right side.

around the electrodes to reduced magnetic field fringing effects and increase the inductance-per-unit length. Although the magnetic field of PT8 has yet to be measured, it is assumed that the ferrite blocks will remove the fringing effects of the finite parallel-plate geometry and thus provide a uniform magnetic field with an L' value of approximately 6.3 nH/cm. PT8 has the highest value of L' out of all the thrusters used in this study.

It should be noted that all of the electrode sets actually have a slight flare or expansion which implies that the electrodes in the "parallel-plate" thruster are not actually parallel. In addition, the width of the plates (the outer electrode radius in the case of the coaxial design) gradually increases. The flaring is an attempt to match the natural free-molecular expansion of the gas jet as it leaves the propellant injection holes. Measuring the inductance-per-unit-length accurately, however, is difficult potentially precluding these thrusters from the modeling efforts described in Chapter 3.

C.2   Performance of PT6 and PT7

PT6 and PT7 are practically identical and can use either coaxial or parallel-plate electrode sets for testing purposes, as shown in Fig. C.1. The inductance-per-unit-length has been shown theoretically to play an important role in thruster performance in Chapter 3. The parallel-plate and coaxial electrode sets have a similar total length with an inductance-per-unit-length of approximately 4 nH/cm and 2 nH/cm, respectively. This gives a factor of two for the theoretically expected performance increase of the parallel-plate geometry. In the data presented here, both the coaxial and parallel-plate electrode sets are made entirely of stainless steel. Results from testing both electrode sets are shown in Figs. C.2, C.3, and C.4.
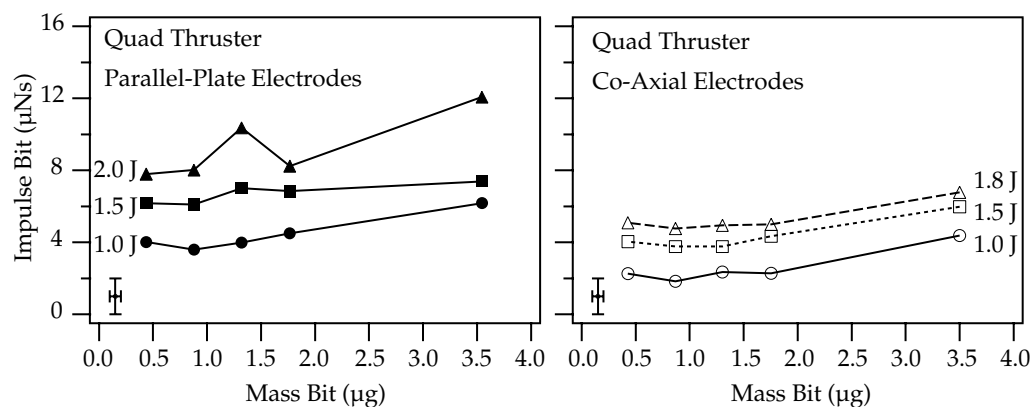
Figure C.2: Average impulse bit of the quad thruster at three different energies and with two different electrode sets. A sample error bar for this data set is also shown.

Figure C.2 shows a graph of the average impulse bit over a wide range of mass bit values. The impulse bit magnitude is relatively constant for each energy level and electrode geometry until a slight increase at the largest mass bit values. The impulse bit also increases linearly with energy level for each electrode geometry. The parallel-plate electrode set shows a higher impulse bit magnitude than the coaxial thruster at the same energy level by a factor of 1.6 on average.

Figure C.3 shows the efficiency of the both geometries over a wide range of specific impulse values. At specific impulse values greater than approximately 300 s, the efficiency is linearly proportional to the specific impulse. Below 300 s, however, the efficiency is relatively constant. The specific impulse values below 300 s correspond to the highest mass bit values. In both geometries, efficiency is not a strong function of energy. The parallel-plate geometry, however, has a higher efficiency magnitude and slope (impulse-to-energy ratio) than the coaxial geometry.

Figure C.4 shows the impulse-to-energy ratio over a range of mass bit values. The impulse-to-energy ratio is generally constant and not a strong function of energy over the range of mass bit values up to the highest value as typical of an electromagnetic accelerator. The impulse-to-energy ratio for the parallel-plate quad thruster is on average higher than the coaxial quad thruster by a factor of 1.6. Although this is not as much as the theoretical prediction based on the larger inductance-per-unit-length of the parallel-plate geometry, it does show a significant increase in performance. The operation below expected performance could be the result of the canting of the current sheet as seen in the Imacon fast framing camera photographs shown in the next section.
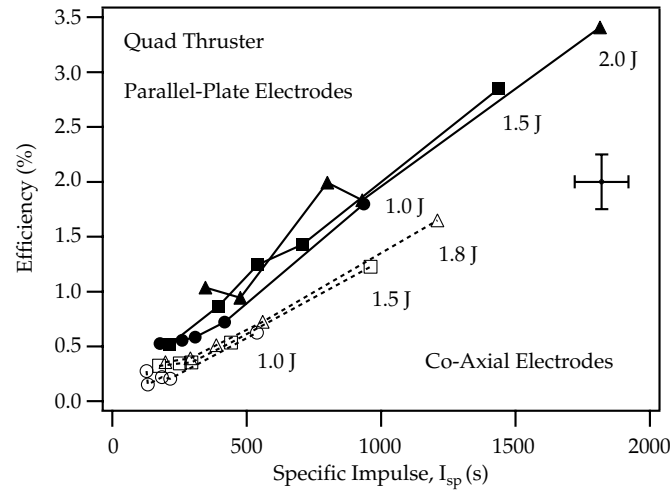
Figure C.3: Efficiency of the quad thruster at three different energies and with two different electrode sets. A sample error bar for this data set is also shown.

C.3   Performance of PT8

The PT6 with parallel-plate electrodes and PT8 were tested over many different mass bits at 2 J/pulse to form a GFPPT performance database using both argon and water vapor for propellant. Measurement errors were kept to a minimum; however, shot-to-shot repeatability led to $> 10\%$ standard deviations on average impulse bit values. Figure C.5 shows the complete performance database plotted against mass bit and specific impulse. The sample error bars given for all the graphs indicate the relative error for a typical data point in the center of the graph. As shown in graph (a) and (b), the highest efficiency, 19%, occurred at the lowest mass bit, 0.07 μg, and highest specific impulse, 12,000 s, using water vapor for propellant in the PT8 thruster. The highest value of impulse-to-energy, 8 μN/W, occurred at the highest mass bit, 4 μg, and lowest specific impulse, 500 s, using argon for propellant using PT8. Overall the efficiency of PT8 is an additional percent higher than tests at similar conditions with PT6 although this increase is within the error bars of the measurements. The impulse-to-energy ratio at the higher argon mass bits was increased close to 20% over PT6 data, yet the impulse-to-energy ratio with PT8 at low mass bits is less. In a narrow range of similar operating conditions for PT8 with both argon and water vapor propellants, it can be seen that the water vapor had a slightly higher efficiency and impulse-to-energy ratio although this trend, again, is close to the limit of accuracy of the measurements.

Putting the data together from operation with both propellants, general trends in performance can be identified. As seen most obviously in graph (a) of Fig-
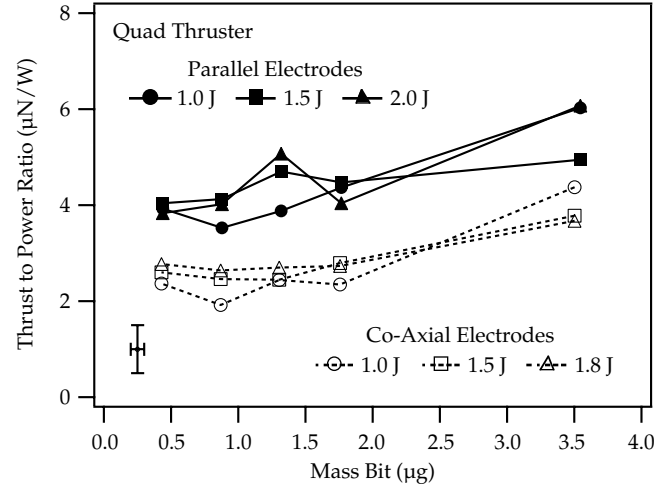
Figure C.4: Impulse-to-energy ratio of the quad thruster at three different energies and with two different electrode sets. A sample error bar for this data set is also shown.

ure C.5, there are two trends or *modes* of operation below and above close to 0.5 μg. These modes have been noticed before with PT5 and allow a GFPPT to be designed around a particular mission. If the mission requires large slew maneuvers or, in general, short duration maneuvers, then a higher impulse-to-energy ratio is important and the thruster should be designed to operate at higher mass bits. If low-power operation and propellant mass is the most important consideration, then the thruster should be designed to operate at low mass bit levels where the efficiency is the highest. In any case, as shown in Ref. [31] and others, these thrusters are suited to missions that require a total change in velocity (ΔV) close to the magnitude of the specific impulse (or about ten times less than the exhaust velocity). Choosing a higher specific impulse for the same mission will decrease the propellant mass to the point where it is not significant compared to the fixed system masses. Choosing a lower specific impulse will increase propellant requirements above their optimum level.

C.4   Effects of Recent Modifications to GFPPT Designs

As mentioned previously, three modifications to the quad thruster PT8 and the thruster pulse control modulator involved changing the propellant loading, adding a pair of ferrite blocks, and changing the discharge initiation system. The effect of each modification was found through experimental measurements of change in
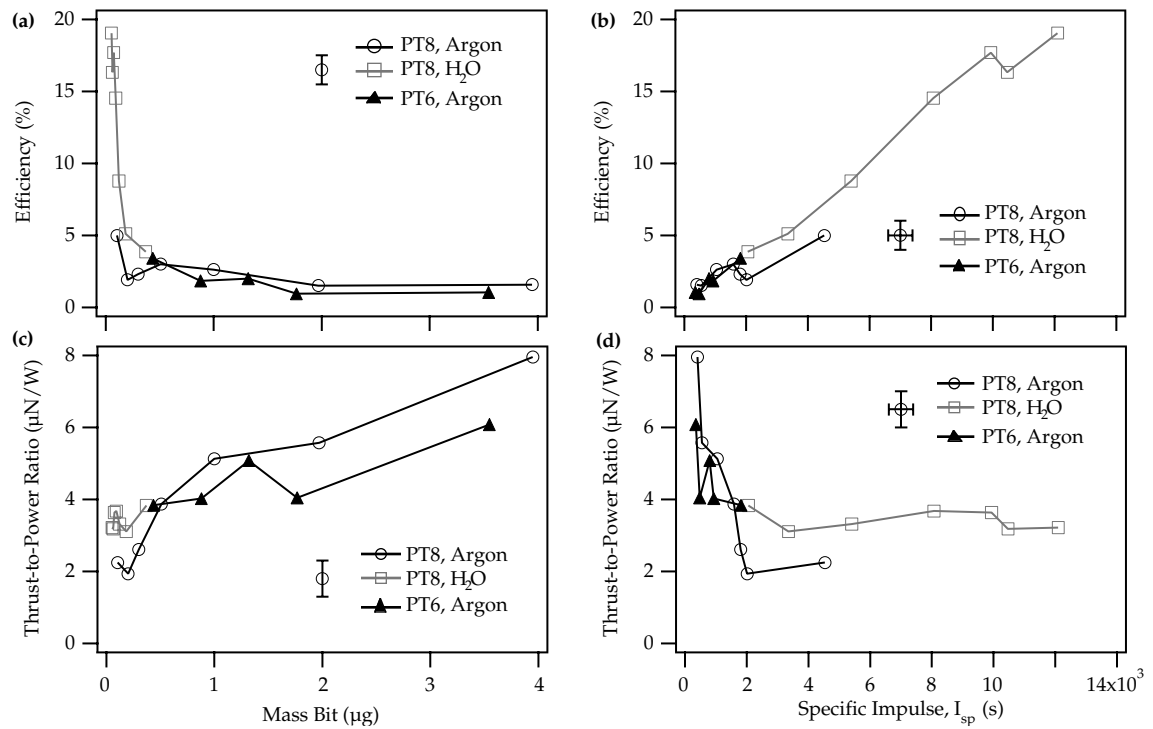
Figure C.5: Efficiency and impulse-to-energy ratio plotted against both mass bit and specific impulse for PT6 with argon and PT8 with argon and water vapor. All data shown is taken at 2 J per pulse. A sample error bar for this data set is also shown.

performance. Although the thruster performed better than its predecessor, PT6, overall, the improvements cannot be correlated to one modification in particular. This section of the appendix will document the effects of each modification.

C.4.1   Propellant Loading

The propellant loading was modified by changing the location of the propellant injection and the amount of time between pulses for the gas to flow into the electrode gap. The location of the propellant injection was moved directly across from the spark plug providing a propellant flow perpendicular to the thrust axis. This change should increase the amount of time required for the propellant to reach the end of the electrodes and improve the propellant utilization efficiency. As shown in Chapter 3, as more of the propellant is loaded towards the backplate or breech of the thruster, the dynamic efficiency of sweeping up the gas should be improved. If the gas has enough time to progress past the end of the electrodes, then the electrode gap becomes more and more uniformly filled and dynamic losses can be as high as 50%. Previous measurements of steady-state thrust using room temperature argon for propellant in PT6 showed that the average exhaust velocity was close to 400 m/s as expected for an isentropic expansion. In PT8 the same test at typical operational mass flow rates showed a reduced average exhaust velocity of just over 300 m/s with smaller mass flow rates having exhaust velocities close to 350 m/s. With the electrode length in PT8 being close to 5 cm, the propellant begins to leak out of the electrode volume after only about 150 μs. This speed dictates greater than a 6 kHz pulse frequency during the burst to effectively use all the propellant. Using water vapor, the gas kinetic velocity at room temperature will increase by a factor of 1.6 to nearly 500 m/s requiring repetition rates as high as 10 kHz. Testing at various pulse frequencies using water vapor, however, did not affect the impulse bit to a large extent as shown in Figure C.6. Unfortunately the repetition rate could not be raised as high as 10 kHz due to the minimum required charging time for the main capacitor bank. It should be noted that as higher capacitance levels are used, longer charging times are required, reducing the maximum possible pulse frequency. In future designs, combinations of various electrode lengths and gas molecular weights will have to be chosen to improve propellant utilization.

C.4.2   Ferrite Blocks

Ferrite blocks were added to the electrodes to focus the discharge and reduce the stray magnetic fields and inductance. In a real parallel-plate electrode geometry, the magnetic field is not entirely contained in the electrode gap. Fringing effects and a non-uniform magnetic field can reduce the performance and increase ex-
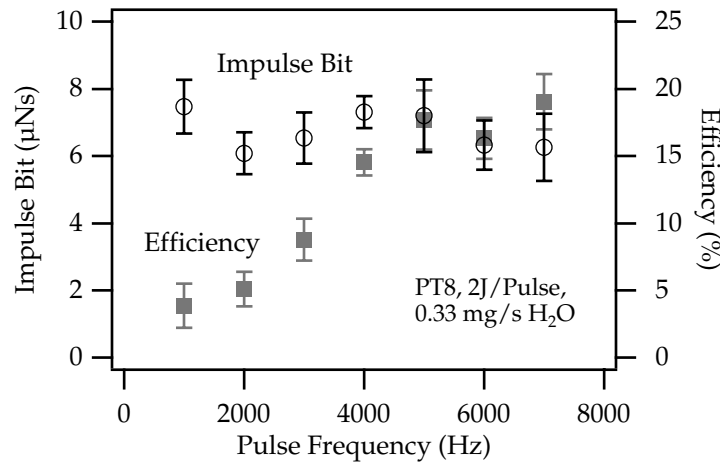
Figure C.6: Impulse bit and efficiency as a function of pulse frequency for PT8 using water vapor for propellant at 2 J per pulse.

haust beam divergence. The ferrite blocks should not have allowed any magnetic field or current to escape from the electrode volume thereby improving performance. On testing the thruster with and without the ferrite blocks at otherwise the same operating conditions, however, no noticeable change in impulse was detected. It was surmised that with the new, more enclosed shape of the electrodes compared to the open, flared design of PT6, most of the current was contained in the discharge volume regardless of the ferrite blocks. This electrode design has a significantly higher amount of surface area, however, which could lead to larger wall losses at the low mass bit values and off-set any benefit from the more contained discharge. In any case, improving the beam divergence of the exhaust and increasing the inductance-per-unit-length of the discharge are still considered beneficial to the design.

C.4.3   Initiation Driving Voltage

The spark plug design and driving voltage characteristics were changed to improve the lifetime by reducing erosion rates. Using an RF frequency voltage on the spark plug allowed a much lower breakdown voltage, and therefore lower energy, than the semi-conductor surface flash-over spark plugs used in previous GFPPT designs. In erosion tests it was shown that erosion rates were close to 0.1 μg per pulse, again all from the spark plug. Although this is nearly a 50% reduction in mass loss rate, it is still significant when compared to the lowest mass bits used in these tests, 0.07 μg with water vapor. The spark plugs are still viewed as the limiting factor in determining the lifetime of these devices. In a typical mission of
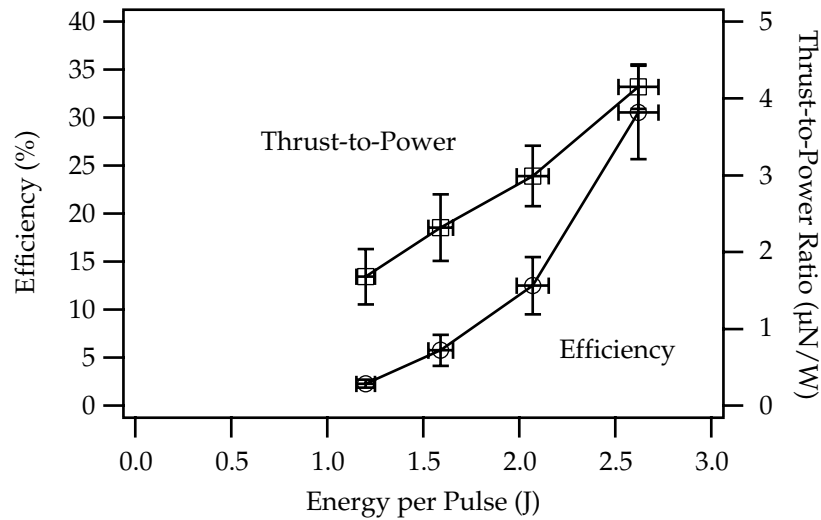
Figure C.7: Efficiency and impulse-to-energy ratio as a function of energy per pulse for water vapor propellant at a constant mass bit of 0.07 μg.

10^8 pulses, 10 g of spark plug material (nearly 1/3 of its current total mass) would be lost at the these erosion rates. Future tests will include operation at even lower voltages and energies or, perhaps, a new initiation scheme involving ultraviolet light flashes.

C.5   Importance of Energy on Performance

The final performance test of PT8 consisted of keeping the mass bit of water vapor constant while increasing the energy. As shown in Figure C.7, the impulse-to-energy ratio increases linearly and the efficiency increases with the square of the energy. The direct benefits of operation at higher energy are seen from this plot; however, higher energy requires higher voltage or higher capacitance which increases system mass. Operation at a constant energy and higher levels of capacitance was also shown to improve performance, proportional to the square root of the capacitance. Although these tests were conducted on a thruster with coaxial electrodes, the performance scaling is expected to be the same. It should be noted, however, that at these low mass bits (more mass is being ablated from the spark plug than water vapor) ablation of material could also be contributing to the increase impulse at higher energy. At higher mass bits in PT5, the impulse-to-energy ratio was seen to be constant with energy, and efficiency only improved linearly with energy. More erosion rate experiments at different energy levels need to be conducted to verify these trends in performance. In any case, operation at higher

energy and mass bit should lead to higher performance

C.6 Imacon Pictures of PT7 Discharge

A series of ten Imacon photographs were taken to form an entire "pulse history" of a discharge from the quad thruster with parallel-plate electrodes as shown in Fig. C.8. The exposures were taken with different timing delays relative to the spark plug charging voltage signal, thereby providing a complete description of the discharge propagation. Each exposure contributed approximately three frames to the compilation spaced at 2 μs intervals. For example, frame (a), (k), and (u) are all from the same Imacon exposure of the same discharge. Approximately 0.2 μs of delay was added for each exposure by changing the timing of the trigger delay generator. All the pictures were taken during one of the life-tests at 2 J/pulse and 0.5 μg/pulse of xenon propellant. Many other discharge exposures show that the discharge is visually very repeatable. A sample voltage and current history are shown in Fig. C.9.

Four important features are apparent in the pulse history:

1. The luminous front seen in frames (c) through (j) is not perpendicular to the electrodes. If this represents the front of the current sheet, then the acceleration vector of the propellant is not orientated along the electrodes and a significant profile inefficiency could be present.

2. The luminous front seems to stop at a particular point on the cathode while continuing to move along the anode. In the earlier frames it appears as if the brightest illumination comes from the cathode near the spark plug for many frames while the brightest region near the anode moves down to the end of the electrode.

3. There is a second luminous front that is ring-shaped and extends around the electrodes, especially outside of the anode, as seen in frames (g) through (o) and even later in frames (s) and (u). This ring appears to start near the backplate of the thruster after about 1.5 μs and moves along the electrodes slowly in comparison to the first luminous front motion.

4. Once again, as in the PT5 Imacon photographs, there is a bright plume near the spark plug sometimes very late in the discharge when the capacitor is almost completely discharged (for example, frame(v)). It is speculated that this plume is made up of glowing hot particles ablated from the cathode or spark plug.

The current sheet canting (item 1) and the plasma leaking out of the discharge chamber (item 3) could be indications of reduction in performance. Although
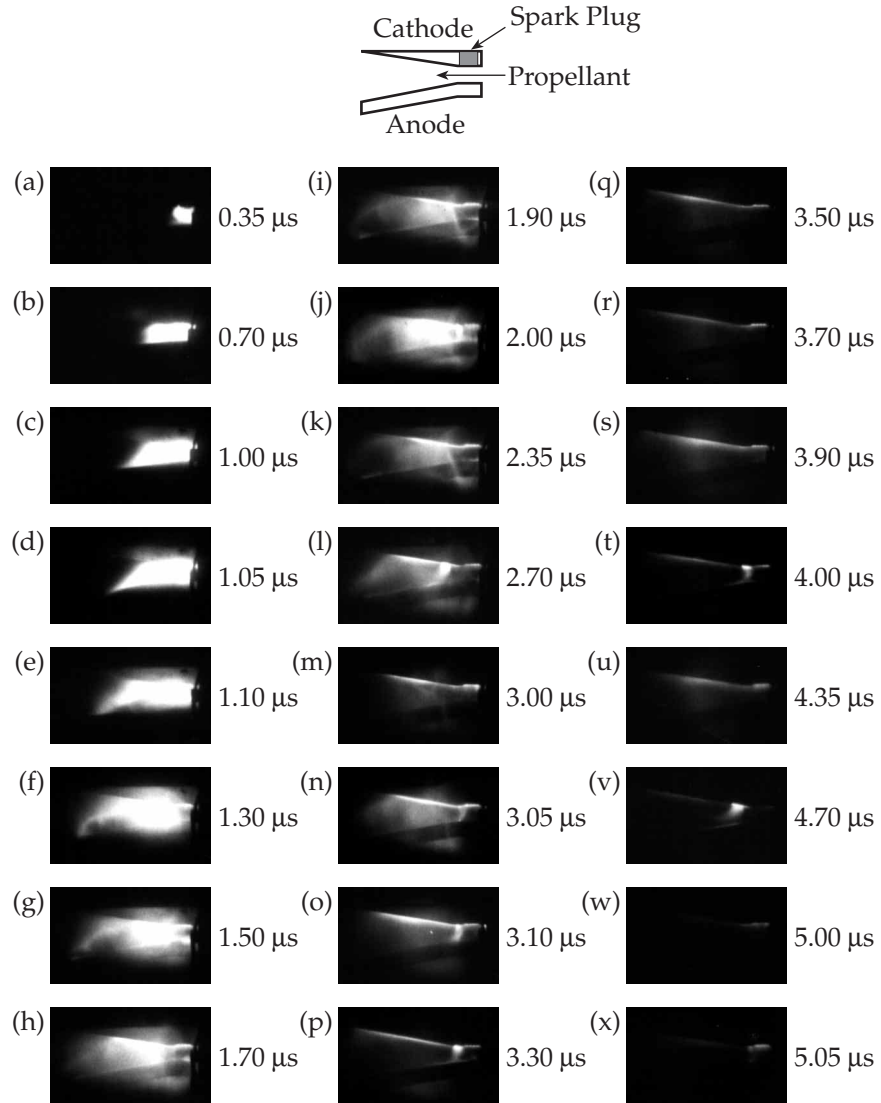
Figure C.8: Compiled Imacon frames of the quad thruster. Time from spark plug capacitor discharge are shown to the right of each frame.
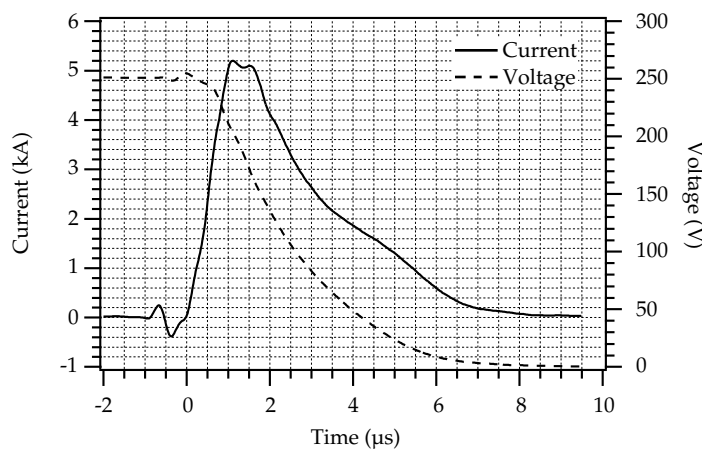
Figure C.9: Current and voltage history for a 2.0 J, 0.5 μg (xenon) per pulse discharge of the quad thruster with parallel-plate electrodes.

not explicitly correlated, the performance of the parallel-plate thruster fell about 20% short of its expected theoretical value. More experiments including filtered Imacon photographs, magnetic field, and gas pressure measurements need to be conducted in order to verify the profile inefficiency suggested by the un-filtered Imacon photographs. A detailed study of this problem is underway at EPPDyL and a recently produced quicktime movie of the current sheet evolution in a long parallel-plate accelerator can be seen in Ref. [107]. In addition, the source of the late-time plume near the spark plug should be investigated as well as the implications of the second ring-like luminosity pattern present in the discharge pictures.

Appendix D

Erosion Rate and Lifetime Study

This appendix covers erosion rate measurements conducted at NASA JPL on PT7 using xenon propellant (see also Ref. [77] by Ziemer, et al).

D.1 Erosion Rate Measurements and Observations of Electrode Wear

Operational lifetime is a critical issue for electric propulsion devices. At impulse bit levels of 10 μNs per pulse, GFPPTs will be expected to perform $10^6 - 10^9$ pulses during a typical mission. To measure erosion rates over a fraction of this expected lifetime, a quad thruster with parallel-plate electrodes (stainless steel cathode and titanium anode) was pulsed 2 million times at three different operating conditions. This appendix summarizes the set-up and experimental protocol for the erosion rate measurements and presents the results including pictures taken before, during, and after the test. The spark plug is believed to be the major limit to thruster lifetime and its erosion is also documented here. All photographs of electrode wear and spark plug damage are at the end of this appendix.

D.1.1 Experimental Set-up and Protocol

The erosion rate experiment was conducted in three phases with three different thruster operating conditions. During most of the phases in the experiment, the thruster was run in a burst mode with five pulses per burst and four bursts per second. As this test was not designed to be a test of valve lifetime, a steady flow of xenon was used the entire time the thruster was operating. With propellant flowing, tank pressure did not exceed 5×10^{-5} torr during any test. Each electrode, the insulator, and the spark plug were weighed and photographed before and after each phase of the testing. The erosion rate for each piece is calculated from the
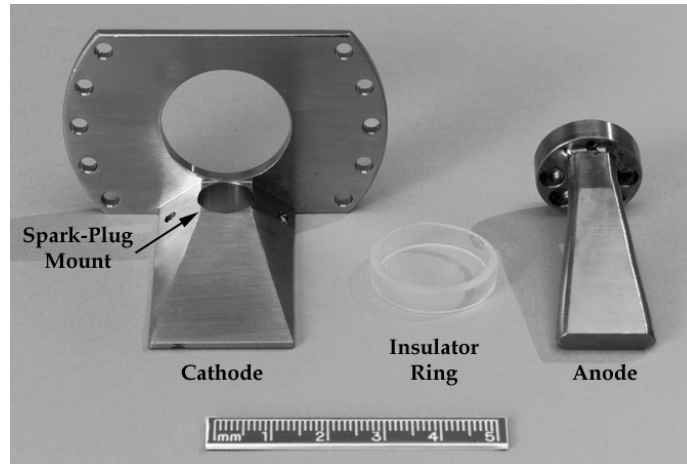
Figure D.1: Quad thruster stainless steel cathode, quartz insulator ring, and titanium anode after 100 pulses.

mass difference before and after each phase and is described in terms of an average mass loss per pulse. During the tests, the cathode backplate temperature was monitored by a type K thermocouple electrically insulated from the discharge with one layer of kapton tape and attached to the cathode by a nylon bolt.

Figure D.1 shows the stainless steel cathode, quartz insulator, and titanium anode after 100 test pulses were fired to ensure a functioning system. The picture shows the side of the electrodes that are exposed to the discharge with the spark plug removed from the hole in the back of the cathode. In assembly, the anode is turned over so that both electrodes have a slight flare or expansion.

Before and after each phase of the test, the thruster is disassembled and the electrodes, insulating ring, spark plug, and mounting hardware were placed in clean, separate zip-lock bags for transport. The pieces were weighed in JPL's measurement and calibration lab on a microgram Sartorius balance that had been recently calibrated to a ± 0.0001 g precision. The electrode mounting hardware mass did not change significantly over the entire experiment and is not included in this analysis. As a result of the erosion near the interface of the spark plug and cathode, the pieces became fused together during the first phase of the experiment. The mass of the cathode, spark plug, and the spark plug mounting screws were, therefore, combined into the "cathode assembly" and the erosion rate of the thruster cathode and spark plug cannot be differentiated.

D.1.2   Electrode Mass Change over Two Million Pulses

The erosion rate experiment was broken up into a one-million-pulse test over two days and two five-hundred-thousand-pulse tests each taking a day. All three phases of the experiment were conducted at different thruster operating conditions. A table showing the operating conditions and mass change for each phase of the experiment is shown in Table (D.1). The data set shows that the cathode lost a significant amount of mass on each phase of the experiment while the anode and the insulator both gained a slight amount of mass, approximately 10% of what was lost from the cathode. Table (D.2) shows the average mass loss per pulse and mass loss per coulomb of stored charge in the main discharge capacitor.

The amount of mass loss per pulse from the cathode is very similar in magnitude during each phase of the experiment, regardless of operating conditions. The mass loss per coulomb from the cathode, however, decreases in each phase. It should be noted here that erosion of the cathode assembly appears to be concentrated near the spark plug cathode ring. This is discussed further in Section D.1.3. The thruster anode and insulator both gained mass somewhat proportionally to the cathode mass loss rate. With close to 0.2 μg of total electrode material eroded per pulse, the mass loss rate of the thruster hardware is very nearly the amount of propellant mass used for each pulse, especially during the third phase of the experiment. This brings up the question of the true thruster performance over the lifetime of the device. If erosion products make up a significant amount of the accelerated mass, then performance might change as the erosion rate changes. It should also be noted, however, that the erosion rates might be larger in the high pulse-rate erosion test compared to the performance measurement experiments where one burst was typically fired every 100 seconds.

During each phase of the experiment, the temperature of the cathode backplate was monitored regularly. In each case, the temperature started at room temperature and increased to a steady level within two hours of the start of the test. For the 1 J/pulse test, the average power was 20 W and the electrode temperature reached a steady-state of 70 °C. For the 2 J/pulse tests, the average power was 40 W and the electrode reached a steady-state temperature of 100 °C. During continuous operation, glowing particles were seen to exist near the spark plug and to occasionally be projected out of the thruster discharge chamber into the tank indicating possible local heating near the spark plug. The electrodes themselves could have been much hotter than the measured temperatures at the backplate of the stainless steel cathode due to the lack of heat conduction through the slim electrodes.

After each phase of the experiment, the electrodes were removed from the thruster and photographed (all photographs are shown at the end of this section). Figure D.1 shows the clean electrodes after only 100 pulses. Figures D.2 and D.3 show the anode after one and two million accumulated pulses, respectively. The pictures show flakes of gray accumulated material near the back of the electrode.

Phase	Total Number of Pulses Accumulated	Operating Conditions (per pulse)	Thruster Hardware			Total (g)
			Cathode Assembly (g)	Anode (g)	Insulator (g)	
	100	1 J, 0.5 μg	93.7913	19.6949	1.1879	114.6741
I	1002400	1 J, 0.5 μg	93.5800	19.7244	1.1898	114.494
	Gain/Loss		**-0.2113**	**+0.0295**	**+0.0019**	**-0.180**
II	1502900	2 J, 0.5 μg	93.4540	19.7413	1.1899	114.385
	Gain/Loss		**-0.1260**	**+0.0169**	**+0.0001**	**-0.109**
III	1991300	2 J, 0.25μg	93.3470	19.7501	1.1904	114.288
	Gain/Loss		**-0.1070**	**+0.0088**	**+0.0005**	**-0.097**

Table D.1: Mass loss for thruster hardware over the 2 million pulse erosion rate experiment. The mass gain or loss (+/-) for each phase is shown in bold.

Phase	Total Number of Pulses Accumulated	Operating Conditions (per pulse)	Cathode Assembly (μg/pulse) (μg/C)	Anode (μg/pulse) (μg/C)	Insulator (μg/pulse) (μg/C)	Total (μg/pulse) (μg/C)
I	1002400	1 J, 0.5 μg	-0.2108	+0.0294	+0.0019	-0.1795
	per Coulomb	0.0113 C	**-18.7**	**+2.61**	**+0.17**	**-15.9**
II	1502900	2 J, 0.5 μg	-0.2517	+0.0338	+0.0002	-0.2177
	per Coulomb	0.0159 C	**-15.8**	**+2.12**	**+0.01**	**-13.7**
III	1991300	2 J, 0.25μg	-0.2191	+0.0180	+0.0010	-0.2001
	per Coulomb	0.0159 C	**-13.7**	**+1.13**	**+0.06**	**-12.5**

Table D.2: Mass loss rate and mass loss per coulomb charge stored in the main discharge capacitor (shown in bold) for thruster hardware over the 2 million pulse erosion rate experiment.

There are also gray and reflective droplets of deposited material further downstream on the electrode. From scanning electron microscope pictures (shown in Figs. D.4 and D.5) and x-ray spectrometry, the flakes were found to be made of stainless steel in both crystalline and particulate form. The top and left sides of Fig. D.4 show the exposed titanium surface of the anode. In addition, as shown in the top-left corner of Fig. D.5, there were sporadic traces of spattered dark material that was identified as aluminum oxide. This material is believed to be provided by the insulating ring between the anode and cathode of the spark plug. The only other possible source of aluminum oxide is from the insulators used in the langmuir triple probes.

After 1.5 million pulses, the anode looked very similar to the way it did after one million pulses. After two million pulses the anode, Fig. D.3, also shows a black patch near the back of the electrode on the top side of the picture. A corresponding dark coloration also appeared on the insulator and on the teflon sealing gasket located behind the electrodes and insulating ring. This is most likely a carbon soot deposit from the teflon gasket.

The stainless steel cathode used in this experiment is shown after one and two million accumulated pulses in Figs. D.6 and D.7, respectively. Both pictures show excessive wear in the region around the spark plug. After the first million pulses, it appears as if only the spark plug itself has eroded away while most of the thruster cathode itself remained intact. At this point, the spark plug was fused to the cathode and two scrapes on the spark plug inner electrode surface (spark plug anode) occurred during the removal attempts. The cathode also shows arc attachment spots further downstream from the backplate. The cathode looked very similar after 1.5 million discharges and is not shown here. After 2 million discharges, it is clear that more cathode material has been eroded although the most severe damage appears again near the spark plug. There is also evidence of melting near the downstream side of the spark plug gap where a large ball of stainless steel is present. At this stage the cathode also shows sign of arc attachment further down the electrode. This could be due to the lower mass bit used during this phase of the experiment. As seen in the performance data, lower mass bits typically have corresponding higher specific impulse and exhaust velocity values indicating that the current sheet might be traveling further down the cathode in the same amount of time for lower mass bits.

After the 2 million pulse test was completed, the stainless steel cathode was exchanged for a titanium one of similar shape making both of the thruster electrodes the same material. All thruster hardware was cleaned with fine sandpaper and acetone before the thruster was re-positioned on the test stand. Figure D.8 shows the titanium cathode assembly with a relatively new spark plug (50,000 pulses) after cleaning. This life-test was designed to study the difference in erosion between the two cathode materials with the thruster operating at 2 J and 0.75 μg of xenon

per pulse. After 90 minutes into the life-test (5 pulses per burst at 4 Hz and 40 W with just over 100,000 pulses fired) the spark plug failed to routinely initiate the discharge. After a resistance check, it was found that the spark plug anode was shorted to the spark plug and thruster cathode which did not allow the spark plug to work properly. Figure D.9 shows the titanium cathode assembly after 100,000 shots. Once again, the stainless steel outer ring of the spark plug shows the largest signs of erosion. It appears that a relatively uniform ring of material has been removed next to the spark plug insulator. Although not clear in the photograph, metal particulates were seen to be across the spark plug insulator ring surface possibly causing the electrical short. It should also be noted that the titanium cathode shows diffuse electrode surface wear well downstream of the backplate. This surface wear extended much farther than the surface wear region of the stainless steel cathode at the same operating conditions. This could indicate that the current sheet propagated along the cathode farther in experiments using titanium electrodes.

Examination of the data from the erosion rate experiments points out some problems and questions for further study. First, the spark plug seems to be the largest source of eroded electrode material (this is examined further in the next section.) Second, the current sheet does not seem to be traveling down the full extent of the stainless steel cathode at relatively moderate mass bit values. The titanium cathode, however, showed a farther progression of attachment points. Unfortunately, the spark plug failed after only 100,000 pulses. More performance and life-tests should be conducted using various electrode materials to resolve these questions.

D.1.3   Visual Spark Plug Erosion

As seen from cathode pictures in both the stainless steel and titanium cathode test, the spark plug outer ring (made of stainless steel and in direct contact with the thruster cathode) erodes very quickly. Figures D.10 through D.13 show a close-up view of the spark plug at the end of each phase of the first erosion-rate experiment. As the tests continued, more and more of the outer spark plug ring was eroded away somewhat preferentially near the downstream side of the spark plug. The spark plug anode (center electrode) and insulator ring showed slight signs of damage as well, although not as severe as the spark plug cathode.

The cause of this erosion is being evaluated. Damage to this extent has not been seen in similar ablative pulsed plasma thruster (APPT) spark plug operations. The surface of the APPT spark plug electrodes, however, gets coated with a thin layer of Teflon during each pulse. It could be that the current discharge initiation circuitry used for the SRL-EPPDyL family of GFPPTs supplies too much energy or power to the spark plug, beyond what it requires to ignite the discharge. It has also been suggested that the spark plug itself is taking up too much of the thruster cathode

surface area. As the current sheet is not allowed to conduct its current through the spark plug anode, there could be large current densities near the edge of the spark plug insulator leading to possibly higher erosion rates in that region.

Figure D.2: Quad thruster titanium anode after 1 million pulses.

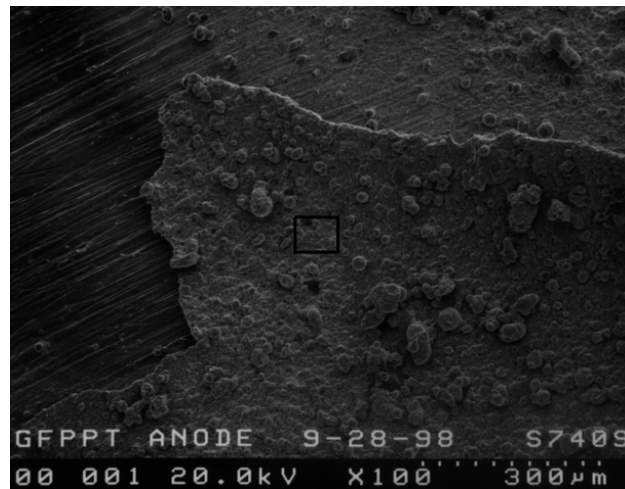Figure D.3: Quad thruster titanium anode after 2 million pulses.

Figure D.4: Scanning electron microscope photograph with 100x magnification of the quad thruster anode after 1 million pulses. The box in the center of the photo shows the area for Fig. D.5.
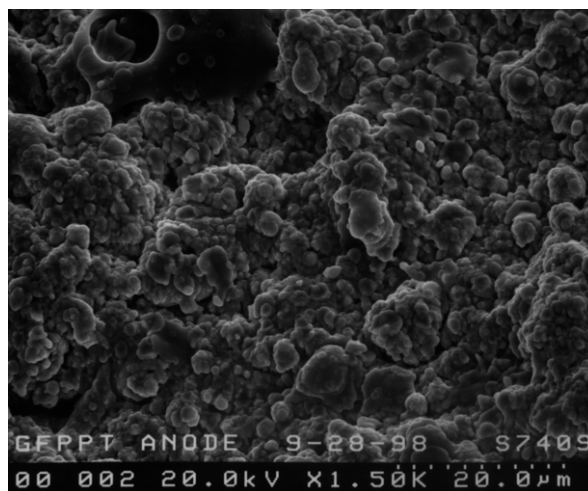

Figure D.5: Scanning electron microscope photograph with 1500x magnification of the quad thruster anode after 1 million pulses.
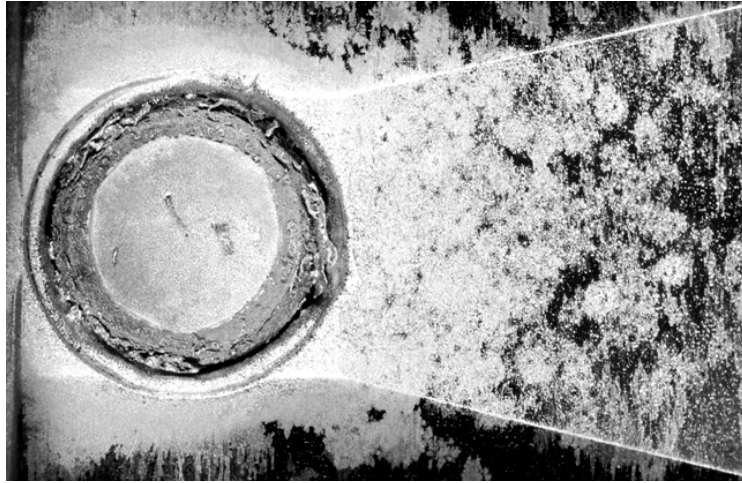
Figure D.6: Quad thruster stainless steel cathode after 1 million pulses.

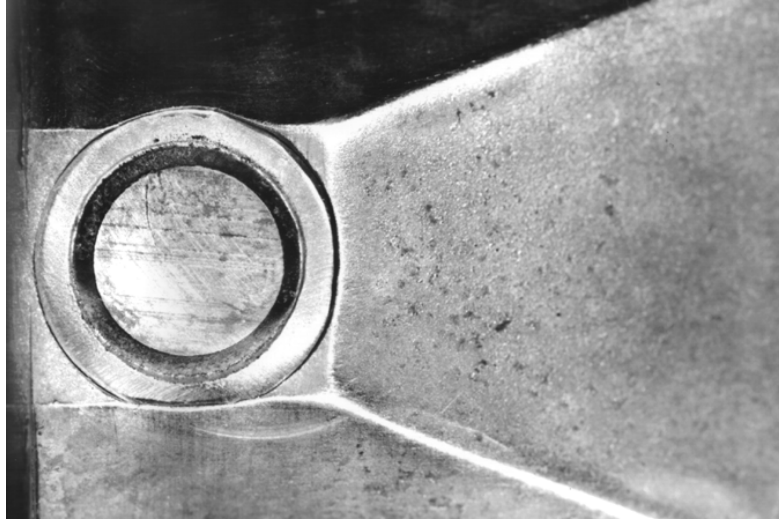Figure D.7: Quad thruster stainless steel cathode after 2 million pulses.

Figure D.8: Quad thruster titanium cathode after cleaning and before life-test. The spark plug had been used for approximately 50,000 pulses before cleaning and life-test.
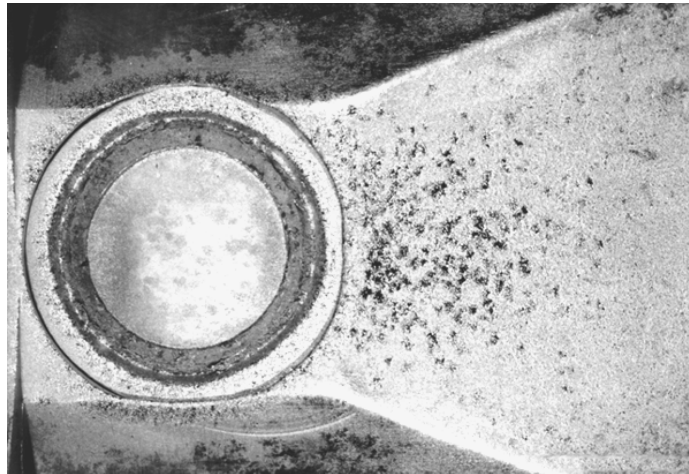

Figure D.9: Quad thruster titanium cathode after 100,000 pulses into life-test.

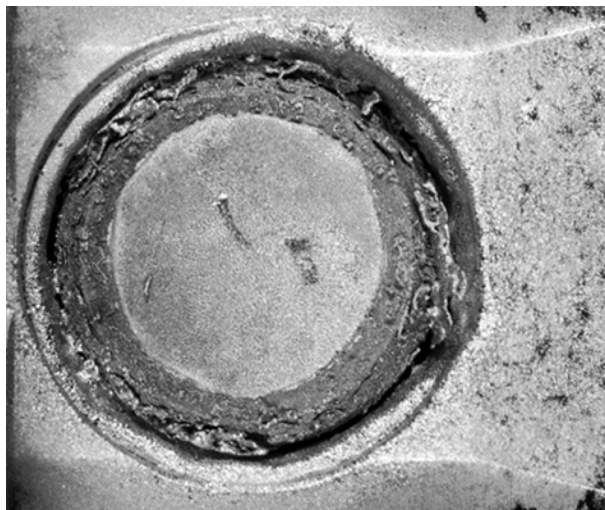Figure D.10: Quad thruster spark plug after 100 pulses.

Figure D.11: Quad thruster spark plug and cathode after 1 million pulses.
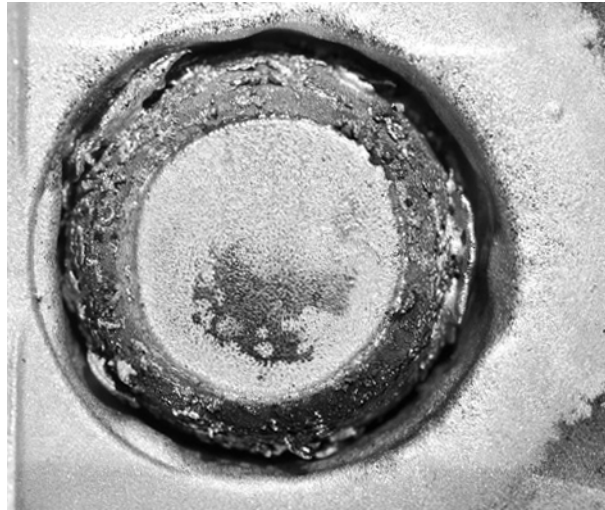
Figure D.12: Quad thruster spark plug and cathode after 1.5 million pulses.

Figure D.13: Quad thruster spark plug and cathode after 2 million pulses.

Bibliography

[1] K.E. Tsiolkovsky. Issledovanie Mirovykh Prostransty Reaktivnymi Pribo-rami (Exploration of Space with Rocket Devices). *Naootchnoye Obozreniye (Scientific Review)*, 1903.

[2] R.G. Jahn. *Physics of Electric Propulsion*. McGraw-Hill, 1969.

[3] Electric Propulsion Special Issue. *Journal of Propulsion and Power*, 14(5), 1998.

[4] E.Y. Choueiri and R.G. Jahn. *Encyclopedia of Physical Science and Technology*, chapter on Electric Propulsion. Academic Press, 2000.

[5] J.E. Polk, R.Y. Kakuda, J.R. Anderson, J.R. Brophy, V.K. Rawlin, M.J. Patterson, J. Sovey, and J. Hamley. Validation of the NSTAR Ion Propulsion System on the Deep Space One Mission: Overview and Initial Results. In 35th *Joint Propulsion Conference*, Los Angeles, California, June 20-24 1999. AIAA 99-2274.

[6] J.W. Barnett. A Review of Soviet Plasma Engine Development. In 21st *International Electric Propulsion Conference*, Orlando, Florida, July 18-20 1990. AIAA 90-2600.

[7] K. Toki, Y. Shimizu, K. Kuriki, and H. Kuninaka. An MPD Arcjet Thruster System for Electric Propulsion Experiment (EPEX). In 30th *Joint Propulsion Conference*, Indianapolis, IN, June 27-29 1994. AIAA 94-2989.

[8] W.L. Ebert, S.J. Kowal, and R.F. Sloan. Operational NOVA Spacecraft Teflon Pulsed Plasma Thruster System. In 25th *Joint Propulsion Conference*, Monterey, California, July 10-12 1989. AIAA 89-2497.

[9] M. Martin. Distributed Satellite Missions and Technologies - The TechSat 21 Program. In *AIAA Space Technology Conference & Exposition*, Albuquerque, NM, September 28-30 1999. AIAA 99-4479.

[10] S.W. Benson, L.A. Arrington, W.A. Hoskins, and N.J. Meckel. Development of a PPT for the EO-1 Spacecraft. In 35th *Joint Propulsion Conference*, Los Angeles, California, June 20-24 1999. AIAA 99-2276.

[11] S. Domitz, H.G. Kosmahl, P. Ramins, and N.J. Stevens. Survey of Electromagnetic Accelerators. Technical Report TN D-3332, NASA, 1965.

[12] R.H. Frisbee and S.D. Leifer. Evaluation of Propulsion Options for Interstellar Missions. In 34th *Joint Propulsion Conference*, Cleveland, Ohio, July 13-15 1998. AIAA 98-3403.

[13] S.R. Oleson, R.M. Myers, C. Kluever, J.P. Riehl, and F.M. Curran. Advanced Propulsion for Geostationary Orbit Insertion and North-South Station Keeping. In 31st *Joint Propulsion Conference*, San Diego, California, June 10-12 1995. AIAA 95-2513.

[14] J. Riehl, L. Gefert, R. Myers, E. Pencil, J. McAdams, and D. Kusnierkiewicz. Low Power Electric Propulsion for Minor Body Applications. In 31st *Joint Propulsion Conference*, San Diego, California, June 10-12 1995. AIAA 95-2812.

[15] H.S. Tsien. Take-Off from Satellite Orbit. *Journal of the American Rocket Society*, 23(4):233–236, 1953.

[16] D.B. Langmuir. Low-Thrust Flight: Constant Exhaust Velocity in Field-Free Space. In H.S. Seifert, editor, *Space Technology*. John Wiley and Sons, Inc., 1959.

[17] A.V. Larson, L. Liebing, and R. Dethlefsen. Experimental and Evaluation Studies of a Coaxial Plasma Gun Accelerator. Technical Report CR-54710, NASA, 1966.

[18] R.M. Myers. Low Power Pulsed MPD Thruster System Analysis and Applications. In 29th *Joint Propulsion Conference*, Monterey, California, June 28-30 1993. AIAA 93-2391.

[19] E.Y. Choueiri, A.J. Kelly, and R.G. Jahn. Mass Savings Domain of Plasma Propulsion for LEO to GEO Transfer. *Journal of Spacecraft and Rockets*, 30(6):749–754, 1993.

[20] A. Spitzer. Novel Orbit Raising Strategy Makes Low Thrust Commercially Viable. In 24th *International Electric Propulsion Conference*, Moscow, Russia, September 1995. IEPC 95-212.

[21] R.J. Vondra and K.I. Thomassen. A Flight Qualified Pulsed Plasma Electric Thruster for Satellite Control. In 10th *Electric Propulsion Conference*, Lake Tahoe, Nevada, October 31-November 2 1973. AIAA 73-1067.

[22] E.Y. Choueiri. Optimization of Ablative Pulsed Plasma Thrusters for Stationkeeping Missions. *Journal of Spacecraft and Rockets*, 33(1):96–100, 1996.

[23] N.J. Meckel, R.J. Cassady, R.D. Osborne, W.A. Hoskins, and R.M. Myers. Investigation of Pulsed Plasma Thrusters for Spacecraft Attitude Control. In 25th *International Electric Propulsion Conference*, Cleveland, Ohio, August 24-28 1997. IEPC 97-128.

[24] R.M. Myers and S.R. Oleson. Small Satellite Electric Propulsion Options. In 29th *Intersociety Energy Conversion Engineering Conference*, Monterey, California, August 7-11 1994. AIAA 94-4137.

[25] J. Mueller. Thruster Options for Microspacecraft: A Review and Evaluation of Existing Hardware and Emerging Technologies. In 33rd *Joint Propulsion Conference*, Seattle, WA, July 6-9 1997. AIAA 97-3058.

[26] J. Mueller. *Thruster Options for Microspacecraft: A Review an Evaluation of State-of-the-Art and Emerging Technologies*, volume 187 of *AIAA Progress in Astronautics and Aeronautics*, chapter 3. AIAA, 2000.

[27] J.E. Pollard. In-Space Mission Requirements. In 35th *Joint Propulsion Conference*, Los Angeles, California, June 20-24 1999. AIAA 99-2609.

[28] J.J. Blandino and R.J. Cassady. Propulsion Requirements and Options for the New Millennium Interferometer (DS-3) Mission. In 34th *Joint Propulsion Conference*, Cleveland, OH, July 13-15 1998. AIAA 98-3331.

[29] R.L. Staehle et al. Exploration of Pluto. *Acta Astronautica*, 30:289–310, 1993.

[30] Jet Propulsion Laboratory. NASA Facts: Europa Orbiter. Technical report, NASA, 1999.

[31] J.K. Ziemer, E.Y. Choueiri, and R.G. Jahn. Scaling Laws for Pulsed Electric Propulsion with Application to the Pluto Mission. In 24th *International Electric Propulsion Conference*, Moscow, Russia, September 1995. IEPC 95-147.

[32] R.M. Patrick. High-Speed Shock Waves in a Magnetic Annular Shock Tube. *The Physics of Fluids*, 2(6):589–598, November-December 1959.

[33] N.H. Kemp and H.E. Petschek. Theory of the Flow in the Magnetic Annular Shock Tube. *The Physics of Fluids*, 2(6):599–608, November-December 1959.

[34] J. Marshal. Performance of a Hydromagnetic Plasma Gun. *The Physics of Fluids*, 3(1):134–135, January-February 1960.

[35] T.J. Gooding, B.R. Hayworth, and R.H. Lovberg. Instabilities in a Coaxial Plasma Gun. *AIAA Journal*, 1(6):1289–1292, June 1963.

[36] P. Gloersen, B. Gorowitz, and J.H. Rowe. Some Characteristics of a Two-Stage Repetitively Fired Coaxial Gun. *IEEE Transactions on Nuclear Science*, pages 249–265, January 1964.

[37] P.J. Hart. Plasma Acceleration with Coaxial Electrodes. *The Physics of Fluids*, 5(1):38–47, January 1962.

[38] C.J. Michels and P. Ramins. Performance of Coaxial Plasma Gun with Various Propellants. In *Proceedings of an International Symposium on Plasma Guns, Physics of Fluids Supplement (Part II, Vol. 7(11))*, pages S71–S74, November 1964.

[39] B. Gorowitz, T.W. Karras, and P. Gloersen. Performance of an Electrically Triggered Repetitively Pulsed Coaxial Plasma Engine. *AIAA Journal*, 4(6):1027–1031, June 1966.

[40] A.V. Larson, T.J. Gooding, B.R. Hayworth, and D.E.T.F. Ashby. An Energy Inventory in a Coaxial Plasma Accelerator Driven by a Pulse Line Energy Source. *AIAA Journal*, 3(5):977–979, May 1965.

[41] P.J. Hart. Modified Snowplow Model for Coaxial Plasma Accelerators. *Journal of Applied Physics*, 35(12):3425–3431, December 1964.

[42] P.M. Mostov, J.L. Neuringer, and D.S. Rigney. Electromagnetic Acceleration of a Plasma Slug. *The Physics of Fluids*, 4(9):1097–1104, September 1961.

[43] C.J. Michels, J.E. Heighway, and A.E. Johansen. Analytical and Experimental Performance of Capacitor Powered Coaxial Plasma Guns. *AIAA Journal*, 4(5):823–830, May 1966.

[44] T.W. Karras, B. Gorowitz, and P. Gloersen. Neutral Mass Density Measurements in a Repetitively Pulsed Coaxial Plasma Accelerator. *AIAA Journal*, 4(8):1366–1370, August 1966.

[45] L.C. Burkhardt and R.H. Lovberg. Current Sheet in a Coaxial Plasma Gun. *The Physics of Fluids*, 5(3):341–347, March 1962.

[46] R.H. Lovberg. The Measurement of Plasma Density in a Rail Accelerator by Means of Schlieren Photography. *IEEE Transactions on Nuclear Science*, pages 187–198, January 1964.

[47] R.L. Burton and R.G. Jahn. Acceleration of a Plasma by a Propagating Current Sheet. *The Physics of Fluids*, 11(6):1231–1237, June 1968.

[48] W.R. Ellis and R.G. Jahn. Ion Density and Current Distributions in a Propagating Current Sheet, Determined by Microwave Reflection Technique. *Journal of Plasma Physics*, 3(2):189–213, February 1969.

[49] F.J. Fishman and H. Petschek. Flow Model for Large Radius-Ratio Magnetic Annular Shock-Tube Operation. *The Physics of Fluids*, 5:632–633, 1962.

[50] R.H. Lovberg. Schlieren Photography of a Coaxial Accelerator Discharge. *The Physics of Fluids*, 8(1):177–185, January 1965.

[51] R.H. Lovberg. Investigation of Current-Sheet Microstructure. *AIAA Journal*, 4(7):1215–1222, July 1966.

[52] R.G. Jahn and W. von Jaskowsky. Structure of a Large-Radius Pinch Discharge. *AIAA Journal*, 1(8):1809–1814, August 1963.

[53] R.G. Jahn and W. von Jaskowsky. Current Distributions in Large-Radius Pinch Discharges. *AIAA Journal*, 2(10):1749–1753, October 1964.

[54] R.L. Burton. *Structure of the Current Sheet in a Pinch Discharge*. PhD thesis, Princeton University, 1966.

[55] L. Liebing. Motion and Structure of a Plasma Produced in a Rail Spark Gap. *The Physics of Fluids*, 6:1035–1036, 1963.

[56] J.C. Keck. Current Distribution in a Magnetic Annular Shock Tube. *The Physics of Fluids*, 5:630–632, 1962.

[57] W.H. Bostick. Hall Currents and Vortices in the Coaxial Plasma Accelerator. *The Physics of Fluids*, 6(11):1598–1603, November 1963.

[58] R.B. Johansson. Current Sheet Tilt in a Radial Magnetic Shock Tube. *The Physics of Fluids*, 8(5):866–871, May 1965.

[59] J.R. MacLelland, A.S.V. MacKenzie, and J. Irving. Schlieren Photography of Rail-Tube Plasmas. *The Physics of Fluids*, 9:1613–1615, 1966.

[60] T.E. Markusic and E.Y. Choueiri. Visualization of Current Sheet Canting in a Pulsed Plasma Accelerator. In 26th *International Electric Propulsion Conference*, Kitakyushu, JAPAN, October 17-21 1999. IEPC 99-206.

[61] C.J. Michels. Some Transient ELectrical Characteristics of the Exhaust of a Self-Crowbarred Coaxial Plasma Gun. Technical Report TN D-2571, NASA, 1964.

[62] A.C. Eckbreth, K.E. Clark, and R.G. Jahn. Current Pattern Stabilization in Pulsed Plasma Accelerators. *AIAA Journal*, 6(11):2125–2132, November 1968.

[63] A.V. LaRocca. Solid Propellant Electrical Thrustors for Attitude Control and Drift Correction of Space Vehicles. In 5th *Electric Propulsion Conference*, San Diego, California, March 7-9 1966. AIAA 66-229.

[64] W.J. Guman. Solid Propellant Pulsed Plasma Micro-Thruster Studies. In 6th *Aerospace Sciences Meeting*, New York, New York, January 22-24 1968. AIAA 68-85.

[65] W.J. Guman, R.J. Vondra, and K.I. Thomassen. Pulsed Plasma Propulsion System Studies. In 8th *Electric Propulsion Conference*, Stanford, California, August 31-September 2 1970. AIAA 70-1148.

[66] A. Solbes and R.J. Vondra. Performance Study of a Solid Fuel Pulsed Electric Microthruster. In 9th *Electric Propulsion Conference*, Bethesda, Maryland, April 17-19 1972. AIAA 72-458.

[67] D.J. Palumbo and W.J. Guman. Effects of Propellant and Electrode Geometry on Pulsed Ablative Plasma Thruster Performance. In *11th Electric Propulsion Conference*, New Orleans, Louisiana, March 19-21 1975. AIAA 75-409.

[68] W.J. Guman. Designing Solid Propellant Pulsed Plasma Thrusters. In *11th Electric Propulsion Conference*, New Orleans, Louisiana, March 19-21 1975. AIAA 75-410.

[69] K. Yuan-Zhu. Experimental Research of Relationship Between PPT Parameters. In 18th *International Electric Propulsion Conference*, Alexandria, Virginia, September 30-October 2 1985. AIAA 85-2065.

[70] N.J. Meckel, W.A. Hoskins, R.J. Cassady, R.M. Myers, S.R. Oleson, and M. McGuire. Improved Pulsed Plasma Thruster System for Satellite Propulsion. In 32nd *Joint Propulsion Conference*, Lake Buena Vista, Florida, July 1996. AIAA 96-2735.

[71] J.K. Ziemer, E.A. Cubbin, E.Y. Choueiri, and D. Birx. Performance Characterization of a High Efficiency Gas-Fed Pulsed Plasma Thruster. In 33rd *Joint Propulsion Conference*, Seattle, Washington, July 6-9 1997. AIAA 97-2925.

[72] J.K. Ziemer, E.Y. Choueiri, and D. Birx. Trends in Performance Improvements of a Gas-Fed Pulsed Plasma Thruster. In 25th *International Electric Propulsion Conference*, Cleveland, Ohio, August 24-28 1997. IEPC 97-040.

[73] J.K. Ziemer and E.Y. Choueiri. Dimensionless Performance Model for Gas-Fed Pulsed Plasma Thrusters. In 34th *Joint Propulsion Conference*, Cleveland, Ohio, July 13-15 1998. AIAA 98-3661.

[74] J.K. Ziemer, T.E. Markusic, E.Y. Choueiri, and D. Birx. Effects of Ignition on Discharge Symmetry in Gas-Fed Pulsed Plasma Thrusters. In 34th *Joint Propulsion Conference*, Cleveland, Ohio, July 13-15 1998. AIAA 98-3803.

[75] J.K. Ziemer, E.Y. Choueiri, and D. Birx. Is the Gas-Fed PPT an Electromagnetic Accelerator? An Investigation Using Measured Performance. In 35th *Joint Propulsion Conference*, Los Angeles, California, June 20-24 1999. AIAA 99-2289.

[76] J.K. Ziemer, E.Y. Choueiri, and D. Birx. Comparing the Performance of Co-Axial and Parallel-Plate Gas-Fed PPTs. In 26th *International Electric Propulsion Conference*, Kitakyushu, JAPAN, October 17-21 1999. IEPC 99-209.

[77] J.K. Ziemer and E.Y. Choueiri. Performance and Erosion Measurements of Gas-Fed Pulsed Plasma Thrusters at NASA Jet Propulsion Laboratory. Technical Report EPPDyL-JPL99a, Princeton University, March 1999.

[78] P. Gloersen, B. Gorowitz, and J.T. Kenney. Energy Efficiency Trends in a Coaxial Gun Plasma Engine System. *AIAA Journal*, 4(3):436–441, March 1966.

[79] J.K. Ziemer. A Review of Gas-Fed Pulsed Plasma Thruster Research over the Last Half-Century. Technical report, Princeton University, 2000.

[80] D.J. Vargo. Electromagnetic Acceleration of a Variable-Mass Plasma. Technical Report TN D-2164, NASA, 1964.

[81] M. Rosenbluth. Infinite Conductivity Theory of the Pinch. Technical Report LA-1850, Los Alamos, 1954.

[82] M. Andrenucci, M. Caprili, and R. Lazzeretti. Theoretical Performance of Pulsed Coaxial Plasma Guns. Technical report, Universita di Pisa, 1972.

[83] D.E.T.F. Ashby. Energy Loss in Pulsed Coaxial Plasma Guns. *AIAA Journal*, 3(6):1045–1047, June 1965.

[84] J. Blandino, D. Birx, J.K. Ziemer, and E.Y. Choueiri. Performance and Erosion Measurements of the PT8 Gas-Fed Pulsed Plasma Thruster. Technical Report EPPDyL-JPL99b, NASA Jet Propulsion Laboratory, August 1999.

[85] N.A. Black and R.G. Jahn. Dynamic Efficiency of Pulsed Plasma Accelerators. *AIAA Journal*, 3(6):1209–1210, June 1965.

[86] D.E.T.F. Ashby, T.J. Gooding, B.R. Hayworth, and A.V. Larson. Exhaust Measurements on the Plasma from a Pulsed Coaxial Gun. *AIAA Journal*, 3(6):1140–1142, June 1965.

[87] J. Keck. Current Speed in a Magnetic Annular Shock Tube. In *Proceedings of an International Symposium on Plasma Guns, Physics of Fluids Supplement (Part II, Vol. 7(11))*, pages S16–S27, November 1964.

[88] W.J. Guman and W. Truglio. Surface Effects in a Pulsed Plasma Accelerator. *AIAA Journal*, 2(7):1342–1343, July 1964.

[89] E. Antonsen, R.L. Burton, and F. Rysanek. Energy Measurements in a Co-axial Electromagnetic Pulsed Plasma Thruster. In 35th *Joint Propulsion Conference*, Los Angeles, California, June 20-24 1999. AIAA 99-2292.

[90] I. Kohlberg and W.O. Coburn. A Solution for Three Dimensional Rail Gun Current Distribution and Electromagnetic Fields of a Rail Launcher. *IEEE Transactions on Magnetics*, 31(1):628–633, 1995.

[91] M.E. Brady and G. Aston. Pulsed Plasma Thruster Ignitor Plug Ignition Characteristics. *Journal of Spacecraft and Rockets*, 20(5):450–451, 1983.

[92] E.A. Cubbin, J.K. Ziemer, E.Y. Choueiri, and R.G. Jahn. Laser Interfero-metric Measurements of Impulsive Thrust. *Review of Scientific Instruments*, 68(6):2339–2346, 1997.

[93] T.W. Haag. PPT Thrust Stand. In 31st *Joint Propulsion Conference*, San Diego, California, July 1995. AIAA 95-2917.

[94] R.L. Burton, K.E. Clark, and R.G. Jahn. Measured Performance of a Multi-megawatt MPD Thruster. *Journal of Spacecraft and Rockets*, 20(3):299–304, 1983.

[95] E.Y. Choueiri and J.K. Ziemer. Quasi-Steady Magnetoplasmadynamic Thruster Measured Performance Database. In 34th *Joint Propulsion Conference*, Cleveland, Ohio, July 13-15 1998. AIAA 98-3472.

[96] E.A. Cubbin. Laser Interferometry for Pulsed Plasma Thruster Performance Measurement. Master's thesis, Princeton University, 1997.

[97] k. Thom, J. Norwood, and N. Jalufka. Velocity Limitation of a Coaxial Plasma Gun. In *Proceedings of an International Symposium on Plasma Guns, Physics of Fluids Supplement (Part II, Vol. 7(11))*, pages S67–S70, November 1964.

[98] L. Aronowitz and D.P. Duclos. Characteristics of the Pinch Discharge in a Pulsed Plasma Accelerator. In E. Stuhlinger, editor, *Electric Propulsion Development*, volume 9 of *Progress in Astronautics and Rocketry*. Academic Press, 1963.

[99] D. Keefer and R. Rhodes. Electromagnetic Acceleration in Pulsed Plasma Thrusters. In 25th *International Electric Propulsion Conference*, Cleveland, Ohio, August 24-28 1997. IEPC 97-035.

[100] P.J. Turchi and P.G. Mikellides. Modeling of Ablation-fed Pulsed Plasma Thrusters. In 31st *Joint Propulsion Conference*, San Diego, California, June 10-12 1995. AIAA 95-2915.

[101] P.G. Mikellides, P.J. Turchi, et al. Theoretical Studies of a Pulsed Plasma Microthruster. In 25th *International Electric Propulsion Conference*, Cleveland, Ohio, August 24-28 1997. IEPC 97-037.

[102] B. Gorowitz, P. Gloersen, and T.W. Karras. Steady State Operation of a Two-Stage Pulsed Coaxial Plasma Engine. In 5th *Electric Propulsion Conference*, San Diego, California, March 7-9 1966. AIAA 66-240.

[103] R.H. Lovberg. Inference of Plasma Parameters from Measurement of E and B Fields in a Coaxial Accelerator. In *Proceedings of an International Symposium on Plasma Guns, Physics of Fluids Supplement (Part II, Vol. 7(11))*, pages S57–S61, November 1964.

[104] W.R. Ellis. *An Investigation of Current Sheet Structure in a Cylindrical Z-pinch*. PhD thesis, Princeton University, 1967.

[105] T.M. York. *Pressure Distribution in the Current Sheet Structure of a Dynamic Pinch Discharge*. PhD thesis, Princeton University, 1968.

[106] T.M. York and R.G. Jahn. Pressure Distribution in the Structure of a Propagating Current Sheet. *The Physics of Fluids*, 13(5):1303–1309, May 1970.

[107] T.E. Markusic. Movie of a parallel-plate gas-fed pulsed plasma thruster discharge. http://www.princeton.edu/∼eppdyl/.